REPORT NO.
UCB/EERC-88/08
JUNE 1988

EARTHQUAKE ENGINEERING RESEARCH CENTER

ANALYSIS OF NEAR-SOURCE WAVES: SEPARATION OF WAVE TYPES USING STRONG MOTION ARRAY RECORDINGS

by
ROBERT B. DARRAGH

PREFACE

by
BRUCE A. BOLT

Report to the National Science Foundation

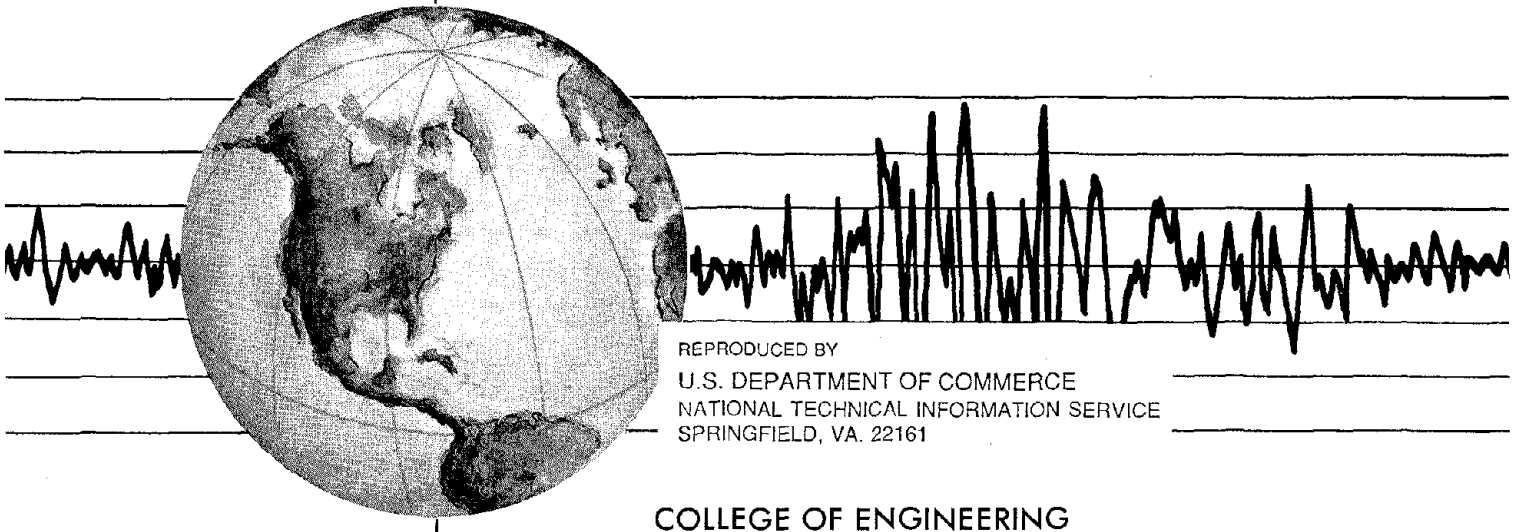

COLLEGE OF ENGINEERING

UNIVERSITY OF CALIFORNIA AT BERKELEY

For sale by the National Technical Information Service, U.S. Department of Commerce, Springfield, Virginia 22161

See back of report for up to date listing of EERC reports.

50272-101

REPORT DOCUMENTATION PAGE	1. REPORT NO. NSF/ENG-88045	2.	3. PB91-212621

4. Title and Subtitle
Analysis of Near-Source Waves: Separation of Wave Types Using Strong Motion Array Recordings

5. Report Date
June 1988

6.

7. Author(s)
Robert B. Darragh

8. Performing Organization Rept. No.
UCB/EERC-88/08

9. Performing Organization Name and Address
Earthquake Engineering Research Center
University of California, Berkeley
1301 S 46th St.
Richmond, CA 94804

10. Project/Task/Work Unit No.

11. Contract(C) or Grant(G) No.
(C)
(G) CEE 84-17856

12. Sponsoring Organization Name and Address
National Science Foundation
1800 G. St. NW
Washington, DC 20550

13. Type of Report & Period Covered

14.

15. Supplementary Notes

16. Abstract (Limit: 200 words)

Algorithms are developed for the separation and identification of seismic wave types in the near-source region. Two large earthquakes (M_L = 6.3, 6.2) recorded by over twenty-five digital, three component accelerometers that make up SMART 1 (Strong Motion Array Taiwan 1), are used to demonstrate the methods.

A sub-array of the SMART 1 array, consisting of the center station and the inner and middle rings, is used to analyze the ground acceleration wavefield. Two complimentary analyses of the cross-spectral matrix are applied to the three rotated components of ground acceleration. Frequency-wavenumber spectral analysis demonstrates that the mixture of wave types that propagated across a 2 km radius sub-array was different for the two earthquakes. In contrast, the polarization of the wavefields over the 2 km sub-array was similar for the two earthquakes. For both earthquakes, polarized (coherent), broadband P-wave energy and S-wave energy, significantly different than noise at the 95 percent confidence level, was observed. A crustal anomaly or "heterogeneous scattering center" has been located 1 to 1.5 km southeast of the array center and is estimated to be at a depth between 1.5 and 2.0 km.

17. Document Analysis a. Descriptors
array
spectral analysis
polarization
body wave
surface wave
coherence

b. Identifiers/Open-Ended Terms
heat source
P-wave energy
S-wave energy

c. COSATI Field/Group

18. Availability Statement:	19. Security Class (This Report)	21. No. of Pages
Release Unlimited	unclassified	159
	20. Security Class (This Page) unclassified	22. Price

ANALYSIS OF NEAR-SOURCE WAVES:

SEPARATION OF WAVE TYPES USING STRONG MOTION ARRAY RECORDINGS

by

Robert B. Darragh

PREFACE

by

Bruce A. Bolt

Report to the National Science Foundation

Report No. UCB/EERC-88/08
Earthquake Engineering Research Center
University of California
Berkeley, California

June 1988

Analysis of near-source waves:
Separation of wave types using strong motion array recordings

Robert Bernard Darragh

PREFACE

This report is one of a series arising from research on seismic strong ground motion based on the measurements made by the large-scale digital array of accelerometers in Taiwan, called SMART 1. This array became operational in September 1980 and through 1988 has recorded over 3000 accelerograms from 50 local earthquakes. Peak ground accelerations up to 0.33g and 0.34g have been recorded on the horizontal and vertical components, respectively. A preliminary discussion of the operation of the array and some earlier research results was given in the report UCB/EERC-82/13 (August 1982) by B. A. Bolt, C. H. Loh, J. Penzien, Y. B. Tsai and Y. T. Yeh. A second report in the EERC series was published in 1985 entitled, "Estimation of Seismic Wave Coherency and Rupture Velocities Using SMART 1 Strong-Motion Array Recordings," by N. A. Abrahamson (UCB/EERC-85/02). An up-to-date summary of related research through 1986 entitled, "The SMART 1 Accelerograph Array (1980-1987): A Review," by N. A. Abrahamson, B. A. Bolt, R. B. Darragh, J. Penzien and Y. B. Tsai, can be found in *Earthquake Spectra,* 3, 263-287, 1987.

From its inception, the array has provided key information on both seismological and earthquake engineering problems. One crucial question that is common to both disciplines is the identification of wave types in near-field ground motions. As is well known, seismic waves of body and surface types in the far-field (relative to the source dimension) have largely separated into a definitive succession so that an asymptotic theory can explain the major part of the motion. In sharp contrast, in the near-field, accelerograms are often complicated by lack of separation of wave types, in part due to the effect of the spreading of the dislocation on the extended fault plane. As well, in both near and far-fields, complexities arise from wave scattering from local structural variations in the rocks and soils along the propagation path.

The present report by R. B. Darragh addresses the question of identification of seismic waves recorded by accelerographs relatively near the earthquake source. The waves may be called strong motion in that they have peak accelerations that are in excess of 0.1g. Wave

separation is analyzed by making use of the phasing properties of the spatial array of ground motion sensors. One useful method is the decomposition of propagating wave fields using frequency-wavenumber spectral analysis. A more traditional seismological method, extended by Darragh to data of the SMART 1 type, is wave discrimination through mapping of orbits of the particles during the ground motion. This attention to the vector properties of the wave motion is called polarization analysis. The polarization method is shown to be an effective way to estimate the relative proportions of wave types mixed in the strong ground motion.

Finally, it is well known that, in many cases, spatial variation in ground motion arises from local geological effects. This report shows that array analysis permits the identification of major strong motion scatterers near recording sites. Variation of the intensity of shaking and coherency can thus be better understood and quantified for engineering requirements (see "Seismic Strong Motion Synthetics," B. A. Bolt, Editor, Academic Press, 1987).

Readers of this report can obtain digital records from the SMART 1 research program in standard formats on request from the undersigned at the Seismographic Stations, University of California at Berkeley.

Bruce A. Bolt

ABSTRACT

Algorithms are developed for the separation and identification of seismic wave types in the near-source region. Two large earthquakes recorded by over twenty-five digital, three component accelerometers that make up SMART 1 (Strong Motion Array Taiwan 1), are used to demonstrate the methods: the 29 January 1981 earthquake (M_L=6.3, epicentral distance to array center: 30 km) and the 16 January 1986 earthquake (M_L=6.2, epicentral distance to array center: 22 km).

A sub-array of the SMART 1 array, consisting of the center station and the inner and middle rings, is used to analyze the ground acceleration wavefield. Two complimentary analyses of the cross-spectral matrix are applied to the three rotated components of ground acceleration. The incident wavefield is first decomposed by frequency-wavenumber spectral analysis into either broadband plane waves or broadband spherical waves when the source of the waves is within the array. Each spectral peak may be interpreted as a body, surface or scattered wave each propagating across the sub-array with its own apparent horizontal velocity and direction. Secondly, polarization analysis estimates the broadband or narrowband polarization of the ground acceleration wavefield and provides a lower bound estimate of the coherence ("incoherency") of the wavefield.

Frequency-wavenumber spectral analysis demonstrates that the mixture of wave types that propagated across a 2 km radius sub-array was different for the two earthquakes. For example, broadband planar P-wave energy was observed for six to seven seconds during the 1981 earthquake, but for only two to three seconds during the 1986 earthquake at the 90 percent (approximate) confidence level. Broadband planar S-wave energy was observed for four to five seconds during the 1981 earthquake, but for only one to two seconds during the 1986 earthquake at the 90 percent (approximate) confidence level. In various time windows, the ground acceleration wavefield has been decomposed into multiple wave arrivals, for example, P and S, P and Rayleigh, and S and Love. Rotations of the azimuth of the peak

plane wave power that have been associated with propagation of the fault source rupture are not observed, at the 90 percent (approximate) confidence interval, for either large earthquake.

In contrast, the polarization of the wavefields over the 2 km sub-array was similar for the two earthquakes. For both earthquakes, polarized (coherent), broadband P-wave energy and S-wave energy, significantly different than noise at the 95 percent confidence level, was observed. Polarization of the S-wavefields between 0.5 and 0.7 was, generally, less than polarization of the P-wavefields of approximately 0.8. For both earthquakes the polarization of the surface wave coda was, generally, not significantly different than noise at the 95 percent confidence level.

A crustal anomaly or "heterogeneous scattering center" has been located 1 to 1.5 km southeast of the array center and is estimated to be at a depth between 1.5 and 2.0 km. This heterogeneity produced scattered, strongly polarized energy on both the horizontal components of ground motion prior to the direct S-wave onset during the 1986 earthquake. For the 1981 earthquake, the direct and scattered wavefields are not separable because the hypocenter, the crustal anomaly and the array center are collinear.

Acknowledgments

I would like to thank Professor Bruce Bolt for supporting my interest in strong motion seismology and for many discussions. Professors David Brillinger, Lane Johnson, Joseph Penzien and Dr. Robert Uhrhammer provided many helpful comments.

I thank my fellow graduate students, especially Dr. Patty Murtha-Stoffregen, Alberto Michelini, Cathy Stark, Anthony Lomax and S. J. Chiou. Dr. Norman Abrahamson was available for many helpful discussions, and provided the frequency-wavenumber software. Also, special thanks to Dr. Belinda Martineau for her careful review. Russell Sell and the staff of the seismographic station provided valuable technical assistance and functioning computers.

The continued support of the faculty and staff of the Institute of Earth Sciences in Taiwan of the SMART 1 project is gratefully acknowledged. This work was partially supported by the National Science Foundation grant CEE 84-17856.

Finally, I thank my family and friends for their support.

Table of Contents

ANALYSIS OF NEAR-SOURCE WAVES: SEPARATION OF WAVE TYPES USING STRONG MOTION ARRAY RECORDINGS

CHAPTER 1: INTRODUCTION AND REVIEW OF PREVIOUS STUDIES

Earthquake ground motions consist of two fundamental varieties of elastic waves: body waves of P and S type and Love and Rayleigh surface waves. Identification of these waves on seismograms has been a central problem in seismology since Oldham (1900) first identified the "preliminary tremors" and the "large waves" on seismograms from distant earthquakes. For a distant earthquake the identification of the elastic waves is facilitated by their temporal separation from one another due to their different propagation velocities. In the near-source region the records of elastic waves are likely to be complicated and difficult to interpret because reflected, refracted, direct, converted and scattered energy from many different areas of the source can arrive at the observer simultaneously. Analyses that provide an estimate of the mixture of wave types as a function of time in the near-source region of large earthquakes are required for the realistic synthesis of ground motions for use in engineering design.

One expects ground motions recorded in near-source regions to have some wave patterns analogous to patterns of small amplitude ground motions recorded from distant earthquakes. When that expectation is valid there should be initially ground motions made up primarily of the longitudinal P-waves. Later in the ground motion record, depending on the distance between the receiver and the source, there would be an onset of S-waves that will be superimposed on the P-waves still arriving from other areas of the moving source. The large amplitude ground motion will continue, a mixture of S and P-waves, but the S motions become dominant later in the record. Still later, Love surface waves mixed with body waves should be present on the horizontal components, while Rayleigh surface waves mixed with body waves should be present on the vertical and radial components. Depending on the distance of the receiver from the causative fault and on the intervening Earth structure, the surface waves will be dispersed into wave trains with certain frequency

characteristics (e.g. Hanks, 1975; Hartzell, *et al.*, 1978). The record coda is likely to be significantly affected by the depth of the ruptured fault; for large focal depths it is less likely that a significant train of surface waves will be present in the strong motion records.

The elasto-dynamic equations of motion provide a theoretical framework to calculate the ground displacement in near-source regions. Following Aki and Richards (1980), the displacement, **u**, due to a double-couple point source in an infinite homogeneous medium is given by

$$\mathbf{u}(\mathbf{x},t) = \frac{1}{4\pi\rho}\mathbf{A}^N\frac{1}{r^4}\int_{r/\alpha}^{r/\beta}\tau M_o(t-\tau)d\tau$$

$$+ \frac{1}{4\pi\rho\alpha^2}\mathbf{A}^{IP}\frac{1}{r^2}M_0(t-\frac{r}{\alpha}) + \frac{1}{4\pi\rho\beta^2}\mathbf{A}^{IS}\frac{1}{r^2}M_o(t-\frac{r}{\beta}) \qquad (1.1)$$

$$+ \frac{1}{4\pi\rho\alpha^3}\mathbf{A}^{FP}\frac{1}{r}\dot{M}_o(t-\frac{r}{\alpha}) + \frac{1}{4\pi\rho\beta^3}\mathbf{A}^{FS}\frac{1}{r}\dot{M}_o(t-\frac{r}{\beta}) \quad ,$$

where ρ, α, β, r and $\mathbf{x}$ are the density, P-wave velocity, S-wave velocity, source to receiver distance and receiver position, respectively. The vectors $\mathbf{A}^N$, $\mathbf{A}^{IP}$, $\mathbf{A}^{IS}$, $\mathbf{A}^{FP}$ and $\mathbf{A}^{FS}$ are the radiation patterns for the near-field, intermediate-field P, intermediate-field S, far-field P and far-field S-waves, respectively. These terms depend only on the geometry that exists between the source and receiver. The time dependent seismic moment is given by

$$M_o(t)=\mu\bar{u}(t)A \quad , \qquad (1.2)$$

where A is the area of the shear dislocation of average slip ($\bar{u}(t)$) and shear modulus (μ), where it has been assumed for the derivation of equation (1.1) that the moment tensor, **M**, has zero trace. Equation (1.1) consists of three body wave terms; the near-field, the intermediate-field (P-wave and S-wave) and the far-field (P-wave and S-wave). The far-field displacements attenuate as r^{-1} and are proportional to the particle velocity at the source. The onset times at the receiver are given by (r/α) and (r/β) for the P-wave and the S-wave, respectively. The far-field P-wave has only a radial component in its radiation pat-

tern (A^{FP}), and the far-field S-wave has only a transverse component in its radiation pattern (A^{FS}). The near-field displacements attenuate as approximately r^{-2} and are non-zero after the onset time of the far-field P-wave. The terms that decay as r^{-2}, the intermediate-field terms, are proportional to particle displacement at the source. The intermediate-field displacements are also non-zero after the onset time of the far-field P-wave. The near-field and intermediate-field P and S-waves are composed of both radial and transverse components. In general, the far-field terms from a point source dominate when the distance from the source is such that $\beta/\omega r \ll 1$, where ω is the angular frequency of the wave. At short distances all the terms may be of equal importance; this occurs, for example, at a distance of 300m or less for 10 Hz waves or at a distance of 30 km or less for 0.1 Hz waves. For a finite dimension source, r must also be large compared to the source dimension in order for the far-field terms to dominate the ground motions (Brune, 1976).

For surface waves, the source to receiver distance (r) may have to be at least five times greater than the source plus receiver depths in order for the Rayleigh pulse to be observed as produced from a SV-wave line source embedded in an elastic half space (Aki and Richards, 1980). Using this criterion one might expect the Rayleigh waves to be poorly developed in the near-source region of a large earthquake; however, other effects not considered in this simple model (e.g. vertical and lateral variations of structure and velocity, as well as, higher Rayleigh wave modes) may change this critical distance. Brune (1976) estimated that surface waves may be the predominant waves generating large amplitude ground motions when the distance between the source and the receiver is comparable to, or greater than, the earthquake source depth. Observational evidence of surface waves at epicentral distances of 30 km and greater is available for, for example, the 1971 San Fernando earthquake (Hanks, 1975) and the 1974 Acapulco earthquake (Hartzell, *et al.*, 1978). The velocity gradients in the sediments beneath the San Fernando and Los Angeles basins produced the strongly dispersed surface waves observed in the San Fernando displacement records. For the Acapulco earthquake, the observed high frequency (1-4 Hz) dispersed

surface waves may have been the result of the trapping of energy in a fairly well defined region close to the surface, below which there was little change in wave velocity (Hartzell, *et al.*, 1978).

An example of the mixing of wave types, observed in the near-source region of the 1971 San Fernando earthquake, is described by Bolt (1972) in a ray theory interpretation of the Pacoima accelerogram. (Pacoima is located approximately 8 km from the fault surface.) Predominantly P-waves arrived from the source for approximately the first 6.7 seconds on the vertical component, S-waves arrived 1.7 to approximately 8.0 seconds after the initial P-wave onset. Later in the record, Rayleigh waves arrived approximately 4.25 seconds after the initial P-wave onset on the vertical and horizontal components in agreement with Brune (1976). Surface wave energy generally increased throughout the record after this time.

In another single-station analysis of strong motion records from the 1971 San Fernando earthquake, Vidale (1986) analyzed three accelerograms along a North-South profile spaced over approximately 26 km. The nearest accelerometer was located approximately 11 km from the surface trace of the ruptured fault. In an effort to help identify the predominant wave type three component analysis of the polarization of the wavefield as a function of time was estimated. Monochromatic seismic waves exhibit simple polarization (see Chapter 2.4). When the two horizontal components of the seismic wave field are in phase, the wave is linearly (or plane) polarized. Estimates of both the planar and angular polarization (averaged over a three second window) allowed Vidale (1986) to identify the SV, Love and Rayleigh waves on the San Fernando earthquake records.

These two wave type separation studies were restricted due to the fact that dense array observations of the ground motion were not available. Using only single station recordings it was not possible to estimate wave slowness or to estimate the mixture of waves as a function of time.

Two additional examples of studies using polarization analysis are those of Archuleta (1982) and Niazi (1982, 1985) on the 1979 Imperial Valley earthquake. Both studies used

the polarization of the wave field at individual stations to obtain information about the rupture dynamics. Archuleta (1982) estimated the polarization of the particle velocities on the horizontal components of ground motion recorded at two stations near the Imperial fault. The magnitude of the polarization is given by the square-root of the vector sum of the two horizontal components of particle velocity; the angle of polarization is given by the arc tangent of the ratio of the two horizontal components of particle velocity (e.g. Kanasewich, 1981). Archuleta observed an initial polarization in the 50° direction due to near-field ground motions, followed by a polarization reversal to 230° with the arrival of the S-waves. Niazi (1982,1985) studied the temporal variation in the polarization angle for the low frequency (< 1 Hz) P-waves at accelerometers 1, 2 and 3 in the linear El Centro Differential array, located 5.6 km from the Imperial fault. Assuming the P-wave is linearly polarized and the Earth velocity structure is laterally homogeneous, the major axis of a rose diagram for horizontal components of particle polarization will point in the direction of the source from which the wave originated. Niazi measured the direction of polarization during the first five seconds of the 1979 recordings and found that the main axis of the rose diagrams rotated counterclockwise by as much as 50°. After five seconds the accelerations were dominated by shear wave arrivals precluding further estimation of the P-wave polarization.

The subject of this dissertation is the identification of individual wave types and the determination of the percentage of the different types within the mixture of waves observed in the near-source region of large earthquakes. These identifications and determinations are carried out using data from many accelerographs densely positioned in an array. Previously, data from dense accelerograph arrays have been used to study the spatial variation of ground motions during large local earthquakes (Smith, *et al.*, 1982; Loh, *et al.*, 1982; Bolt, *et al.*, 1984; Abrahamson and Bolt, 1985; Oliveira, *et al.*, 1985; Niazi, 1986). Such studies provide estimates of the magnitudes of the strains produced by spatial variation in ground motions. Such estimates are required for the earthquake resistant design of such large structures as bridges and pipelines.

A second importance of studies using data collected from accelerograph arrays has been to estimate dynamic source properties of a rupturing fault. For example, Spudich and Cranswick (1984) used recordings of the 1979 Imperial Valley, California earthquake at the five station El Centro Differential array. They applied a cross-correlation procedure, using a moving time window, to measure the apparent slowness on the vertical and horizontal components of the P and S-waves as they impinged on the array. Due to the close proximity of this array and the Imperial fault, the 30 km length rupture produced a variation of 150° in the direction of propagation of the waves. Based on detailed knowledge of the Earth velocity structure between the array and the Imperial fault, the apparent slownesses of waves observed at the El Centro Differential array were correlated with a source position on the fault surface (assuming that the observed ground motions were composed solely of P and S-waves). As a result of this correlation, Spudich and Cranswick were able to observe changes in the rupture velocity as a function of time. Difficulties with the analysis included the short length of the array (213 m) and restriction to scalar slowness caused by the linearity of the array. Abrahamson (1985) used recordings taken at the Strong Motion Array Taiwan number 1 (SMART 1) to observe rupture propagation during a M_L=6.3 earthquake on 29 January 1981 (Event 5). Twenty-seven SMART 1 stations, located approximately 30 km NNW of the epicenter, recorded the earthquake. The rupture length was estimated to be 19 km by integrating the rupture velocity which varied between 2.1 km/sec and 4.9 km/sec. This analysis was impeded by geometric considerations; due to the short rupture length and the fault orientation relative to the SMART 1 array, variation in the direction of body wave propagation was approximately 30°.

To attain the seismological goals of this dissertation, analytical techniques had to be applied that would separate ground motions recorded at an array of accelerometers into wave types as a function of time. Suites of ground motion data that had wide dynamic range, low noise, common time base and significant redundancy would be clearly advantageous to work with. The SMART 1 array, located near the city of Lotung in the northeast

corner of Taiwan, provided such data. I have used data collected from a subset of the SMART 1 array. This subset consists of a maximum of 25 force-balanced triaxial accelerometers configured in two concentric circles of radii 200m and 1000m. These rings are referred to as I (inner) and M (middle). There are twelve evenly spaced stations on each ring (numbered 1 through 12) and a central station (C-00). The circular array suits the omni-directional azimuthal distribution of likely potential sources of strong earthquakes in northeastern Taiwan. The SMART 1 array and the data recorded by the array are described in more detail elsewhere (Bolt *et al.*, 1982; Abrahamson, 1985; Appendix A of this dissertation).

Two large earthquakes that occurred near the SMART 1 array have been selected for analysis: Event 5, (M_L=6.3, epicentral distance to array center = 30.2 km, focal depth = 25.2 km) that occurred on 29 January 1981 04:51 UTC and was recorded by 17 sub-array stations; and Event 39, (M_L=6.5, epicentral distance to array center = 22.2 km, focal depth = 10.2 km) that occurred on 16 January 1986 13:04 UTC and was recorded by 23 sub-array stations. The peak horizontal ground acceleration recorded at the array is in excess of 0.24g for both events.

In previous studies of recordings from the SMART 1 array, Loh and Penzien (1984) identified wave types by estimating a principal variance ratio. This ratio is defined as the cross-correlation in the minor principal direction (x_o) at frequency (f_o) divided by the cross-correlation in the major principal direction (ϕ_o) at frequency f_o. The statistic ranges over the values 0 to 1. Low values of the ratio correspond to a single wave type dominating the ground motion. Event 5 recordings during a 7.0 second time window containing the large amplitude ground accelerations were examined from various station pairs. These authors concluded that on the horizontal components the Rayleigh waves are the primary source of energy for frequencies less than approximately 2.5 Hz and SH and perhaps Love waves are the primary source of energy for frequencies from 2.5 to 6 Hz. (The observation of surface waves at a distance comparable to the focal depth is in agreement with Brune,

1976.) Above 6 Hz, the ground motion contained many scattered wave arrivals and could not be characterized as a single wave type. Loh and Peng (1985) analyzed the three component accelerograms from the same event using particle motions to identify P, SV and SH waves at different frequencies. These authors identified SV waves at 1.17 Hz, SH and SV waves at 2.87 Hz and P waves in the frequency band between 5.0 and 8.0 Hz. Both of these studies used single stations or station pairs to identify the wave types.

Abrahamson (1985) used 27 stations simultaneously in a narrowband frequency-wavenumber (f-$\vec{k}$) analysis (see Chapter 2.3). The essential feature of f-$\vec{k}$ analysis is the decomposition of the incident wave field into constituent monochromatic plane waves, each having its own propagation velocity and its own direction of travel (see e.g. Bullen and Bolt, 1985). After such decomposition the various seismic waves can be identified, as body or surface waves incident from different directions, using conventional seismic wave discrimination techniques (slowness, polarization, particle motions, etc.). Using an estimate of the apparent horizontal wave slowness, Abrahamson (1985) qualitatively demonstrated that this technique could be used to determine, under certain circumstances, the percentage of coherent P or S-waves as a function of time in the strong motion record. At 2 Hz on the vertical component and during a time window after the direct S-wave onset, Abrahamson observed two distinct peaks in the f-$\vec{k}$ spectrum, one at the P-wave slowness (s=0.09 sec/km) and one at the S-wave slowness (s=0.3 sec/km). The amplitude of the P-wave peak was approximately 3 db lower than the amplitude of the S-wave peak, an observation indicating that, at 2 Hz in this time window, there is slightly more S energy than P energy.

The central body of this work is a detailed analysis of the cross-spectral matrix for the three components of rotated ground accelerations from two large earthquakes recorded at the SMART 1 array. Two complimentary methods of analysis of the cross-spectral matrix are used. The f-$\vec{k}$ method, extended to a broad range of frequencies, provides a decomposition of the cross-spectral matrix into broadband coherent, planar waves as a function of time. The second technique, calculated from the invariants of the cross-spectral matrix,

decomposes the ground accelerations into broadband polarized, planar waves as a function of time. For the first time, analysis of data recorded by an array of accelerographs and utilizing these broadband techniques provides, from ground accelerations recorded within 30 km of the source, a quantitative measure of the mixture of wave types as a function of time.

The structure of this dissertation is as follows. Chapter 2 describes in detail the methods of computation of the cross-spectral matrix and the frequency-wavenumber estimate, and the polarization analysis used in the following chapters. Chapter 3 employs a broadband f-$\vec{k}$ method in a sliding time window analysis of strong ground motions. The azimuth and apparent horizontal slownesses of broadband coherent, planar P, S and surface waves are estimated as a function of time. Multichannel data allow the estimation of a cross-spectral matrix containing all the necessary information on the polarization of the wavefield. In chapter 4, the wavefield, in sliding time windows, is decomposed into broadband, polarized planar waves by using estimates of the invariants of the cross-spectral matrix. The frequency dependent degree of polarization is estimated as a function of time. Chapter 5 compares the results obtained using these two methods, discusses the implications of the results for the generation of synthetic seismograms, and makes recommendations for future research.

CHAPTER 2: METHODS OF COMPUTATION

2.1 Introduction

Both the frequency-wavenumber (f-$\vec{k}$) analysis of chapter 3 and the polarization analysis of chapter 4 are primarily based on information contained in the cross-spectral matrix (S(ω)). A clear understanding of the cross-spectral matrix and some of its basic properties is, therefore, necessary in order to conduct these analyses. The notation given here follows Brillinger (1981).

2.2 The Cross-spectral Matrix

The recorded ground accelerations at the jth station of the SMART 1 array, $\vec{u}(\vec{r}_j,t)$, represent a three dimensional wavefield. The locations of the array stations are given by $\vec{r}_j = (x_j,y_j,z_j)$. Estimates of the cross-spectral matrix are commonly constructed from the recorded signals, $\vec{u}(\vec{r}_j,t)$, in one of the following two ways. S(ω) is the Fourier transform of the matrix of cross-covariances and is given by

$$\mathbf{S}(\omega) = \frac{1}{2\pi}\sum_{\alpha=-\infty}^{\infty} \mathbf{c}(\alpha)\, e^{-i\omega\alpha} \qquad \text{for} \quad -\infty < \omega < \infty \quad . \tag{2.2.1}$$

The component (c_{ab}) of the matrix **c** is the cross-covariance of the ath component of the time series $\vec{u}(\vec{r}_j,t)$ t=0,±1,... with the bth component of the time series $\vec{u}(\vec{r}_k,t)$ t=0,±1,... . The elements of the smoothed cross-spectral matrix are also given by

$$S_{jk}(\omega) = \sum_{m=-M}^{M} a_m d_u^T(\vec{r}_j,\omega+\frac{2\pi m}{T})\overline{d_u^T(\vec{r}_k,\omega+\frac{2\pi m}{T})} \tag{2.2.2}$$

where $d_u^T(\vec{r}_j,\omega)$ is the T length discrete Fourier transform of the ath component of $\vec{u}(\vec{r}_j,t)$ and is given by

$$d_u^T(\vec{r}_j,\omega) = \Delta t\sum_{t=0}^{T-1} u_a(\vec{r}_j,t)e^{-i\omega t} \quad , \tag{2.2.3}$$

where the overbar indicates the complex conjugate. The sample interval (Δt) is equal to

0.01 second for the digitally recorded SMART 1 data. The weights or tapers, a_m, are normalized so that they sum to unity. A Hamming window function is a common choice for a_m (McLaughlin, 1983; Abrahamson and Bolt, 1987). Implicit in equation (2.2.2) is the dependence of $S(\omega)$ on the frequency bandwidth given by $\Delta\omega = 2\pi(2M+1)/T\Delta t$. The estimate of $S(\omega)$ in (2.2.1) is unbiased when the spectra are flat (Jenkins and Watts, 1969).

The estimate of the cross-spectral matrix is smoothed over 2M+1 near-neighbor frequencies where the values are assumed to be independent, identically-distributed complex normal variates. The smoothing is applied to the individual cross-spectral estimates, (2.2.2), and not to the Fourier spectral estimates, (2.2.3). The complex Fourier transform values have a mean of zero, but the product in (2.2.2) has a non-zero mean over narrow frequency bands (Abrahamson, 1985).

Equation (2.2.2) can be rewritten as

$$S_{jk}(\omega) = \sum_{m=-M}^{M} a_m A_j(\omega_m) A_k(\omega_m) e^{i(\phi_j(\omega_m)-\phi_k(\omega_m))} \quad , \tag{2.2.4}$$

where $A_j(\omega_m)$ and $\phi_j(\omega_m)$ are the Fourier amplitude and phase, respectively. For a single deterministic signal, the arithmetic mean for the complex exponential of the phase differences in equation (2.2.4) is zero so that smoothing a slow deterministic signal over a broad frequency band results in $S_{jk}(\omega) = 0$ and the signal is destroyed. An alternative (Abrahamson, personal communication) is to define the cross-spectral matrix using a weighted geometric mean. The elements of the cross-spectral matrix are then given by

$$S_{jk}(\omega) = \prod_{m=-M}^{M} [A_j(\omega_m) A_k(\omega_m) e^{i(\phi_j(\omega_m)-\phi_k(\omega_m))}]^{a_m} \quad , \tag{2.2.5}$$

and can be rewritten as

$$S_{jk}(\omega) = \prod_{m=-M}^{M} [A_j(\omega_m) A_k(\omega_m)]^{a_m} \exp[i \sum_{m=-M}^{M} a_m(\phi_j(\omega_m)-\phi_k(\omega_m))] \quad . \tag{2.2.6}$$

For a single deterministic signal with constant slowness, the phase difference between stations, unwrapped to remove the 2π phase jumps, is linear with respect to frequency. The

cross-spectral matrix defined in (2.2.6) can then be smoothed over an arbitrarily wide frequency band without destroying the deterministic signal as long as the phase differences are unwrapped and the weights, a_m, are symmetric; that is, $a_m = a_{-m}$.

The following are some elementary properties of the cross-spectral matrix.

1) $S(\omega)$ is an NxN matrix, where N is the number of stations.

2) $S(\omega)$ is Hermitian, that is, $S(\overline{\omega}) = S^{\tau}(\omega)$ where the superscript τ denotes the transpose. The eigenvalues of $S(\omega)$ are real and positive; the eigenvectors are generally complex valued. For numerical analysis, each eigenvalue of $S(\omega)$ is perfectly conditioned; that is, the (absolute) change in an eigenvalue is not more than the (absolute) change in $S(\omega)$. In other words, the problem of determining eigenvalues of Hermitian matrices is always well posed; the solution is well determined by the data, $\vec{u}(\vec{r}_j,t)$ (Noble and Daniel, 1977; Parlett, 1980).

3) $S(\omega)$ is non-negative definite; that is, $\vec{\alpha}^{\tau}S(\omega)\vec{\alpha} \geq 0$ for all Nx1 vectors $\vec{\alpha}$ with complex entries.

4) Upon normalizing the Fourier spectral estimates in (2.2.3) to remove the site effects or the effects of uniform attenuation, $S(\omega)$ in (2.2.2) becomes the matrix of exponential phase differences whose elements are given by

$$S_{jk}(\omega) = \sum_{m=-M}^{M} a_m \exp[i(\phi_u^T(\vec{r}_j,\omega+\frac{2\pi m}{T})-\phi_u^T(\vec{r}_k,\omega+\frac{2\pi m}{T}))] \quad , \tag{2.2.7}$$

with phase

$$\phi_u^T(\vec{r},\omega) = \tan^{-1}[\frac{\mathrm{Im}(d_u^T(\vec{r},\omega))}{\mathrm{Re}(d_u^T(\vec{r},\omega))}] \quad . \tag{2.2.8}$$

2.3 Frequency-wavenumber Methods

The reader is referred to Capon (1969), McLaughlin (1983), Abrahamson (1985), Brillinger (1985) and Abrahamson and Bolt (1987) for more information on the conventional (CV), the high-resolution (HR) and the maximum-likelihood estimates of the power in the wavefield. These methods assume that the incident wavefield is composed of plane waves, each with its own apparent propagation velocity and direction across the array (see Bullen and Bolt, 1985).

The conventional (or beamforming) estimate of the power spectrum is

$$P^C(\vec{k},\omega) = \frac{1}{N^2}\vec{\vec{U}}^{\tau}(\vec{k})\mathbf{S}(\omega)\vec{U}(\vec{k}) \quad , \tag{2.3.1}$$

where $U_j(\vec{k}) = \exp(i\vec{k} \cdot \vec{r}_j)$ are the elements of the beamsteering vector. The statistical properties of the estimate are discussed by Capon and Goodman (1970) and Capon (1971). The 90% confidence interval in decibels is approximately given by

$$\pm\frac{20}{(k-1)^{1/2}} \quad , \tag{2.3.2}$$

where k is the number of degrees of freedom for an χ^2_k-variate (Blackman and Tukey, 1959). For the conventional estimate, k=4M+2 where the cross-spectrum has been smoothed over 2M+1 near-neighbor frequencies.

The high resolution estimate of the power spectrum is

$$P^{HR}(\vec{k},\omega) = [\vec{\vec{U}}^{\tau}(\vec{k})\mathbf{S}^{-1}(\omega)\vec{U}(\vec{k})]^{-1} \quad . \tag{2.3.3}$$

The statistical properties of the HR estimate are also discussed by Capon and Goodman (1970) and Capon (1971) who show that $P^{HR}(\vec{k},\omega)$ is a biased estimate. This bias is easily removed by scaling the HR estimate by $\frac{2M+1}{2M-N+2}$. As for the conventional method, the 90% confidence interval in decibels is approximately

$$\pm\frac{20}{(k-1)^{1/2}} \quad , \tag{2.3.4}$$

(Blackman and Tukey, 1959), although for the HR estimate, k = 2(2M-N+2) in the χ^2_k distribution. For the chi-squared distribution to be valid the cross-spectral matrix must be smoothed over at least as many near-neighbor frequencies as there are stations ($2M+1 \geq N$). Table 2.1 gives the frequency bandwidths as a function of the number of stations (N) and the length of the Fourier transform (T). To obtain bandwidths of 1 Hz or less for the entire SMART 1 array requires a Fourier transform of approximately 4096 points, longer than most of the recorded acceleration time series (that range from 25 to 30 seconds, 2500 to 3000 sample points). For narrowband f-$\vec{k}$ estimates, the requirement that $2M+1 \geq N$ leads to a decrease in the validity of the statistical distribution as N decreases (see Abrahamson, 1985) and a trade-off between spatial sample redundancy and spatial aliasing.

Table 2.1

TIME SAMPLES (T)	SMALLEST FREQUENCY $(T\Delta t)^{-1}$ (Hz)	NUMBER OF STATIONS (N)	SMOOTHING (M)	MINIMUM BANDWIDTH $2M(T\Delta t)^{-1}$ (Hz)
128	0.7813	13	6	9.38
		25	12	18.75
		37	18	28.13
256	0.3906	13	6	4.69
		25	12	9.38
		37	18	14.06
512	0.1953	13	6	2.34
		25	12	4.68
		37	18	7.03
1024	0.0977	13	6	1.17
		25	12	2.34
		37	18	7.03
2048	0.0488	13	6	0.59
		25	12	1.17
		37	18	1.76
4096	0.0244	13	6	0.29
		25	12	0.59
		37	18	0.88

The maximum-likelihood f-$\vec{k}$ estimate of the power spectrum (Brillinger, 1985) is given by

$$P^{ML}(\vec{k},\omega) = \frac{\vec{U}^{*T}(\vec{k})\mathbf{S}^{-1}(\omega)\vec{U}(\vec{k})}{\vec{U}^{*T}(\vec{k})\mathbf{S}'^{-1}(\omega)\vec{U}(\vec{k})} - 1 \quad , \tag{2.3.5}$$

where the components of the modified cross-spectral matrix, S'(ω), are given by

$$S'_{jk}(\omega) = \sum_{\substack{m=-M \\ m\neq 0}}^{M} a_m d_u^T(\vec{r}_j, \omega + \frac{2\pi m}{T}) \overline{d_u^T(\vec{r}_k, \omega + \frac{2\pi m}{T})} \quad . \tag{2.3.6}$$

The maximum-likelihood estimate of the power spectrum compares the power at a discrete center frequency (ω) with a weighted sum of power at neighboring frequencies. For this reason, the estimate may be sensitive to the assumption that the signal is a single harmonic.

Other estimates of the power spectra have been made by, for example, Lacoss (1971), Pisarenko (1972) and Shumway (1983). Lacoss (1971) reviews the maximum entropy method; Pisarenko (1972) introduces a class of non-linear estimates of which the conventional and high-resolution estimates are special cases. These estimates are the weighted means of the eigenvalues of the covariance matrix (e.g., the arithmetic mean or the geometric mean). Shumway assumes that noise is spatially white in his derivation of an estimate (Shumway, 1983).

2.3.1 Narrowband Frequency-wavenumber Estimates

Using the conventional estimate of the power spectrum, narrowband f-$\vec{k}$ estimates are obtained from (2.3.1) by smoothing the cross-spectral matrix over the required number of near-neighbor frequencies. However, for narrowband f-$\vec{k}$ estimation to be valid using the HR or the maximum likelihood estimate of the power spectrum, the cross-spectral matrix must be smoothed over at least as many frequencies as there are stations. Because most of the array stations are generally used in making an estimate, large bandwidths are required when analyzing data gathered with SMART 1 (see Table 2.1). This requirement leads naturally to the use of broadband frequency-wavenumber estimates.

2.3.2 Broadband Frequency-wavenumber Estimates

When making broadband f-$\vec{k}$ estimates care must be taken not to destroy deterministic signals. As mentioned in section 2.2, one method (Abrahamson, personal communication)

smooths the cross-spectral matrix by a weighted geometric mean of estimates at nearby frequencies (see (2.2.5) and (2.2.6)). Alternatively, Bostwick *et al.*, (1985), Spudich (1986) and Spudich and Oppenheimer (1986) suggest working in the slowness plane instead of the wavenumber plane. Direct body waves arrive at the array with constant slowness for all frequencies, whereas the sidelobes and aliases of the impulse response are at constant wavenumber and therefore appear at different slownesses for different frequencies. Peaks corresponding to signals in the f-$\vec{k}$ spectra for different frequencies in the slowness plane will sum constructively, side lobes and alias peaks will sum destructively. This process is called slowness stacking. The range of frequencies used for either smoothing the cross-spectral matrix or slowness stacking depends on the aperture of the array and the frequency content of the signal. The lower frequency limit is determined by the width of the peaks in the slowness plane and is a function of array aperture (see, for example, Davis and Regier, 1977; Spudich and Oppenheimer, 1986) and the smallest frequency in the Fourier domain (Table 2.1). The upper frequency limit is determined solely by the upper frequency limit of the spectral content of the signal. Tests with synthetic data reported by Spudich (1986) have shown slowness stacking to be effective in distinguishing between spurious peaks and real signals.

Both of these methods appear to work equally well for non-dispersive body waves from a single source. However, care must be used when analyzing sections of seismograms that record dispersive surface waves that have arrived at the array with varying slownesses.

Figures 2.1a and 2.1b show the SMART 1 sub-array impulse response for the conventional f-$\vec{k}$ method. The bandwidth of the estimate is approximately from 1.1 to 9.8 Hz. The width of the central peak is determined by the array aperture and the width determines the resolution of the conventional estimate in the wavenumber or slowness domain.

In chapter 3, broadband f-$\vec{k}$ estimates produced by slowness stacking are applied to the recorded ground motions before the surface wave arrivals. The later part of the strong motion record consisting of a mixture of body and surface waves may be conveniently

analyzed using either broadband f-$\vec{k}$ analysis, provided the surface waves are only weakly dispersed, or narrowband f-$\vec{k}$ analysis.

2.3.3 Frequency-wavenumber Estimates With Multiple Signals

As has been discussed, in the near-source region of a large earthquake multiple waves may arrive at the receiver simultaneously. Various researchers have studied this problem using narrowband f-$\vec{k}$ estimates. Woods and Lintz (1973) demonstrated that the HR method can resolve two closely spaced plane waves at 4.1 Hz when the CV method may not. Cox (1973) observed that when multiple interfering plane waves are present the resolving power of the HR technique is similar to that of the CV technique. Der and Flinn (1975) used an eigenvector decomposition of the cross-spectral matrix to show that two plane waves could be independently resolved using data gathered at an array if the waves are not of comparable amplitude or if the slowness of one wave did not coincide with a side lobe of the beam pattern directed at the other wave. Goldstein and Archuleta (1985, 1986, 1987) compare an algorithm named Multiple Signal Characterization (MUSIC) with the HR method. MUSIC is also based on an eigenvalue decomposition of the cross-spectral matrix and locates multiple closely spaced plane wave sources and automatically selects the most energetic N-1 sources where N is the number of receivers.

Bostwick, *et al.*, (1985) and Spudich (1986) have studied multiple signals using broad-band f-$\vec{k}$ methods. These authors report that they have been able to resolve multiple signals arriving at similar slownesses and azimuths, in synthetic data using slowness stacking of conventional estimates of the power spectra. Under these circumstances results using the HR method may be difficult to interpret. When several signals are present, Shumway (1983) suggests a step-wise procedure: first estimate the dominant signal and remove it to obtain a residual series, then compute the estimate of the power spectrum again with the residual series. Detection statistics for determining the presence of a signal are discussed in Shumway (1983) and Brillinger (1985).

In chapter 3, the conventional estimate of the power spectrum will be stacked over slowness for eleven frequency estimates. The bandwidth used in these calculations is between 1.1 and 9.8 Hz and between 1.1 and 5.1 Hz on the vertical and horizontal components, respectively. These spectra are interpreted in terms of planar, broadband seismic waves propagating across SMART 1.

2.3.4 Frequency-wavenumber Estimates Of Spherical Waves

It has been suggested (see Aki 1969, 1982) that the scattering of body and surface waves by inhomogeneities in the crust and conversion between these wave types is responsible for the seismic coda. At least two scattering processes contribute to the generation of seismic codas. Strong forward scattering (see, e.g. Chernov, 1960) has the effect of summing a large number of multipathed signals that travel along various ray paths between the source and the receiver. A second scattering mechanism occurs locally and is caused by heterogeneities in the Earth near the array. (Modeled as self-similar velocity fluctuations in the crust by Frankel and Clayton, 1986). Howe (1973) predicts that for this local scattering an equipartitioning of scattered energy occurs among all wavenumbers; thus the energy arrives from all directions. A combination of these two mechanisms may provide a good qualitative description of P, S and surface wave codas (Scheimer and Landers, 1974).

The conventional f-$\vec{k}$ analysis (see (2.3.1)) employs a plane wave model for the wave field that is applicable when the distance between the source and the array is much larger than the sub-array diameter, 2 km in this study. Scattered and converted waves may be important in the near-source region of large earthquakes. For wave sources close to or within the array (e.g. scatterers) a spherical wave model for the wave field is required. To calculate the conventional f-$\vec{k}$ estimate of the power for spherical waves requires modification of only the beam steering vector ($U_j(\vec{k})$). For a point source located at $\vec{r}_j$ and an array station located at $\vec{r}_k$,

$$U_j(\vec{r}_j) = \exp(\frac{i\omega r}{c}) \quad , \tag{2.3.7}$$

where r is the distance between the point source and the array station, c is the phase velocity and ω is the angular frequency. The power, given by

$$P^C(\vec{r}_j,\omega) = \frac{1}{N^2}\vec{\vec{U}}^*(\vec{r}_j)\mathbf{S}(\omega)\vec{U}(\vec{r}_j) \tag{2.3.8}$$

is calculated over a two-dimensional grid for point source location in which the depth of the point source is held constant.

In section 3.4, f-$\vec{k}$ estimates of the power spectrum calculated from (2.3.8) are stacked over slowness for eleven frequencies. These spectra are interpreted in terms of spherical, broadband seismic waves propagating across SMART 1 from a point source within, or near, the array.

2.4 Polarization Analysis

2.4.1 Introduction

The polarization properties of electromagnetic fields in the disciplines of optics and radio transmission form the basis of much of the theory to be presented (e.g. Born and Wolf, 1980). The term polarization describes the directional properties of either a vector process or a wavefield in a real vector space. Following Samson (1973) and Samson and Olson (1980), the concept of polarization will be further generalized to a unitary space in section 2.4.2. Linearly polarized wave motion occurs when $\mathbf{S}(\omega)$ in (2.3.8) has only one non-zero eigenvalue. Conversely, a completely unpolarized wavefield occurs when all the eigenvalues of $\mathbf{S}(\omega)$ are equal.

It is well known that elastic waves in the Earth have distinct polarization patterns (see Aki and Richards, 1980; Bullen and Bolt, 1985). In primarily laterally homogeneous structures the following properties are commonly observed in the far-field. The P-wave is non-dispersive and its power ranges primarily between 0.1 and 10+ Hz. The wave is polarized linearly in the direction of propagation and thus its motion exists primarily on vertical and radial components. The S-wave is non-dispersive and has power ranging primarily between

0.1 and 10+ Hz. The S-wave is polarized transversely to the direction of propagation and thus its motion exists primarily on vertical and radial components (SV) or on the transverse component (SH). The Love wave is dispersive and its power ranges primarily between 0.01 and 5.0+ Hz and is polarized primarily in the transverse direction. The Rayleigh wave is dispersive and has power primarily between 0.01 and 5.0+ Hz. This wave is polarized primarily in the vertical-radial plane for the fundamental mode. It usually exhibits retrograde particle motion. In higher modes the Rayleigh wave may exhibit either prograde or retrograde particle motions in the vertical-radial plane (see e.g. Mooney and Bolt, 1966). In anisotropic media, both body and surface waves are three-dimensionally polarized (Crampin, 1977).

For equation (1.1) in the near-source region, the radiation patterns for the near-field term and the intermediate-field P and S-wave terms have components in the radial, longitudinal and transverse directions. In the horizontal plane the near-field terms and the far-field S-wave term are oppositely polarized. The near-field, intermediate-field P-wave and far-field P-wave all have the same polarization in the radial direction (Aki and Richards, 1980). Also, conversion between P and SV energy at the free surface may produce phase differences between different components of motion for incident SV waves (Nuttli, 1961) and Rayleigh waves (Aki and Richards, 1980). Polarization anomalies have also been observed for teleseismic waves propagating in an anisotropic upper mantle (Kirkwood and Crampin, 1981).

Earlier work using the polarization properties of elastic waves concentrated on the design of filters to separate body waves into compressional and shear phases or to enhance or attenuate surface waves as desired (see Flinn, 1965; Mims and Sax, 1965; Montalbetti and Kanasewich, 1970). Smart and Sproules (1981) designed a polarization filter to estimate the back-azimuth of earthquakes. Plešinger, *et al.*, (1986) defined an average coordinate system to determine onset time, pulse duration and wave type for waves of arbitrary polarization. A relatively complete summary of the theory and applications of polarization

filters in seismology is given in Kanasewich (1981).

2.4.2 Array Polarization Method

The polarization of a wavefield recorded using an array of stations can be analyzed by examining the eigenstructure of the cross-spectral matrix (2.2.2). The characteristic equation of $S(\omega)$ is given by

$$\Psi(\omega) = \sum_{l=0}^{N} \alpha_l \lambda^l = 0 \quad , \tag{2.4.1}$$

where λ is an eigenvalue of $S(\omega)$ and α_l can be expressed in terms of the N scalar invariants of the matrix: $(\mathrm{tr}(S^l),\ l = 1,N)$ (see Mal'cev, 1963). The eigenvalues are real since $S(\omega)$ is Hermitian (see section 2.2). The first few coefficients are

$$\alpha_N = 1.0 \quad ,$$
$$\alpha_{N-1} = -trS \quad ,$$
$$\alpha_{N-2} = \frac{1}{2}((trS)^2 - trS^2) \quad ,$$
$$\alpha_{N-3} = -\frac{1}{N}(trS^3 - \frac{3}{2}(trS)(trS^2) + \frac{1}{2}(trS)^3) \quad ,$$

and $\alpha_0 = \det S$ for all N. Following Samson and Olson (1978) the cross-spectral matrix can be expressed in a set of N^2 outer products, $\vec{u}_j\vec{u}_k^{+}(j,k = 1,N)$. The vectors $\vec{u}_j$ form a complete orthonormal basis in a unitary subspace, that is, $\vec{u}_j^{+}\vec{u}_k = \delta_{jk}$. The symbol (+) denotes the Hermitian adjoint or the complex conjugate of the transpose and δ_{jk} is the kronecker δ. If $\vec{u}_j$ are the eigenvectors of $S(\omega)$ then the expansion has the form

$$S(\omega) = \sum_{j=1}^{N} \lambda_j \vec{u}_j \vec{u}_j^{+} \tag{2.4.2}$$

for $\lambda_j(j = 1,N)$.

Equation (2.2.2) for the cross-spectral matrix contains all the necessary information on the polarization of a wavefield. The frequency dependent degree of polarization, $\beta(\omega)$, is a scalar invariant of $S(\omega)$ and also depends on the frequency bandwidth of $S(\omega)$ given in

section 2.2 ($\Delta\omega=2\pi(2M+1)/T\Delta t$). When $\mathbf{S}(\omega)$ is computed for a wavefield containing a single polarized wave the cross-spectral matrix has only one non-zero eigenvalue. For this case, $(tr\mathbf{S})^2 = tr\mathbf{S}^2$ and $\alpha_{N-2} = 0$ and one can choose the degree of polarization,

$$\beta^2(\omega) = 1 - \frac{(tr\mathbf{S})^2 - tr\mathbf{S}^2}{(tr\mathbf{S})^2 - \frac{1}{N}(tr\mathbf{S})^2} \quad (N>1). \tag{2.4.3}$$

Equation (2.4.3) can be rewritten as

$$\beta^2(\omega) = \frac{N tr\mathbf{S}^2 - (tr\mathbf{S})^2}{(N-1)(tr\mathbf{S})^2} \quad (N>1), \tag{2.4.4}$$

where $0 \leq \beta^2(\omega) \leq 1$ (Samson, 1973; Samson and Olson, 1980). Equation (2.4.4) does not require the diagonalization of $\mathbf{S}(\omega)$. It may also be rewritten in terms of the eigenvalues of $\mathbf{S}(\omega)$ in a unitary space as

$$\beta^2(\omega) = \frac{1}{2(N-1)(tr\mathbf{S})^2} \sum_{j,k=1}^{N} (\lambda_j - \lambda_k)^2 \quad (N>1). \tag{2.4.5}$$

Other functions can be used. For example,

$$\beta(\omega) = \frac{\lambda_1}{tr\mathbf{S}} \tag{2.4.6}$$

can be used to estimate the polarization of the wavefield. Note that both (2.4.5) and (2.4.6) require the diagonalization of the cross-spectral matrix.

In (2.4.4), if a wavefield is composed of a single linearly polarized wave then $\beta^2(\omega) = 1$; or, if the wavefield is isotropic noise then $\beta^2(\omega) = 0$. If one wishes to measure the degree of polarization in a real vector space the equivalent formula is

$$\beta_R^2(\omega) = \frac{N tr(\mathrm{Re}\mathbf{S})^2 - (tr\mathbf{S})^2}{(N-1)(tr\mathbf{S})^2} \quad (N>1). \tag{2.4.7}$$

If a wavefield contains two polarized waves then two eigenvalues of $\mathbf{S}(\omega)$ are non-zero and $\alpha_{N-3} = 0$. In analogy with (2.4.3) one can estimate $\beta_2^2(\omega)$ that indicates whether a wave is restricted to a plane in unitary space. In this sense

$$\beta_2^2(\omega) = 1 - \frac{trS^3 - \frac{3}{2}(trS)(trS^2) + \frac{1}{2}(trS)^3}{(\frac{1}{N^2} - \frac{3}{2N} + \frac{1}{2})(trS)^3} \quad (N>2). \tag{2.4.8}$$

In a real vector space the equivalent formula is

$$\beta_{2R}^2(\omega) = 1 - \frac{tr(\mathrm{Re}S)^3 - \frac{3}{2}(trS)(tr(\mathrm{Re}S)^2) + \frac{1}{2}(trS)^3}{(\frac{1}{N^2} - \frac{3}{2N} + \frac{1}{2})(trS)^3} \quad (N>2). \tag{2.4.9}$$

These estimates can be extended to include cases where more than two eigenvalues of $S(\omega)$ are non-zero. Broadband estimates of the polarization of a wavefield may also be constructed from narrowband estimates by averaging narrowband estimates over the desired bandwidth.

Since the estimates of the polarization of the wavefield are constructed from scalar invariants of $S(\omega)$, (e.g. trS and trS^2) the value of the measure does not depend on the coordinate system of the instrument. This rotational invariance does not hold for the coherence of the wavefield that depends on the coordinate system. Following Samson (1980) the coherence of the wavefield in a unitary space is

$$\gamma^2(\vec{u}_j, \vec{u}_k, \omega) = \frac{tr(\mathbf{U}_{jk}\mathbf{S})tr(\mathbf{U}_{kj}\mathbf{S})}{tr(\mathbf{U}_{jj}\mathbf{S})tr(\mathbf{U}_{kk}\mathbf{S})} \quad (N\geq 2) \tag{2.4.10}$$

where $\mathbf{U}_{jk} = \vec{u}_j \vec{u}_k^{+}$. The coherence of the wavefield is related to the polarization of the wavefield by

$$\max\gamma^2(\vec{u}_j, \vec{u}_k, \omega) \geq \beta^2(\omega) \quad (N>2) \tag{2.4.11}$$

or by

$$\max\gamma^2(\vec{r}_j, \vec{r}_k, \omega) = \beta^2(\omega) \quad (N=2) \tag{2.4.12}$$

where $\vec{r}_j$ and $\vec{r}_k$ are real orthonormal vectors. The polarization of the wavefield thus provides a rotationally invariant lower bound on the coherence of the wavefield.

Estimates of the polarization of a wavefield are inherently biased. The bias is caused by two factors. If the noise in the data is spatially anisotropic the estimates can assume large values even when no signal is present. Second, since the estimates are from a small number of frequency samples, (2M+1), the estimates may have large biases (Jenkins and Watts, 1968).

The noise in recorded accelerations can come from four sources; instrument noise, recording noise (e.g. quantizing errors in digital recording), naturally occurring noise and signal generated noise. The instrument and recording noise are negligible for events 5 and 39 due to the large recorded signal amplitudes. A sample of naturally occurring noise was recorded by the pre-event memory. Generally, the amplitude of the ground motion before the P-wave onset is ± one count (0.96 gals). Signal generated noise is difficult to evaluate because it is likely to be non-stationary as well as correlated and mixed with the signal.

Samson (1983) proposes an asymptotic correction for $\beta^2(\omega)$ that assumes 2M+1>>N. The first term in the this correction is

$$\frac{N}{(N-1)(2M+1)} \left(1 + \frac{3(tr\mathbf{S}^2)^2}{(tr\mathbf{S})^4} - \frac{4tr\mathbf{S}^3}{(tr\mathbf{S})^3}\right) \quad . \tag{2.4.13}$$

Samson shows that the bias decreases as N increases in two examples. For the estimates of the polarization of a wavefield in chapter four, N>2M+1 so that the asymptotic expansion is not valid. The "jack-knife" method has also been advocated (Tukey, 1958, Samson, 1983) to estimate the bias. This method assumes that the weights, a_m, in (2.2.2) are equal. It is unclear how one might apply the "jack-knife" method when making estimates of the cross-spectral matrix when unequal weights are used in (2.2.2).

In chapter four, estimates of the polarization of the wavefield (e.g., $\beta^2(\omega)$ and $\beta_2^2(\omega)$) are made for two large earthquakes recorded at SMART 1. These estimates are calculated for identical time windows and bandwidths as were used for the f-$\vec{k}$ calculations of chapter three. The estimates of the polarization are interpreted in terms of broadband polarized waves arriving at the sub-array and provide a lower bound on the wavefield coherence.

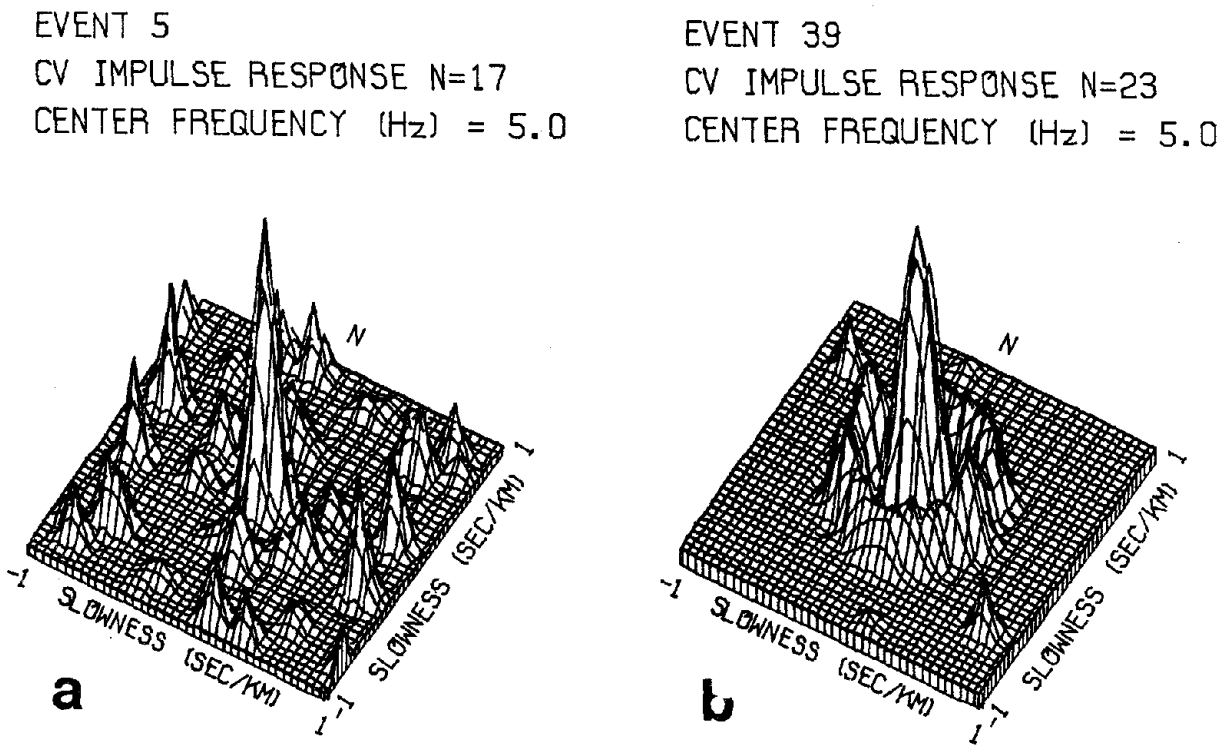

Figure 2.1: The broadband conventional frequency-wavenumber impulse response for event 5 (a) and event 39 (b) using the SMART 1 sub-array consisting of the center, inner and middle rings. The impulse response is computed by slowness stacking over 11 frequencies from 1.1 to 9.8 Hz.

CHAPTER 3: SEPARATION OF WAVE TYPES USING FREQUENCY-WAVENUMBER METHODS

3.1 Introduction

In this chapter, the mixture of wave types in the near-source region of two large earthquakes recorded at SMART 1 is estimated as a function of time (see figure 3.1 and table 3.1). Using conventional f-$\vec{k}$ analysis (see 2.3.1 or 2.3.8) one estimates the best fit of a broadband plane wave or spherical wave to the rotated ground accelerations. The conventional estimate of the plane wave power is chosen because it is robust with respect to multiple signals, slowness stacking of the estimate suppresses aliases and the estimate does not require the inversion of the singular cross-spectral matrix. The plane wave power in each of ten time windows is estimated at eleven distinct frequencies over a slowness grid extending to 1 sec/km in both horizontal directions. The estimated values of the plane wave power are separated by 0.05 sec/km. The plane wave power is then stacked at constant slowness over the 11 frequencies to obtain a bandwidth of 1.1 to 9.8 Hz on the vertical component and 1.1 to 5.1 Hz on the horizontal components. An estimate of the broadband plane wave power displayed as a function of slowness is given in figure 3.3. From its peak the plane wave power is contoured down in decibels (db). The lowest contour shown is 7 db from the peak. This contour corresponds to the 90 percent (approximate) confidence interval in (2.3.2) when K=10 (M=2) for a single narrowband f-$\vec{k}$ estimate of the plane wave power. Lower power levels are not shown. For the broadband f-$\vec{k}$ estimate of the plane wave power, assuming the plane wave power is roughly constant for each of the eleven narrowband estimates, the 90 percent (approximate) confidence interval is $\pm 4db$ (with $K \approx 22$ and $M \approx 5$ in (2.3.2)). In this chapter the 90 percent (approximate) confidence interval for broadband estimates of apparent horizontal velocity or peak azimuth is shown in parentheses after the estimate.

A time window of 256 samples, 2.56 seconds, is used for all of the f-$\vec{k}$ calculations.

Samples in the frequency domain are separated by 0.39 Hz (table 2.1). The start of the first time window is 2.0 seconds after the instrument at the first station in the array was triggered (see figures 3.5a, 3.10a). The starts of the ten overlapping time windows are separated by 1.0 second. Only data collected from stations in the center, inner and middle rings of SMART 1 are used to estimate the plane wave power because plane waves propagating at an apparent slowness of less than approximately 0.64 sec/km would not propagate across the 4 km aperture of the entire array in 2.56 seconds. The SMART 1 subarray station configuration is shown in figure 3.2 for event 5 and in figure 3.9 for event 39.

A peak in the broadband plane wave power may be identified as a P, S or surface wave by arrival time, apparent horizontal slowness and propagation direction across the array (see figure 3.3). The P and S-wave slownesses in the focal region are approximated by the inner circle (5.5 km/sec) and the outer circle (3.3 km/sec), respectively. Because the horizontal component of wave slowness is a constant of the ray path, a peak located within the outer circle may be interpreted as an S-wave and a peak located within the inner circle may be interpreted as either a P or a S-wave. A peak located outside of these circles may be interpreted as a surface or a scattered wave with slower apparent horizontal propagation velocity. A peak in the spectrum at a non-epicentral azimuth may be interpreted as scattered energy. Strong forward scattered waves and converted waves may be identified by their arrival times and apparent horizontal slownesses across the sub-array.

Table 3.1: Taiwan Earthquake Data

EVENT	DATE	M_L	DISTANCE TO C-OO (km)	DEPTH (km)	AZIMUTH FROM NORTH	NUMBER OF STATIONS	MAX. ACC. (cm/sec/sec) V	EW	NS
5	29 JAN 81	6.3	30.2	25.2	149°	16(H), 17(V)	97.4	168.5	259.8
39	16 JAN 86	6.5	22.2	10.2	64°	23	333.6	258.4	327.5

3.2 Application To Simulated Ground Accelerations

The conventional f-$\vec{k}$ method described above has been applied to two types of simulated ground accelerations. In the first example the f-$\vec{k}$ spectrum of a random wavefield, an

approximation of the wavefield produced by the scattering model of Howe (1973), for the sixteen stations in the event 5 sub-array configuration (figure 3.2) is estimated. The radial accelerations have an approximately uniform distribution between ± 200cm/sec^2. The contoured broadband plane wave power as a function of horizontal slowness is shown in figure 3.3. The spectra of the random wave fields are characterized by low broadband plane wave power, even though the accelerations range up to 200 cm/sec^2. At the 90 percent (approximate) confidence level, there is no single preferred broadband plane wave propagating across the sub-array. For example, in figure 3.3a the apparent horizontal velocity is 1.7(∞, 1.0) km/sec. The azimuth of the peak plane wave power is poorly determined, ranging from 0° to 360° at the 90 percent (approximate) confidence level. Many broadband plane waves with different apparent horizontal slownesses (or, equivalently, wavenumbers) and directions of propagation describe the random wave field input in both examples.

In the second example, the radial accelerations from station C-00 for time windows six and seven (see figure 3.5b for the C-00 radial seismogram and the time window locations) are the input accelerations at each of the sixteen stations for the event 5 sub-array configuration (figure 3.2). The homogeneous input accelerations model a single, vertically propagating, broadband plane wave. The contoured broadband plane wave power (figure 3.4) is centered at zero slowness. The 90 percent (approximate) confidence interval, (∞, 15.0) km/sec, in time window six is smaller than the corresponding interval, (∞, 8.6) km/sec, in time window seven. The difference is due to the peak broadband plane wave power in time window seven, primarily containing S-wave coda and surface wave energy, being 3.8 decibels below the peak broadband plane wave power in time window six that contains the direct S-wave onset. The homogeneous wave field in these simulations is well described by a single, broadband, vertically propagating plane wave at the 90 percent (approximate) confidence level. The conventional f-$\vec{k}$ estimate of the power spectrum accurately describes both the random and the homogeneous wavefield in both examples.

3.3 Application To SMART 1 Ground Accelerations

3.3.1 Event 5

Abrahamson (1985) initially studied event 5 in detail and he estimated the hypocentral parameters of the mainshock and twenty aftershocks. The aftershocks delineated a zone extending approximately 19 km west from the mainshock hypocenter. A narrow-band, sliding time window, high resolution f-$\vec{k}$ analysis of the ground accelerations was interpreted as showing propagation of the rupture front through an angle of approximately 30° subtended at the array. The estimated rupture velocity varied from 2.1 to 4.9 km/sec.

In the current study, seventeen stations are used in the f-$\vec{k}$ analysis of the vertical component, however, only 16 stations are used for the f-$\vec{k}$ analysis of the horizontal components because the east-west component at station M-11 malfunctioned. Figure 3.5 displays the vertical, radial and transverse components of the ground acceleration at five stations. These stations are aligned along the source-array center direction in such a way that plane waves from the hypocenter move across the stations at approximately their apparent horizontal slownesses. On the vertical component (figure 3.5a) it is difficult to follow any wave arrival across the array. On the horizontal components (figures 3.5b and 3.5c), however, one can follow, for example, the largest wave motion across the array.

Figure 3.6 shows the variation in peak broadband plane wave power with time for each of the three components of ground acceleration. The peak vertical broadband plane wave power remains fairly constant between 7 and 63 $(cm/sec)^2$. The peak horizontal broadband plane wave power reaches a maximum after the direct S-wave onset in time windows four through seven and varies between 0.11 and 1900 $(cm/sec)^2$.

Figures 3.7a-3.7j are contour plots of broadband plane wave power as a function of the apparent slowness of the three rotated components of ground acceleration for the time windows indicated in figure 3.5. The epicenter for event 5 is at an azimuth of 149°. Thus, one expects most of the energy to propagate across the array from the southeast quadrant.

Time windows zero through three contain the direct P-wave arrival and the P-coda portion of the seismogram; the direct S-wave onset is in time window four.

For these first four time windows (figures 3.7a-3.7d) the vertical component may be interpreted as a single broadband planar P-wave propagating across the array at an apparent horizontal velocity of 8.9 km/sec from an azimuth of 153°. For time window zero, the 90 percent (approximate) confidence intervals for the apparent horizontal velocity and azimuth are (15.0, 5.6) km/sec and (123°, 180°), respectively. The horizontal components may be interpreted as non-vertically incident P-waves (radial), scattered waves or P waves that have been converted to S-waves close to the sub-array (figures 3.7a-3.7d). The peak broadband plane wave power on the horizontal components gradually increases with time and parallels an increase in broadband plane wave power on the vertical component as direct, converted or scattered waves continue to arrive at the sub-array. A more complete discussion of scattered waves is presented in section 3.4 using a spherical wave model for the wavefield (2.3.8).

Time windows four through six (figures 3.7e-3.7g) contain the largest horizontal ground accelerations and the direct S-wave arrival. On the vertical component in time window four both a P-wave at an apparent horizontal velocity of 8.9(30.0, 6.0) km/sec and a SV-wave at an apparent horizontal velocity of 3.7 km/sec are identified. The SV-wave is more clearly seen on the radial component at an azimuth of 158°(135°, 165°) and at an apparent horizontal velocity of 3.7(5.1, 2.6) km/sec. The peak plane wave power of the SV-wave on the vertical component is approximately 3 db lower than the P-wave peak in agreement with a previously published high resolution, narrowband f-$\vec{k}$ estimate (Abrahamson, 1985). The SH-wave on the transverse component has an apparent horizontal velocity of 2.5(9.0, 1.8) km/sec. In time windows five and six on the vertical component the wavefield consists of both a P-wave at an apparent horizontal velocity of 8.9 km/sec and an azimuth of 117°, and a Rayleigh wave at an apparent horizontal velocity of 2.6 km/sec and an azimuth of 157°. The counterclockwise rotation of the azimuth of the P-wave by 36° in

time windows four and five is not significantly different from the epicentral azimuth given by the 90 percent (approximate) confidence interval. The Rayleigh wave peak in time window five is 3 db lower than the P-wave peak, while in time window six the Rayleigh wave peak is slightly higher than the P-wave peak. In time window six (figure 3.7g) on the vertical component, surface wave, P-wave and scattered energy are present. The similarity of the vertical spectrum (figure 3.7g) to the random wavefield (figure 3.3) is apparent. The vertical wavefield may thus be interpreted as being composed of many broadband plane waves with different wavenumbers (slownesses).

On the horizontal components in time windows five and six the wavefield may be interpreted as a single broadband planar S-wave from the epicentral azimuth. The apparent horizontal velocity of the S-wave on the radial component is greater than its apparent horizontal velocity on the transverse component by 0.6 to 1.1 km/sec. The difference in the apparent horizontal velocity of the two components is not significant at the 90 percent (approximate) confidence level. From time window four to six the azimuth of the peak broadband plane wave power on the radial component rotates from 158° to 143°. The azimuth of the peak broadband plane wave power on the transverse component remains constant at 150° to 149° and then shifts 6° in time window seven to 143°. The observed rotations of the azimuth of the peak broadband plane wave power are not significant at the 90 percent (approximate) confidence level. An isolated peak in the spectra corresponding to Love or Rayleigh waves is not observed on the horizontal components (figures 3.7f and 3.7g) due to the large broadband plane wave power in the S-wave and the small difference in slowness (wavenumber) between the wave types.

The final three time windows (figures 3.7h-3.7j) contain primarily S-waves, surface waves and coda waves. In time windows seven through nine the wavefield on the vertical component may be interpreted as scattered energy from many directions or, equivalently, many wavenumbers (see sections 2.3.4, 3.4 and figure 3.3). The scattered waves have broadband plane wave power comparable to the broadband plane wave power in the direct

P-wave because the wave power on the vertical component in time windows seven through nine is comparable to the wave power in time windows zero through three. The broadband plane wave power on the transverse component in time window seven is elongated along the epicentral azimuth by the arrival of the Love wave at an azimuth of approximately 144°. The final two time windows for the horizontal components (particularly the transverse) show a rotation in the azimuth of the peak broadband plane wave power to approximately 180°. This peak may be interpreted as surface waves with an apparent horizontal velocity of 2.2(12.3, 1.5) km/sec and an azimuth of 180°(125°, 270°) (figure 3.7i, transverse component). Both the epicentral region and the end of the rupture as defined by Abrahamson (1985) are within the 90 percent (approximate) confidence interval. Scattered waves from non-epicentral azimuths are also mixed with surface waves in these last two time windows on the horizontal components.

In summary, an interpretation of the ground accelerations in event 5 in terms of broadband planar waves has demonstrated that;

1) from the epicentral azimuth the P-wave energy propagates across the sub-array for approximately six to seven seconds at an apparent horizontal velocity of 8.9(15.0, 5.6) km/sec; an S-wave propagates across the sub-array for approximately four to five seconds at an apparent horizontal velocity of 3.7(5.1, 2.6) km/sec on the radial component and 3.4(6.0, 2.3) km/sec on the transverse component; surface waves from the epicentral azimuth propagate across the sub-array at an apparent horizontal velocity of 2.2(12.3, 1.5) km/sec. For both horizontal components the apparent horizontal velocity of the peak broadband plane wave power across the sub-array increases with time during the S-wave arrival suggesting that the S-waves arrive with steeper angles of incidence. The increase in apparent horizontal velocity is not, however, significant at the 90 percent (approximate) confidence level.

2) simultaneous arrivals of P and SV waves and of P and Rayleigh waves are observed on the vertical component. On the transverse component both SH and Love waves are observed at the sub-array within the same time window.

3) scattered or converted arrivals on all components of the ground accelerations are observed at levels of broadband plane wave power comparable with the broadband plane wave power of body wave arrivals. The broadband plane wave power in these converted waves increases with time due to an increase in the broadband plane wave power of the P-waves arriving at the sub-array. P-wave energy converted or scattered to S-wave energy is probably recorded on the horizontal components before the onset of the direct S-wave. Scattered waves dominate the wavefield in the last time windows, especially on the vertical component.

4) the azimuth of the peak broadband plane wave power on the vertical component (153°(123°, 180°)) does not vary from time window zero to three, but rotates through 36° to 117° with the direct S-wave arrival in time window four. The azimuth of the peak broadband plane wave power during the S-wave arrival rotates counterclockwise by 12° on the radial component and 6° on the transverse component. None of these azimuths are significantly different from the epicentral azimuth at the 90 percent (approximate) confidence level. The sense of these rotations of the peak broadband plane wave power is opposite to that of the rotations observed using the high resolution, narrowband plane wave analysis by Abrahamson (1985) and an explanation is required.

In the study by Abrahamson (1985) the estimate of the peak S-wave azimuth of the narrowband plane wave power was limited by four factors. First, the time dependent S-wave azimuth was smoothed over one-second time windows. Second, the bandwidth was limited to 1.0±0.8 Hz. Third, confidence levels could not be estimated for the high-resolution statistic because the number of stations used in the estimate was greater than the number of frequencies used to estimate the cross-spectral matrix ($2M+1<N$). Fourth, the wave type associated with the peak narrowband plane wave power was assumed to be the S-wave. In figure 3.8 of this study a narrowband (1.2±0.78 Hz) conventional estimate of the plane wave power for the transverse component for time windows four through nine is shown. (For a description of the time windows see figure 3.5c.) The 90 percent (approxi-

mate) confidence interval for these narrowband estimates is ± 7db from (2.3.2). The azimuth of the peak narrowband plane wave power rotates clockwise from 153°(67°, 255°) in time window four to 174°(134°, 169°) in time window nine in agreement with Abrahamson (1985). However, surface waves are the dominant wave type in time windows seven through nine. They are identified by their apparent horizontal velocity and arrival time. In time window four the apparent horizontal velocity of the peak narrowband plane wave power is 4.5(∞, 1.5) km/sec and is interpreted as an SH-wave. In time window eight the apparent horizontal velocity of the peak narrowband plane wave power is 2.2(6.4, 1.2) km/sec and is interpreted as a Love wave. The apparent horizontal velocities, however, are not significantly different at the 90 percent (approximate) confidence level due to the small difference in slowness (wavenumber) between the wave types. For the SH-wave in time windows four through six, the azimuth of the peak narrowband plane wave power rotates counterclockwise by 7°, consistent with the 6° rotation observed above for the broadband estimate of the plane wave power. For the Love waves in time windows seven through nine, the azimuth of the peak narrowband plane wave power rotates clockwise through 5°. Neither of these rotations of the azimuth of the peak narrowband plane wave power are significant at the 90 percent (approximate) confidence level. In summary, the differences between the two analyses are primarily due to the contamination of the estimate of the peak azimuth of the peak narrowband plane wave power for the S-waves by surface waves of greater plane wave power near 1.0 Hz and with azimuths near 174°.

3.3.2 Event 39

Event 39 occurred 8 km closer to the array than did event 5 (figure 3.1). The recorded peak ground accelerations are the largest recorded at the SMART 1 array through December 1986. The locations of the twenty-three stations used in the following f-$\vec{k}$ analysis are shown in figure 3.9.

Figure 3.10 displays the vertical, radial and transverse components of the ground accelerations recorded at five stations in the array for event 39. The stations are aligned

along the source-array center direction so that plane waves from the hypocenter move across the stations at approximately their apparent slownesses. It is difficult to follow any particular wave arrival on the vertical component (figure 3.10a). On the horizontal components (figures 3.10b and 3.10c), however, one can easily follow, for example, the largest amplitude arrival across the array. Figure 3.11 shows the variation of peak broadband plane wave power with time for each of the three components. All three components have maximums in peak broadband plane wave power near the time of the direct S-wave arrival. The peak vertical plane wave power varies from 19 to 826 $(cm/sec)^2$, while the peak broadband horizontal plane wave power ranges over five orders of magnitude over time windows zero through nine.

Figures 3.12a-3.12j are contour plots of broadband plane wave power for the three rotated components of ground acceleration as a function of slowness. (The time windows used in the f-$\vec{k}$ calculations are shown at the bottom of figure 3.10.) The epicenter for event 39 is at an azimuth of 64°. Thus, one would expect most of the recorded power to be located in the northeast quadrant as can be observed in figure 3.12a for the vertical component.

The first two time windows (figures 3.12a and 3.12b) contain the P-wave from the hypocenter and P-coda energy before the direct S-wave onset (in time window three). On the vertical component the energy arrives from the northeast quadrant although the peak broadband plane wave power is rotated 40° to 50° counterclockwise of the epicentral azimuth. The epicentral azimuth is included, however, within the 90 percent (approximate) confidence level. The apparent horizontal velocity across the sub-array in time window one is 4.9(20.0, 3.6) km/sec which implies that the P-wave velocity in the hypocentral region can be no greater than 3.6 km/sec at the 90 percent (approximate) confidence level since slowness is a constant of the ray path. The apparent horizontal P-wave velocity of 4.9(20.0, 3.6) km/sec in event 39 is less than the 8.9(15.0, 5.6) km/sec observed in event 5. The hypocenter of event 5 is 15 km deeper and 8 km further from the array center than the

hypocenter of event 39. Waves from event 5 probably travel a more nearly vertical path near the sub-array than waves from event 39 and therefore produce larger apparent horizontal velocities. In time windows two through eight (figures 3.12b-3.12h) the peak of the broadband plane wave power on the vertical component has an apparent horizontal velocity greater than 6.3 km/sec. The azimuth of the peak broadband plane wave power varies greatly because the vertical ground accelerations are composed of nearly vertical incident waves. In time window six, a secondary peak located along the epicentral direction may be interpreted as a Rayleigh wave propagating across the sub-array. The Rayleigh wave is more clearly identified on the radial component and has an apparent horizontal velocity of 3.7(∞, 1.7) km/sec and an azimuth of 68°(0°, 360°). This secondary peak is approximately 2 db down from the maximum broadband plane wave power (150 $(cm/sec)^2$). The final time window for the vertical component has a peak at an azimuth of 276° that may be interpreted as a scattered wave crossing the sub-array at an apparent horizontal velocity of 2.0 km/sec.

The horizontal accelerations in the first two time windows have low amplitude and broadband plane wave power. On the horizontal components in time windows zero and one the peak broadband plane wave power arrives from non-epicentral azimuths that are generally to the southeast. These are scattered waves that are observed at higher broadband plane wave power levels in time windows two through four on the transverse component and time windows two and three on the radial component. The peak broadband plane wave power of these scattered waves generally increases with time and ranges up to 2340 and 2119 $(cm/sec)^2$ for the radial and transverse components, respectively in time window four. The direct S-wave onset is in time window three. The onset is obscured by the greater broadband plane wave power of the scattered waves at the 90 percent (approximate) confidence level. Scattered arrivals will be further discussed in section 3.4 using a broadband spherical wave model for the wavefield (2.3.8).

In time window four, the direct SV-wave is observed on the radial component at an azimuth of 72°(0°, 360°) and an apparent horizontal velocity of 3.2(∞, 1.4) km/sec. The broadband plane wave power in the transverse component in time window four is again dominated by waves scattered from an azimuth of 153°.

The broadband plane wave power is at a maximum in time window five for both horizontal components. Based on average travel times, both S and surface waves arrive at the array during this time window. However, only one peak is observed along the epicentral azimuth at an apparent velocity of 3.7(∞, 1.6) km/sec on the radial component. In time windows five through nine the peak azimuth of the horizontal wavefield ranges from 56° to 74° on the radial component and from 63° to 74° on the transverse component. The 90 percent (approximate) confidence interval for these azimuths are both (0°, 360°) due to the broad peaks in the spectrum that within the ±4 db contour usually include zero slowness. The wavefield may be interpreted as broadband planar S-waves from the epicentral region in time windows four and five mixed increasingly with surface waves in the later time windows. The S and surface waves have apparent horizontal velocities of approximately 3.2 and 2.7 km/sec, respectively. Many of the other peaks in figures 3.12e-3.12j may be interpreted as scattered waves from various azimuths.

The event 39 wavefield has been interpreted in terms of broadband plane waves. In summary, a direct P-wave arriving from the epicentral direction at an apparent velocity of 4.9(20.0, 3.6) km/sec is observed in the first two time windows. It is followed by nearly vertical incident waves on the vertical component in the later time windows. The arrival of both a P-wave and a Rayleigh wave can be seen on the vertical component in time window six. The Rayleigh wave has an apparent horizontal velocity of 3.7(∞, 1.7) km/sec on the radial component. The early horizontal time windows are dominated by scattered waves followed by the direct S-wave, with large broadband plane wave power and an apparent horizontal velocity of 3.2(∞, 1.4) km/sec observed in time window four. After the S-wave onset the azimuth of the peak broadband plane wave power varies by 12° for both

horizontal components in time windows five through seven. There is an indication for both the S-wave and the surface waves that the azimuth of the peak broadband plane wave power rotates counterclockwise through roughly 10°. These rotations of the azimuth of the peak broadband plane wave power are suggestive of source propagation, however, at the 90 percent (approximate) confidence level the differences in the azimuth of the peak broadband plane wave power are not significant. Scattered waves are increasingly mixed with both S-waves and surface waves throughout the record.

3.4 Scattered Waves

Using conventional f-$\vec{k}$ analysis of SMART 1 recordings, both event 5 and 39 have been interpreted as containing scattered wave arrivals. For example, in the later time windows for both event 5 and 39 the energy on the vertical component arriving from many directions or wavenumbers is a result of local scattering. Also, in event 39 the energy recorded on both horizontal components before the direct S-wave onset arrives from an azimuth (180°(83°, 255°), time window three) that is significantly different from the source azimuth of 64° (see figures 3.12b-3.12e). This non-epicentral azimuth energy may be interpreted as side-scattering of the P-wave from a crustal anomaly or heterogeneous scattering center close to SMART 1 (Darragh and Abrahamson, 1986; Abrahamson and Darragh, 1987). Aki (1982) shows that for side-scattering, P to S and P to P scattered waves are roughly comparable in amplitude, and thus transfer energy to both the radial and transverse components. This can be observed for event 39 in figures 3.12b-3.12e. Scattered energy from the epicentral direction on the vertical component is difficult to observe in the nearly vertical wavefield recorded during event 39.

Figure 3.13 is a contour plot of the power of the transverse ground accelerations estimated from a spherical wave f-$\vec{k}$ analysis, (2.3.8), in event 39 during time window three (figure 3.12d). The spherical wave power from sources at a depth of 1.75 km in a region 6 km by 6 km centered on the station C-00 is contoured. The peak is centered 1.0(0.7, 1.5)

km southeast of the array at an azimuth of 125°(103°, 162°). The peak broadband spherical wave power is 20 percent larger than the corresponding broadband plane wave model (figure 3.12d). In figure 3.14 the peak broadband spherical wave power is plotted as a function of depth. At a depth of 1.75 km the spherical broadband wave power peaks at 1234 $(cm/sec)^2$ (figure 3.13). Wave power greater than 491 $(cm/sec)^2$ (the -4db power level) indicates that the depth is not well constrained between the surface and 3 km beneath the surface at the 90 percent (approximate) confidence level. Below 3 km, estimates of the peak broadband spherical wave power are limited by the aperture of SMART 1.

Note that the epicentral azimuth of event 5 lies within the 90 percent (approximate) confidence level for the azimuth of the peak broadband plane wave power in figure 3.13. For event 5 the wavefield on the horizontal components before the direct S-wave onset may now consequently be interpreted as waves scattered and converted by the crustal anomaly southeast of the array. The energy in the P-wave is transferred to both scattered and converted, P and S-waves. Scattered S-waves are observed at the array since the array, the heterogeneity and the epicenter are not co-linear.

In summary, scattered energy in the codas of events 5 and 39 is an important feature of the recorded ground accelerations. A crustal anomaly (scatterer) located 1.0 km southeast of the array center at a depth of 1.75 km produced scattered waves of broadband spherical wave power ranging to 1234 $(cm/sec)^2$, especially on the horizontal components, during event 39. Due to the lack of sub-surface information southeast of the array the crustal anomaly cannot be correlated with a geological feature at this time.

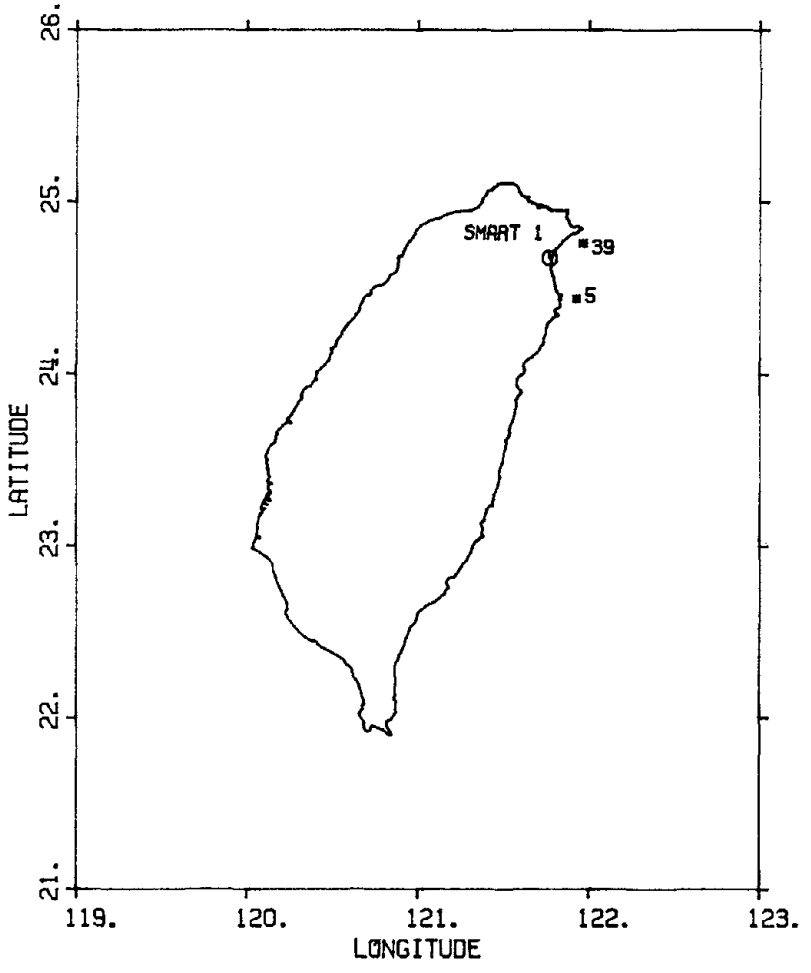

Figure 3.1: The location of the SMART 1 array (octagon) in northeast Taiwan and the epicenters of events 5 and 39 (stars).

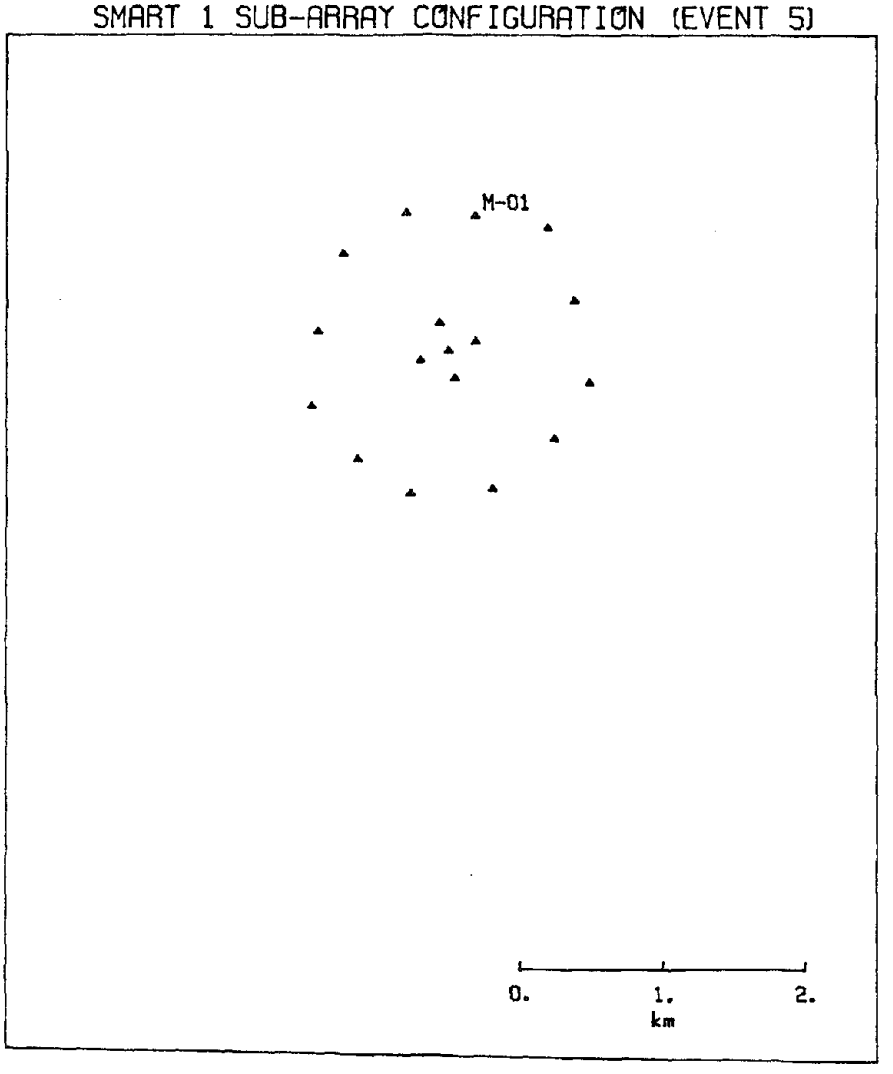

Figure 3.2: The SMART 1 sub-array configuration for event 5. The locations of the stations are shown as stars.

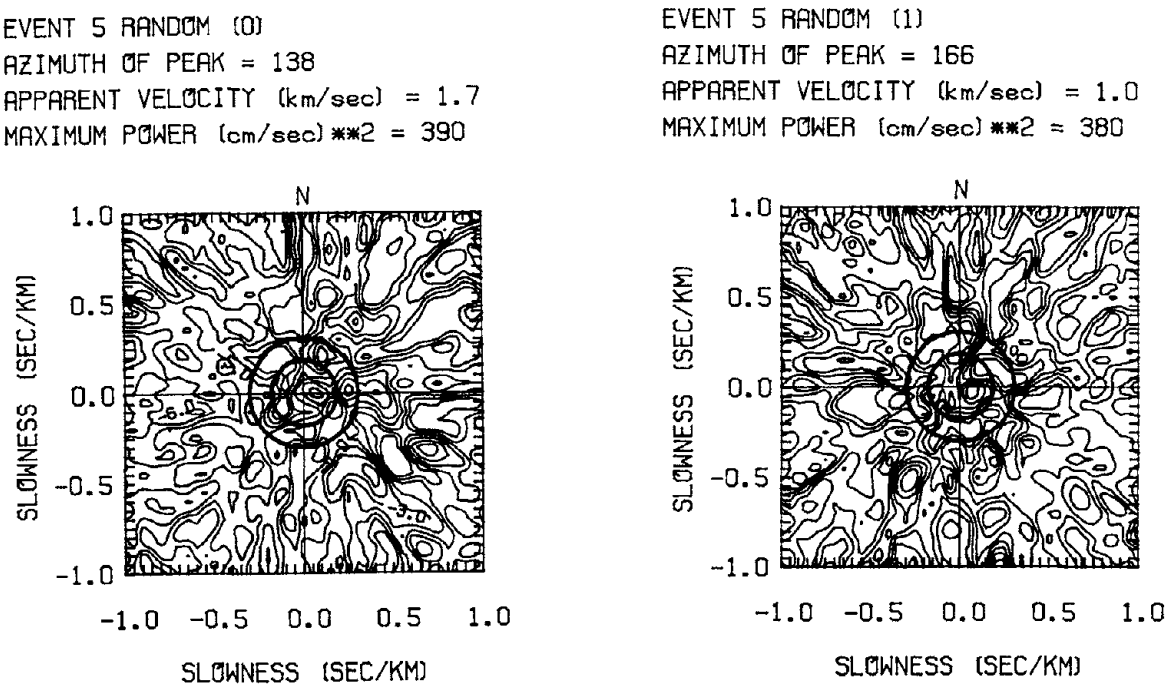

Figure 3.3: The broadband conventional frequency-wavenumber spectra of a random radial wavefield for the event 5 sub-array configuration.

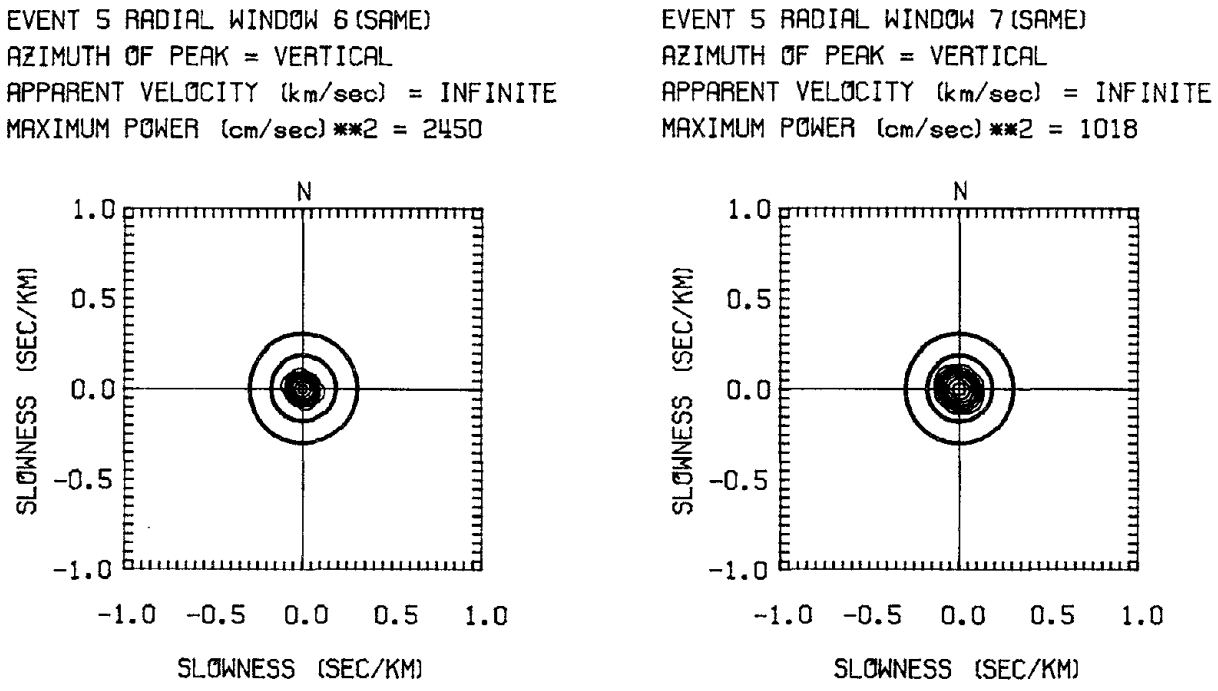

Figure 3.4: The broadband conventional frequency-wavenumber spectra of a homogeneous radial wavefield for the event 5 sub-array configuration.

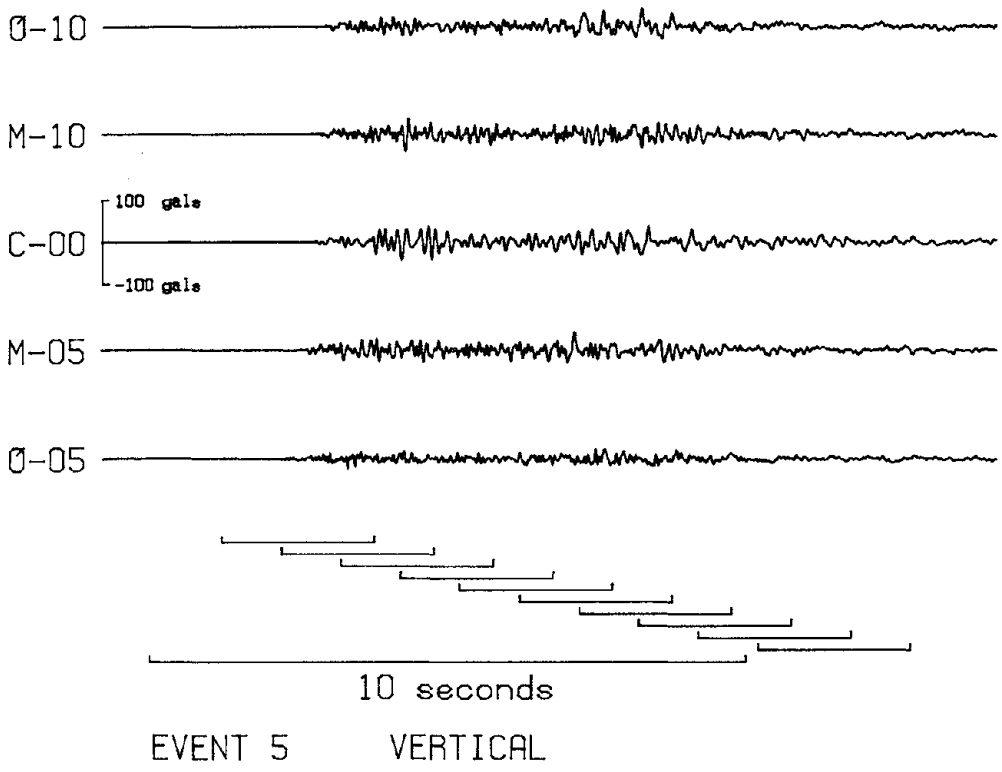

Figure 3.5a: Vertical component accelerograms recorded at five stations in the array during the 29 January 1981 event. The records are aligned on absolute time and are plotted according to increasing epicentral distance. The ten time windows used in the analysis are also shown.

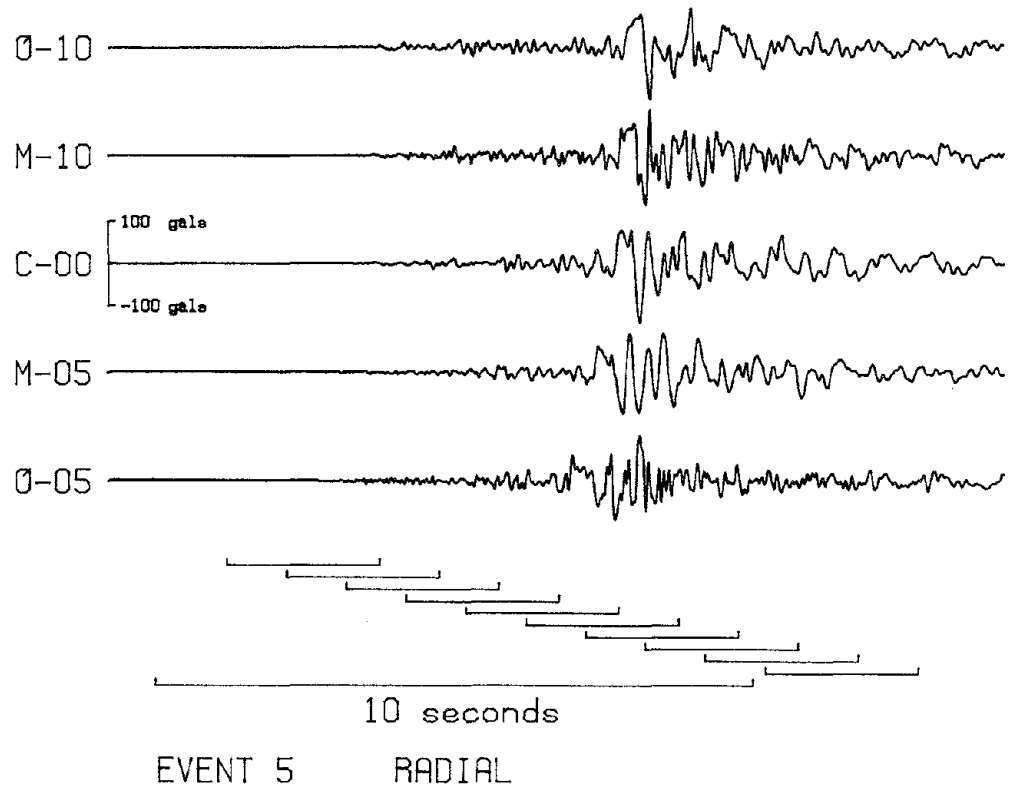

Figure 3.5b: Radial component accelerograms recorded at five stations in the array during the 29 January 1981 event. The records are aligned on absolute time and are plotted according to increasing epicentral distance. The ten time windows used in the analysis are also shown.

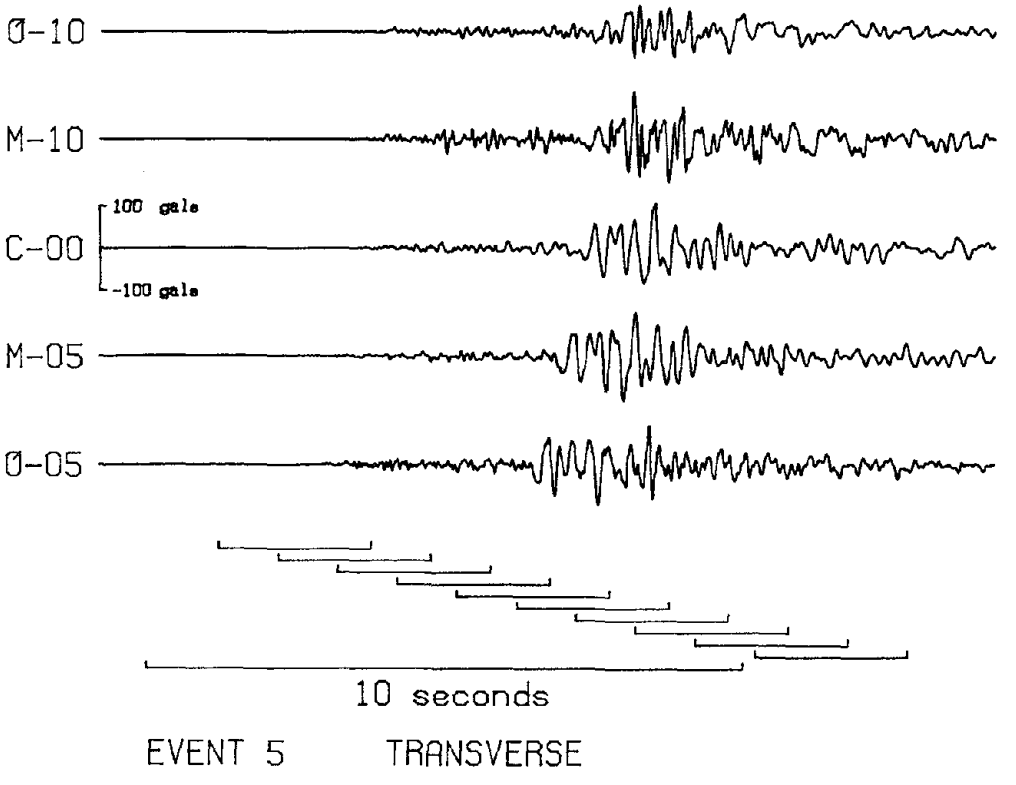

Figure 3.5c: Transverse component accelerograms recorded at five stations in the array during the 29 January 1981 event. The records are aligned on absolute time and are plotted according to increasing epicentral distance. The ten time windows used in the analysis are also shown.

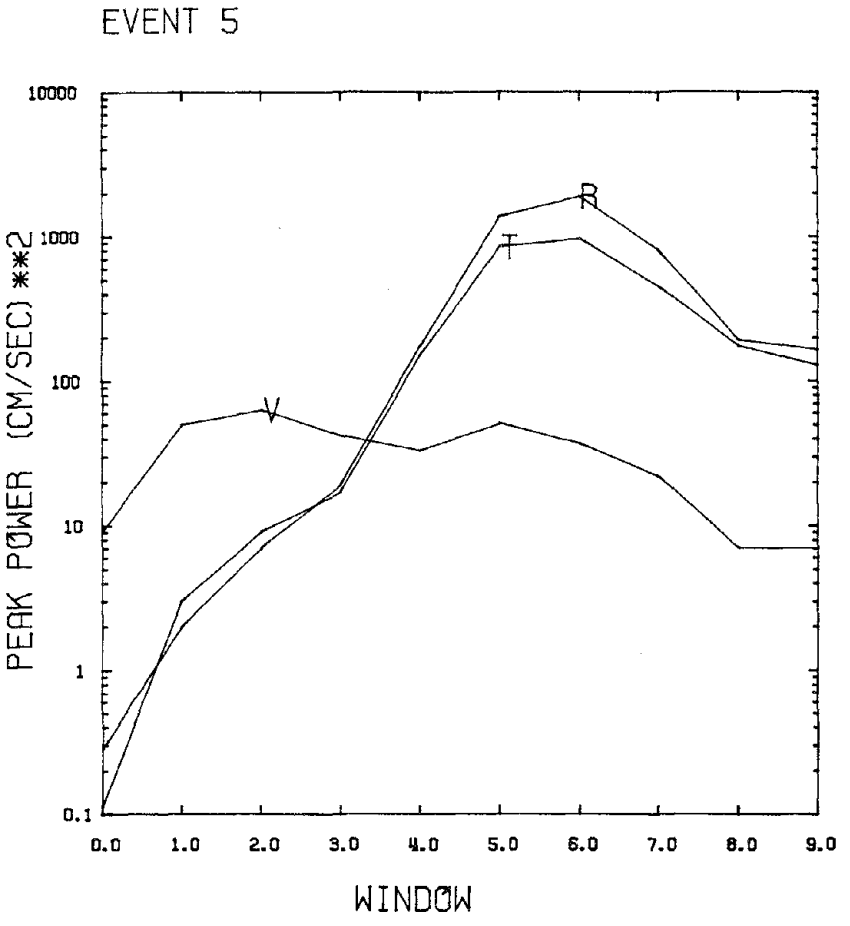

Figure 3.6: The peak power for the vertical (V), radial (R) and the transverse (T) component for the 10 windows shown at the bottom of figure 3.5.

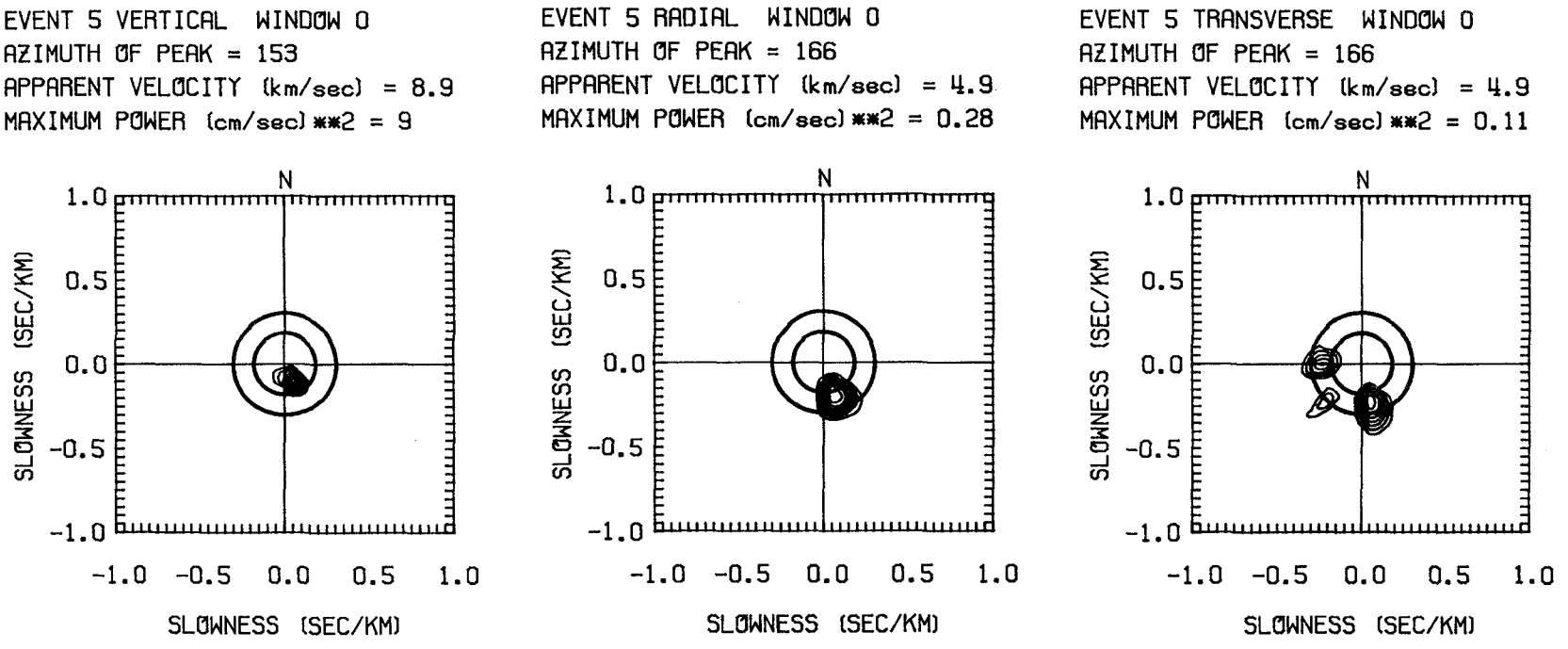

Figure 3.7a: The broadband conventional frequency-wavenumber spectra for the vertical (left), radial (center) and transverse (right) components of ground acceleration recorded during event 5 for time window 0.

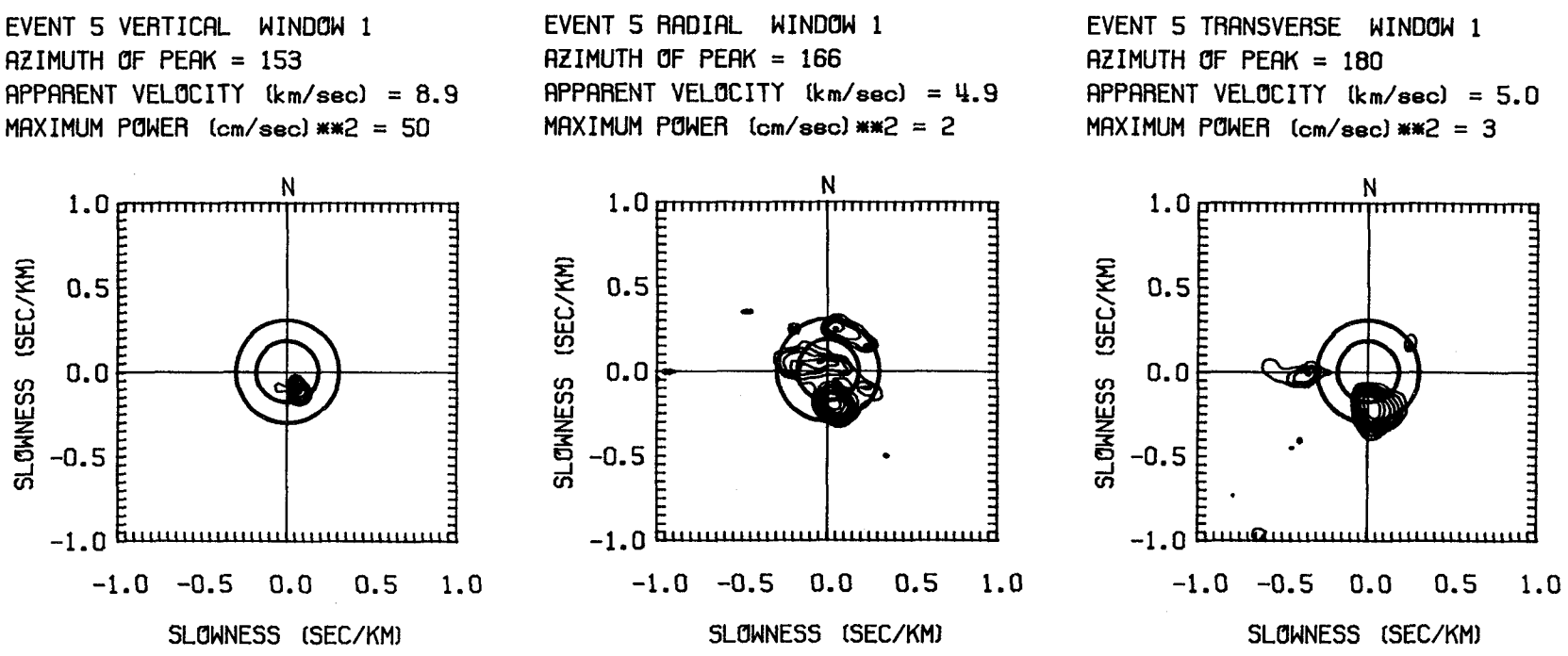

Figure 3.7b: The broadband conventional frequency-wavenumber spectra for the vertical (left), radial (center) and transverse (right) components of ground acceleration recorded during event 5 for time window 1.

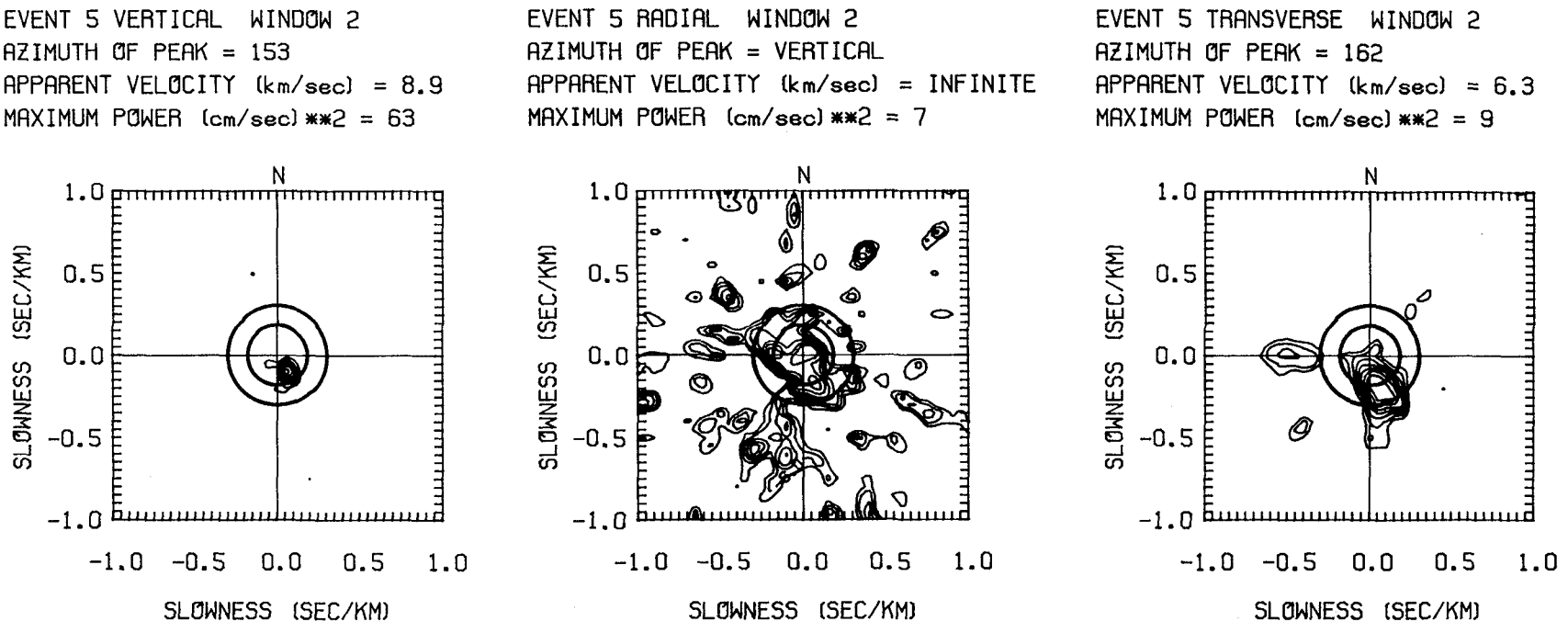

Figure 3.7c: The broadband conventional frequency-wavenumber spectra for the vertical (left), radial (center) and transverse (right) components of ground acceleration recorded during event 5 for time window 2.

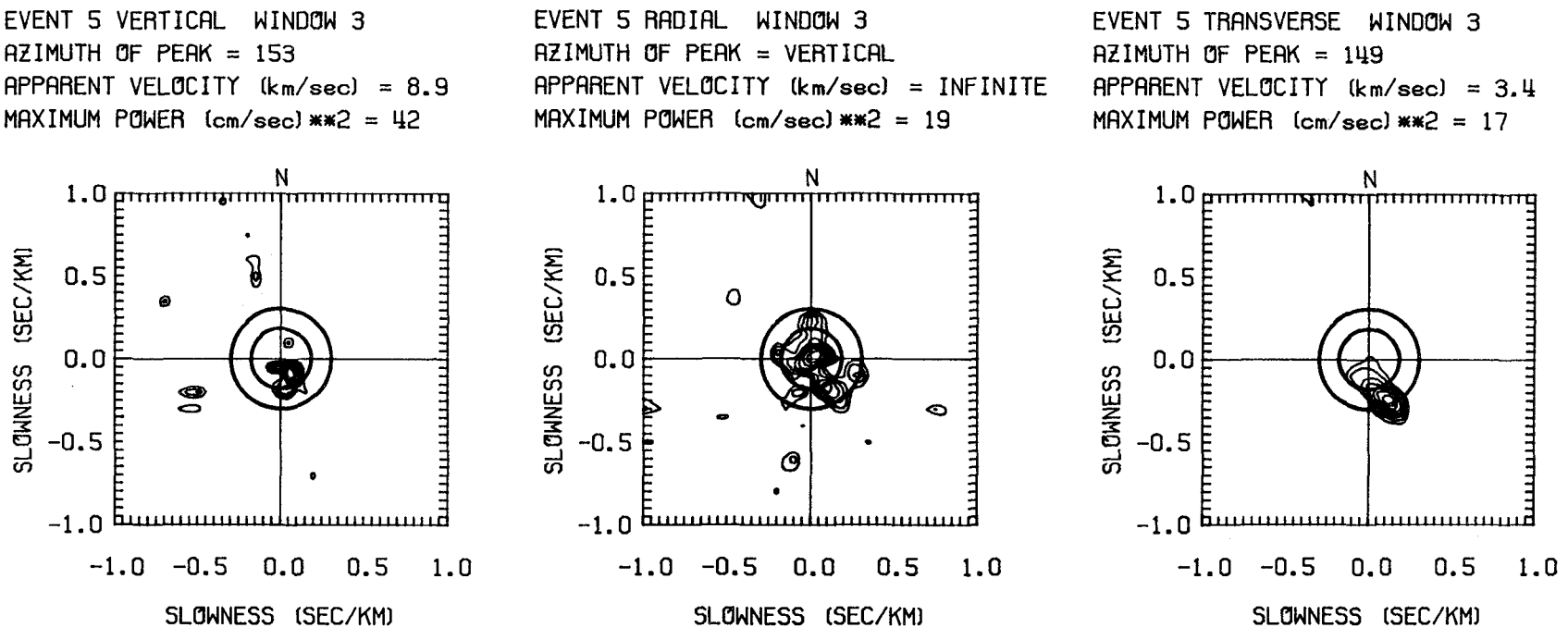

Figure 3.7d: The broadband conventional frequency-wavenumber spectra for the vertical (left), radial (center) and transverse (right) components of ground acceleration recorded during event 5 for time window 3.

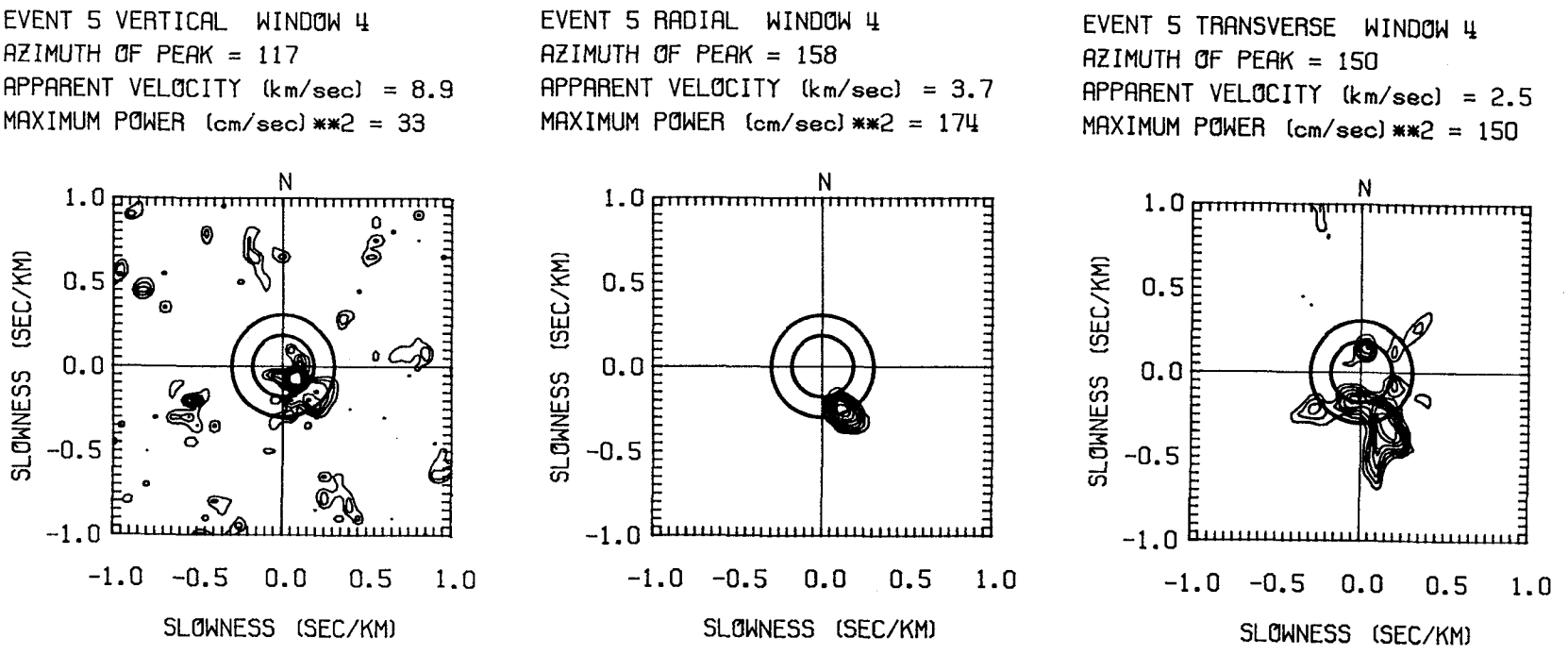

Figure 3.7e: The broadband conventional frequency-wavenumber spectra for the vertical (left), radial (center) and transverse (right) components of ground acceleration recorded during event 5 for time window 4.

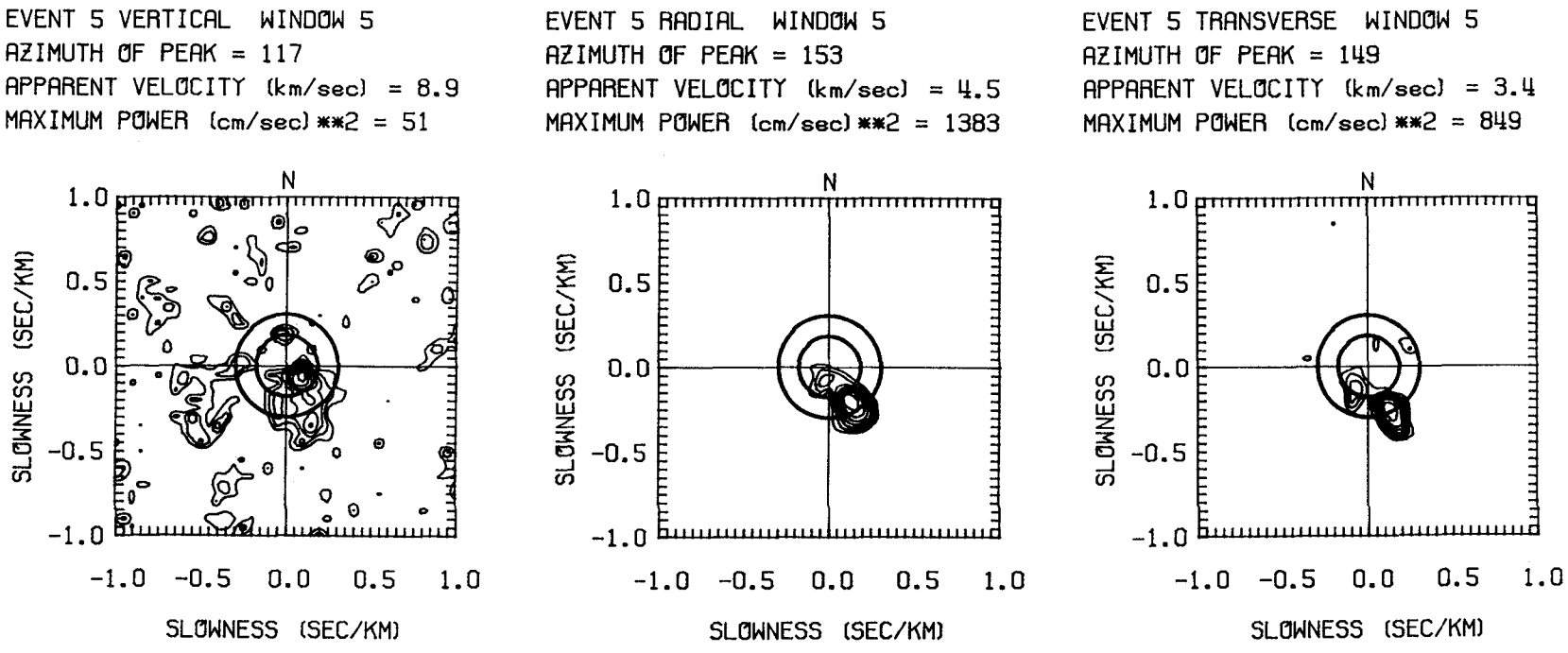

Figure 3.7f: The broadband conventional frequency-wavenumber spectra for the vertical (left), radial (center) and transverse (right) components of ground acceleration recorded during event 5 for time window 5.

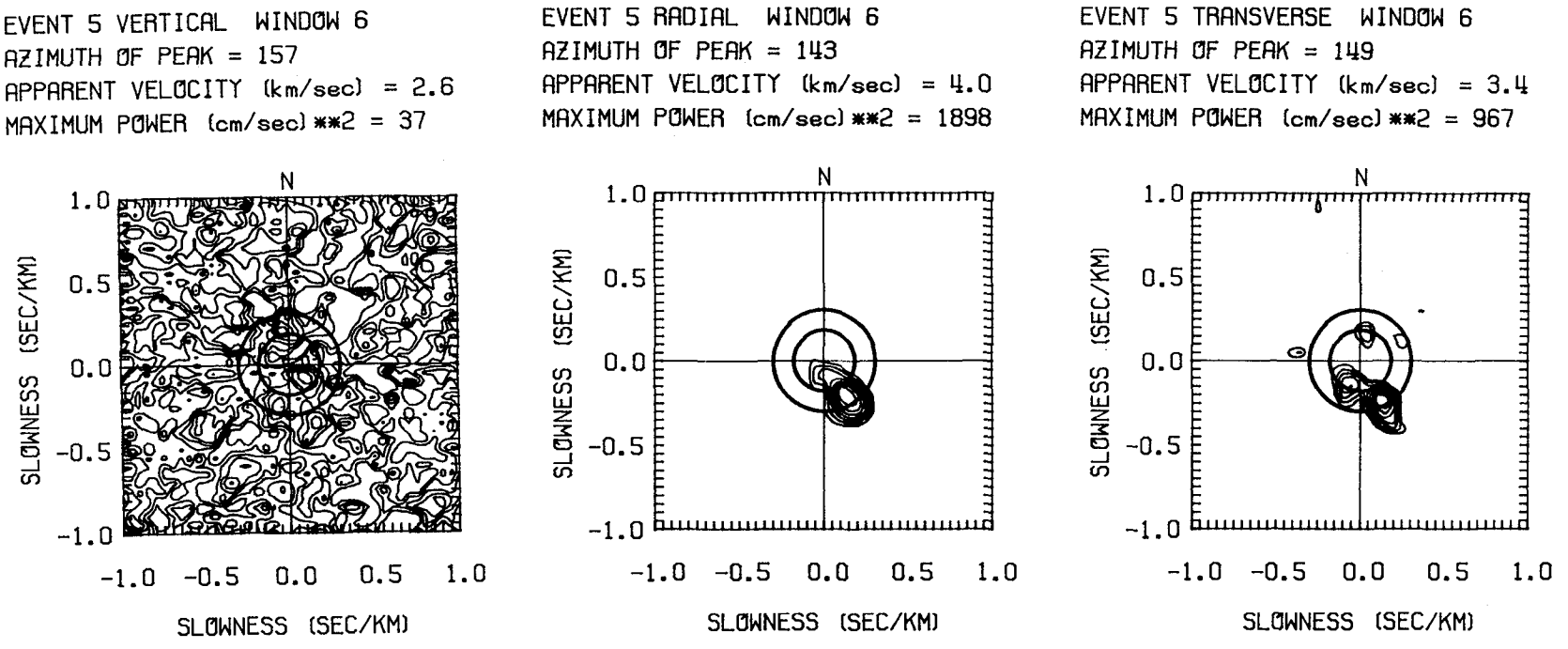

Figure 3.7g: The broadband conventional frequency-wavenumber spectra for the vertical (left), radial (center) and transverse (right) components of ground acceleration recorded during event 5 for time window 6.

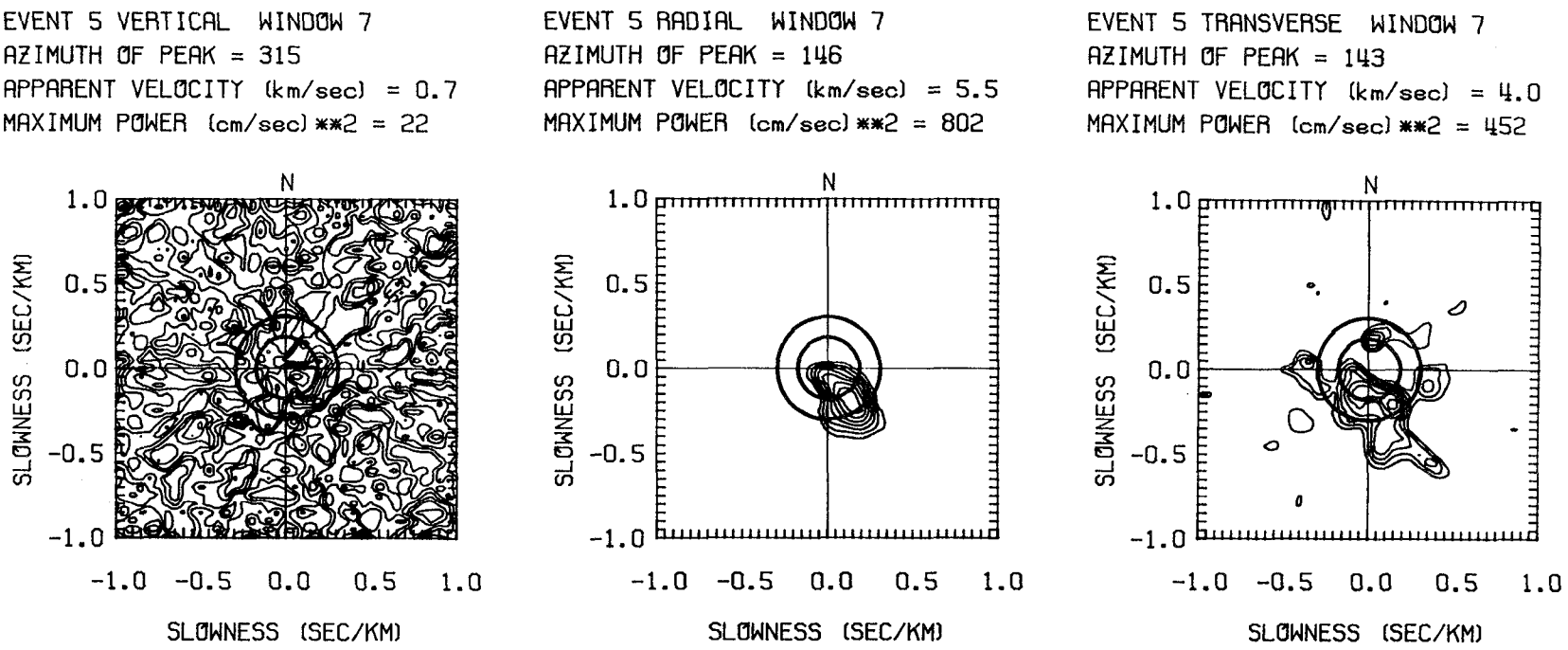

Figure 3.7h: The broadband conventional frequency-wavenumber spectra for the vertical (left), radial (center) and transverse (right) components of ground acceleration recorded during event 5 for time window 7.

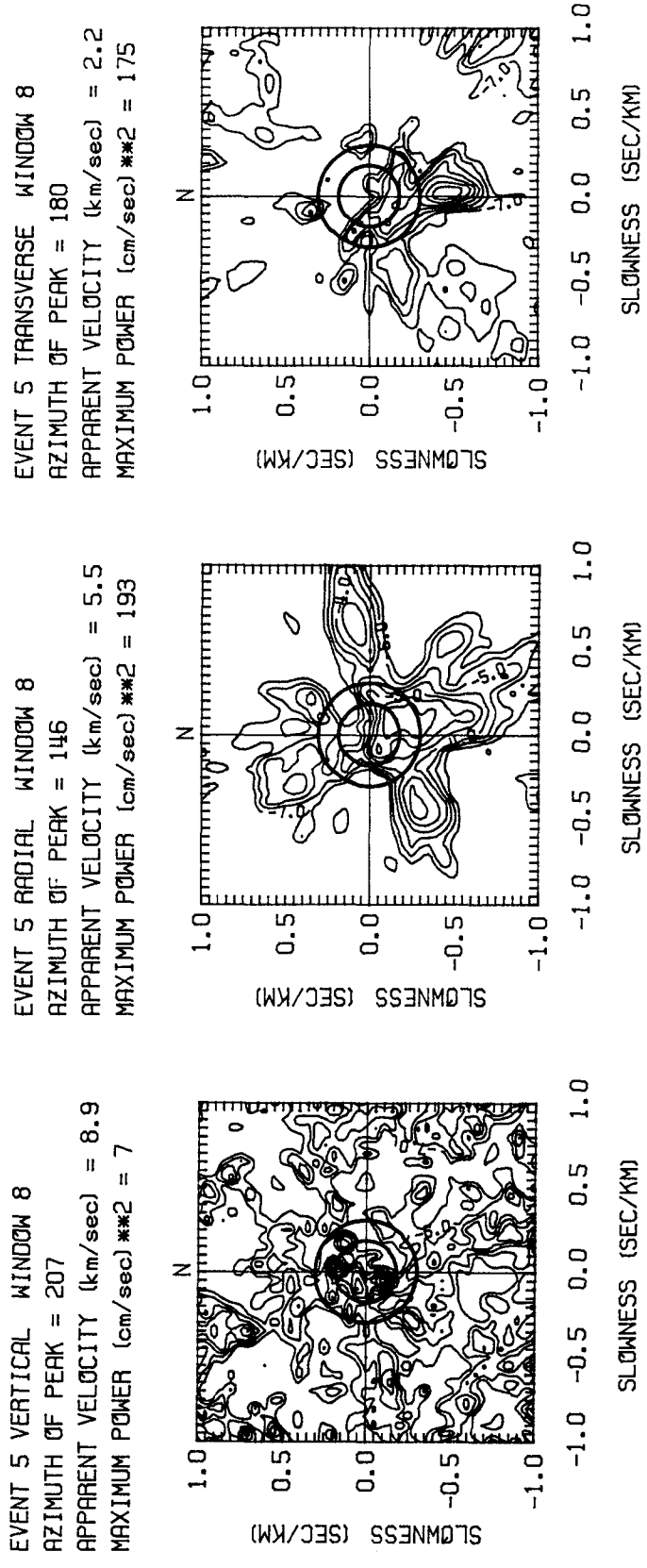

Figure 3.7i: The broadband conventional frequency-wavenumber spectra for the vertical (left), radial (center) and transverse (right) components of ground acceleration recorded during event 5 for time window 8.

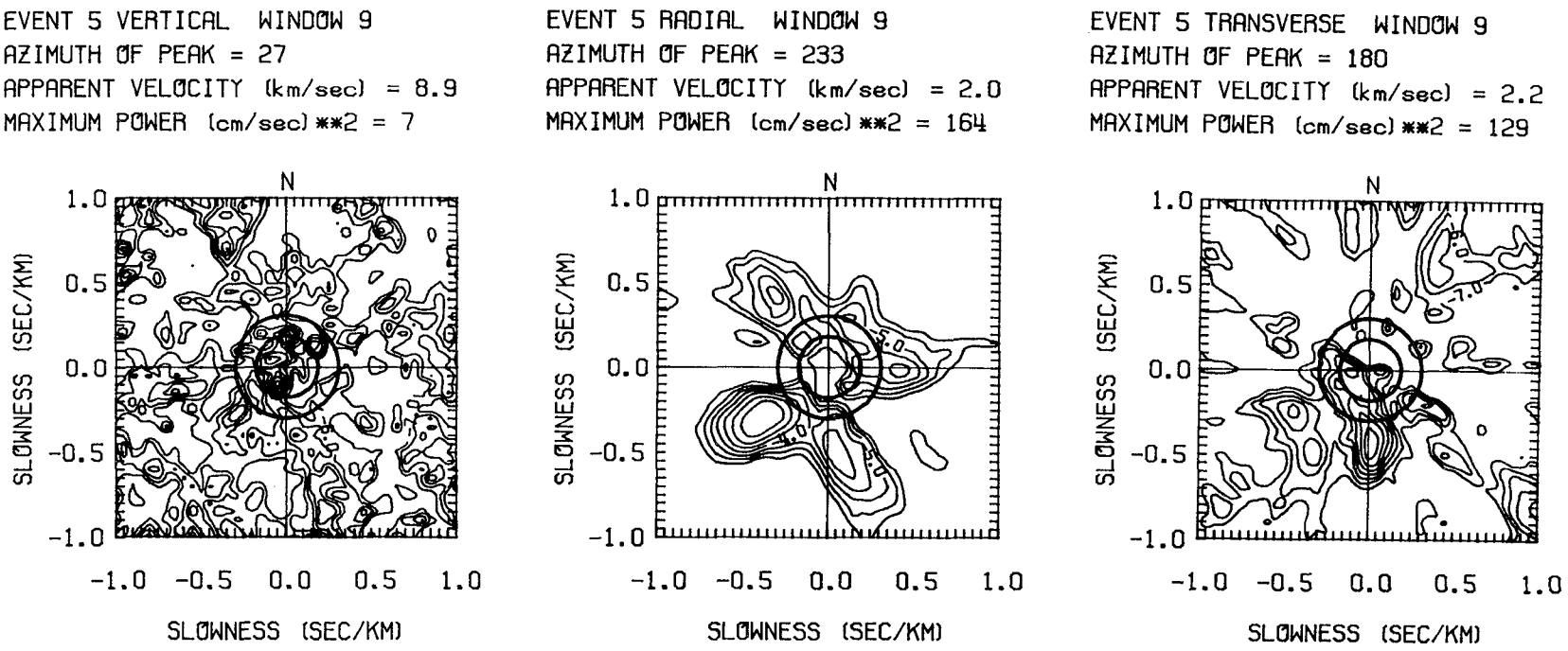

Figure 3.7j: The broadband conventional frequency-wavenumber spectra for the vertical (left), radial (center) and transverse (right) components of ground acceleration recorded during event 5 for time window 9.

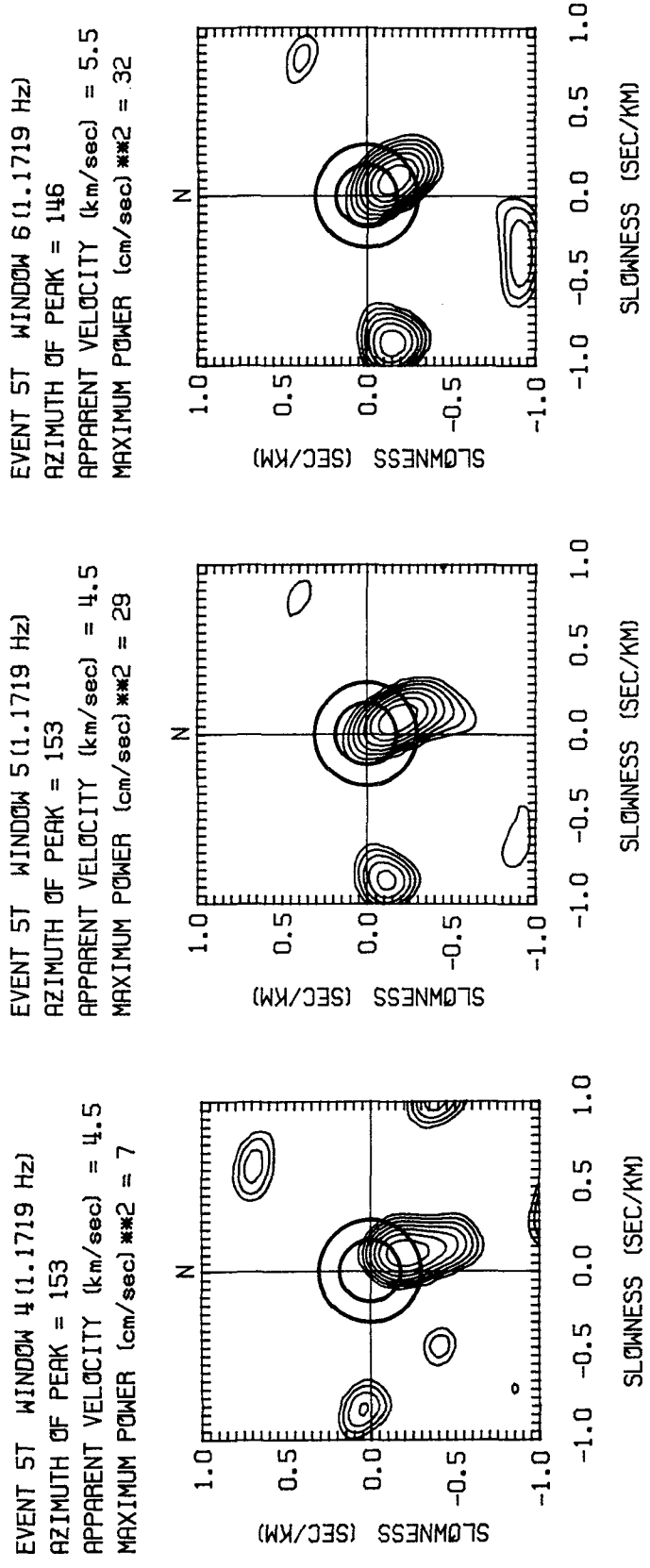

Figure 3.8: The narrowband conventional frequency-wavenumber spectra for the transverse components of ground acceleration recorded during event 5 at 1.1±0.78 Hz for time windows 4 (left) 5 (center) and 6 (right).

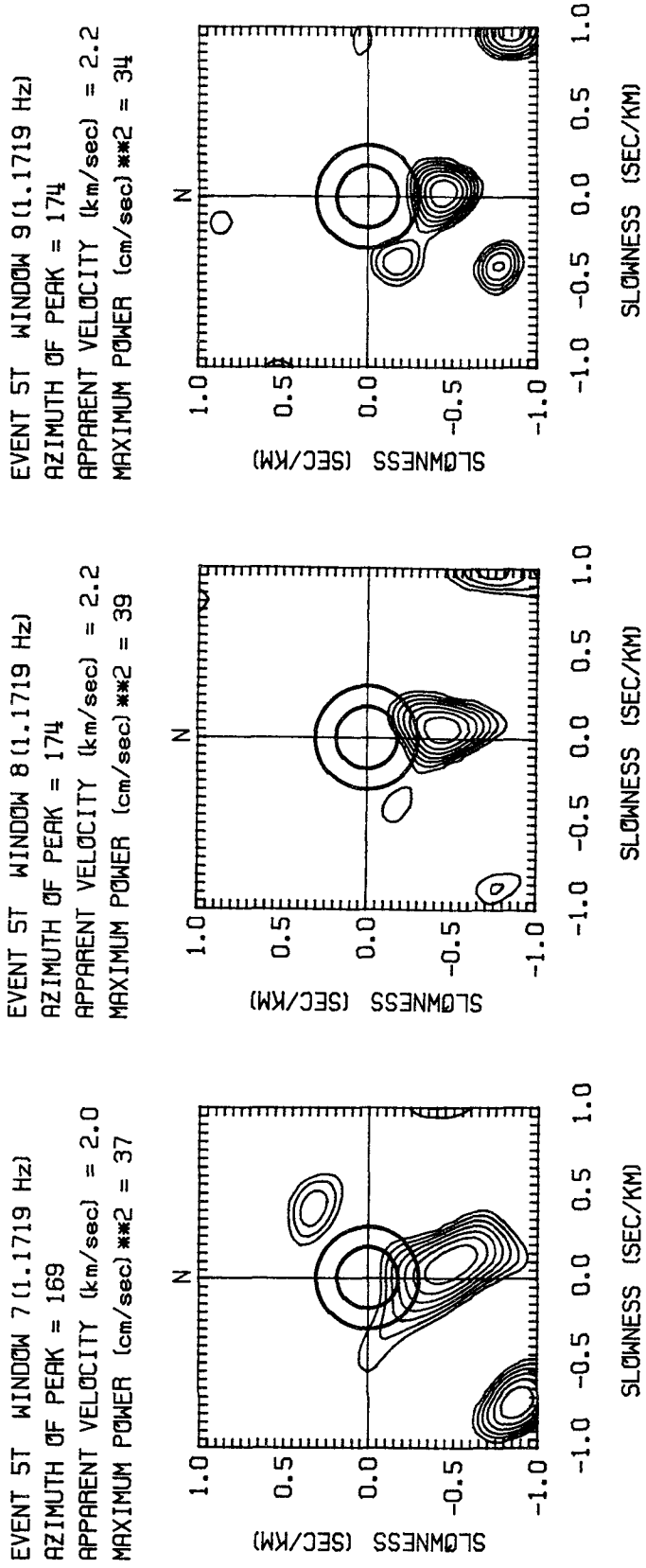

Figure 3.8(continued): The narrowband conventional frequency-wavenumber spectra for the transverse components of ground acceleration recorded during event 5 at 1.1±0.78 Hz for time windows 7 (left) 8 (center) and 9 (right).

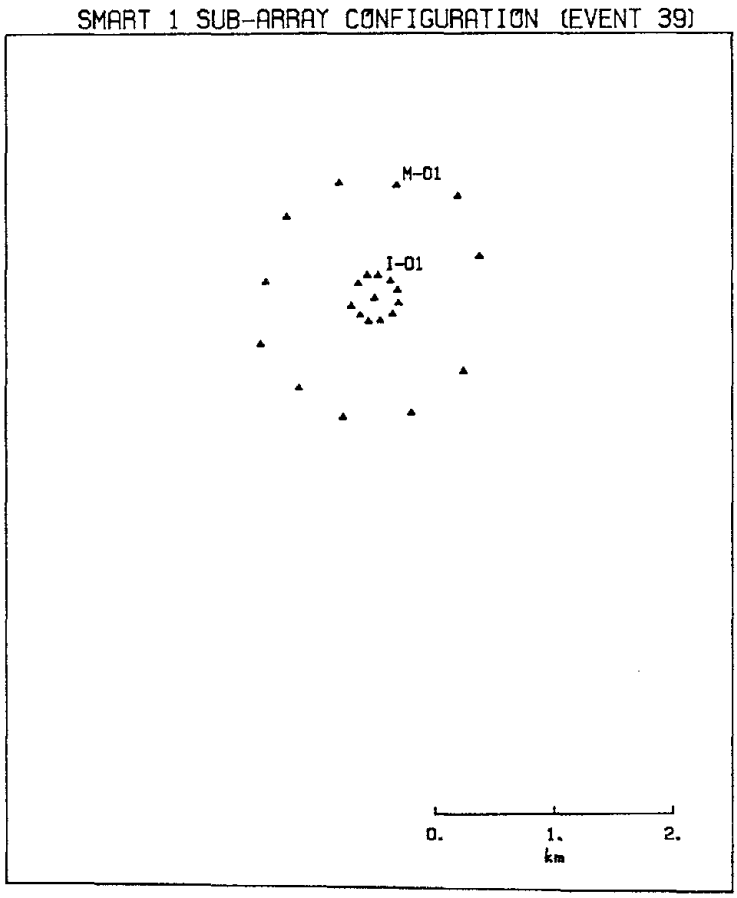

Figure 3.9: The SMART 1 sub-array configuration for event 39. The locations of the stations are shown as stars.

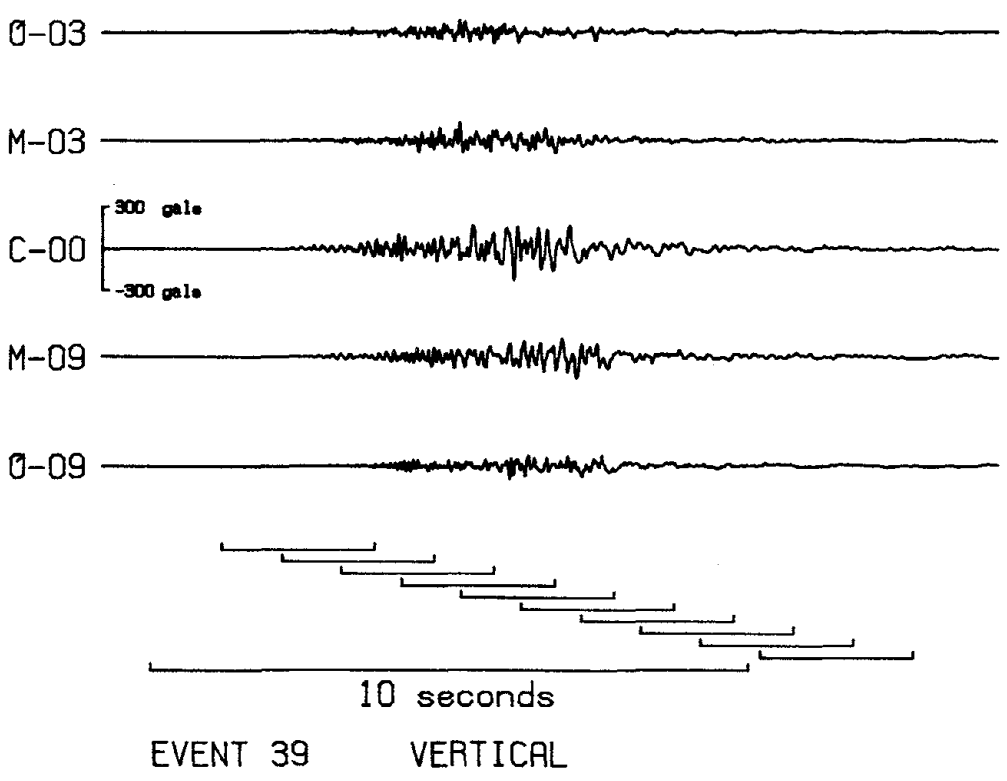

Figure 3.10a: Vertical component accelerograms recorded at five stations in the array during the 16 January 1986 event. The records are aligned on absolute time and are plotted according to increasing epicentral distance. The ten time windows used in the analysis are also shown.

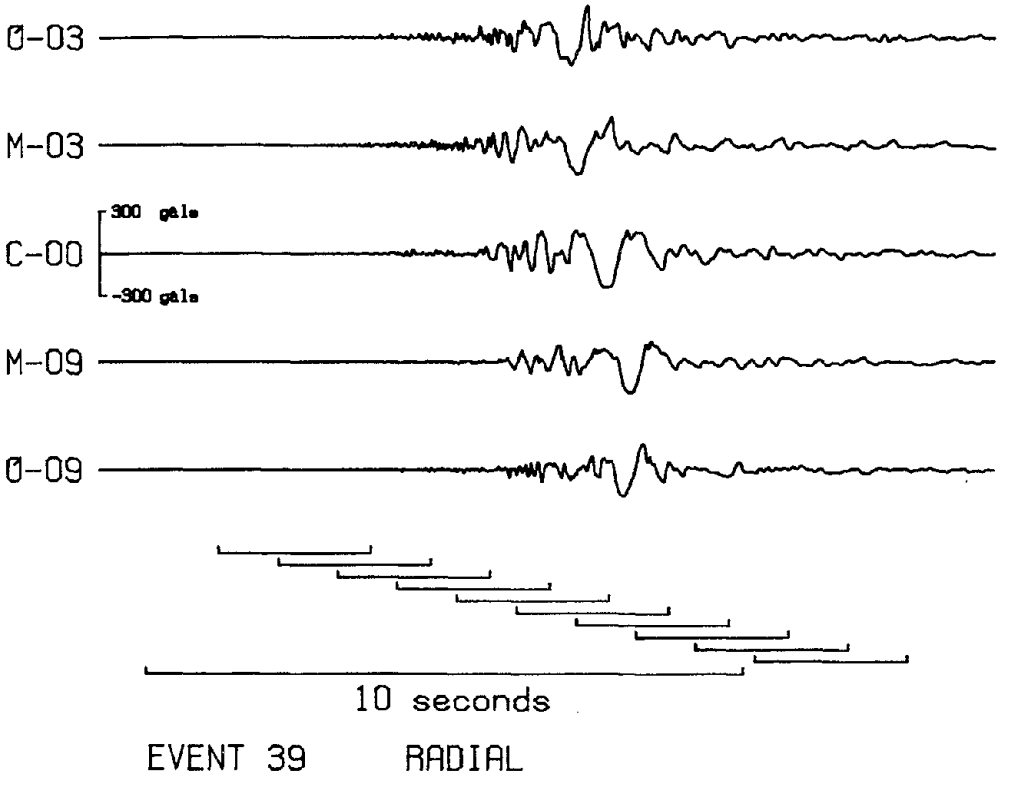

Figure 3.10b: Radial component accelerograms recorded at five stations in the array during the 16 January 1986 event. The records are aligned on absolute time and are plotted according to increasing epicentral distance. The ten time windows used in the analysis are also shown.

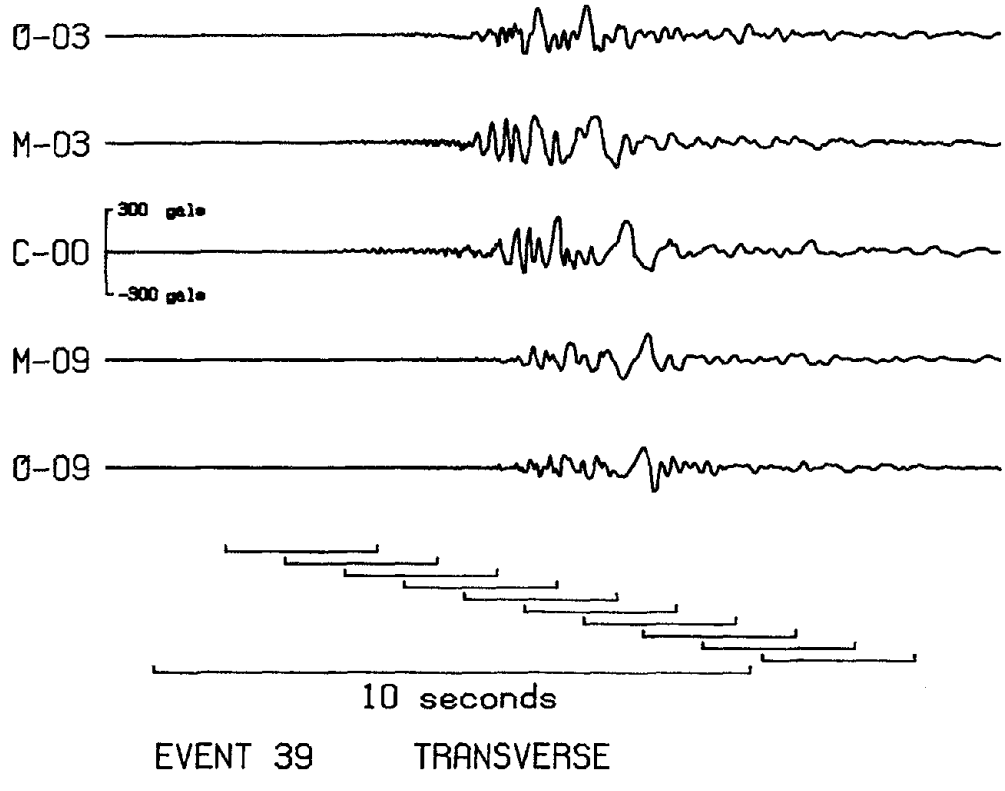

Figure 3.10c: Transverse component accelerograms recorded at five stations in the array during the 16 January 1986 event. The records are aligned on absolute time and are plotted according to increasing epicentral distance. The ten time windows used in the analysis are also shown.

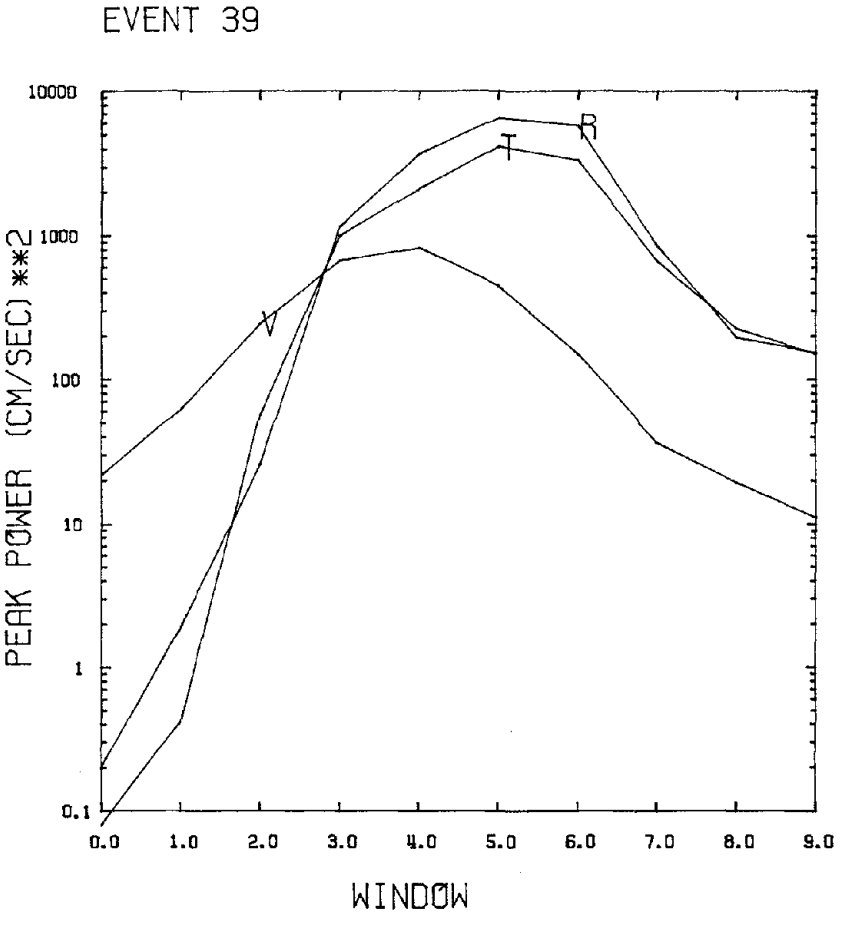

Figure 3.11: The peak power for the vertical (V), radial (R) and the transverse (T) component for the 10 windows shown at the bottom of figure 3.10.

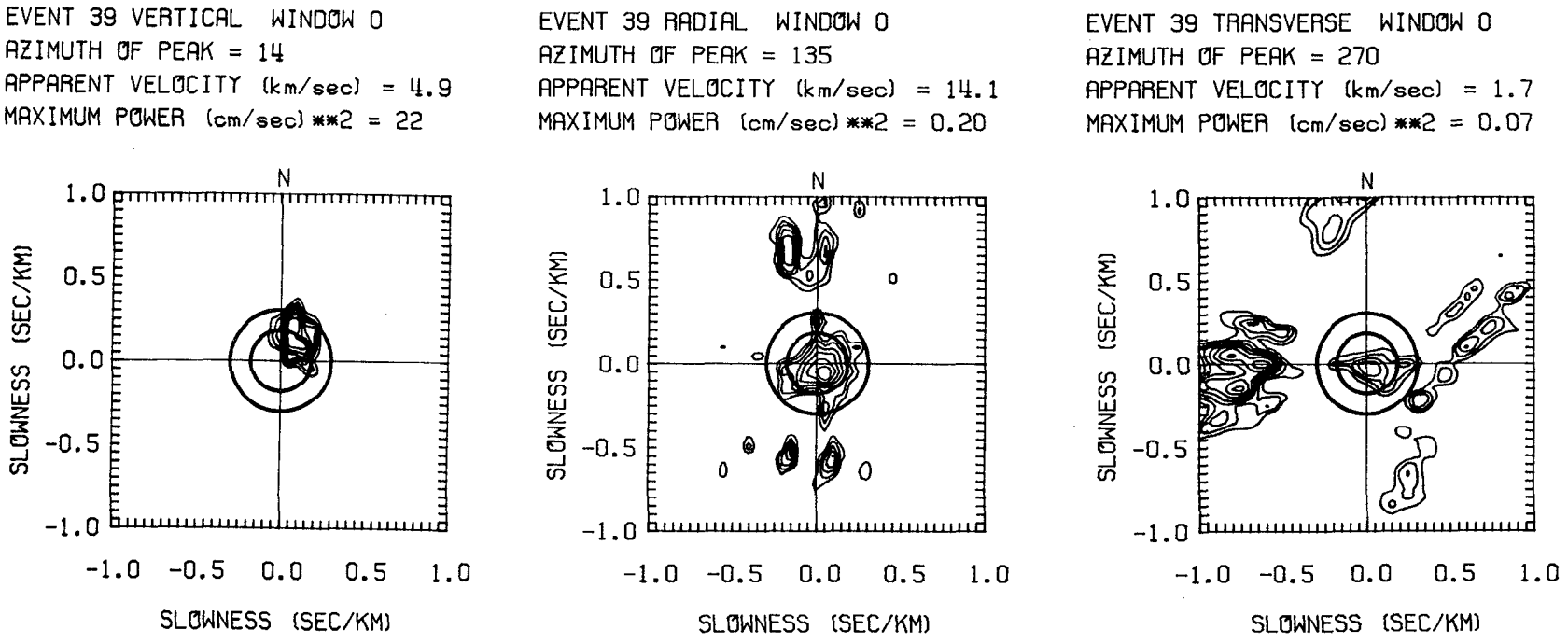

Figure 3.12a: The broadband conventional frequency-wavenumber spectra for the vertical (left), radial (center) and transverse (right) components of ground acceleration recorded during event 39 for time window 0.

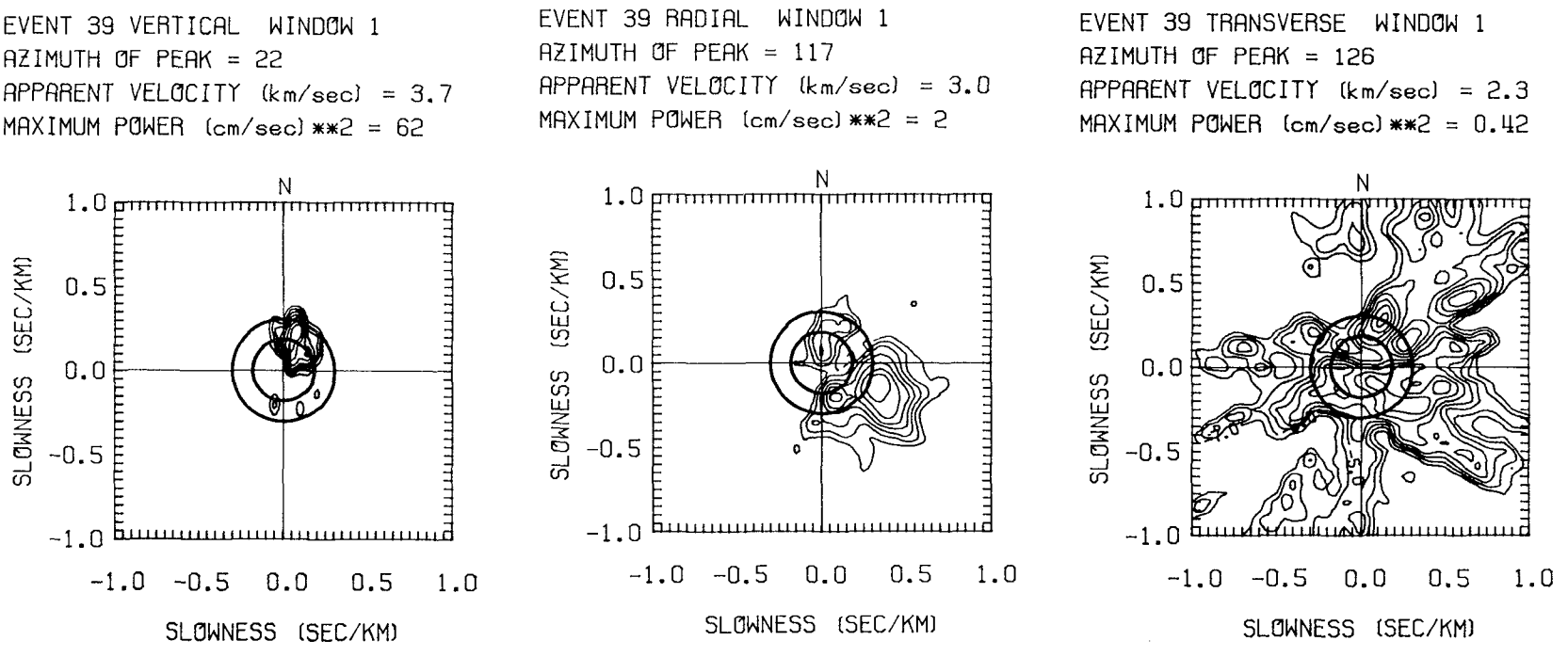

Figure 3.12b: The broadband conventional frequency-wavenumber spectra for the vertical (left), radial (center) and transverse (right) components of ground acceleration recorded during event 39 for time window 1.

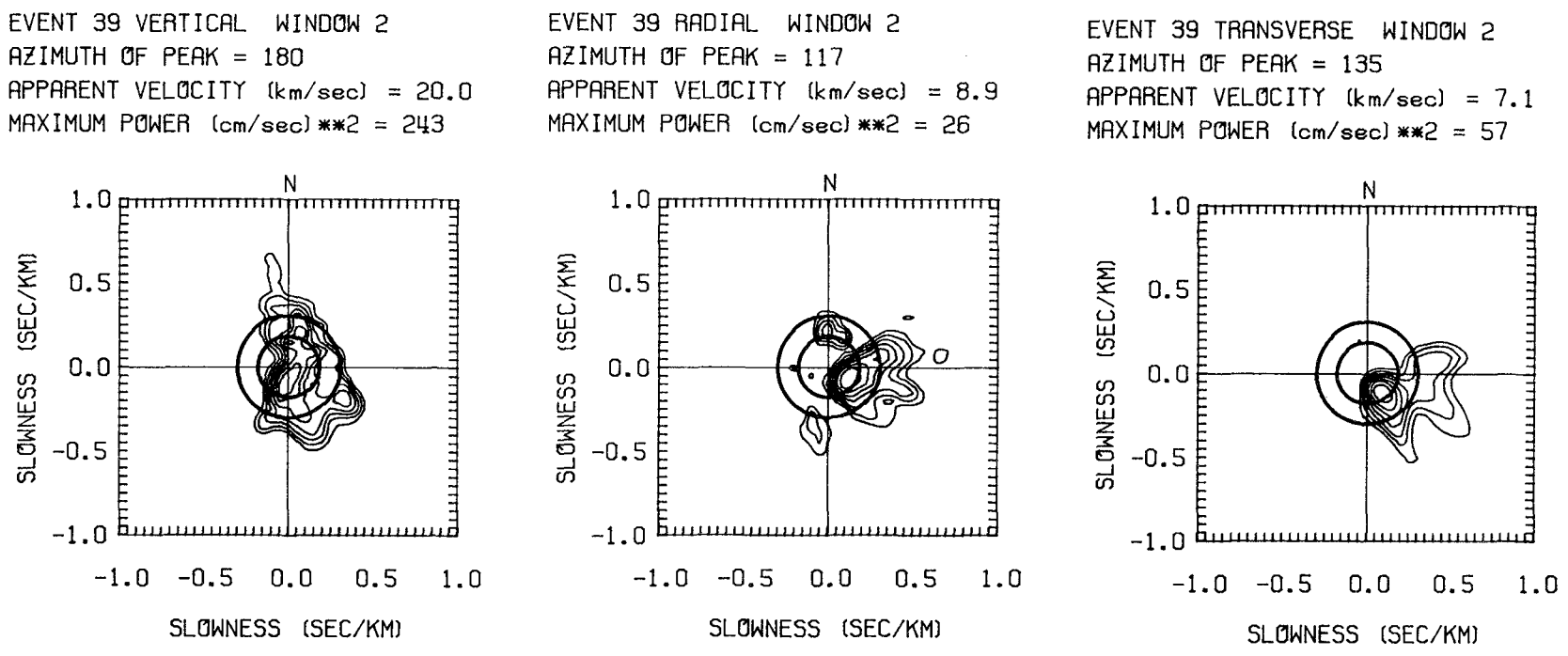

Figure 3.12c: The broadband conventional frequency-wavenumber spectra for the vertical (left), radial (center) and transverse (right) components of ground acceleration recorded during event 39 for time window 2.

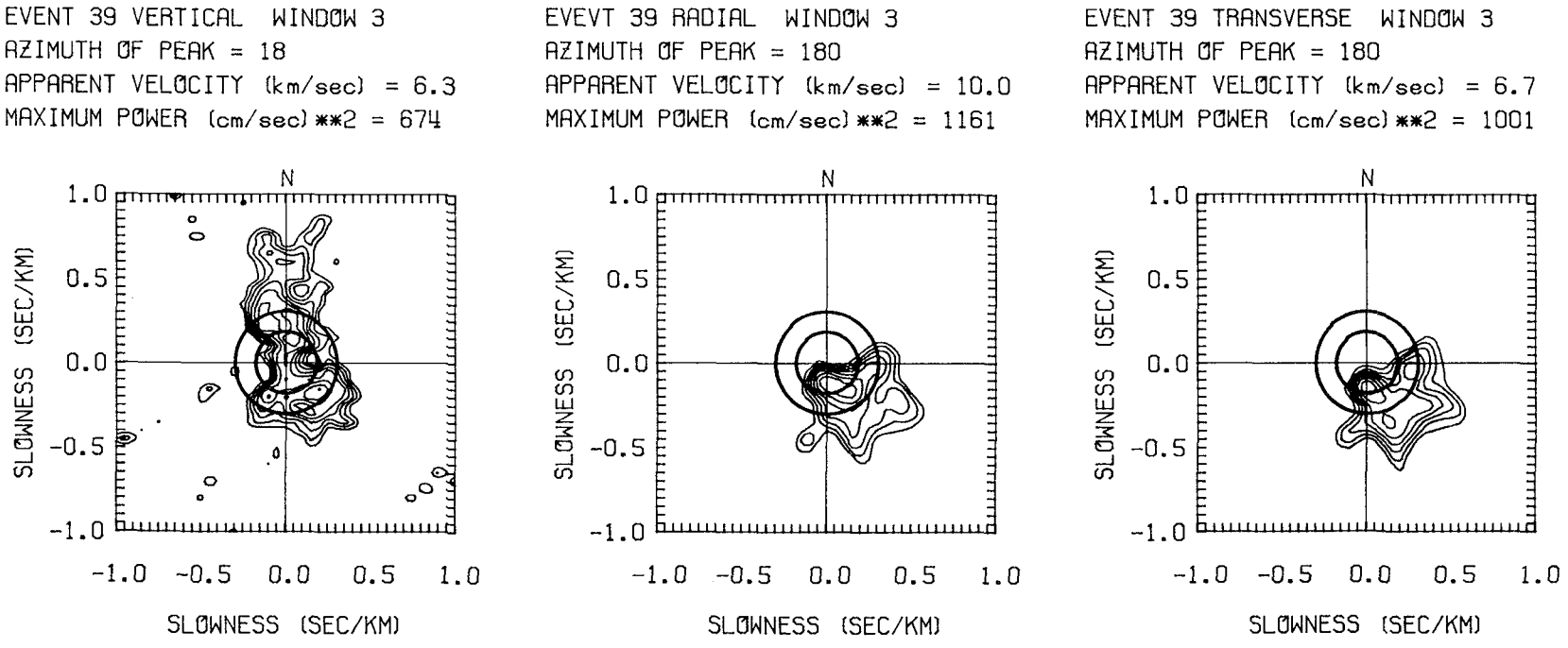

Figure 3.12d: The broadband conventional frequency-wavenumber spectra for the vertical (left), radial (center) and transverse (right) components of ground acceleration recorded during event 39 for time window 3.

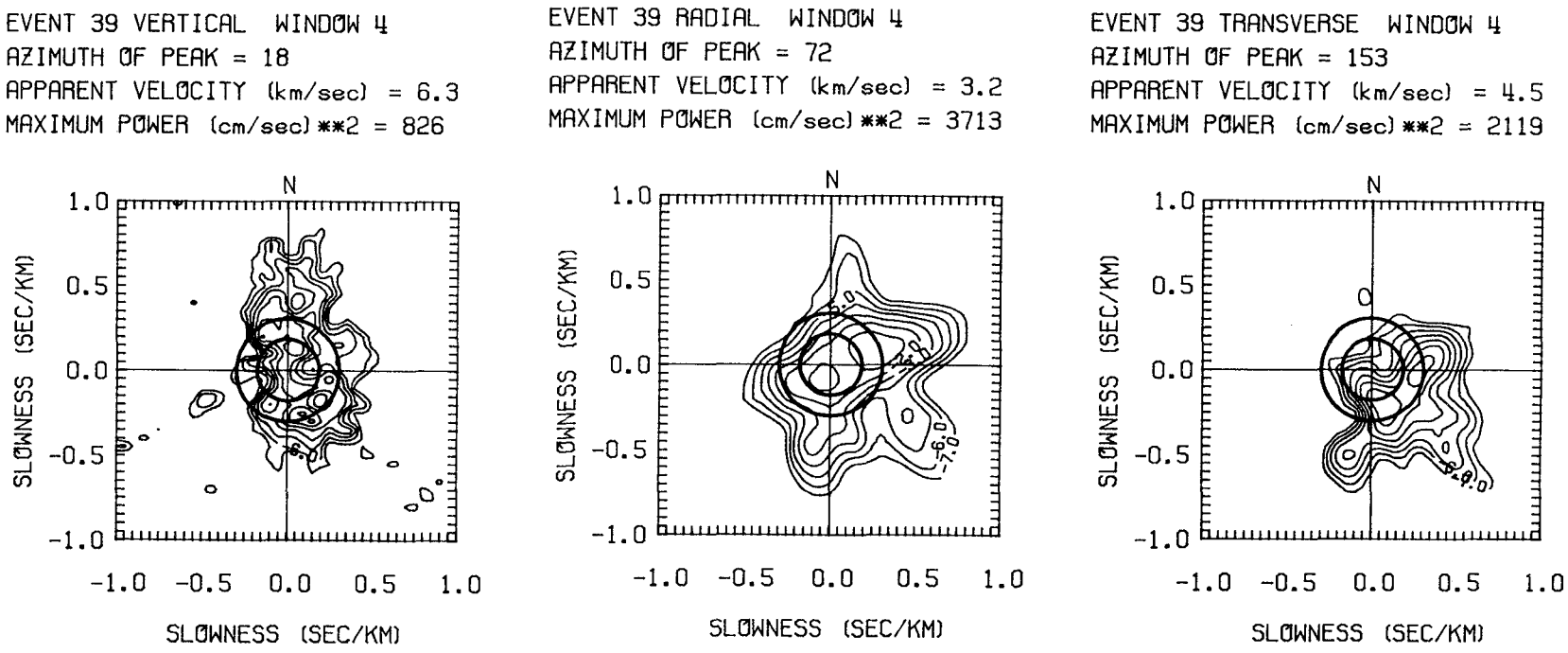

Figure 3.12e: The broadband conventional frequency-wavenumber spectra for the vertical (left), radial (center) and transverse (right) components of ground acceleration recorded during event 39 for time window 4.

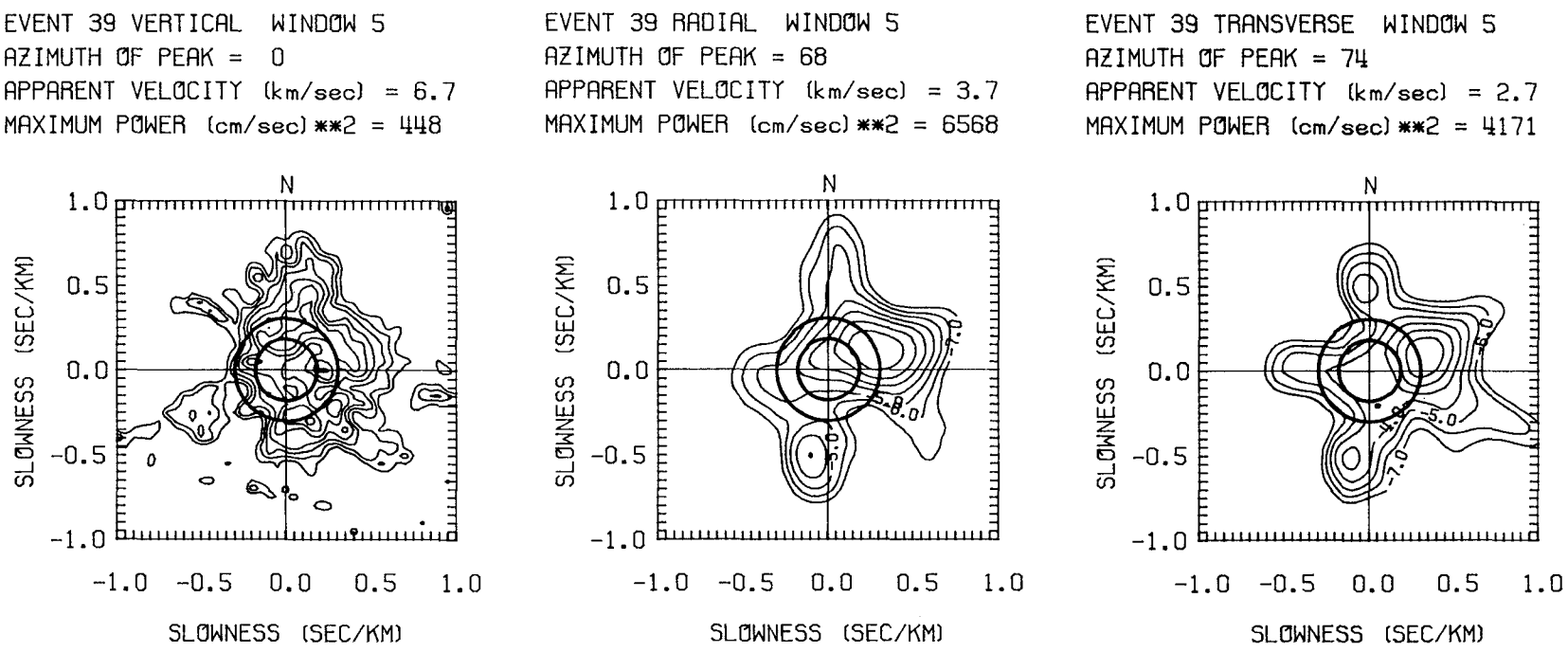

Figure 3.12f: The broadband conventional frequency-wavenumber spectra for the vertical (left), radial (center) and transverse (right) components of ground acceleration recorded during event 39 for time window 5.

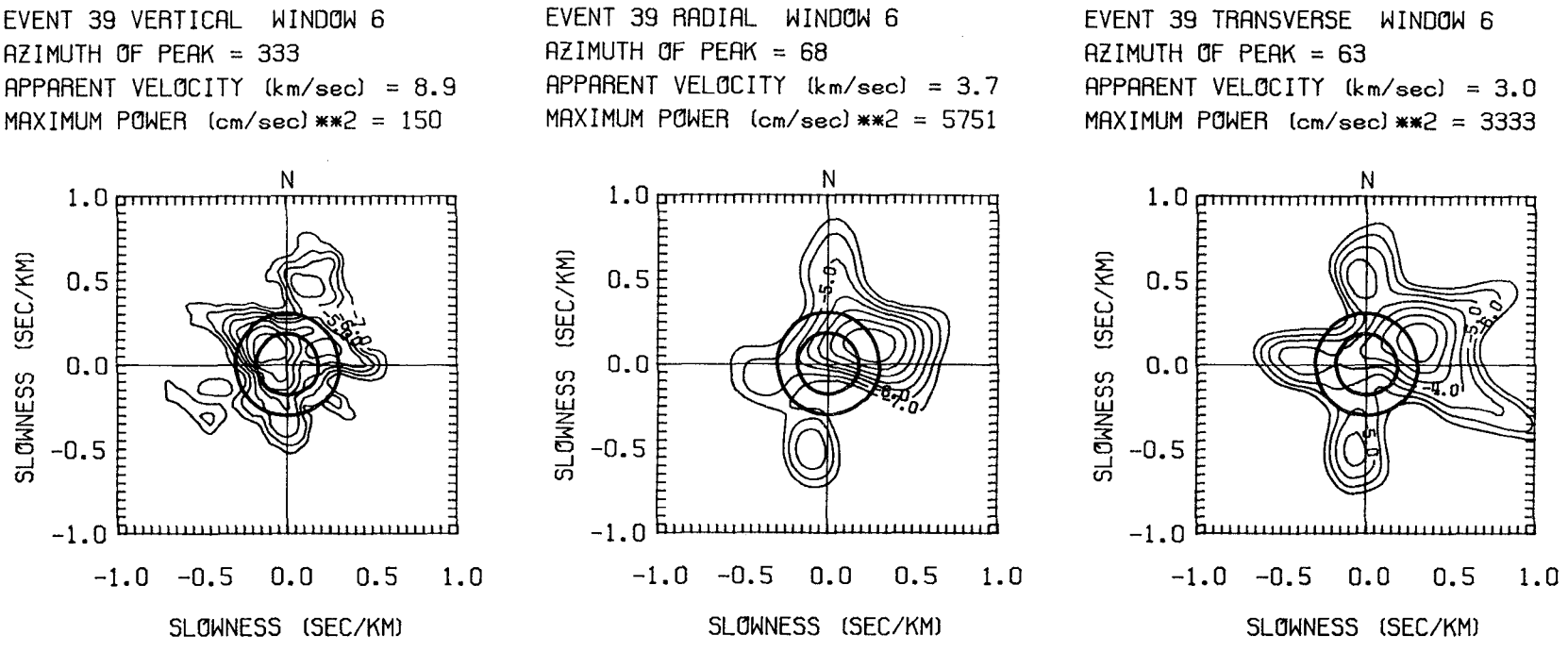

Figure 3.12g: The broadband conventional frequency-wavenumber spectra for the vertical (left), radial (center) and transverse (right) components of ground acceleration recorded during event 39 for time window 6.

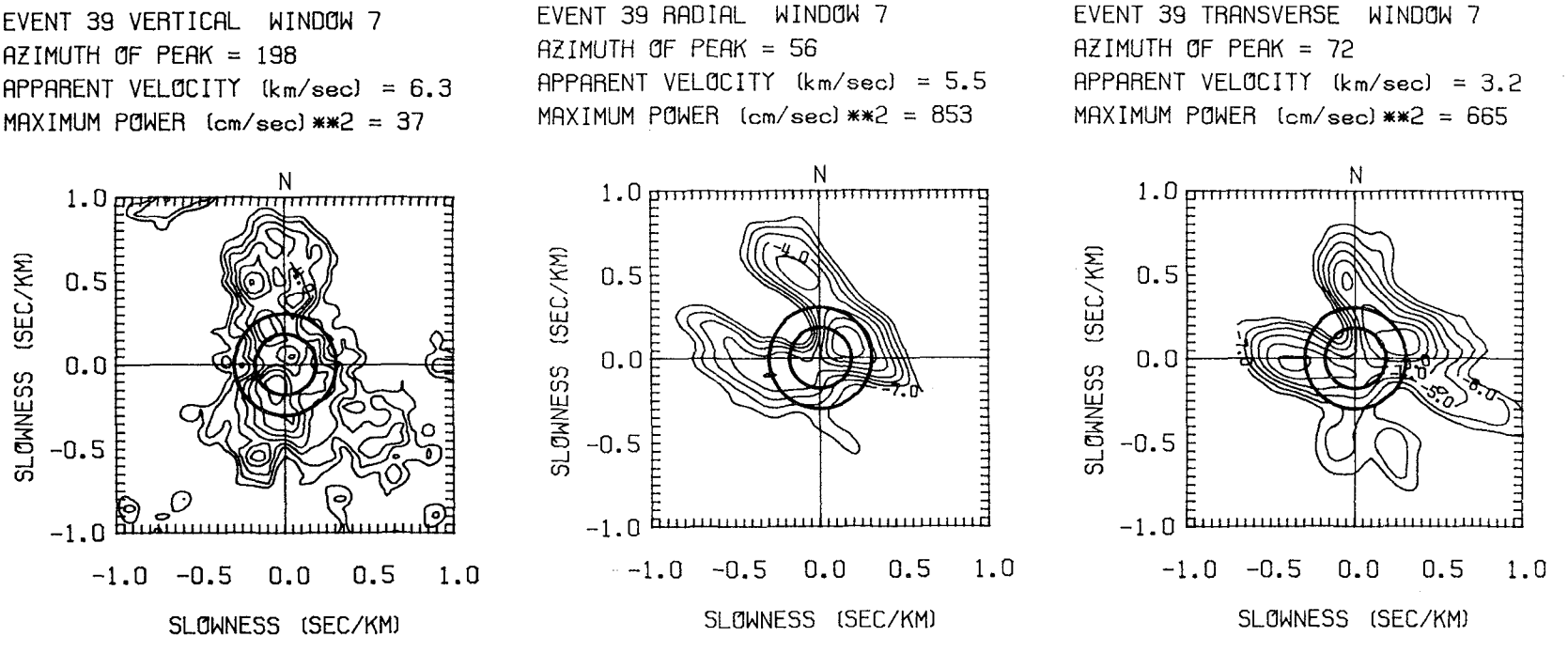

Figure 3.12h: The broadband conventional frequency-wavenumber spectra for the vertical (left), radial (center) and transverse (right) components of ground acceleration recorded during event 39 for time window 7.

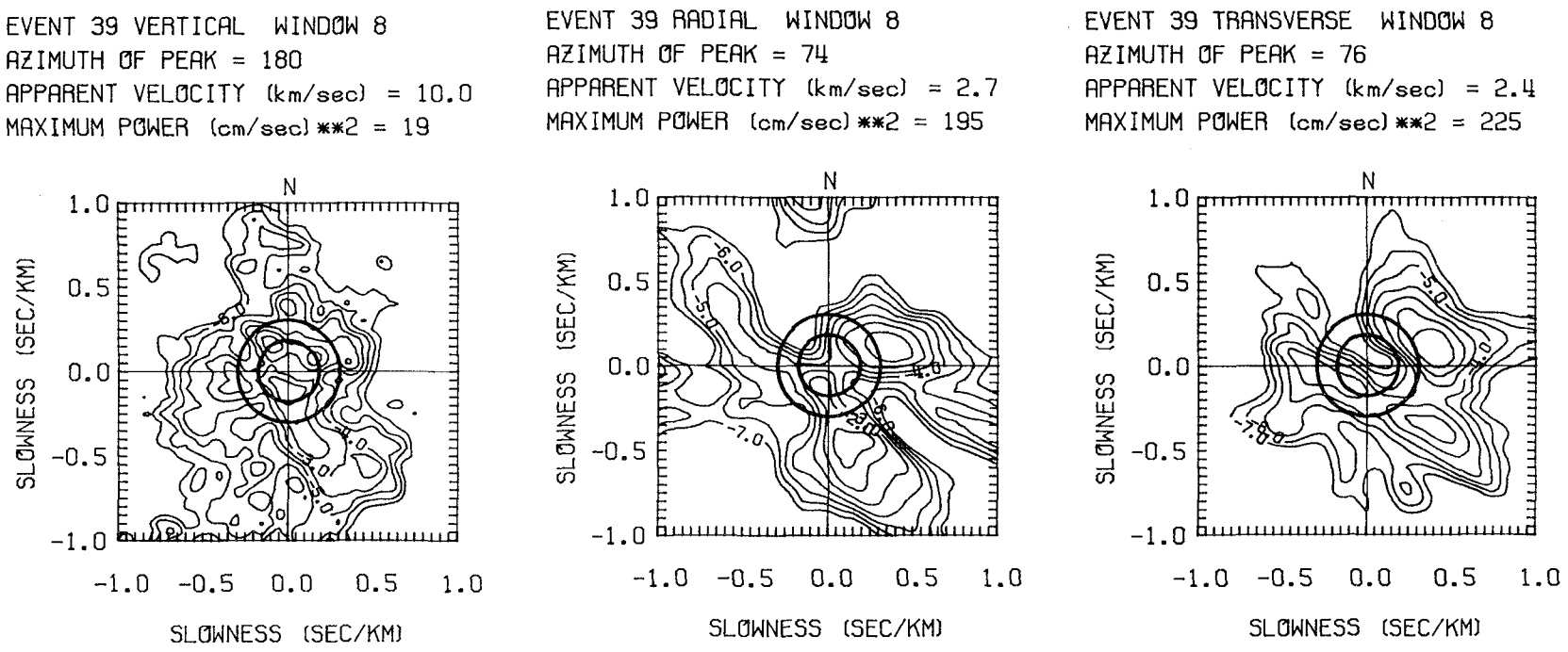

Figure 3.12i: The broadband conventional frequency-wavenumber spectra for the vertical (left), radial (center) and transverse (right) components of ground acceleration recorded during event 39 for time window 8.

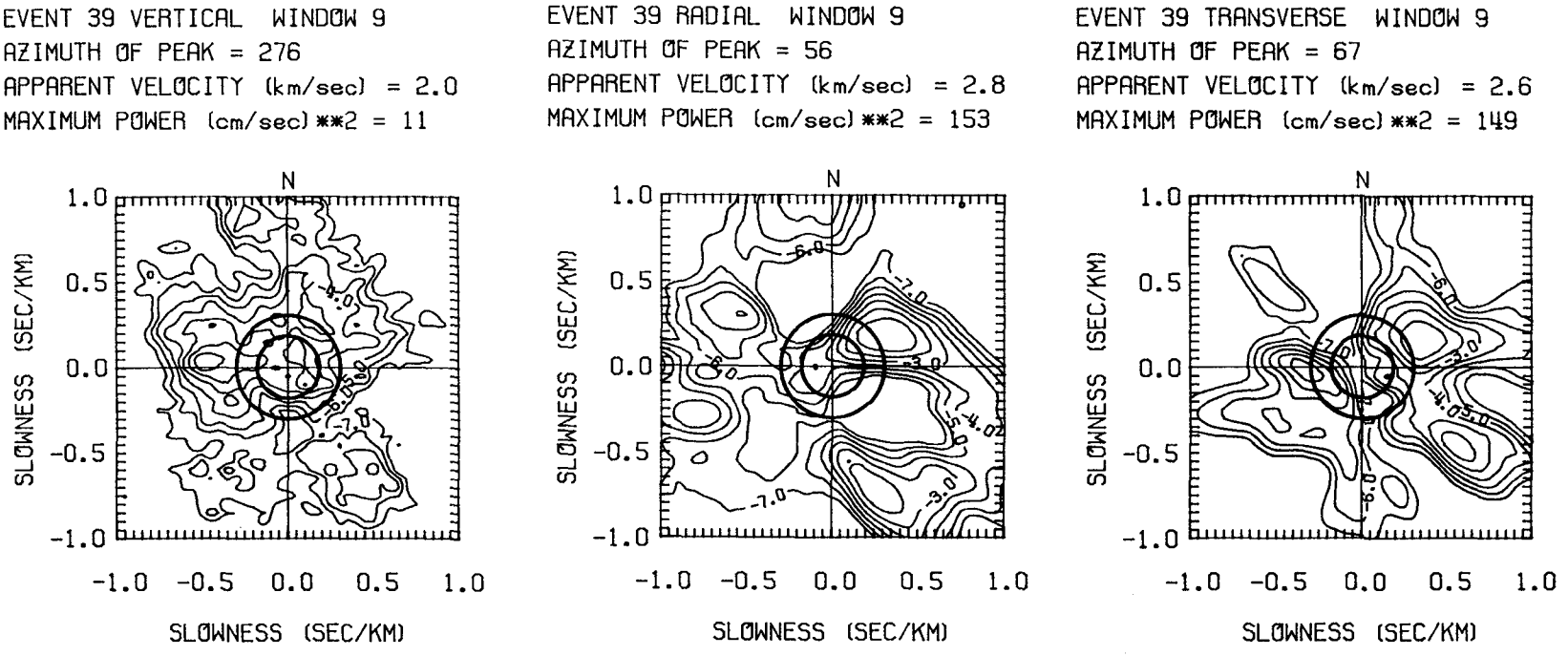

Figure 3.12j: The broadband conventional frequency-wavenumber spectra for the vertical (left), radial (center) and transverse (right) components of ground acceleration recorded during event 39 for time window 9.

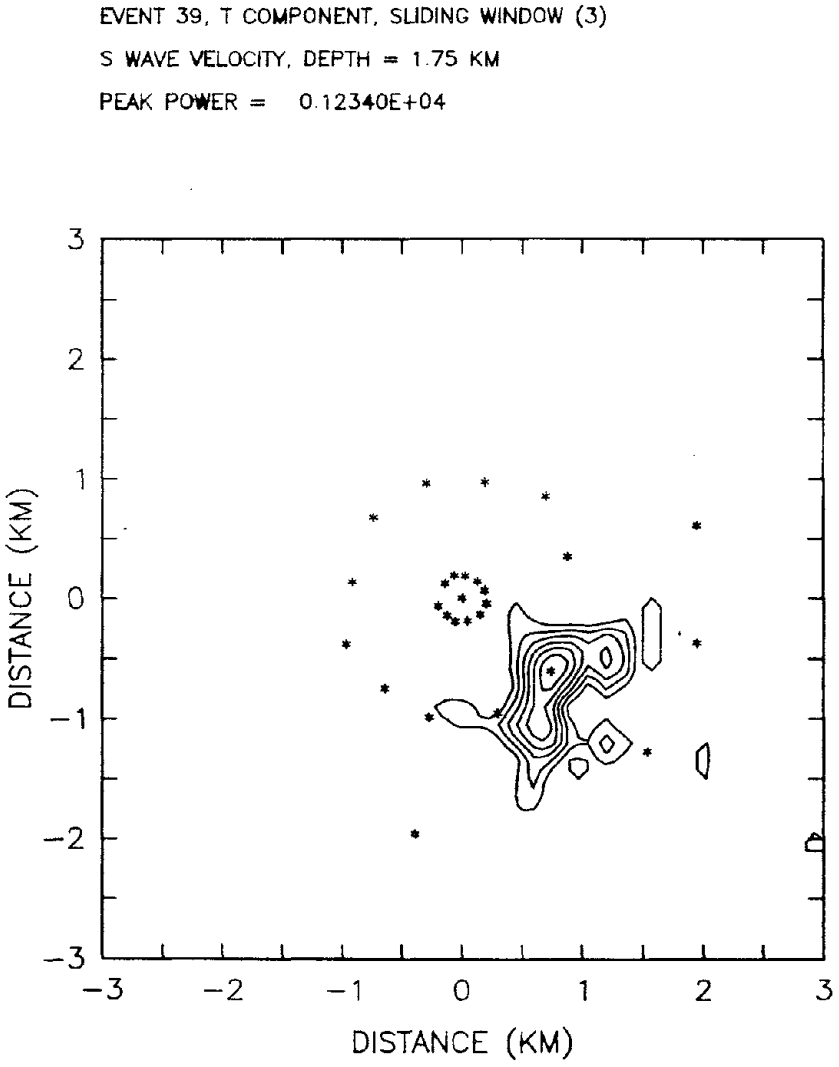

Figure 3.13: The broadband conventional frequency-wavenumber spectra modified for spherical waves for the transverse component of event 39 in time window 3. The station locations are shown as stars. Note that the sub-array has been augmented by stations in the outer ring to improve the estimate of the location of the heterogeneity (from Abrahamson and Darragh, 1987).

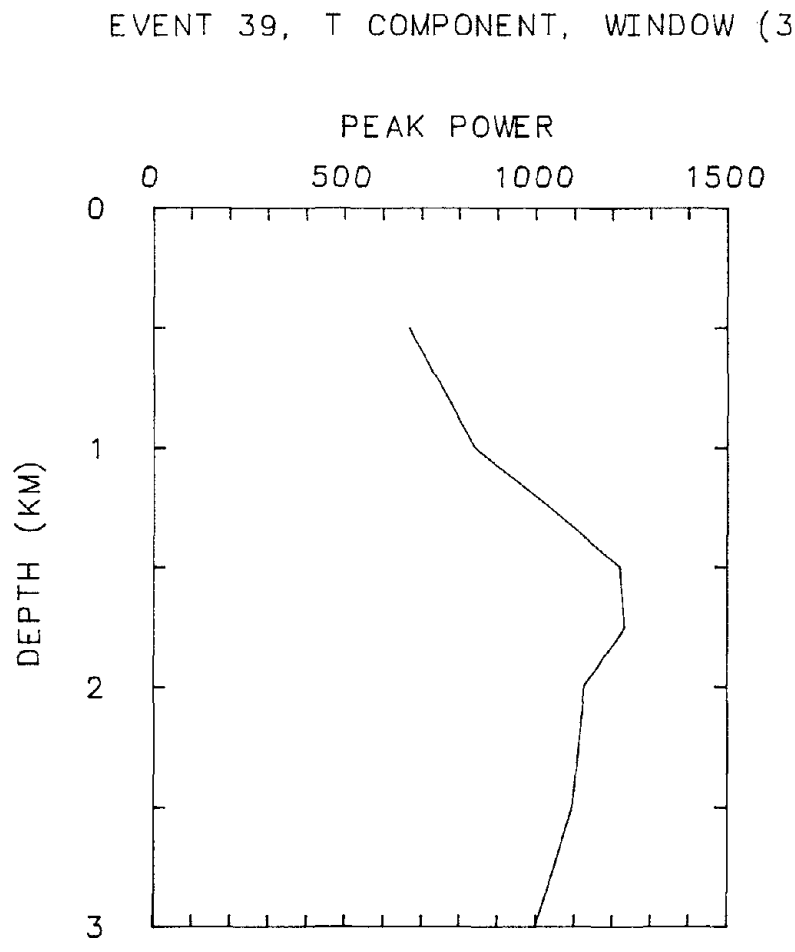

Figure 3.14: Peak power from the conventional frequency-wavenumber spectra modified for spherical waves as a function of point source depth (from Abrahamson and Darragh, 1987).

CHAPTER 4: POLARIZATION ANALYSIS

4.1 Introduction

In this chapter, the polarization of the wavefields of two large earthquakes recorded at SMART 1 (see figure 3.1 and table 3.1) is estimated. The goal of this analysis is to interpret the wavefields in terms of polarized waves at the array. The narrowband degree of polarization of the wavefield, $\beta^2(\omega)$ in equation (2.4.3) or $\beta_2^2(\omega)$ in equation (2.4.8), is estimated as a function of both center frequency and time. The maximum narrowband plane wave power from the conventional estimate of the power, (2.3.1), and the eigenvalues of the cross-spectral matrix, $S(\omega)$ in equation (2.2.2), are also estimated for identical center frequencies and time windows. Broadband estimates of the degree of polarization of the wavefields, along with standard errors, are obtained from ($\hat{\beta}^2(\omega)$ or $\hat{\beta}_2^2(\omega)$) by averaging these estimates over the appropriate bandwidth. A single polarized broadband wave arriving at the array can be identified from a single eigenvalue dominating the spectra of $S(\omega)$ in combination with estimates of $\beta^2(\omega)$ near unity. Two polarized broadband waves arriving at the array in the same time window can be identified from near unity estimates of $\beta_2^2(\omega)$ combined with two eigenvalues dominating the spectra of $S(\omega)$.

As in chapter 3, a time window that includes 256 samples is used in all calculations. The start of the first time window for each event is 2.0 seconds after the instrument at the first station in the array was triggered (see figures 3.5a and 3.10a). The starts of the ten overlapping time windows are separated by 1.0 second. Only data collected from the central station and from stations in the inner and middle rings of SMART 1 have been used to estimate the degree of polarization of the wavefield. The SMART 1 sub-array station configuration is shown in figure 3.2 for event 5 and in figure 3.9 for event 39.

Narrowband estimates for each of the parameters examined in this chapter have been calculated at eleven center frequencies. For all three components of ground motion the smallest allowable center frequency is 1.17 Hz when a time window including 256 samples

and a smoothed frequency domain estimate of $S(\omega)$ is used (table 2.1). The largest center frequency is 8.98 Hz for the vertical component and 5.08 Hz for both of the horizontal components. The center frequency is increased in steps of 0.78 Hz for the vertical component and 0.39 Hz for the horizontal components. The estimate of $S(\omega)$ in the frequency domain is smoothed over five nearby frequencies (M=2 in (2.2.2)). The nearby frequencies are separated by 0.39 Hz (table 2.1) and produce a bandwidth of 1.56 Hz for the narrowband estimates of all three components. Without frequency domain smoothing in calculating the estimate of $S(\omega)$, all of the estimates of the polarization of the wavefields would equal unity. Such a result is analogous to estimates of coherence without averaging (smoothing) where again all estimates would equal unity. However, smoothing in the frequency domain also increases the number of large eigenvalues in the eigenspectra of $S(\omega)$ because the nearby frequencies are not independent as is assumed for frequency domain smoothing. This fact complicates the interpretation of wavefields in terms of broadband polarized waves. Generally, 2M+1 large eigenvalues result from smoothing the cross-spectral matrix over 2M+1 nearby frequencies. In this analysis there are, generally, five (M=2) eigenvalues that occur within four decades of the largest eigenvalue (e.g. figure 4.1).

4.2 Application To Simulated Ground Accelerations

The degree of polarization for wavefields resulting from two types of simulated ground acceleration has been estimated in order to study the sensitivity and bias of such estimates. In the first example, the degree of polarization of a random (white noise) wavefield for the sixteen stations in the sub-array configuration used in analyzing event 5 (figure 3.2) is estimated. The radial accelerations have an approximately uniform distribution of $\pm 200 cm/sec^2$. The narrowband estimates of the polarization of the wavefield, the narrowband peak plane wave power and the eigenvalues of $S(\omega)$ are shown, as a function of center frequency, in figure 4.1. The conventional narrowband peak estimate of the plane wave power is nearly constant as is expected for a random wavefield. The narrowband estimates of $\beta^2(\omega)$ and $\beta_2^2(\omega)$ illustrate the bias in these estimates due to the polarization of

white noise. The broadband estimates for the degree of polarization of the wavefield with the standard errors of the means of the estimates are $\hat{\beta}^2(\omega)$=0.34±0.016 and $\hat{\beta}_2^2(\omega)$=0.74±0.015. Because random wavefields are better described by multiple polarized waves than by a single polarized wave, $\hat{\beta}_2^2(\omega) > \hat{\beta}^2(\omega)$. In this example, the three largest eigenvalues of S(ω) are of the same order (figure 4.1). Since the estimate of $\beta_2^2(\omega)$ for a random wavefield is 0.74, it is expected that this estimate of the polarization of the wavefield will generally be near unity and of limited utility for the separation of polarized waves. Based on this simulation the relative size of the largest eigenvalues of S(ω) and $\hat{\beta}^2(\omega)$ provide useful information on the polarization of a random wavefield.

For the second example, the radial component of ground acceleration recorded at station C-00 during time window six (see figure 3.5b for the C-00 radial seismogram and the time window location) is the input acceleration for each of the sixteen stations in the subarray configuration used in analyzing event 5 (figure 3.2). Using this analysis, these homogeneous input accelerations model a single, vertically propagating, broadband plane wave. The narrowband estimates are given, as a function of center frequency, in figure 4.2. All of the narrowband estimates of the polarization of the wavefield and, therefore, the broadband estimates of the polarization of the wavefield equal unity. The eigenspectra of S(ω) is dominated by a single eigenvalue in this example. For each of the eleven center frequencies the largest eigenvalue is approximately 10^{17} times larger than the next largest eigenvalue. One concludes from this example that $\hat{\beta}^2(\omega)$ and the eigenstructure of S(ω) provide information useful in analyzing the polarization of a homogeneous wavefield.

4.3 Application To SMART 1 Ground Accelerations

Figures 4.3 through 4.8 display $\hat{\beta}^2(\omega)$, $\hat{\beta}_2^2(\omega)$, the narrowband peak conventional estimate of the plane wave power and the normalized eigenvalues of S(ω) within a factor of 10^4 of the largest eigenvalue. Three time windows during event 5 are shown in figures 4.3

through 4.5: direct P-wave onset (time window one), direct S-wave onset (time window five) and coda (time window nine). Three time windows during event 39 are shown in figures 4.6 through 4.8: direct P-wave onset (time window zero), P-coda (time window two) and S-wave and surface wave arrivals (time window five). This choice of time windows allows a discussion of the salient features of the polarization of recorded wavefields at SMART 1.

Generally, $\hat{\beta}^2(\omega)$ varies more than $\hat{\beta}_2^2(\omega)$ due to the large bias in $\hat{\beta}_2^2(\omega)$. Values of $\hat{\beta}^2(\omega)$ near unity are typically associated with a single eigenvalue that dominates the spectra of $S(\omega)$. The second largest eigenvalue of $S(\omega)$ is usually a factor of 10 or more smaller than the largest eigenvalue of $S(\omega)$ in this case. Conversely, low values of $\hat{\beta}^2(\omega)$ are generally associated with two or more eigenvalues that dominate the spectra of $S(\omega)$. The other large eigenvalues of $S(\omega)$ are usually within a factor of 10 of the largest eigenvalue of $S(\omega)$ in this case. Low values of $\hat{\beta}^2(\omega)$ may also be produced by low values of the peak narrowband plane wave power. Values of $\hat{\beta}^2(\omega) < 0.44$ are not significantly different from white noise (at approximately the 95 percent confidence level) based on a t-test for the difference between means.

4.3.1 Event 5

For the current study of event 5 the records from sixteen stations are used in the polarization analysis. Table 4.1 summarizes the broadband estimate of the polarization of the wavefield, $\hat{\beta}^2(\omega)$, along with the standard error of the mean for each of ten time windows (see figure 3.5). The bandwidth of these estimates is from 1.17 to 8.98 Hz on the vertical component and from 1.17 to 5.08 Hz on both horizontal components.

On the vertical component, $\hat{\beta}^2(\omega)$ decreases with time from a maximum value of 0.77 $\pm$ 0.042 in time window zero (see table 4.1). The broadband polarization of the wavefield is not significantly different than white noise in time windows six through nine, in agreement with the frequency-wavenumber analysis described in section 3.3.1. On the horizontal

components, $\hat{\beta}^2(\omega)$ decreases after the P-wave onset until the onset of the direct S-wave occurs in time windows four and five. The estimate of $\beta^2(\omega)$ decreases again in time windows six through nine and is not significantly different from white noise in time windows eight and nine based on a t-test for the difference between means. The largest broadband polarizations occur during the P-wave onset in time windows zero and one on all three components and during the S-wave onset in time window four on the transverse component and time window five on the radial component. For most of the event, the broadband polarization of the ground acceleration wavefield is significantly different than white noise on each component (at approximately the 95 percent confidence level) based on a t-test for the difference between means.

Table 4.1 Broadband Estimate of the Polarization of the Wavefield for Event 5

COMPONENT	POLARIZATION ESTIMATE *	TIME WINDOW 0	1	2	3	4
VERTICAL	$\hat{\beta}^2(\omega)$	0.77(0.042)	0.76(0.002)	0.66(0.043)	0.56(0.040)	0.50(0.034)
RADIAL	$\hat{\beta}^2(\omega)$	0.77(0.034)	0.70(0.006)	0.61(0.034)	0.57(0.022)	0.62(0.051)
TRANSVERSE	$\hat{\beta}^2(\omega)$	0.72(0.039)	0.70(0.045)	0.62(0.051)	0.50(0.030)	0.71(0.028)
COMPONENT	POLARIZATION ESTIMATE *	TIME WINDOW 5	6	7	8	9
VERTICAL	$\hat{\beta}^2(\omega)$	0.45(0.027)	0.43(0.037)	0.43(0.028)	0.40(0.027)	0.42(0.020)
RADIAL	$\hat{\beta}^2(\omega)$	0.72(0.021)	0.54(0.036)	0.49(0.043)	0.39(0.022)	0.43(0.033)
TRANSVERSE	$\hat{\beta}^2(\omega)$	0.64(0.036)	0.52(0.034)	0.47(0.025)	0.37(0.018)	0.42(0.023)

* The standard error of the mean $\frac{\sigma}{\sqrt{N}}$ is given in parenthesis following the broadband estimate of $\beta^2(\omega)$ (2.4.3).

Figure 4.3 (time window one) depicts plots of $\hat{\beta}^2(\omega)$, $\hat{\beta}_2^2(\omega)$, the peak narrowband conventional estimate of the power and the normalized eigenvalues of $S(\omega)$ as a function of center frequency for the three rotated components of ground acceleration recorded during event 5. For each of the components, $\hat{\beta}^2(\omega)$ varies from approximately 0.5 to 1.0 as a function of center frequency. As expected for estimates of the narrowband polarization of the wavefield near unity, the second largest eigenvalue of the cross-spectral matrix is a factor of

10 smaller than the largest eigenvalue.

At 3.52 Hz on the vertical component (figure 4.3a) the narrowband polarization of the wavefield is a minimum. For a similar time window on the vertical component accelerograms from event 5 Abrahamson (1985) observed a minimum in the relative coherence between 3.5 and 4.0 Hz. From (2.4.11), $\hat{\beta}^2(\omega)$ provides a biased lower bound for the coherence of the wavefield. Since, as noted above, the estimate of $\beta^2(\omega)$ and the conventional estimate of the plane wave power are correlated, we can conclude that the minimum in coherence and in narrowband polarization of the wavefield are explained by the low plane wave power near 3.5 Hz.

In figure 4.4a (time window five), the narrowband polarization of the vertical ground acceleration wavefield is not significantly different than white noise at approximately the 95 percent confidence level based on a t-test for the difference between means. Time window five contains the arrival of P, S and Rayleigh wave energy (see section 3.3.1). Estimates of the polarization of the wavefield cannot be used to identify these multiple wave arrivals because of the large bias in $\hat{\beta}_2^2(\omega)$. Generally, in this time window, there are one or two eigenvalues within a factor of 10 of the largest eigenvalue for all eleven center frequencies.

On the radial component for time window five (figure 4.4b), the narrowband polarization as a function of center frequency remains fairly constant at 0.72±0.021. In this case, the largest eigenvalue is, approximately, a factor of five larger than the second largest eigenvalue. On the transverse component for time window five (figure 4.4c), the narrowband polarization is, generally, lower than the corresponding estimate for the radial component. The largest narrowband polarization, 0.85, occurs near 3 Hz. For both of the horizontal components in time window five the polarization of the wavefield is significantly different from white noise at greater than the 95 percent confidence level based on a t-test for the difference between means.

For time window nine (figure 4.5), the narrowband polarization of the wavefield is not

significantly different from white noise on all three components (at approximately the 95 percent confidence level based on a t-test for the difference between means). There are multiple eigenvalues within a factor of 10 of the largest eigenvalue for all center frequencies in this time window.

4.3.2 Event 39

For the current study of event 39 the recordings from twenty-three stations are used in the polarization analysis. Table 4.2 summarizes the broadband estimate of the polarization of the wavefield, $\hat{\beta}^2(\omega)$, along with the standard error of the mean for each of ten time windows (shown in figure 3.10). The bandwidth of these estimates is from 1.17 to 8.98 Hz on the vertical component and from 1.17 to 5.08 Hz on both horizontal components.

Table 4.2 Broadband Estimate of the Polarization of the Wavefield for Event 39

COMPONENT	POLARIZATION ESTIMATE *	TIME WINDOW 0	1	2	3	4
VERTICAL	$\hat{\beta}^2(\omega)$	0.82(0.043)	0.78(0.035)	0.71(0.050)	0.60(0.036)	0.55(0.039)
RADIAL	$\hat{\beta}^2(\omega)$	0.73(0.023)	0.71(0.038)	0.70(0.037)	0.79(0.034)	0.64(0.055)
TRANSVERSE	$\hat{\beta}^2(\omega)$	0.54(0.027)	0.64(0.051)	0.82(0.010)	0.78(0.024)	0.56(0.031)
COMPONENT	POLARIZATION ESTIMATE *	TIME WINDOW 5	6	7	8	9
VERTICAL	$\hat{\beta}^2(\omega)$	0.54(0.036)	0.46(0.027)	0.39(0.014)	0.39(0.017)	0.35(0.016)
RADIAL	$\hat{\beta}^2(\omega)$	0.54(0.042)	0.48(0.054)	0.49(0.029)	0.40(0.024)	0.39(0.021)
TRANSVERSE	$\hat{\beta}^2(\omega)$	0.49(0.030)	0.50(0.045)	0.47(0.031)	0.38(0.017)	0.42(0.015)

* The standard error of the mean $\frac{\sigma}{\sqrt{N}}$ is given in parenthesis following the broadband estimate of $\beta^2(\omega)$ (2.4.3).

On the vertical component, $\hat{\beta}^2(\omega)$ decreases with time from a maximum value of 0.82 ± 0.043 in time window zero (see table 4.2). The broadband polarization of the wavefield is not significantly different from white noise in time windows seven through nine based on a t-test for the difference between means. On the horizontal components, $\hat{\beta}^2(\omega)$ is a maximum during time windows two and three that corresponds to the arrival of scattered energy

from the crustal anomaly located 1 to 1.5 km southeast of the array (see section 3.4). The estimate of $\beta^2(\omega)$ generally decreases after the direct S-wave arrival (time window four) and is not significantly different from white noise in time windows eight and nine based on a t-test for the difference between means. For most of the time windows the broadband polarization of the ground acceleration wavefield on each component is significantly different than white noise at approximately the 95 percent confidence level based on a t-test for the difference between means.

Figure 4.6 (time window zero) depicts plots of $\hat{\beta}^2(\omega)$, $\hat{\beta}_2^2(\omega)$, the peak narrowband conventional estimate of the power and the normalized eigenvalues of $S(\omega)$ as a function of center frequency for the three rotated components of ground acceleration for recorded during event 39. Values of $\hat{\beta}^2(\omega) > 0.90$ are estimated at 6.64 Hz, 8.20 Hz and 8.98 Hz with a bandwidth of $\pm$ 0.78 Hz. The peak plane wave power at these center frequencies is approximately 5 $(cm/sec)^2$, a factor of five larger than the peak plane wave power for center frequencies less than 4.5 Hz. The conclusion to be drawn from this data is that for event 39 both large plane wave power and polarization of the wavefield (relative to other center frequencies in the same time window) occurred at high frequencies during the direct P-wave arrival.

During time window two (figure 4.7), scattered energy arrived at the array from the southeast (see section 3.4). The scattered energy consists primarily of P-wave energy converted to S-wave energy on the horizontal components. The broadband polarizations of the wavefield during this window are greater than or equal to 0.70 on all three components. The transverse component (figure 4.7c) has the least scatter around the mean polarization estimate of 0.82 as a function of center frequency. Both the vertical and the radial components have greater scatter in the narrowband estimates of the polarization of the wavefield and some of the estimates are not significantly different than white noise at approximately the 95 percent confidence level based on a t-test for the difference between means. Also, both the peak narrowband plane wave power and $\hat{\beta}^2(\omega)$ are larger as a function of center

frequency than the corresponding estimate on the radial component. The peak narrowband estimate of the plane wave power on the horizontal components is generally a factor of 10 less than the power on the vertical component. The wavefield produced by the scatterer (located approximately 1 km southeast of the center of the array at a depth between 1.5 to 2.0 km) is highly polarized (coherent) at the SMART 1 sub-array (figures 4.7b and 4.7c).

Figure 4.8 consists of plots of the estimates for time window five during which both the direct S-wave arrival and surface wave arrivals occurred at the sub-array. The polarization of the wavefield ($\hat{\beta}^2(\omega)$) in this window is generally less than 0.50. There are in this time window multiple eigenvalues of $S(\omega)$ within a factor of 10 of the largest eigenvalue for all three components.

4.4 Conclusions

The polarization estimate, $\hat{\beta}^2(\omega)$, is summarized as a function of center frequency, component and time window for events 5 and 39 in figures 4.9 and 4.10, respectively. The estimates of the polarization for the eleven center frequencies as a function of time window are shown by the dashed lines. The length of the dash is inversely proportional to frequency, that is, short dashes are used for the higher center frequencies. The 95 percent confidence level for random (white) noise is represented by the solid horizontal line at 0.44.

In general, there is a trend for higher frequencies to have lower polarization (coherence) than lower frequencies on all components. On the vertical component for both events, the polarization of the wavefield generally decreases with time. Both horizontal components for both events have an increase in the polarization of the wavefield associated with the arrival of the direct S wave. Event 39 also has an increase in the polarization of the wavefield in time windows two and three associated with the arrival of scattered energy from the crustal anomaly southeast of the array center.

The polarization (coherence) of strong ground motions over short distances has important implications for waveform modeling and engineering studies of wave "incoherence".

Figures 4.9 and 4.10 provide time and frequency dependent bounds on the polarization (coherence) of wavefields below which deterministic generation of synthetic seismograms are practical.

In summary, the polarization (coherence) analysis of the ground acceleration wavefield recorded at SMART 1 during events 5 and 39 has shown:

1) the direct P wavefield has large polarizations on the vertical component; roughly 0.8.

2) the direct S wavefield has lower polarizations on the horizontal components; between 0.5 and 0.7. The radial component (SV-wavefield), generally, has larger polarizations than the transverse component (SH-wavefield). An exception to this generality occurs during event 5 (time window four) when $\hat{\beta}^2(\omega)$ was greater on the transverse than the radial component.

3) the coda arrivals after the direct S-wave arrival in time windows six through nine have low polarizations of roughly 0.5. The wavefield is not significantly different from white noise at approximately the 95 percent confidence level in the time windows eight and nine based on a t-test for the difference between means.

4) the "scattered wavefield" recorded during event 39 has large broadband polarizations (coherence), greater than 0.7, on all components with a broadband polarization of 0.82 on the transverse component with a frequency bandwidth of approximately 1 to 5 Hz on the horizontal components.

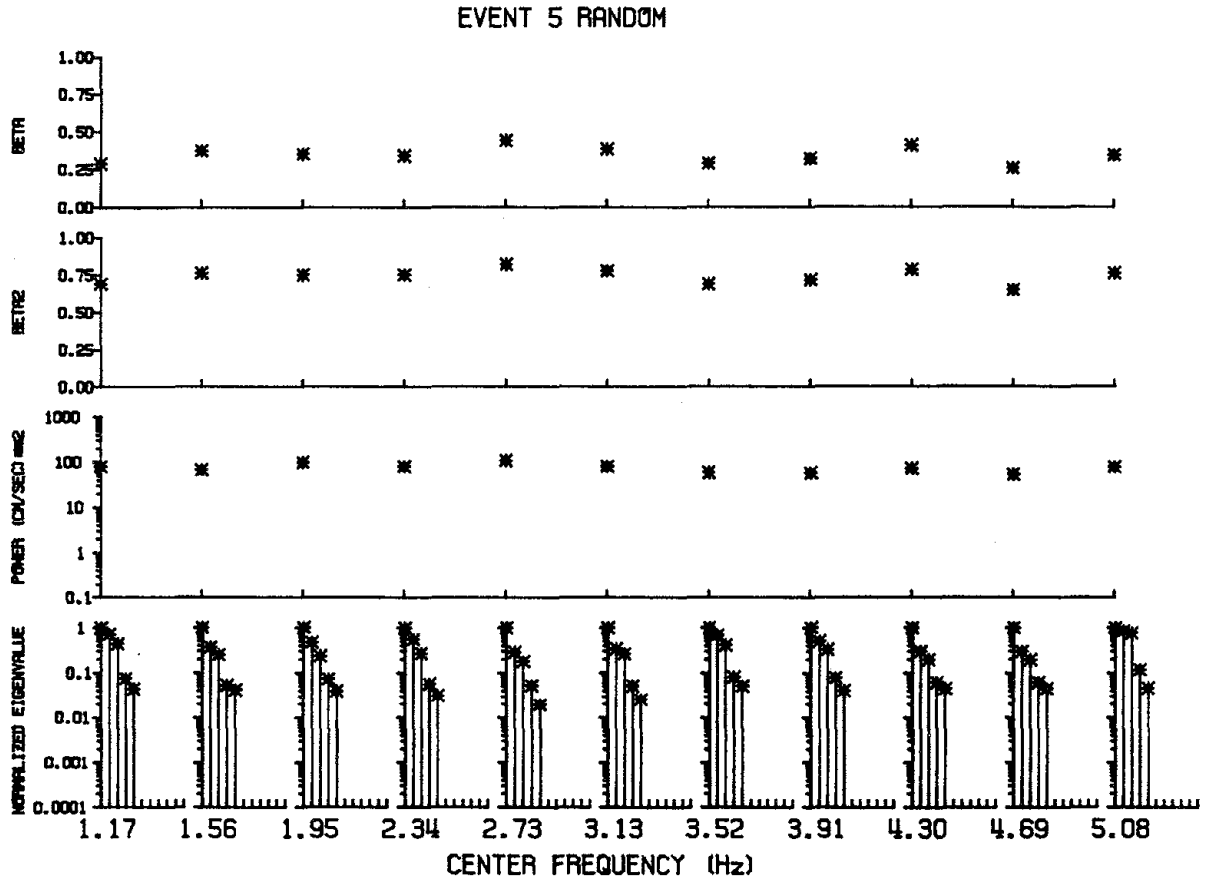

Figure 4.1: Estimates of the polarization of the wavefield, ($\hat{\beta}^2(\omega)$ and $\hat{\beta}_2^2(\omega)$), the peak narrowband plane wave power and the largest normalized eigenvalues of the cross spectral matrix are plotted as a function of center frequency for a random wavefield.

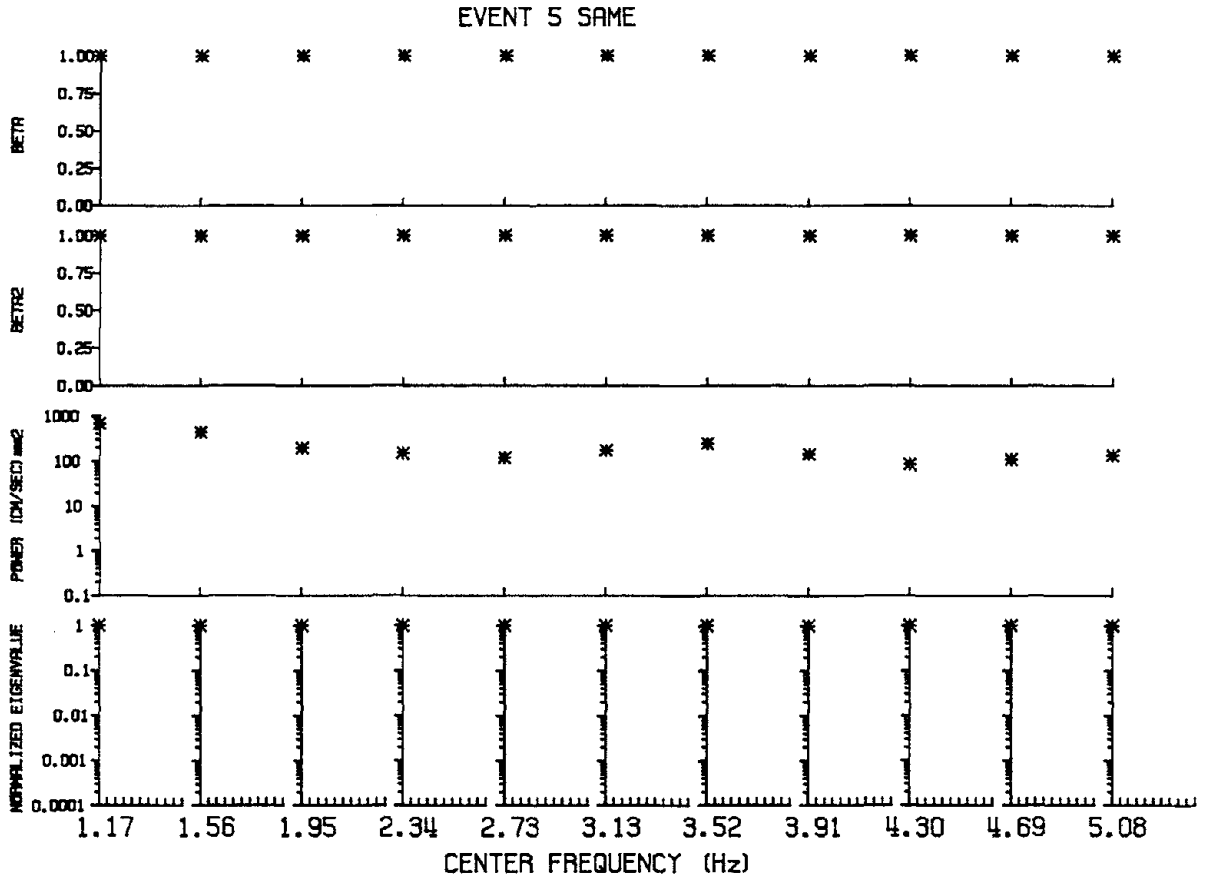

Figure 4.2: Estimates of the polarization of the wavefield, ($\hat{\beta}^2(\omega)$ and $\hat{\beta}_2^2(\omega)$), the peak narrowband plane wave power and the largest normalized eigenvalues of the cross spectral matrix are plotted as a function of center frequency for a homogeneous wavefield.

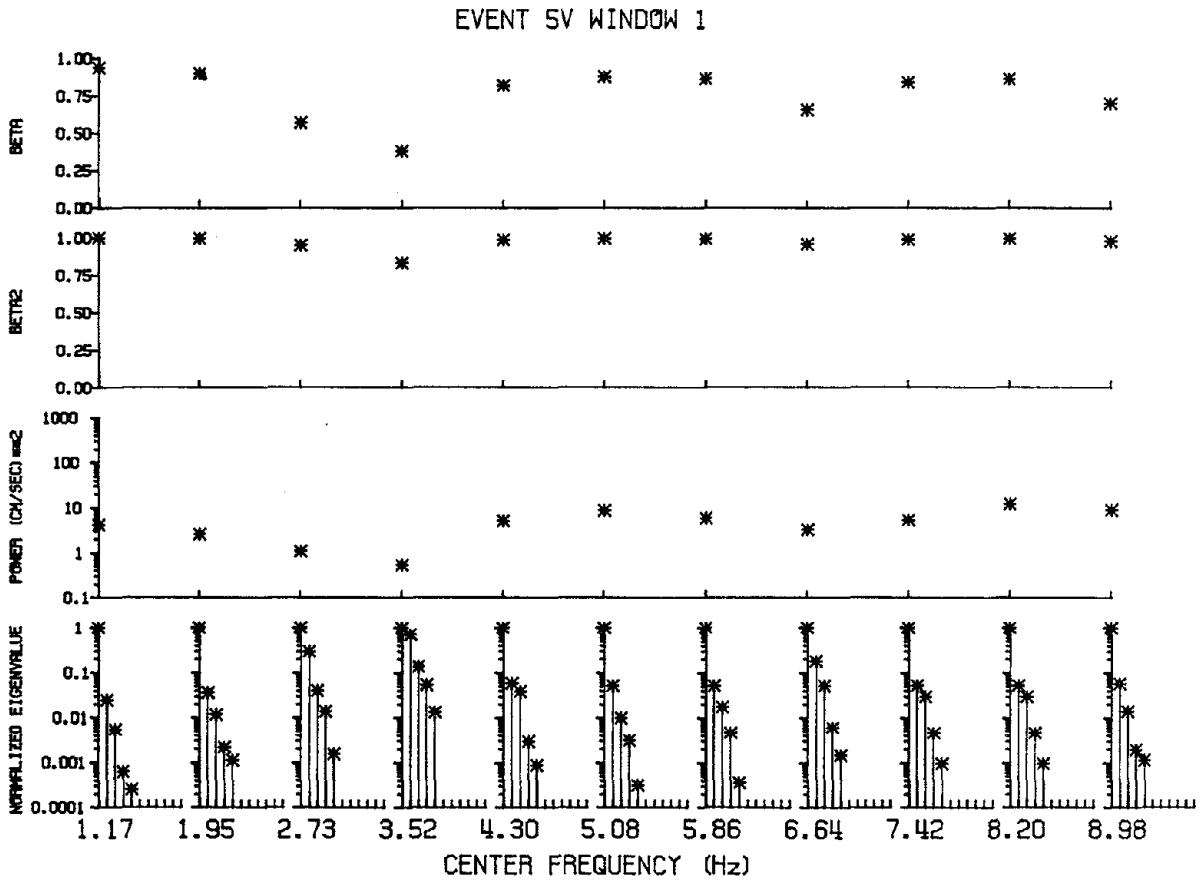

Figure 4.3a: Estimates of the polarization of the wavefield, ($\hat{\beta}^2(\omega)$ and $\hat{\beta}_2^2(\omega)$), the peak narrowband plane wave power and the largest normalized eigenvalues of the cross spectral matrix are plotted as a function of center frequency for the wavefield recorded during event 5 on the vertical component in time window one.

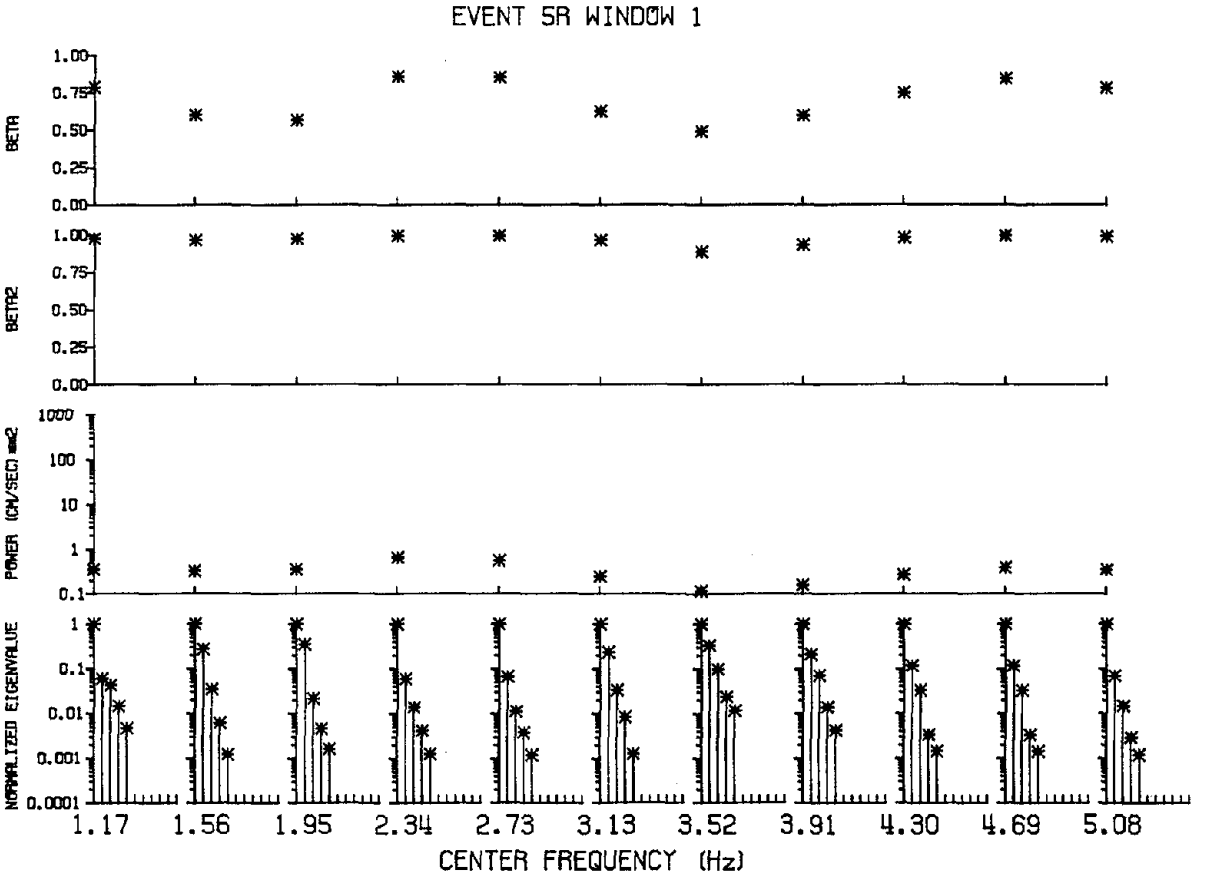

Figure 4.3b: Estimates of the polarization of the wavefield, ($\hat{\beta}^2(\omega)$ and $\hat{\beta}_2^2(\omega)$), the peak narrowband plane wave power and the largest normalized eigenvalues of the cross spectral matrix are plotted as a function of center frequency for the wavefield recorded during event 5 on the radial component in time window one.

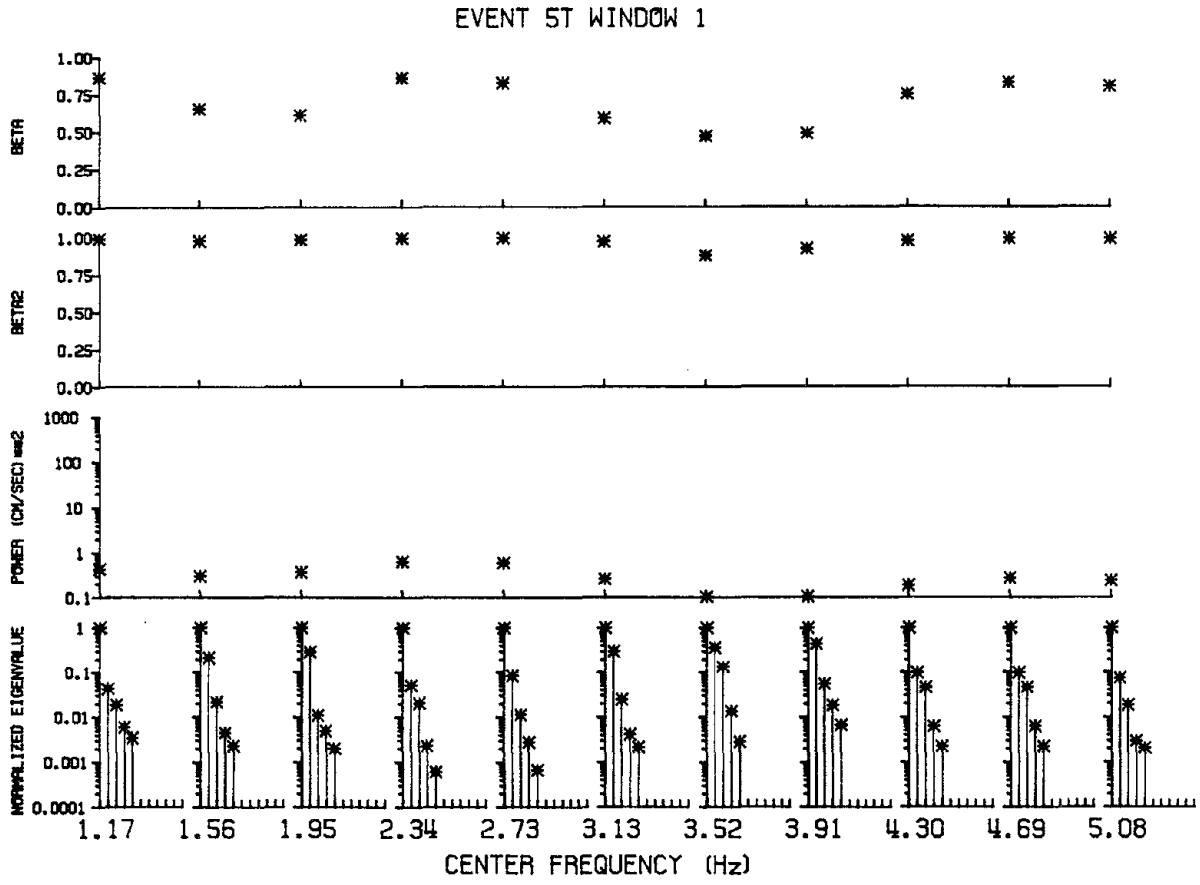

Figure 4.3c: Estimates of the polarization of the wavefield, ($\hat{\beta}^2(\omega)$ and $\hat{\beta}_2^2(\omega)$), the peak narrowband plane wave power and the largest normalized eigenvalues of the cross spectral matrix are plotted as a function of center frequency for the wavefield recorded during event 5 on the transverse component in time window one.

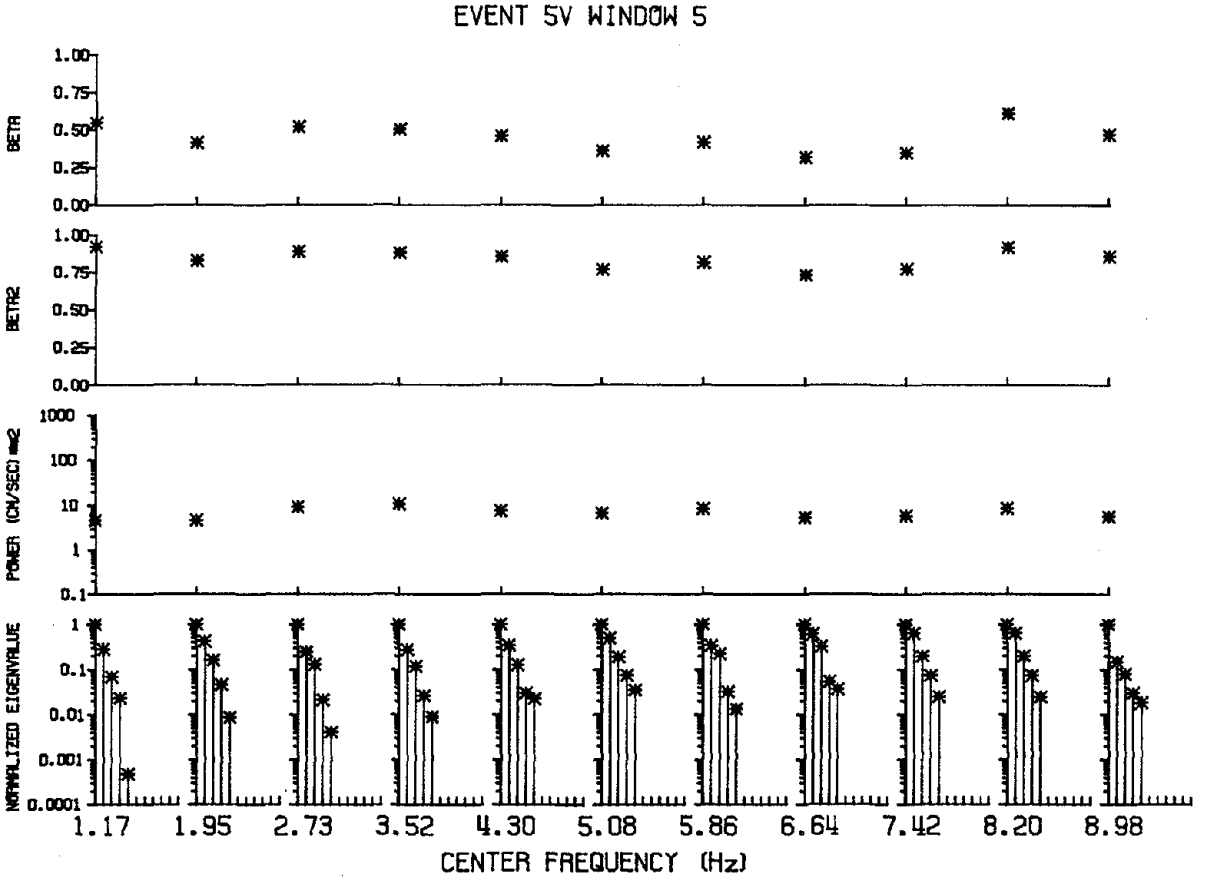

Figure 4.4a: Estimates of the polarization of the wavefield, ($\hat{\beta}^2(\omega)$ and $\hat{\beta}_2^2(\omega)$), the peak narrowband plane wave power and the largest normalize eigenvalues of the cross spectral matrix are plotted as a function of center frequency for the wavefield recorded during event 5 on the vertical component in time window five.

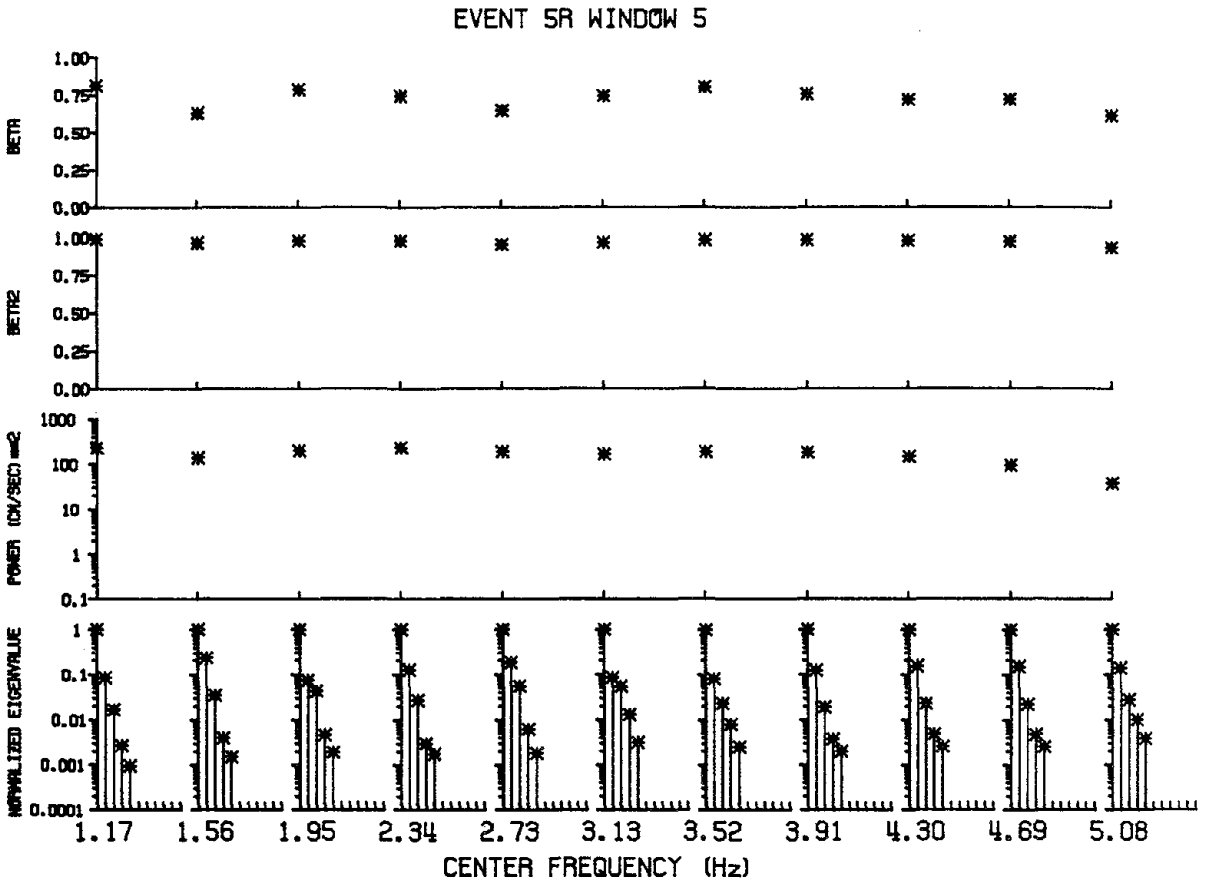

Figure 4.4b: Estimates of the polarization of the wavefield, ($\hat{\beta}^2(\omega)$ and $\hat{\beta}_2^2(\omega)$), the peak narrowband plane wave power and the largest normalized eigenvalues of the cross spectral matrix are plotted as a function of center frequency for the wavefield recorded during event 5 on the radial component in time window five.

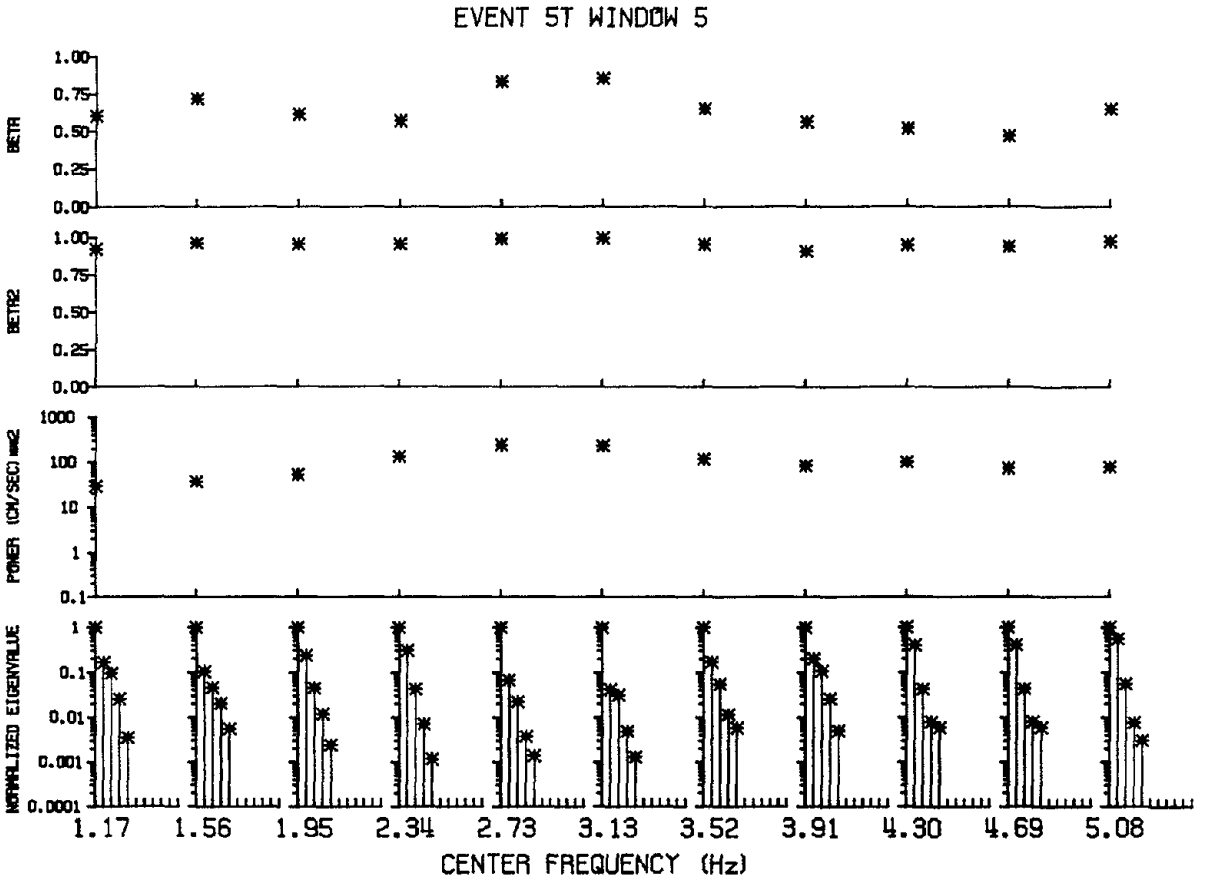

Figure 4.4c: Estimates of the polarization of the wavefield, ($\hat{\beta}^2(\omega)$ and $\hat{\beta}_2^2(\omega)$), the peak narrowband plane wave power and the largest normalized eigenvalues of the cross spectral matrix are plotted as a function of center frequency for the wavefield recorded during event 5 on the transverse component in time window five.

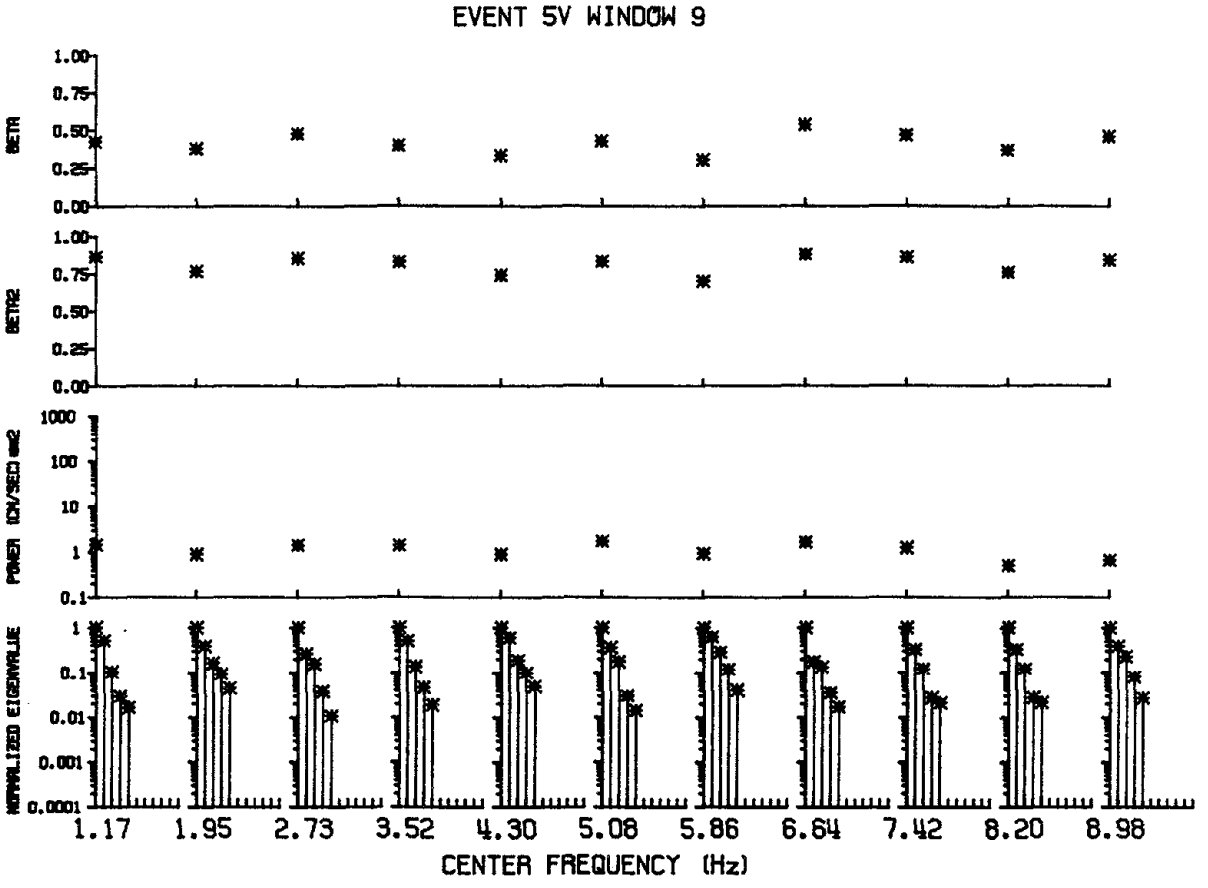

Figure 4.5a: Estimates of the polarization of the wavefield, ($\hat{\beta}^2(\omega)$ and $\hat{\beta}_2^2(\omega)$), the peak narrowband plane wave power and the largest normalized eigenvalues of the cross spectral matrix are plotted as a function of center frequency for the wavefield recorded during event 5 on the vertical component in time window nine.

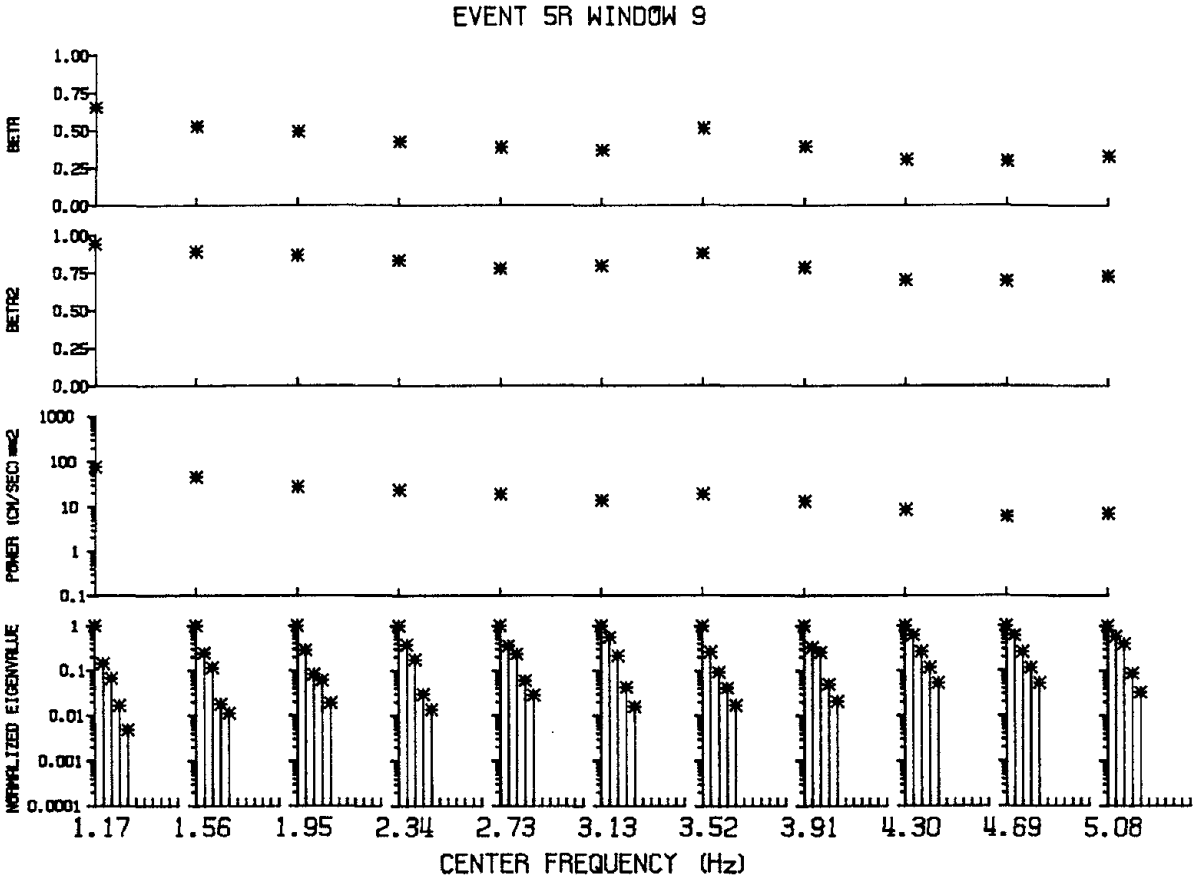

Figure 4.5b: Estimates of the polarization of the wavefield, ($\hat{\beta}^2(\omega)$ and $\hat{\beta}_2^2(\omega)$), the peak narrowband plane wave power and the largest normalized eigenvalues of the cross spectral matrix are plotted as a function of center frequency for the wavefield recorded during event 5 on the radial component in time window nine.

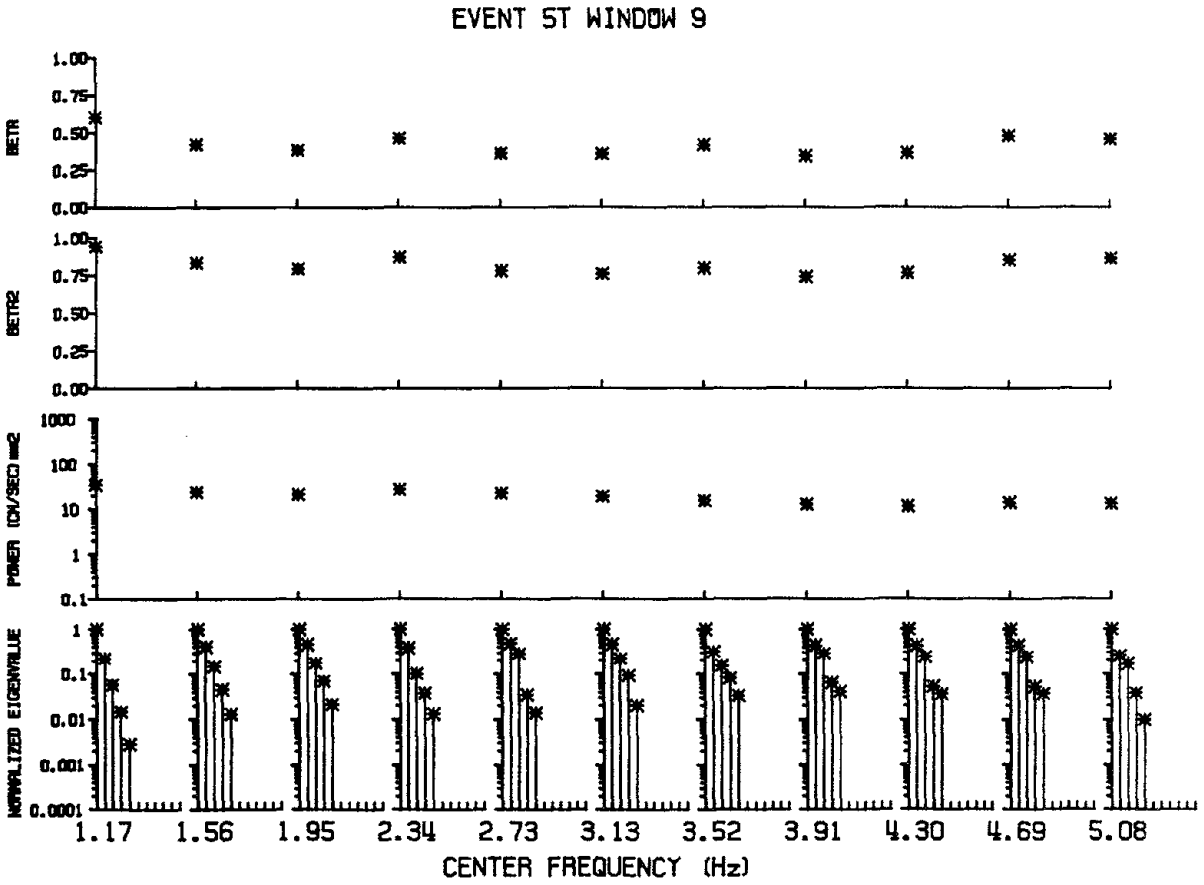

Figure 4.5c: Estimates of the polarization of the wavefield, ($\hat{\beta}^2(\omega)$ and $\hat{\beta}_2^2(\omega)$), the peak narrowband plane wave power and the largest normalized eigenvalues of the cross spectral matrix are plotted as a function of center frequency for the wavefield recorded during event 5 on the transverse component in time window nine.

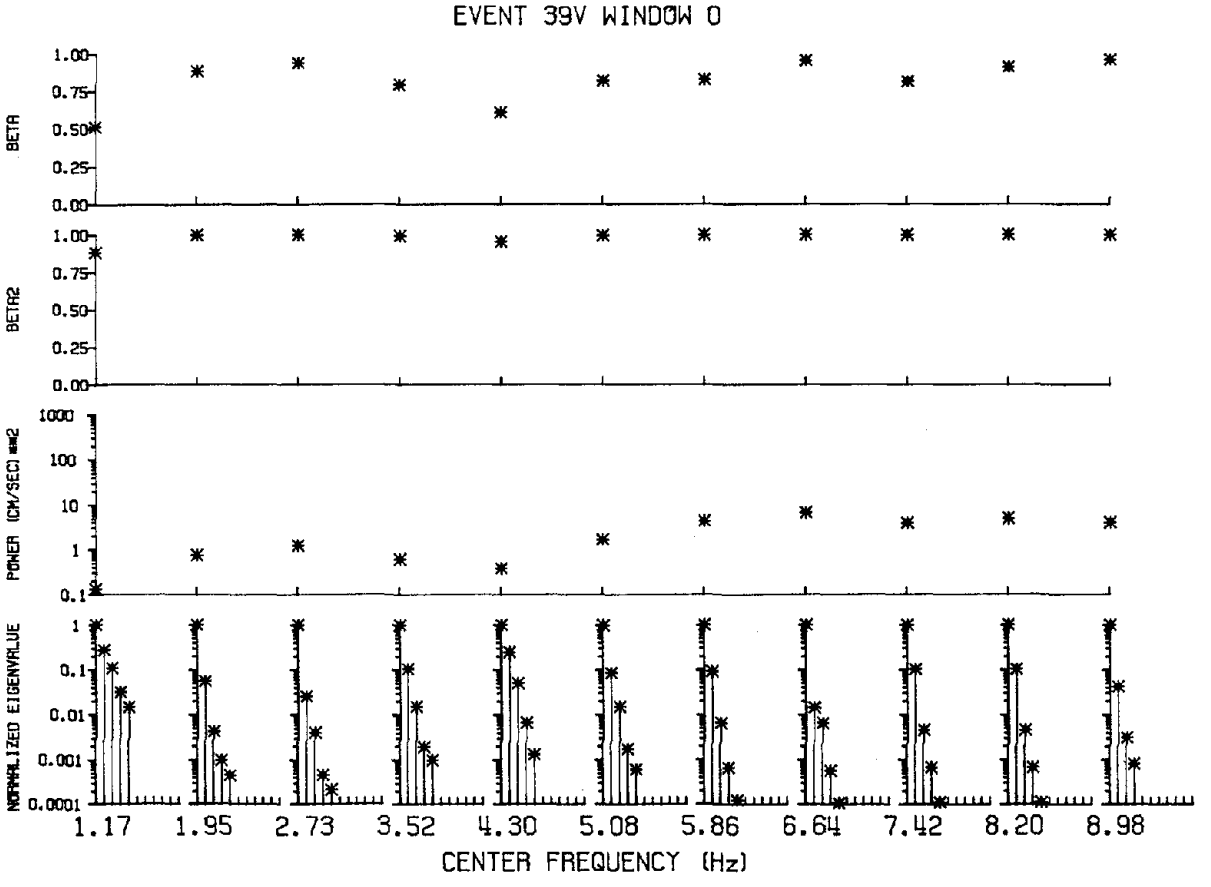

Figure 4.6a: Estimates of the polarization of the wavefield, ($\hat{\beta}^2(\omega)$ and $\hat{\beta}_2^2(\omega)$), the peak narrowband plane wave power and the largest normalized eigenvalues of the cross spectral matrix are plotted as a function of center frequency for the wavefield recorded during event 39 on the vertical component in time window zero.

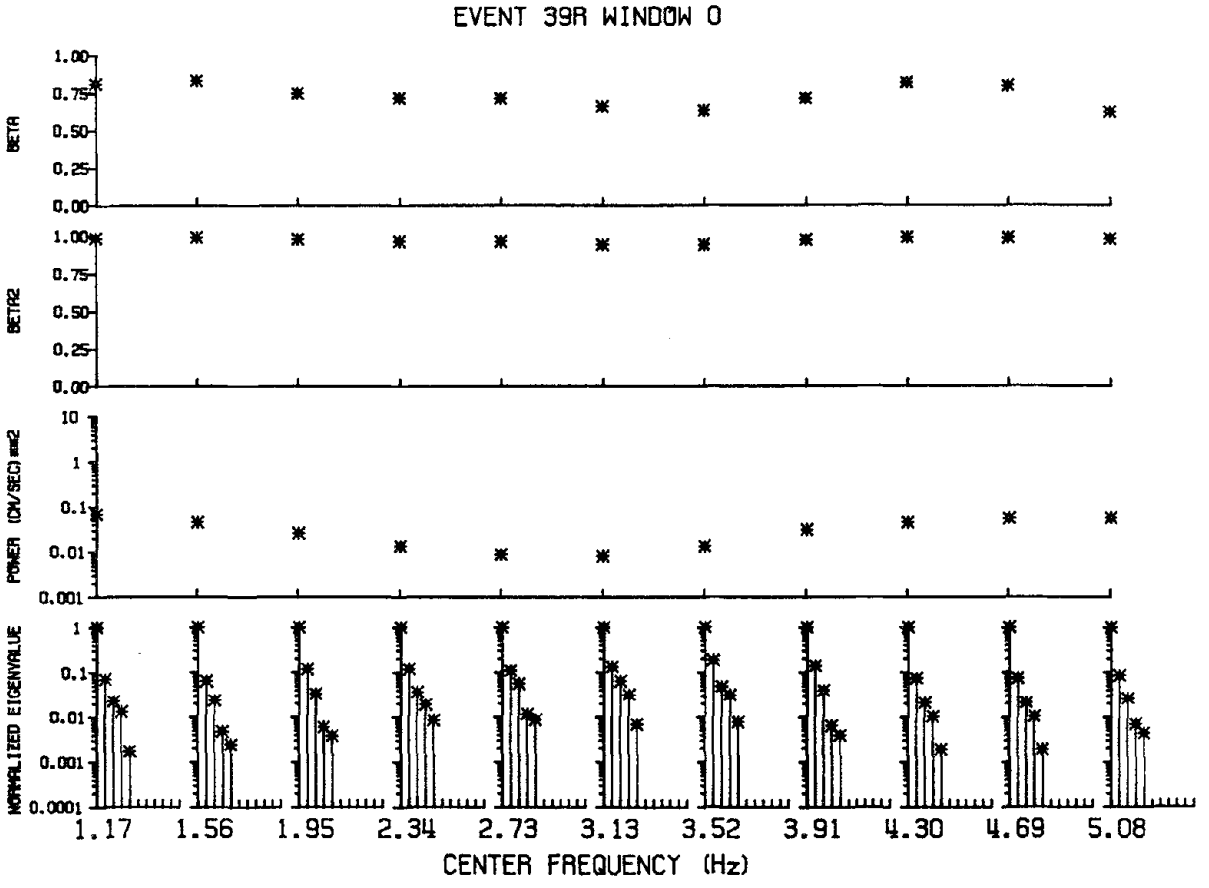

Figure 4.6b: Estimates of the polarization of the wavefield, ($\hat{\beta}^2(\omega)$ and $\hat{\beta}_2^2(\omega)$), the peak narrowband plane wave power and the largest normalized eigenvalues of the cross spectral matrix are plotted as a function of center frequency for the wavefield recorded during event 39 on the radial component in time window zero.

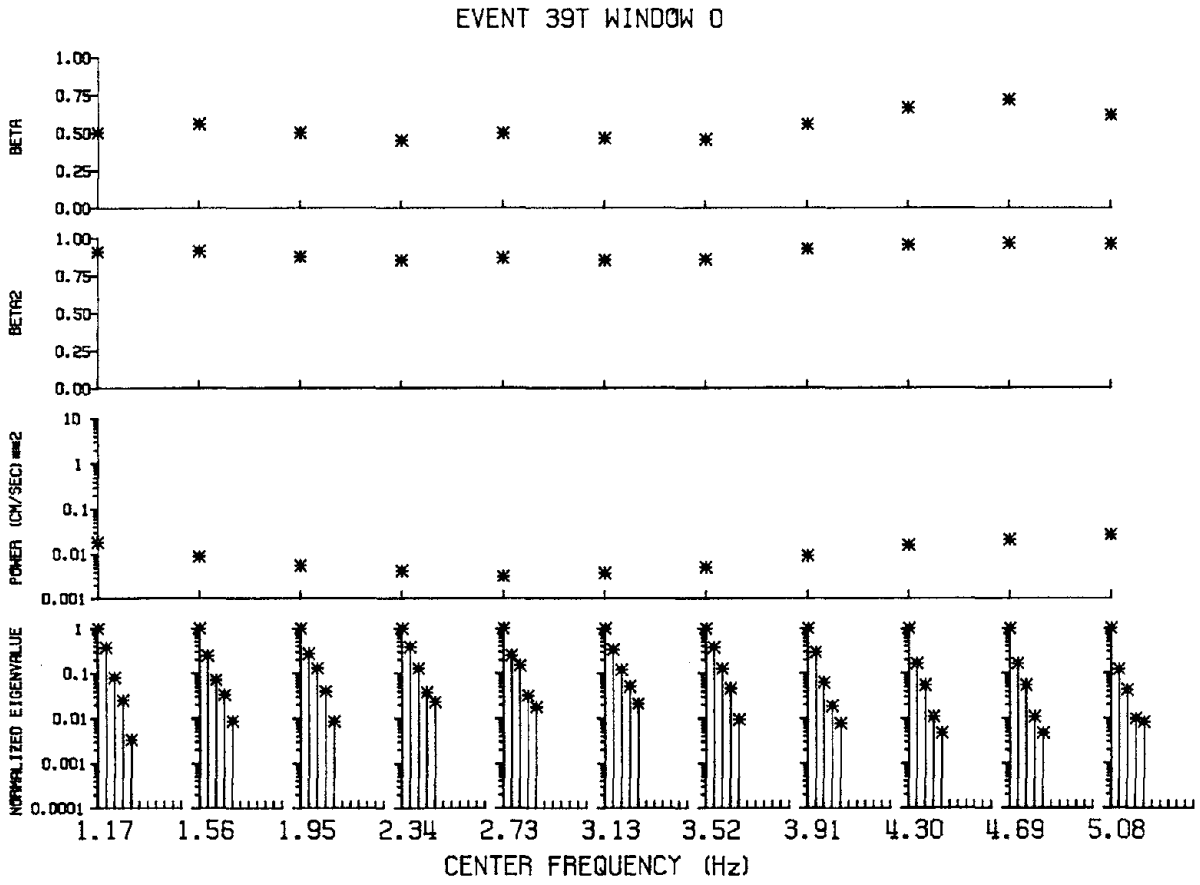

Figure 4.6c: Estimates of the polarization of the wavefield, ($\hat{\beta}^2(\omega)$ and $\hat{\beta}_2^2(\omega)$), the peak narrowband plane wave power and the largest normalized eigenvalues of the cross spectral matrix are plotted as a function of center frequency for the wavefield recorded during event 39 on the transverse component in time window zero.

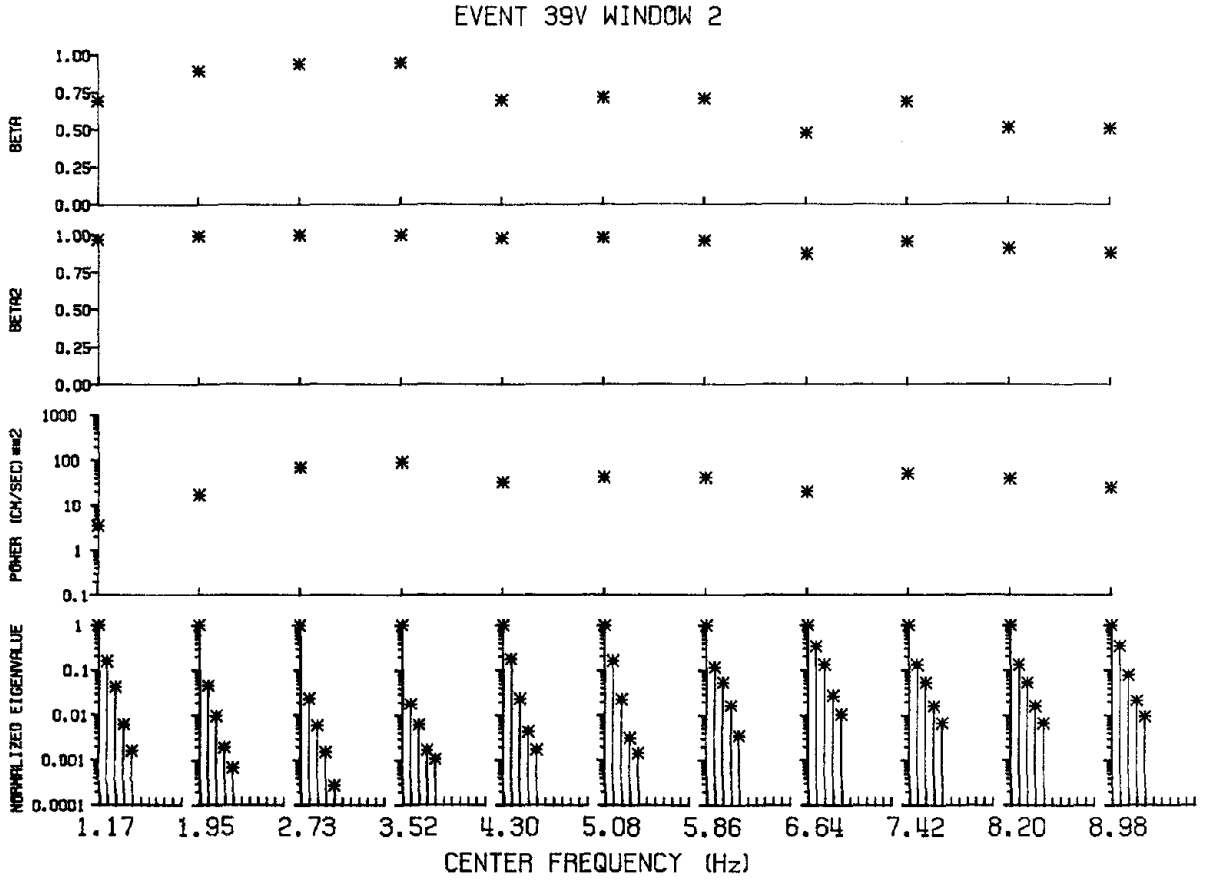

Figure 4.7a: Estimates of the polarization of the wavefield, ($\hat{\beta}^2(\omega)$ and $\hat{\beta}_2^2(\omega)$), the peak narrowband plane wave power and the largest normalized eigenvalues of the cross spectral matrix are plotted as a function of center frequency for the wavefield recorded during event 39 on the vertical component in time window two.

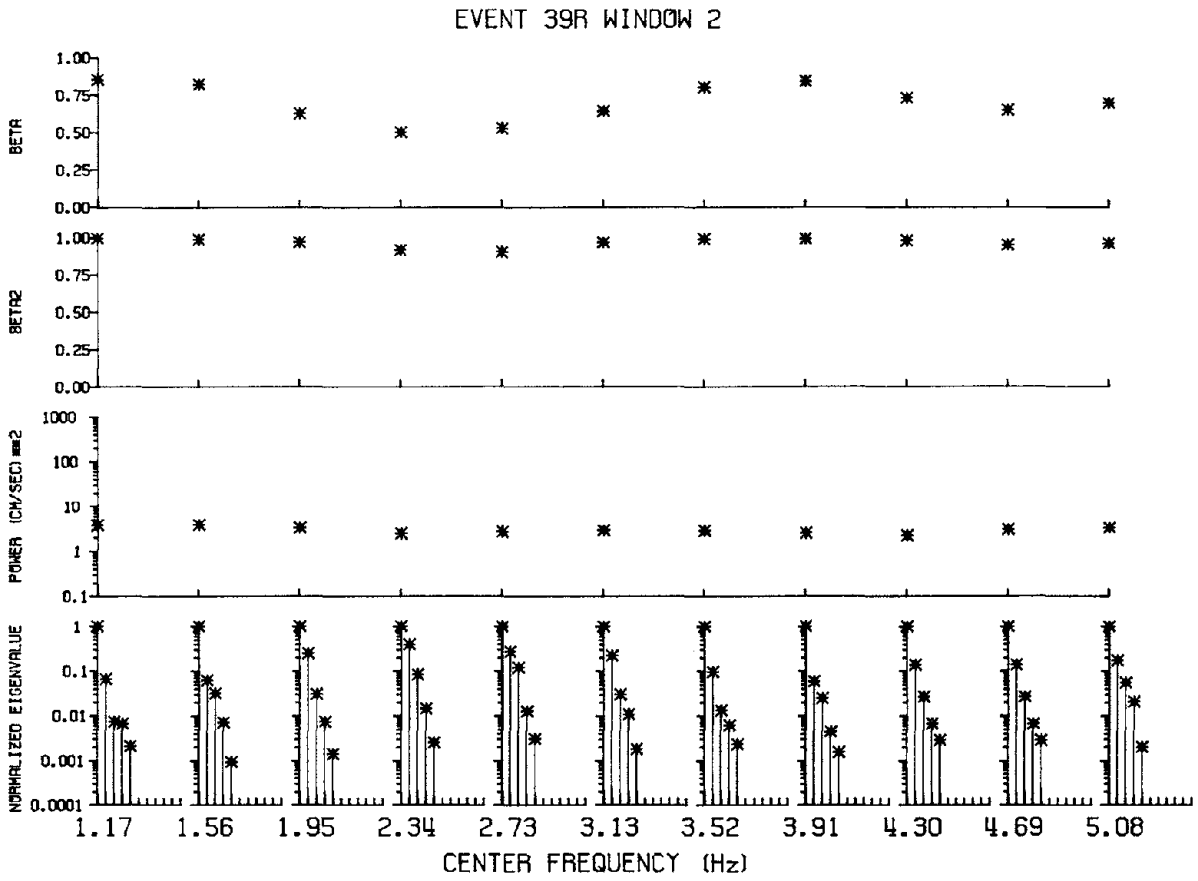

Figure 4.7b: Estimates of the polarization of the wavefield, ($\hat{\beta}^2(\omega)$ and $\hat{\beta}_2^2(\omega)$), the peak narrowband plane wave power and the largest normalized eigenvalues of the cross spectral matrix are plotted as a function of center frequency for the wavefield recorded during event 39 on the radial component in time window two.

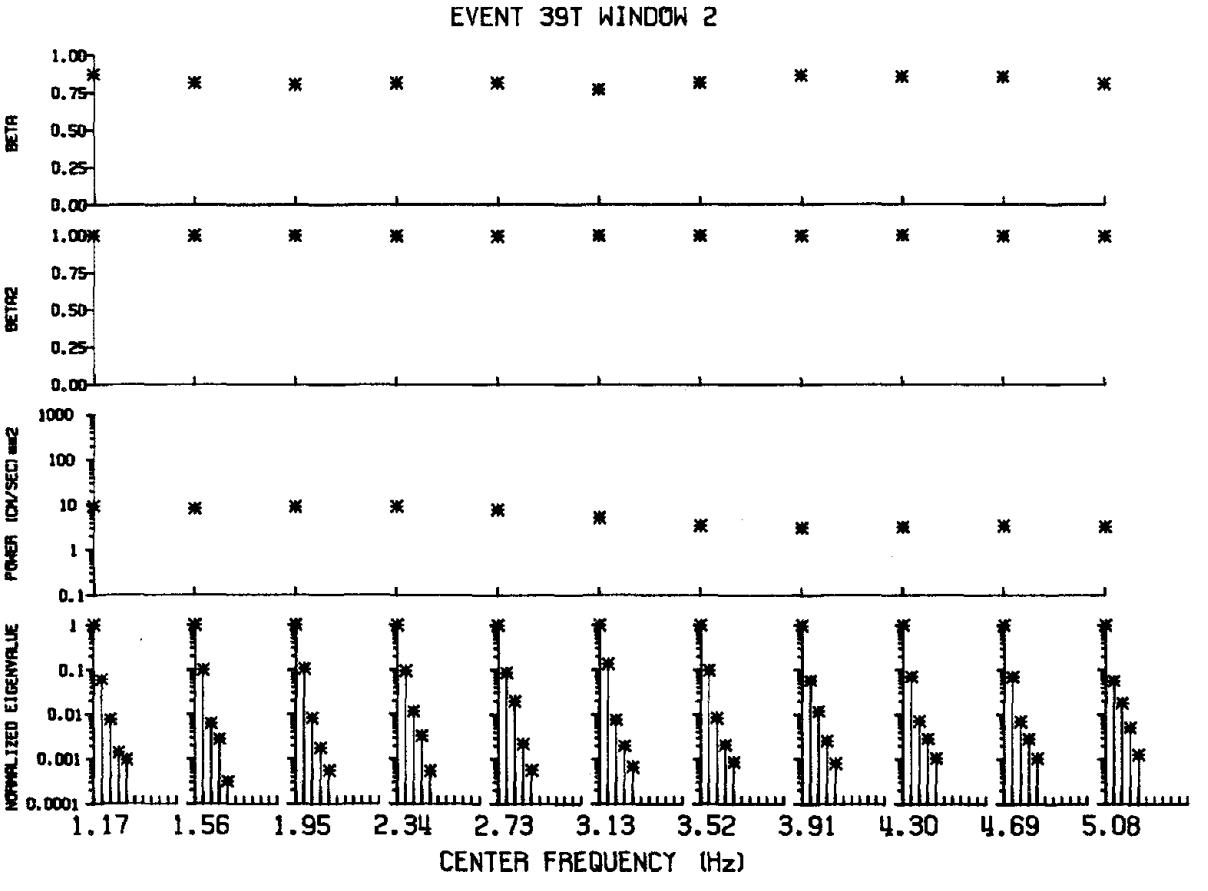

Figure 4.7c: Estimates of the polarization of the wavefield, ($\hat{\beta}^2(\omega)$ and $\hat{\beta}_2^2(\omega)$), the peak narrowband plane wave power and the largest normalized eigenvalues of the cross spectral matrix are plotted as a function of center frequency for the wavefield recorded during event 39 on the transverse component in time window two.

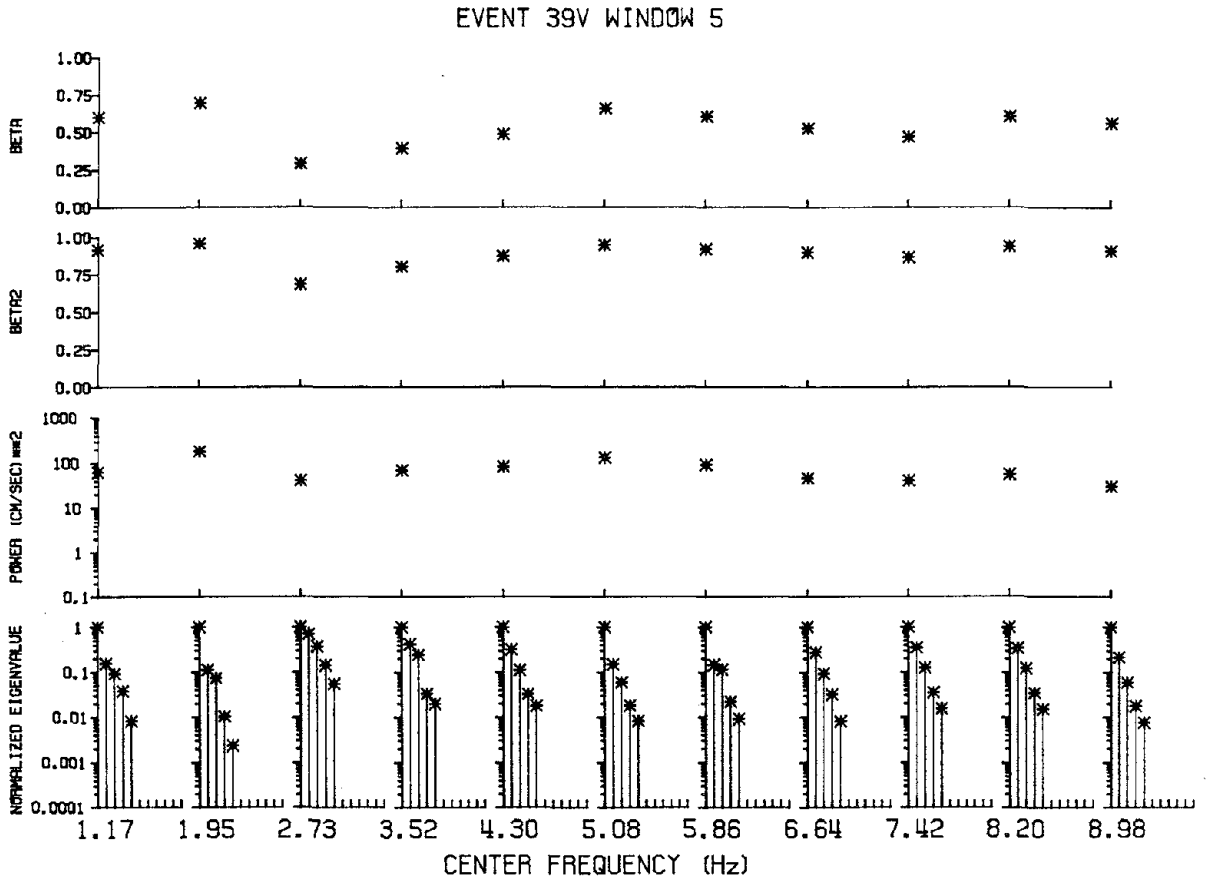

Figure 4.8a: Estimates of the polarization of the wavefield, ($\hat{\beta}^2(\omega)$ and $\hat{\beta}_2^2(\omega)$), the peak narrowband plane wave power and the largest normalized eigenvalues of the cross spectral matrix are plotted as a function of center frequency for the wavefield recorded during event 39 on the vertical component in time window five.

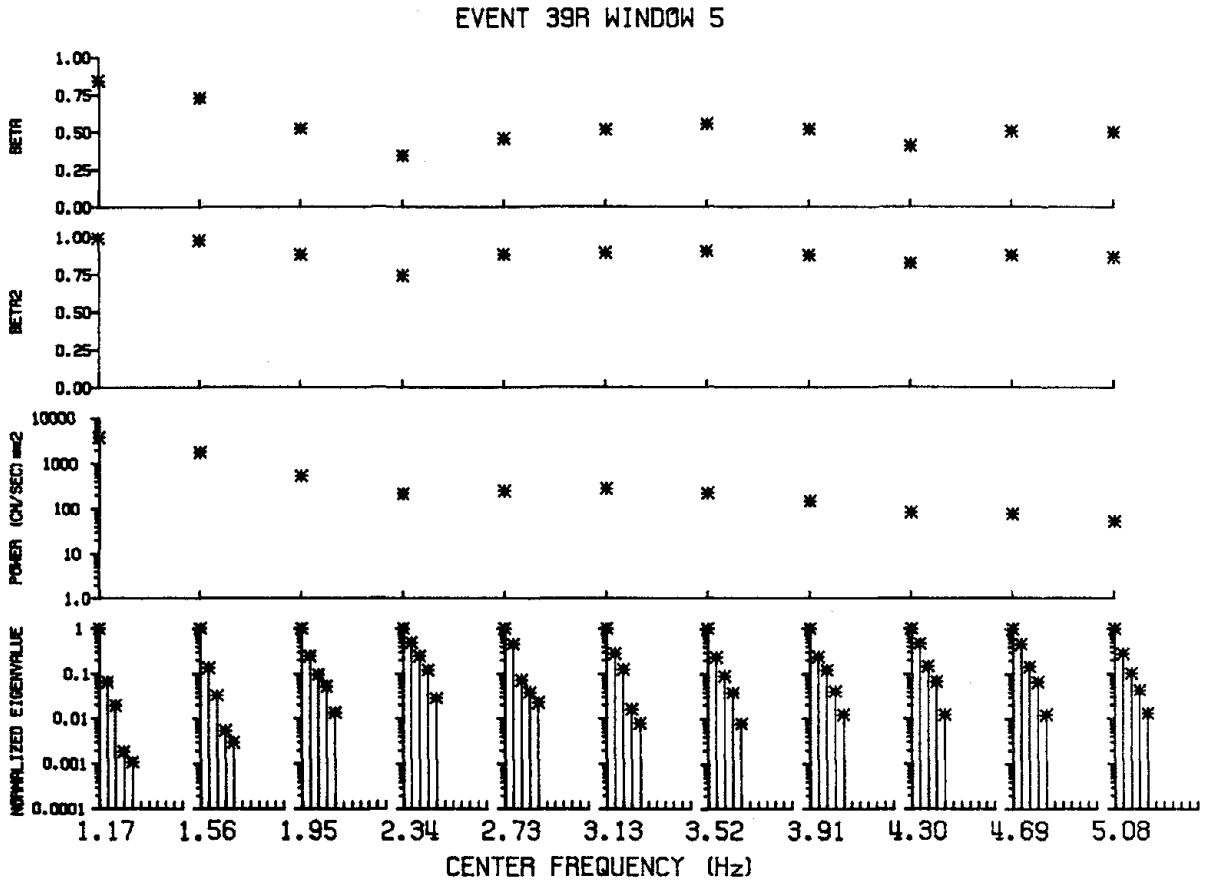

Figure 4.8b: Estimates of the polarization of the wavefield, ($\hat{\beta}^2(\omega)$ and $\hat{\beta}_2^2(\omega)$), the peak narrowband plane wave power and the largest normalized eigenvalues of the cross spectral matrix are plotted as a function of center frequency for the wavefield recorded during event 39 on the radial component in time window five.

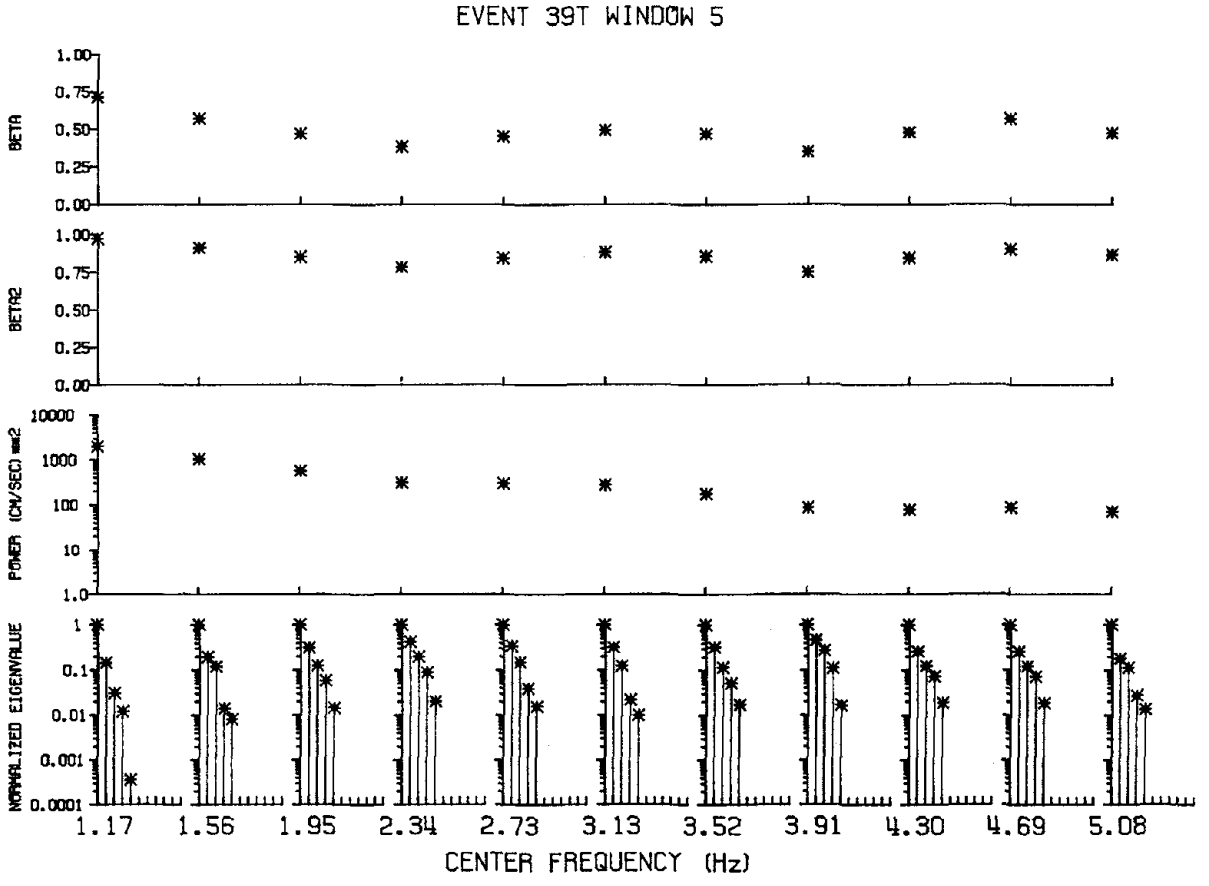

Figure 4.8c: Estimates of the polarization of the wavefield, ($\hat{\beta}^2(\omega)$ and $\hat{\beta}_2^2(\omega)$), the peak narrowband plane wave power and the largest normalized eigenvalues of the cross spectral matrix are plotted as a function of center frequency for the wavefield recorded during event 39 on the transverse component in time window five.

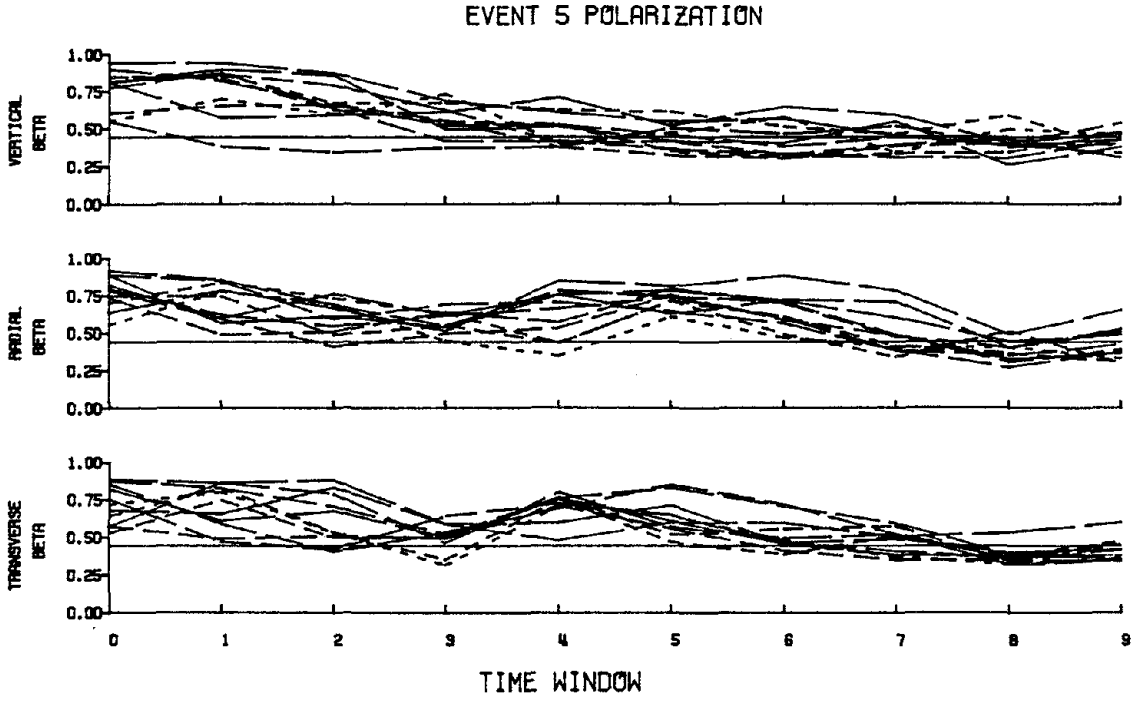

Figure 4.9: Narrowband estimates of the polarization of the wavefield, $\hat{\beta}^2(\omega)$, for each of the three components as a function of time for event 5. The length of the dash is inversely proportional to frequency from 1.17 Hz to 8.98 Hz for the vertical component and from 1.17 Hz to 5.08 Hz on the horizontal components. The 95 percent confidence level for random noise is the solid horizontal line at 0.44.

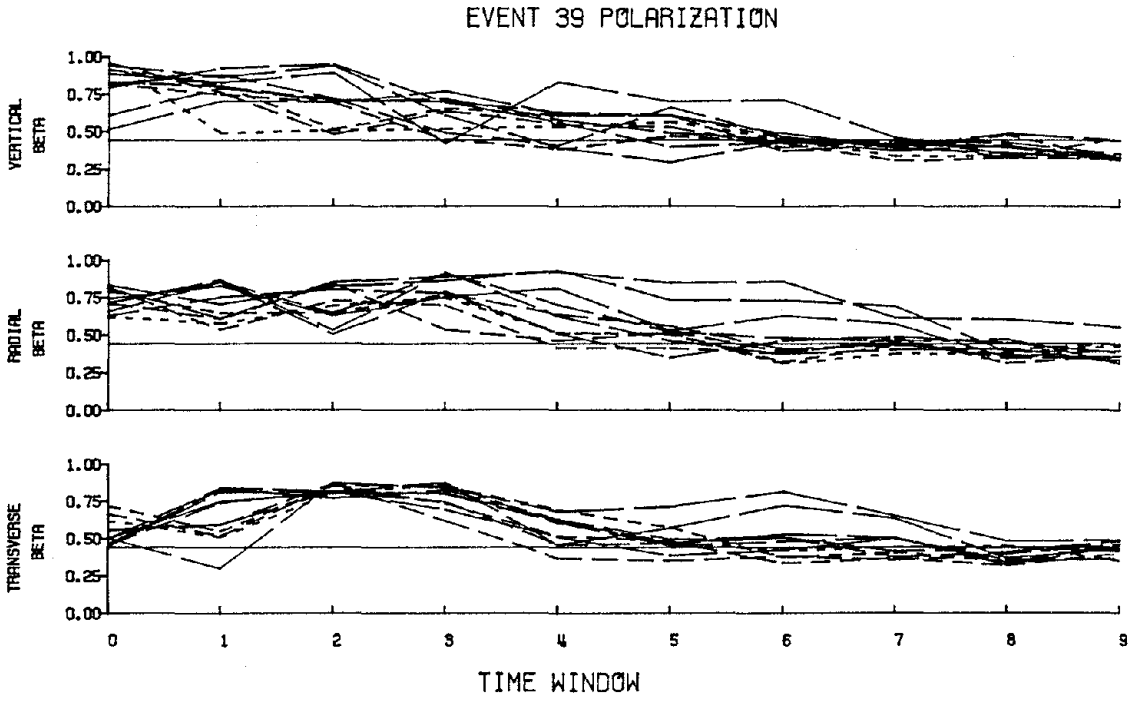

Figure 4.10: Narrowband estimates of the polarization of the wavefield, $\hat{\beta}^2(\omega)$, for each of the three components as a function of time for event 39. The length of the dash is inversely proportional to frequency from 1.17 Hz to 8.98 Hz for the vertical component and from 1.17 Hz to 5.08 Hz on the horizontal components. The 95 percent confidence level for random noise is the solid horizontal line at 0.44.

CHAPTER 5: DISCUSSION AND RECOMMENDATIONS

Discussion

Complimentary studies of the two cross-spectral matrices calculated from the recorded ground accelerations from each of two large earthquakes are described in this dissertation. All the information on the ground acceleration wavefield is contained in the cross-spectral matrix that has been estimated in ten overlapping time windows along the accelerograms since the wavefield is nonstationary. The studies were focused, through manipulations of the cross-spectral matrix, on two different characteristics of the wavefield. Frequency-wavenumber analysis was used to separate the wavefield in each time window in terms of apparent horizontal slowness (velocity), azimuth and time of arrival of the best fit plane wave. The analysis described in chapter four determined the narrowband polarization of the wavefield as a function of time and frequency. These studies demonstrate the following strengths and weaknesses of the two methods of decomposing the seismic wavefield within 30 km of a large earthquake.

Estimates of the polarization of a wavefield are more sensitive to both the assumptions that the wavefield is stationary and independence of the nearby frequency estimates in the smoothing of the cross-spectral matrix than are estimates based on frequency-wavenumber analysis. This sensitivity increased the bias of the polarization estimators and limited their application when multiple wave types arrived at the sub-array. In contrast, frequency-wavenumber spectral analysis allows the interpretation of multiple spectral peaks as multiple wave arrivals in the same time window. This analysis is limited mainly by the width of the central peak in the array impulse response (e.g. figure 2.1). Alternative frequency-wavenumber methods (e.g. high resolution, MUSIC) have narrower central peaks in the array impulse response, however; for example, the high resolution method requires smoothing the cross-spectral matrix over more frequencies than stations for the statistics of the estimate to be valid.

Both methods of analysis depend on the length of the time window chosen for the calculation of the cross-spectral matrix. The length of the time window determines the frequency sampling rate and combined with the number of nearby frequencies used for smoothing determines the lowest center frequency (table 2.1). As the length of the time window increases the estimates of the cross-spectral matrix will vary smoothly as the time window changes gradually along the recorded ground motions. Also, the matrix may be estimated at smaller center frequencies. As the length of the time window decreases the assumption that the wavefield is stationary within the time window is more nearly satisfied. The time window of 256 samples chosen in this study is a compromise between these two goals.

Statistical tests comparing properties of the recorded ground acceleration wavefield to a random (noise) wavefield are simpler to apply in the polarization analysis than in the frequency-wavenumber analysis. In the first case the estimate of the broadband polarization of the wavefield can be compared with the broadband polarization of a random wavefield using a t-test. For the frequency-wavenumber analysis the spectrum of the wavefield may be compared with the spectrum of the random wavefield visually.

The developments outlined in this dissertation have important implications for waveform modeling and enginering applications of the seismic wavefield. Waveform modeling, generally, cannot match the high frequency waves due to a loss of polarization (coherency) at high frequencies and with time in the coda portion of the seismogram. Estimates of the polarization of wavefields as a function of time and frequency provide time-dependent frequency bounds above which deterministic generation of synthetic seismograms are impractical. The estimates also provide an upper bound on the "incoherency" of the wavefield. Estimates of the coherency ("incoherency") of the wavefield are required as a function of frequency and time for engineering analysis of the response of large structures to the seismic wavefield. Estimates of the polarization of wavefields have the additional advantage that they do not depend on the orientation of the recording instrument, whereas,

estimates of the coherency are not rotationally invariant.

A common assumption of soil-structure interaction studies is that the wavefield is vertically incident. However, inclined wavefields can produce rocking and torsions in large structures that may be of importance for design. An estimate of the angle of incidence of the wavefield as a function of frequency and time can be provided by the frequency-wavenumber analysis. Using an estimate of the apparent horizontal slowness one estimates the angle of incidence by assuming a wavefield velocity. For example, using a P-wave velocity of 3.7 km/sec, appropriate for the Miocene slate beneath the SMART 1 array, one estimates an angle of incidence for the P-wavefield in event 5 of approximately 25° from vertical. This method for estimating the angle of incidence of the wavefield can be tested when strong motion accelerometers in the 70m bore-hole (described in Appendix A) in the SMART 1 array are triggered.

Recommendations

The studies described in this dissertation have further demonstrated the power of analyzing earthquake ground motions using array recordings with a common time base as opposed to single station recordings. Both frequency-wavenumber analysis and polarization analysis require multiple recordings of the wavefield.

The frequency-wavenumber analyses of events 5 and 39 would have benefited from additional stations located both within 2 km of the array center and an extension of the array to greater distances. Adding more stations to the interior of the array would provide additional station separation distances and thus a more uniform sampling in wavenumber (lag) space, as well as, an increase in the frequency at which the wavefield could be studied without spatial aliasing. An increase of the array aperture would increase the azimuthal coverage of the seismic source. Such an aperture increase would narrow the size of the frequency-wavenumber confidence intervals allowing for improved estimates of, for example, azimuth, apparent horizontal velocity of the wave field, and depth of the crustal anomaly. Also, smaller confidence intervals would allow for the separation of peaks with

smaller wavenumber differences, especially S and surface waves. An aperture increase would require slanted time windows across the array to allow slowly propagating waves to remain inside the time window without increasing the length of the time window.

The over 3000 SMART 1 seismic recordings of ground motions (48 earthquakes on three components) within, generally, 80 km of the seismic source, are an important set of data and require further analysis. Some areas of future research are outlined below.

As shown in chapters three and four, recordings from a two-dimensional array can be used to identify and separate the P, S and surface waves in strong motion recordings. Analysis of additional SMART 1 recordings would further our progress in identification and separation of wave types. For example, analysis of event 43 (M_L=6.2, epicentral distance to the array center: 6 km) would allow additional tests of the spherical frequency-wavenumber analysis, especially for direct waves from the source region. Event 45 studies (M_S=7.8, epicentral distance to the array center: 79 km) would further test the applicability of these methods of analysis to dispersed surface waves. For event 45, conventional narrowband frequency wavenumber analysis may be more appropriate than broadband frequency-wavenumber analysis to analyze the surface waves due to the dependence of slowness on frequency.

The estimates, described in chapters three and four, of the composition of the wavefields could be tested using waveform modeling. Waveform modeling requires detailed knowledge of the Earth's velocity structure which is not yet well known for Taiwan. However, researchers at the Institute of Earth Sciences in Taiwan are developing a three-dimensional velocity model for northeastern Taiwan.

The dependence of the broadband or narrowband polarization of a wavefield on source mechanism, epicentral distance and focal depth can be studied by examining additional SMART 1 recordings from the other earthquakes besides events 5 and 39. Polarization estimates at various azimuths could be used together with a frequency-wavenumber analysis to study the seismic wave scattering mechanism.

The decompositions of the cross-spectral matrix as described in this dissertation are not limited to multiple station single component analysis. A cross-spectral matrix (2.2.2) can be constructed from multiple station/multiple component time histories. Inclusion in the cross-spectral matrix of multiple components would increase computation time but provide a valuable test of the assumed separability of the wavefield into vertical, radial and transverse components.

References

Abrahamson, N. A. (1985). *Estimation of seismic wave coherency and rupture velocity using the SMART 1 strong motion array recordings* , Ph.D. Thesis, University of California, Berkeley.

Abrahamson, N. A. and B. A. Bolt (1985). The spatial variation of the phasing of seismic strong ground motion, *Bull. Seism. Soc. Am.*, **75**, 1247-1264.

Abrahamson, N. A. and B. A. Bolt (1987). Array analysis and synthesis mapping of strong seismic motion, In: B. A. Bolt (editor), *Strong Motion Synthetics: Computational Techniques Series*, Academic Press, New York.

Abrahamson, N. A. and R. B. Darragh (1987). Origin of scattered waves recorded by the SMART 1 strong motion array, *Seism. Res. Lett. (abstract)*, **58**, 15.

Aki, K. (1969). Analysis of the seismic coda of local earthquakes as scattered waves, *J. Geophys. Res.*, **74**, 615-631.

Aki, K. (1982). Scattering and attenuation, *Bull. Seism. Soc. Am.*, **72**, S319-S330.

Aki, K. and P. G. Richards (1980). *Quantitative Seismology Theory and Methods*, W. H. Freeman ad Co., San Francisco.

Archuleta, R. J. (1982). Analysis of near-source static and dynamic measurements from the 1979 Imperial Valley earthquake, *Bull. Seism. Soc. Am.*, **72**, 1927-1956.

Blackman, R. B. and J. W. Tukey (1959). *The Measurement of Power Spectra*, Dover Publications, Inc. New York.

Bolt, B. A. (1972). San Fernando rupture mechanism and the Pacoima strong-motion record, *Bull. Seism. Soc. Am.*, **62**, 1053-1061.

Bolt, B. A., N. A. Abrahamson and Y. T. Yeh (1984). The variation of strong ground motion over short distances, *Eighth World Conf. Earth. Engin.*, San Francisco. 183-189.

Bolt, B. A., C. H. Loh, J. Penzien, Y. B. Tsai and Y. T. Yeh (1982). Preliminary report on the SMART 1 strong motion array in Taiwan, *EERC Report No. UCB/EERC-82/13*.

Born, M. and E. Wolf (1980). *Principles of Optics*, Pergamon Press, New York.

Bostwick, T. K., P. A. Spudich and D. Oppenheimer (1985). Suppressing aliases and sidelobes in frequency/wavenumber transforms through slowness and frequency, *EOS (abstract)*, **66**, 313.

Brillinger, D. R. (1981). *Time Series Data Analysis and Theory. Expanded Edition.* Holden-Day Inc. San Francisco.

Brillinger, D. R. (1985). A maximum likelihood approach to frequency-wavenumber analysis, *IEEE Trans*, **ASSP-33**, 1076-1085.

Brune, J. N. (1976). The physics of earthquake strong motion, In: C. Lomnitz and E. Rosenblueth (editors), *Seismic Risk and Engineering Decisions*. Elsevier Scientific Publishing Company, New York. 141-177.

Bullen, K. E. and B. A. Bolt (1985). *An introduction to the theory of seismology*. Cambridge University Press, New York.

Capon, J. (1969). High resolution frequency-wavenumber spectrum analysis, *Proc. IEEE*, **57**, 1408-1418.

Capon, J. (1971). Correction to "Probability distribution for estimators of the frequency-wavenumber spectrum, *Proc. IEEE*, **59**, 112.

Capon, J. and N. R. Goodman (1970). Probability distribution for estimators of the frequency-wavenumber spectrum, *Proc. IEEE*, **58**, 1785-1786.

Chernov, L. A. (1960). *Wave propagation in random media*, Mc-Graw-Hill, New York.

Cox, H. (1973). Resolving power and sensitivity to mismatch of optimal array processors, *JASA*, **54**, 771-785.

Crampin, S. (1977). A review of effects of anisotropic layering on the propagation of seismic waves, *Geophys. J. R. astr. Soc.*, **49**, 9-27.

Darragh, R. B. and N. A. Abrahamson (1986). Separation of wave types using the SMART 1 strong motion array recordings, *EOS (abstract)*, **67**, 1097.

Davis, R. E. and L. A. Regier (1977). Methods for estimating directional wave spectra from multi-element arrays, *J. Marine Res.*, **35**, 453-477.

Der, Z. A. and E. A. Flinn (1975). The applicability of principal component analysis to the separation of multiple plane-wave signals, *Bull. Seis. Soc. Am.*, **65**, 627-635.

Flinn, E. A. (1965). Signal analysis using rectilinearity and direction of particle motion, *Proc. IEEE*, **53**, 1874-1876.

Goldstein, P. and R. J. Archuleta (1985). Multiple source seismic array processing, *EOS (abstract)*, **66**, 962.

Goldstein, P. and R. J. Archuleta (1986). Signal analysis using a dense array of seismographs, *Earthquake Notes (abstract)*, **57**, 23.

Goldstein, P. and R. J. Archuleta (1986b). Array analysis of seismic signals, *Geophys. Res. Lett.* **14**, 13-16.

Hanks, T. C. (1975). Strong ground motion of the San Fernando, California, earthquake: ground displacements, *Bull. Seism. Soc. Am.*, **65**, 193-225.

Hartzell, S. H., J. N. Brune and J. Prince (1978). The October 6, 1974 Acalpulco earthquake: an example of the importance of short-period surface waves in strong ground motion, *Bull. Seism. Soc. Am.*, **68**, 1663-1677.

Howe, M. S. (1973). On the kinetic theory of wave propagation in random media, *Philos. Trans. R. Soc. Lond. A.*, **274**, 523-549.

Jenkins, G. M. and D. G. Watts (1968). *Spectral Analysis and its Applications*, Holden Day, San Francisco.

Kanasewich, E. R. (1981). *Time Series Analysis in Geophysics, third edition*, The University of Alberta Press.

Kirkwood, S. C. and S. Crampin (1981). Surface-wave propagation in an ocean basin with an anisotropic upper mantle: observations of polarization anomalies, *Geophys. J. R. astr. Soc.*, **64**, 487-497.

Lacoss, R. T. (1971). Data adaptive spectral analysis methods, *Geophysics*, **36**, 661-675.

Loh, C. H. and K. L. Peng (1985). Identification of SMART-1 array data by multifilter technique, *J. Chinese Inst. Engin.*, **8**, 97-107.

Loh, C. H. and J. Penzien (1984). Identification of wave types and velocities using SMART-1 strong motion array data, *Eighth World Conf. Earth. Engin.*, San Francisco, 191-198.

Loh, C. H., J. Penzien and Y. B. Tsai (1982). Engineering analysis of SMART 1 array accelerograms, *Earth. Engin. Struct. Dyn.*, **10**, 575-591.

Mal'cev, A. I. (1963). *Foundations of Linear Algebra*, W. H. Freeman and Co., San Francisco.

McLaughlin, K. L. (1983). *Spatial Coherency of Seismic Waveforms*, Ph.D. Thesis, University of California, Berkeley.

Mims, C. H. and R. L. Sax (1965). Rectilinear motion direction (REMODE), Seismic Data Laboratory Report 118, Teledyne, Inc., Alexandria, Va. (AD-460-631).

Montalbetti, J. F. and E. R. Kanasewich (1970). Enhancement of teleseismic body phases with a polarization filter, *Geophys. G. R. astr. Soc.*, **21**, 119-129.

Mooney, H. M. and B. A. Bolt (1966). Dispersive characteristics of the first three Rayleigh modes for a single surface layer, *Bull. Seism. Soc. Am.*, **56**, 43-67.

Niazi, M. (1982). Source dynamics of the 1979 Imperial Valley earthquake from near-source observations (of ground acceleration and velocity), *Bull. Seism. Soc. Am.*, **72**, 1957-1968.

Niazi, M. (1985). Spatial coherence of the ground motion produced in the 1979 Imperial Valley earthquake across El Centro Differential Array, *Phys. Earth Planet. Inter.*, **38**, 162-173.

Niazi, M. (1986). Inferred displacements, velocities and rotations of a long rigid foundation located at El Centro Differential Array site during the 1979 Imperial Valley, California, earthquake, *Earth. Engin. Struct. Dyn.*, **14**, 531-542.

Noble, B. and J. W. Daniel (1977). *Applied Linear Algebra; Second Edition*, Prentice-Hall, Inc., New Jersey.

Nuttli, O. (1961). The effect of the Earth's surface on S wave particle motion, *Bull. Seism. Soc. Am.*, **51**, 237-246.

Oldham, R. D. (1900). On the propagation of earthquake motion to great distances, *Philos. Trans. Roy. Soc. Lond.*, **194**, 135-174.

Oliveira, C. S., B. A. Bolt and J. Penzien (1985). Rotational components of surface strong ground motion, *EOS (abstract)*, **66**, 968.

Parlett, B. N. (1980). *The Symmetric Eigenvalue Problem*, Prentice-Hall, Inc., New Jersey.

Pisarenko. V. F. (1972). On the estimation of spectra by means of non-linear functions of the covariance matrix, *Geophys. J. R. astr. Soc.*, **28**, 511-531.

Plešinger, A. , M. Hellweg and D. Seidl (1986). Interactive high-resolution polarization analysis of broad-band seismograms, *J. Geophys.* **59**, 129-139.

Samson, J. C. (1973). Descriptions of polarization states of vector processes: applications to ULF magnetic fields, *Geophys J. R. astr. Soc.*, **34**, 403-419.

Samson, J. C. (1977). Matrix and Stokes vector representations of detectors for polarized waveforms: theory, with some applications to teleseismic waves, *Geophys. J. R. astr. Soc.*, **51**, 583-603.

Samson, J. C. (1980). Comments on polarization and coherence, *J. Geophys.*, **48**, 195-198.

Samson, J. C. (1983). Pure states, polarized waves, and principal components in the spectra of multiple, geophysical time-series, *Geophys. J. R. astr. Soc.*, **72**, 647-664.

Samson, J. C. (1983). The reduction of sample-bias in polarization estimators for multichannel geophysical data with anisotropic noise, *Geophys. J. R. astr. Soc.*, **75**, 289-308.

Samson, J. C. (1986). Estimators of the parameters of polarized waves in geophysical processes, *EOS (abstract)*, **67**, 873.

Samson, J. C. and J. V. Olson (1980). Some comments on the descriptions of polarization states of waves, *Geophys. J. R. astr. Soc.*, **61**, 115-129.

Scheimer, J. and T. E. Landers (1974). Short-period coda of a local event at LASA, In: Semiannual Technical Summary *Seismic Discrimination*, Lincoln Laboratory.

Shumway, R. H. (1983). Replicated time-series regression: an approach to signal estimation and detection, In: D. R. Brillinger and P. R. Krishnaiah (editors), *Handbook of Statistics*, **3**, Elsevier Scientific Publishing Company, New York. 383-408.

Smart, E. and H. Sproules (1981). Regional phase processors, VELA Seismological Center Report VSC-TR-81-19.

Smith, S. W., J. E. Ehrenberg and E. N. Hernandez (1982). Analysis of the El Centro Differential Array for the 1979 Imperial Valley earthquake, *Bull. Seism. Soc. Am.*, **72**, 237-258.

Spudich, P. (1986). Strong ground motion prediction in realistic Earth structures, In: M. L. Jacobson and T. R. Rodriguez (compilers), Natural Earthquake Hazards Reduction Program, Summary of Technical Reports, **XXI**, USGS OFR 86-31, 628-629.

Spudich, P. and E. Cranswick (1984). Direct observation of rupture propagation during the 1979 Imperial Valley earthquake using a short baseline accelerometer array, *Bull. Seism. Soc. Am.*, **74**, 2083-2114.

Spudich, P. and D. Oppenheimer (1986). Dense seismograph array observations of earthquake rupture dynamics, In: S. Das, J. Boatwright and C. H. Scholz (editors), *The Proceedings of the 6th Ewing Symposium on Earthquake Source Mechanics*, Geophys. Monogr. 37-AGU, 285-296.

Tukey, J. W. (1958). Bias and confidence in not quite large samples, *Ann. Math. Statist. (abstract)* **29**, 614.

Vidale, J. E. (1986). Complex polarization analysis of particle motion, *Bull. Seism. Soc. Am.*, **76**, 1393-1405.

Woods, J. W. and P. R. Lintz (1973). Plane waves at small arrays, *Geophysics*, **38**, 1023-1041.

APPENDIX A: THE SMART 1 ACCELEROGRAPH ARRAY

A.1 Introduction

The SMART 1 array is located in the northeast corner of Taiwan near the city of Lotung on the Lanyang Plain (figure A.1). Installation of the array began in September 1980 and was completed in August 1982. The original array consisted of 37 force-balanced triaxial accelerometers placed in three concentric rings of radii 200m, 1000m and 2000m (figure A.1). The three rings are referred to as I (inner), M (middle) and O (outer), respectively. There are twelve equally spaced stations numbered 1 through 12, on each ring and a central station, C-00. The minimum station spacing of 100m controls the spatial aliasing. For an apparent wave velocity of, for example, 1 km/s, the spatial aliasing frequency is 5 Hz. In June 1983, two additional stations were added to the array. These stations, E-01 and E-02, are located 2.8 km and 4.8 km south of the central station, respectively (figure A.1).

Each accelerometer in the SMART 1 array is connected to a digital event recorder with 2g full scale. The accelerometers trigger on all three components of ground motion (nominally 0.02g). The ground motions are digitized as 12-bit words at 100 samples per second. The temporal Nyquist frequency is thus 50 Hz. The dynamic range is 66 db. The digital delay memory has a capacity of 250 samples per channel corresponding to 2.5 seconds of pre-event memory at 100 samples per second.

Each instrument is serviced about once every three days and after each recorded earthquake. Such frequent maintenance is necessary to assure accurate timing and power at the array stations. Over the seven years of use, the performance of the instruments has been excellent; after triggering only one percent of the traces have been unuseable. This success is due to a combination of the extensive testing performed on each accelerometer in Berkeley before shipment to Taiwan (Bolt, *et al.*, 1982) and the careful maintenance of the array by the staff of the Institute of Earth Sciences, Academia Sinica. Additional information on the SMART 1 array is given by Bolt, *et al.* (1982) and by Abrahamson (1985).

It is of general interest that in 1985 the Taiwan Power Company and the Electric Power Research Institute (EPRI) constructed a digitally instrumented three-dimensional array to measure soil-structure interaction of large scaled-structures. The EPRI array is located within the southwest quadrant of the SMART 1 array (figure A.1). This sub-array consists of 15 free-surface accelerometers, supplemented by 8 down-hole accelerometers at depths ranging to 47m. Two models (1/4 and 1/12 scale) of a nuclear power reactor containment vessel have also been instrumented with 14 accelerometers and 20 pressure gauges. The EPRI array began operation in 1986 with the successful recording of event 39 (Tables A.1 and A.2). In 1987, the shallow down-hole accelerometers contained in the smaller EPRI array were complimented by an instrumented 70m bore-hole in the SMART 1 array that will greatly improve the three dimensional studies.

An additional important complimentary feature to SMART 1 data collection is a regional network of strong motion accelerometers, made up of primarily SMA-1 instruments. These are operated, independently from the NSF sponsored project described in this dissertation by the Institute of Earth Sciences and other groups throughout Taiwan.

A.2 Geology

The SMART 1 array is located in a recent alluvial valley (except for the extended array station E-02 that is located on a slate outcrop). The valley triangular in shape, 15 km by 8 km at its widest and longest points, respectively. The area is comprised primarily of rice fields so that the water table is at or near the ground surface. The topography is very flat with elevations across the array ranging between 2.4 and 18.1 meters above sea level. Most of the array stations are at elevations between 4 and 8 meters. Grey silty sands, grey sandy silts, grey silty clays and gravels make up the soils beneath the array, to a depth of 3-18 meters, covering a recent alluvium layer that is approximately 40m thick. P-wave velocities range between 430 to 760 m/sec in the soils and between 1400 to 1700 m/sec in the alluvium (Wen and Yeh, 1984). Below the alluvium are Pleistocene gravels and, as is typical in alluvial fans, the grain size of the gravels increases with depth. The P-wave

velocity in the Pleistocene gravels ranges from 1800 to 2000 m/sec. The bedrock below the gravels consists of Miocene slate through which P-wave velocities are 3300 to 4000 m/sec. Dipping structures are present in the bedrock. The depth to the bedrock from the level of the main array varies from 170m in the south to 600m in the northern part of the array. P-wave velocity profiles for layers beneath the array are given by Wen and Yeh (1984). All of the array stations are situated on soils that are usually classified as "deep cohesionless soil sites" (Seed, *et al.*, 1986), except station E-02 that is classified as a rock site.

In conjunction with the installation of the Taiwan Power Company/EPRI array in 1985, eight bore-holes were drilled in the EPRI array site (figure A.1). One bore-hole was drilled to a depth of 150m and seven holes to 60m below the existing ground surface. The results of analyzing the soil samples obtained during the drilling are reported in World Exploration and Construction Company (1986). For example, samples from the 150m hole predominantly consist of grey sandy silts, grey silty sands, gravels and grey silty clays that are interbedded throughout the hole. HCK Geophysical Company (1986) logged seven of the holes, using crosshole and uphole seismic methods to determine *in situ* P and S wave velocities. From the velocities, Poisson's ratio, shear modulus and Young's modulus were calculated. To depths of 0 to 5m, the P-wave velocity is 370 m/sec, the S-wave velocity is 120 m/sec and Poisson's ratio is 0.441. To depths of 80 to 150m, the P-wave velocity is 1540 m/sec, the S-wave velocity is 480 m/sec and Poisson's ratio is 0.398. Additional velocity and moduli values are shown in Table A.3.

A.3 Seismicity and Tectonics

Taiwan is part of the Ryukyu-Taiwan-Philippine arc system and can be viewed as a tectonic transition zone between two subduction zones with very different geometries. This complicated tectonics in the Taiwan region leads to a high rate of seismicity (figure A.2) occurring with a variety of focal mechanisms. In most cases, the shallow on-shore seismicity does not correlate well with mapped faults, although some clear micro-earthquake concentrations along faults have been observed (Wu, 1978). In the northeast corner of Taiwan

both shallow and intermediate depth earthquakes occur at a high rate (figure A.2) (Tsai, *et al.*, 1977). The location of SMART 1 in this area allows study of strong ground motions produced by earthquakes with a variety of mechanisms at various focal depths. Detailed descriptions of the seismicity and tectonics of Taiwan are given by Wu (1978), Lin and Tsai (1981) and Tsai (1986).

A.4 Available SMART 1 Data

For each of the 48 earthquakes recorded through 1986, the origin time, epicentre, focal depth, magnitude and, when available, the earthquake mechanism are listed in Table A.1. Three magnitudes, M_L, m_b and M_S are listed, when available, in Table A.1. These magnitude types are defined in, for example, Bullen and Bolt (1985). The Institute of Earth Sciences, Academia Sinica estimates the local magnitude, M_L, by converting a locally estimated magnitude (M_D), based on the duration of the recorded waves, to M_L using the empirical formula

$$M_L = 1.04+0.94M_D \quad ,$$

(e.g. Liaw and Tsai, 1981; Yeh, *et al.*, 1982; Chen and Wang, 1985). The duration magnitude, M_D, (not listed in Table A.1) is estimated from recordings from the Taiwan Telemetered Seismic Network. Surface wave magnitude (M_S) and body wave magnitude (m_b) are determined by the International Seismological Centre or the U. S. Geological Survey using teleseismic recordings.

Table A.2 gives the epicentral distance (Δ) to the center of the array (station C-00), the azimuth of the epicenter in relation to the central station, and the number of triggered and operational stations for each event. Also, the largest accelerations recorded for each earthquake for each of the three ground acceleration components are tabulated in Table A.2. With few exceptions, failures of station instruments to trigger were because actual ground accelerations did not reach pre-set trigger levels. The highest ground acceleration recorded by SMART 1 is 333.6 gal (0.34g) during event 39. An epicentral map for the earthquakes

recorded by SMART 1 is given in figure A.3. Most of the earthquakes occurred off-shore, within 80 km of the array. The recorded ground accelerations have been initially processed to produce unfiltered accelerograms. The processing of the digital data includes removing glitches, replacing data drop-outs and removing the mean (DC baseline shift). Unfiltered accelerations for all events are available upon request from Dr. Bruce A. Bolt, Seismographic Station, U. C. Berkeley, Berkeley, CA 94720.

A.5 Events 5 and 39

In this dissertation events 5 and 39 have been analyzed using frequency-wavenumber and polarization methods. The rotated components of ground acceleration recorded at the center, inner and middle ring stations in the SMART 1 sub-array during events 5 and 39 are shown in figures A.4 and A.5, respectively. Because absolute time is maintained at each station, the records can be aligned in strict time order. For both events, the P-waves onsets were recorded by all operating instruments due to the high P-wave amplitudes. In both events 5 and 39, there are variations in the shape and amplitude of the waveforms for the three components and at the different stations. A brief discussion of the significance of these two events is given below.

Event 5, M_L=6.3, is the best studied earthquake recorded by the array. Its recordings (see figure A.4) have been used in numerous studies of spatial coherence (Loh, *et al.*, 1982; Harada, 1984; Abrahamson, 1985; Bolt, *et al.*, 1984; and Harichandran and Vanmarcke, 1986; Abrahamson and Darragh, 1986; and Loh and Su, 1986), effects of non-vertically propagating waves (Bolt, *et al.*, 1982; Loh, *et al.*, 1982; Abrahamson and Bolt 1985; and Tabatabie, *et al.*, 1986), source rupture (Abrahamson, 1985) and separation of wavetypes (Darragh and Abrahamson, 1986; this dissertation). The largest horizontal acceleration recorded at SMART 1 during event 5 was greater than 0.24g. This peak acceleration was not exceeded at SMART 1 for five years.

Event 39, M_L=6.5, was the first event (figure A.5) to produce accelerations exceeding

the peak accelerations recorded during event 5. Free-field accelerations greater than 0.33g were recorded at the array on both the north-south and the vertical components. The ground motions recorded during event 39 demonstrate that significant scattering of seismic waves occurs for frequencies greater than 1 Hz, especially on the horizontal components (Darragh and Abrahamson, 1986; Abrahamson and Darragh, 1987; this dissertation).

References

Abrahamson, N. A. (1985). Estimation of seismic wave coherency and rupture velocity using SMART 1 strong-motion array recordings, *EERC Report No. UCB/EERC-85/02.*

Abrahamson, N. A. and B. A. Bolt (1985). The spatial variation of the phasing of seismic strong ground motion, *Bull. Seism. Soc. Am.*, **75**, 1247-1264.

Abrahamson, N. A. and R. B. Darragh (1987). Origin of scattered waves recorded by the SMART 1 strong motion array, *Seism. Res. Lett.*, **58**, 15.

Bolt, B. A. and N. A. Abrahamson and Y. T. Yeh (1984). The variation of strong ground motion over short distances, *Eighth World Conf. Earth. Engin.*, San Francisco, II, 183-189.

Bolt, B. A., C. H. Loh, J. Penzien, Y. B. Tsai and Y. T. Yeh (1982). Preliminary report on the SMART 1 strong motion array in Taiwan, *EERC Report No. UCB/EERC-82/13.* Bullen, K. E. and B. A. Bolt (1985). *An introduction to the theory of seismology.* Cambridge University Press, New York.

Chen, K. C. and J. H. Wang (1985). The b-value distribution and seismicity maps of the Taiwan region, *Pro. ROC-JAPAN Joint Sem. Mult. Haz. Mit.*, Nat. Taiwan Univ., Taipei, Taiwan, ROC, 69-82.

Darragh, R. B. and N. A. Abrahamson (1986). Separation of wave types using the SMART 1 strong motion array recordings, *EOS*, **67**, 1097.

Harada, T. (1984). Probabilistic modeling of spatial variations of strong earthquake ground displacements, *Eighth World Conf. Earth. Engin.*, San Francisco, II, 605-612.

Harichandran, S. and E. H. Vanmarcke (1986). Stochastic variation of earthquake ground motion in space and time, *J. Engin. Mech.*, **112**, 154-174.

HCK Geophysical Company (1986). Geophysical survey report of Lo-Tung project for Taiwan Power Company.

Liaw, Z. S. and Y. B. Tsai (1981). Relation between Richter magnitude and total seismic signal duration, *Bull. Inst. Earth Sci., Academia Sinica*, **1**, 23-30.

Lin, M. T. and Y. B. Tsai (1981). Seismotectonics in Taiwan-Luzon area, *Bull. Inst. Earth Sci. Academia Sinica*, **1**, 51-82.

Loh, C. H., J. Penzien and Y. B. Tsai (1982). Engineering analysis of SMART 1 array accelerograms, *Earth. Engin. Struct. Dyn.*, **10**, 575-591.

Loh, C. H. and G. W. Su (1986). Relative ground displacements and space-time correlation of ground motions, *Proc. Seventh Japan Earth. Engin. Sym.*, Tokyo, December, 1986.

Seed, H. B., C. Ugas and J. Lysmer (1976). Site-dependent spectra for earthquake resistant design, *Bull. Seism. Soc. Am.*, **66**, 221-243.

Tabatabie, M., N. A. Abrahamson and J. P. Singh (1986). Effect of seismic wave inclination on structural response, *Proc. Third Conf. ASCE.* G. Hart and R. Nelson (editors).

Tsai, Y. B. (1986). Seismotectonics of Taiwan, *Tectonophysics*, **125**, 17-37.

Tsai, Y. B., T. L. Teng, J. M. Chiu and H. L. Liu (1977). Tectonic implications of the seismicity in the Taiwan region, *Mem. Geol. Soc. China*, **2**, 13-41.

Wen, K. L. and Y. T. Yeh (1983). Seismic velocity structure beneath the SMART 1 array *Bull. Inst. Earth Sci. Academia Sinica*, **4**, 51-72.

World Exploration and Construction Co., Ltd. (1986). Geological exploration report on Lo-Tung project for Taiwan Power Company.

Wu, F. T. (1970). Focal mechanisms and tectonics in the vicinity of Taiwan, *Bull. Seism. Soc. Am.* **60**, 2045-2056. 19-35.

Yeh, Y. T., G. W. Ou and C. C. Lin (1982). Determination of local magnitude scale for Taiwan, *Bull. Inst. Earth Sci., Academia Sinica*, **2**, 37-48.

TABLE A.1
Events Recorded by the SMART 1 Array

Event	Origin Time (UTC)	Latitude	Longitude	Depth	Ref	M_L	m_b	M_S	Mechanism
1	80 Oct 18 00:08:23.4	24.36° N	121.89° E	27	I	6.1	5.1	5.7	
2	80 Nov 14 13:37:01.5	24.61° N	121.75° E	78	T	5.9	5.1	4.9	
3	80 Nov 14 13:38:	24.42° N	121.77° E	10	T	5.7			
4	81 Jan 24 14:10:31.6	23.93° N	121.70° E	61	I	5.6	4.8		
5	81 Jan 29 04:51:34.5	24.44° N	121.92° E	25	I	6.3	5.7	5.7	R
6	81 Feb 27 02:27:	24.68° N	121.85° E	76	I	5.5	4.6		
7	81 Mar 02 12:13:46.2	22.88° N	121.47° E	25	I	6.2	5.4	6.2	
8	81 Mar 10 08:24:49.2	24.83° N	122.03° E	10	I	4.8			
9	81 Mar 22 21:25:33	24.70° N	121.8 ° E	5	I	4.2			
10	81 May 03 19:19:49.0	24.69° N	122.23° E	75	I	5.1	3.7		
11	81 Jun 01 11:53:46	24.44° N	121.9 ° E	10	I	5.6	3.5		
12	81 Aug 20 19:03:26	24.86° N	122.04° E	12	I	4.9	4.1		
13	81 Aug 20 20:55:03.7	24.80° N	122.09° E	10	I	4.4			
14	81 Aug 30 18:54:53.6	24.50° N	121.93° E	20	I	5.0			
15	81 Oct 05 13:24:30.5	24.66° N	121.74° E	4	T	3.6			
16	82 Jan 23 14:10:40.7	23.92° N	121.74° E	13	I	6.2	5.6	6.2	
17	82 Feb 21 06:04:37.4	24.79° N	121.90° E	11	I	4.7			
18	82 Feb 28 13:23:36.0	24.81° N	121.92° E	15	I	5.1	4.4		
19	82 Apr 01 04:50:01	24.58° N	122.1 ° E	17	I	4.9			
20	82 Dec 17 02:43:03.8	24.56° N	122.53° E	88	I	6.4	5.9		R/SS
21	83 Apr 26 15:26:40.2	24.67° N	122.63° E	115	I	6.6	5.7		
22	83 May 10 00:15:05.0	24.50° N	121.52° E	19	I	6.4	5.6	5.6	
23	83 Jun 21 14:48:07.9	24.13° N	122.39° E	43	I	6.6	5.8	6.4	R/SS
24	83 Jun 24 09:06:46.3	24.17° N	122.39° E	48	I	6.9	6.0	6.7	R/SS
25	83 Sep 21 19:20:44.4	24.08° N	122.16° E	44	I	6.8	6.0	6.5	R/SS
26	84 Feb 23 12:15:26.0	24.66° N	121.93° E	69	I	5.5	4.6		
27	84 Mar 28 09:11:21.0	24.11° N	122.54° E	57	I	6.3	5.5	5.9	
28	84 Apr 18 01:34:15.0	24.91° N	122.54° E	16	I	5.9	4.9	4.1	
29	84 Apr 23 22:35:04.0	24.94° N	122.11° E	28	I	6.0	5.0		
30	84 Dec 29 01:07:01.7	24.78° N	122.02° E	88	I	6.3	5.4		
31	85 Mar 09 19:51:00.5	24.76° N	122.23° E	4	T	5.9	5.1		
32	85 Jun 12 13:23:13.3	24.59° N	122.23° E	5	T	6.0	4.3	4.1	
33	85 Jun 12 17:22:50.8	24.57° N	122.19° E	3	T	6.5	5.2	5.8	
34	85 Aug 05 13:00:38.6	24.38° N	121.88° E	1	T	5.8	5.2	5.5	
35	85 Aug 12 00:21:33.3	24.71° N	121.79° E	8	T	5.7	4.4		
36	85 Sep 20 15:01:24.0	24.53° N	122.20° E	6	T	6.3	5.3	5.1	
37	85 Oct 26 03:30:39.1	24.41° N	121.83° E	2	T	5.3	4.4		
38	85 Nov 07 05:25:17.8	24.78° N	121.82° E	74	T	5.5	4.8		
39	86 Jan 16 13:04:32.0	24.76° N	121.96° E	10	T	6.5	5.5	5.8	
40	86 May 20 05:25:49.6	24.08° N	121.59° E	16	T	6.5	6.1	6.4	R/SS
41	86 May 20 05:37:31.7	24.05° N	121.62° E	22	T	6.2	5.5		
42	86 Jul 17 00:03:33.5	24.66° N	121.82° E	2	T	5.0			
43	86 Jul 30 11:31:47.5	24.63° N	121.79° E	2	T	6.2	5.6	5.6	
44	86 Jul 30 11:38:31.7	24.64° N	121.80° E	2	T	4.9			
45	86 Nov 14 21:20:01.2	23.96° N	121.84° E	7	T	7.0	6.2	7.8	
46	86 Nov 14 22:34:22.5	23.96° N	121.84° E		P		5.3		
47	86 Nov 14 23:04:36.6	23.96° N	121.84° E		P		6.1	6.3	
48	86 Dec 10 23:55:21.0	23.96° N	121.84° E		P		5.3		

M_L is determined by the Institute of Earth Sciences, Taipei using the Taiwan Telemetered Seismic Network (TTSN).

References for Location and Mechanism:
P=Preliminary Determination of Epicenters (PDE), U. S. Geological Survey
I=Regional Catalog of Earthquakes, International Seismological Centre
T=Institute of Earth Sciences, Academia Sinica, Taiwan

Mechanism:
SS=Strike-Slip
R=Reverse

TABLE A.2
Events Recorded by the SMART 1 Array

Event	M_L	Depth (km)	Δ (km)	Azimuth (Deg)	T/I†	Maximum Accelerations (gal)		
						V	EW	NS
1	6.1	27	36	192	16/21	15.7	22.3	25.4
2	5.9	81	7	168	16/21	31.7	74.4	83.8
3	5.7	10	28	179	13/21	10.7	22.9	24.6
4	5.6	61	83	185	2/27	2.4	8.1	9.0
5	6.3	25	30	149	27/27	97.4	168.5	259.8
6	5.5	6	9	86	10/27	4.4	13.6	12.2
7	6.2	25	201	189	3/27	2.7	6.4	10.5
8	4.8	10	32	57	19/27	16.0	23.5	34.5
9	4.2	5	5	51	12/28	13.1	22.8	19.1
10	5.1	75	48	88	10/28	16.6	21.0	18.3
11	5.6	10	29	152	8/28	10.1	13.2	15.0
12	4.9	12	35	54	18/36	24.4	24.8	37.8
13	4.4	10	36	67	14/36	14.1	33.8	45.9
14	5.0	20	26	139	31/36	17.7	31.6	43.5
15	3.6	4	3	239	29/37	40.5	71.7	55.7
16	6.2	13	84	182	11/36	9.2	23.7	20.2
17	4.7	11	19	47	8/35	22.3	28.2	26.0
18	5.1	15	22	46	24/36	31.1	75.5	97.1
19	4.9	17	36	107	28/35	21.7	43.0	32.8
20	6.4	88	79	99	36/36	33.8	67.0	68.1
21	6.6	115	88	90	11/36	9.9	49.5	25.2
22	6.4	98	31	212	35/37	39.0	75.2	68.4
23	6.6	43	87	125	23/37	13.2	29.0	42.0
24	6.9	48	84	124	31/37	16.4	53.9	69.4
25	6.8	44	68	134	35/37	18.3	37.5	39.3
26	5.5	69	17	95	10/37	8.6	30.1	45.6
27	6.3	57	100	122	11/37	11.8	17.0	20.0
28	5.9	16	83	72	28/37	19.4	65.2	55.6
29	6.0	28	46	57	30/37	30.1	76.9	68.7
30	6.3	88	28	67	32/37	37.4	70.2	84.1
31	5.9	4	48	79	37/39	39.2	108.6	73.7
32	6.0	5	48	101	21/38	17.2	49.7	39.5
33	6.5	3	45	104	36/38	49.2	157.6	103.9
34	5.8	1	34	160	25/38	21.8	36.2	40.4
35	5.7	8	5	26	37/38	74.8	94.3	141.1
36	6.3	6	47	110	36/38	58.6	121.0	87.8
37	5.3	2	30	167	33/38	43.8	56.6	77.2
38	5.5	74	13	26	14/38	15.1	24.6	32.4
39	6.5	10	22	64	36/39	333.6	258.4	327.5
40	6.5	16	67	195	37/38	77.2	224.2	266.4
41	6.2	22	71	192	37/38	30.2	66.2	80.8
42	5.0	2	5	107	38/39	82.0	140.8	151.1
43	6.2	2	6	150	39/39	232.2	244.5	300.6
44	4.9	2	5	141	37/38	39.8	109.1	103.0
45	7.0	7	79	175	36/	110.3	178.0	251.0
46			79	175				
47			79	175				
48			79	175				

† T/I = Number of stations triggered / Number of stations installed.

TABLE A.3
Velocity and Moduli Values
(Courtesy of EPRI)

Depth (m)	P-wave Velocity (m/sec)	S-wave Velocity (m/sec)	Poisson's Ratio	Shear Modulus (kg/cm/cm)	Young's Modulus (kg/cm/cm)
0-5	370	120	0.441	264	761
5-8	810	140	0.485	360	1069
8-13	1270	190	0.488	663	1973
13-31	1330	220	0.486	889	2642
31-34	1330	280	0.477	1440	4254
34-48	1250	250	0.479	1148	3396
48-60	1220	270	0.474	1339	3947
60-80	1470	320	0.475	1881	5549
80-150	1540	480	0.398	4232	11833

Bulk density (ρ) = 1.8 gm/cc

TABLE 4
Unfiltered Peak Ground Accelerations
(Event 39)

Station	Component		
	V (gal)	EW (gal)	NS (gal)
C-00	234.3	225.2	283.1
I-01	229.9	230.8	246.0
I-02	168.5	227.5	257.6
I-03	185.6	190.0	209.6
I-04	224.0	226.9	216.7
I-05	162.8	166.6	192.0
I-06	197.0	165.8	167.3
I-07	132.0	172.3	173.2
I-08	237.1	172.2	195.2
I-09	246.3	184.8	210.4
I-11	223.6	223.5	227.3
I-12	333.6	238.5	253.5
M-01	177.4	181.6	228.4
M-02	316.6	234.0	264.5
M-03	133.2	171.6	254.6
M-05	266.7	212.5	203.3
M-06	307.5	198.5	171.6
M-07	237.4	165.7	273.4
M-08	145.4	176.0	200.7
M-09	156.9	201.1	194.5
M-10	185.5	187.3	187.2
M-11	154.7	243.7	241.7
M-12	162.3	229.4	250.2
O-01	151.0	203.5	241.5
O-02	106.2	258.4	327.5
O-03	88.1	235.1	220.4
O-04	237.1	256.6	302.4
O-05	93.5	209.8	166.1
O-07	122.1	167.6	180.3
O-08	131.6	154.6	265.4
O-09	93.8	195.4	197.6
O-10	107.0	217.2	199.0
O-12	167.5	224.0	217.4
E-01	106.1	203.2	212.6
E-02	73.3	175.8	211.6

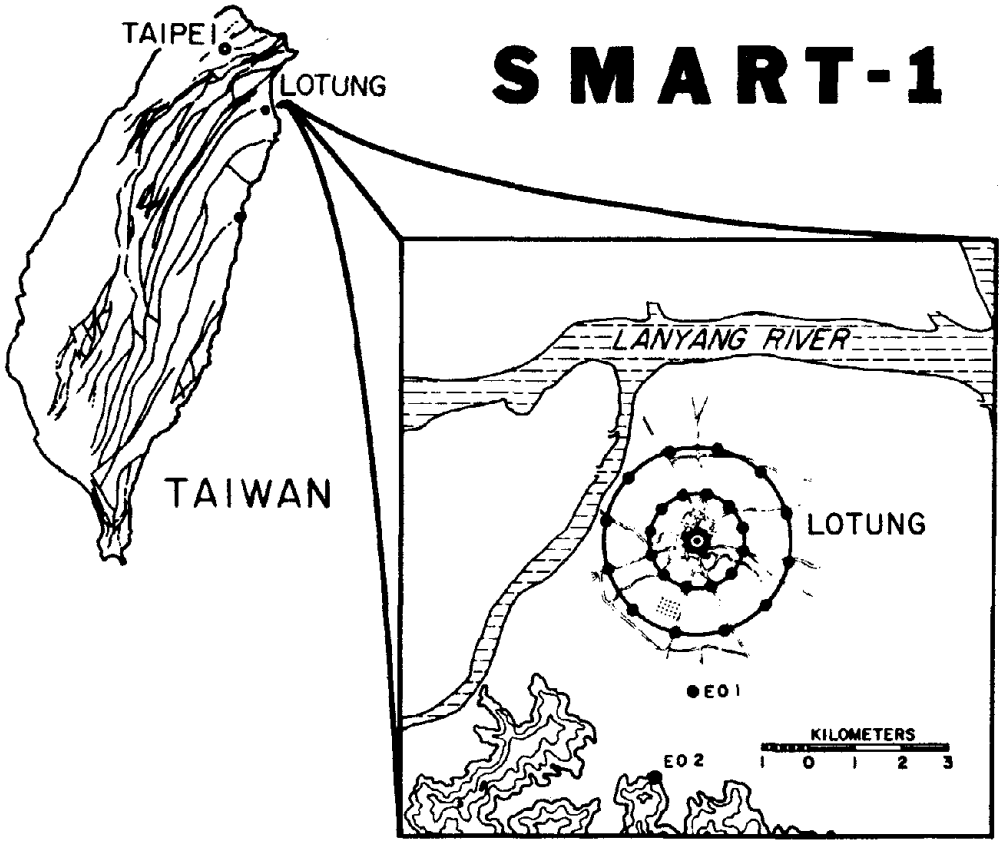

Figure A.1: Location of the SMART 1 array in northeast Taiwan. The EPRI array is located within the stippled region. The stations are shown as solid circles.

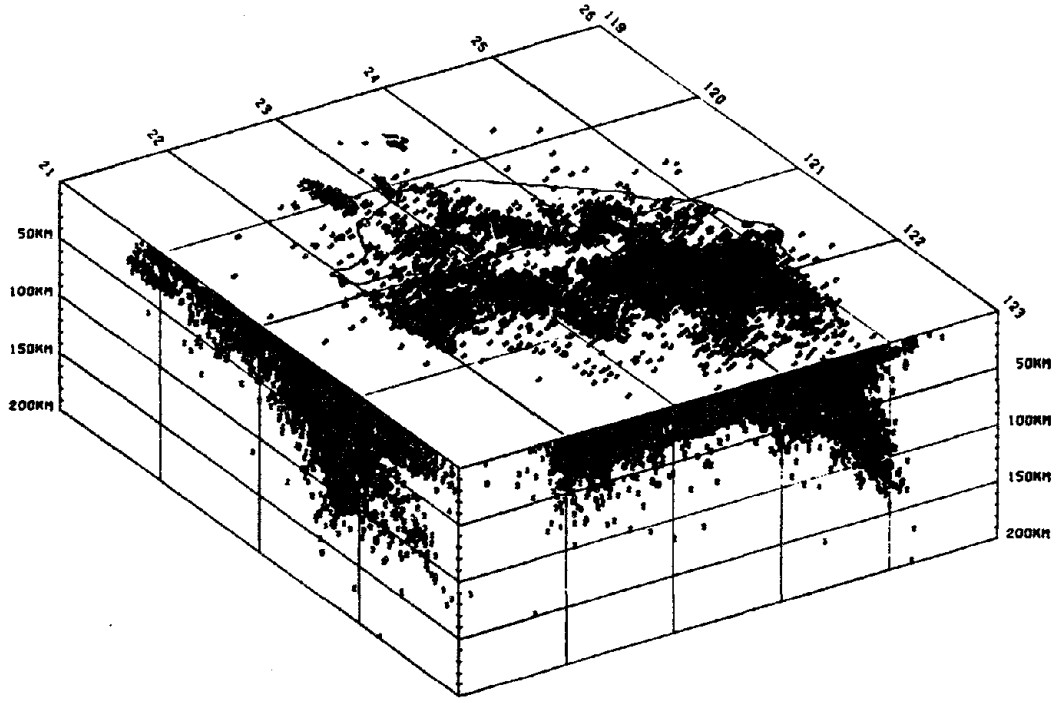

Figure A.2: Projections of hypocenter of the more reliably located earthquakes in the Taiwan region during 1973-1979.

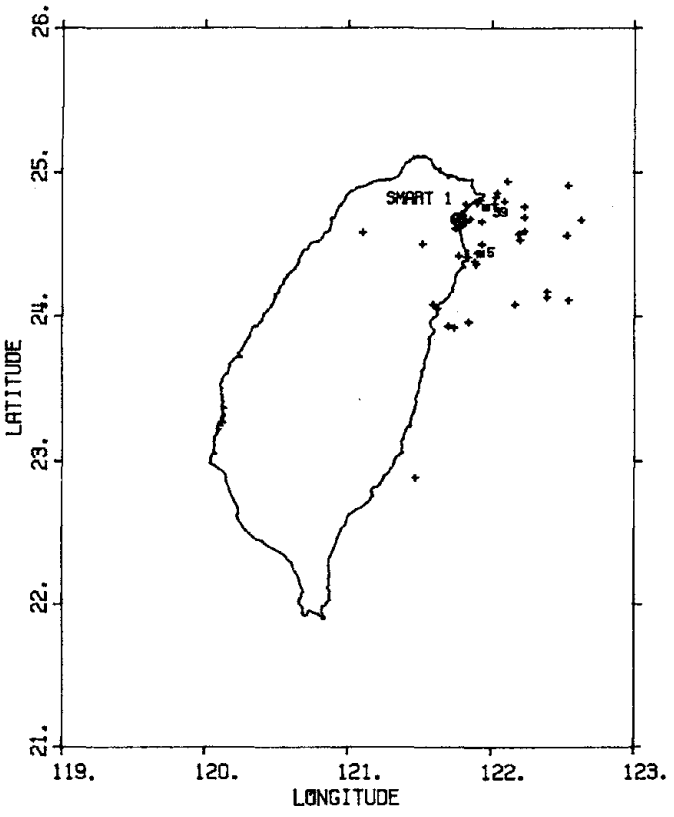

Figure A.3: Epicenter map of earthquakes recorded by the SMART 1 array through 1986. The epicenters are plotted as crosses, except for events 5 and 39 plotted as stars. The array is shown as an octagon.

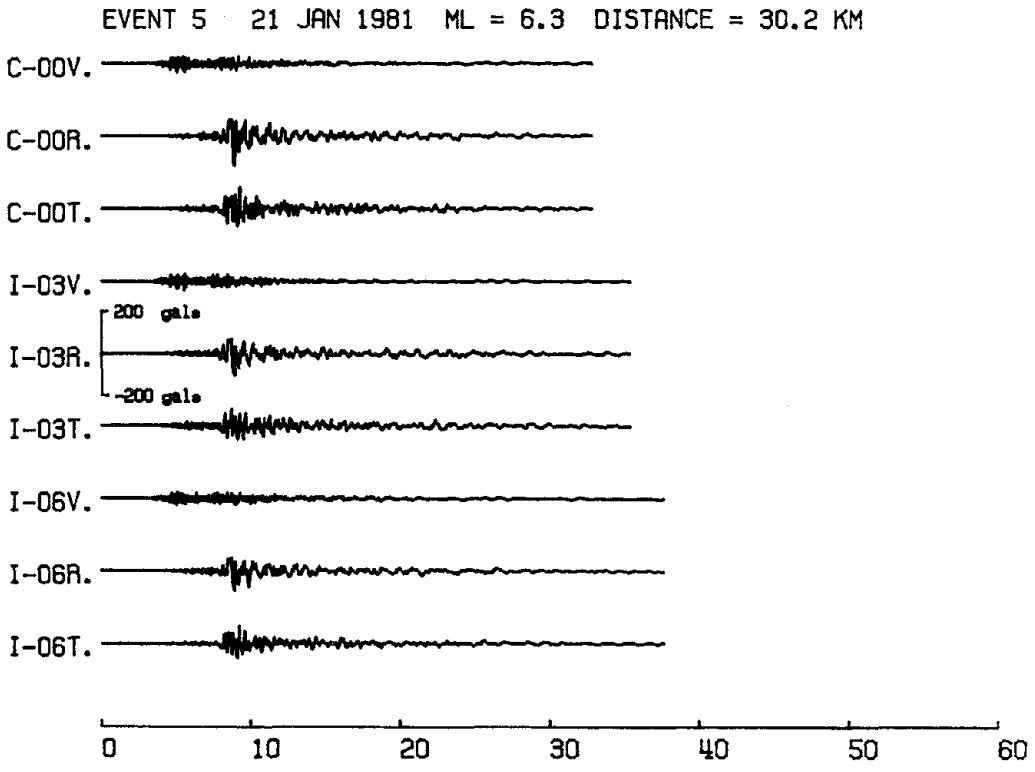

Figure A.4: The three components of ground acceleration from event 5 for the 17(vertical) and 16(horizontal) station sub-array used in this dissertation. No record was obtained from the east-west component of station M-11.

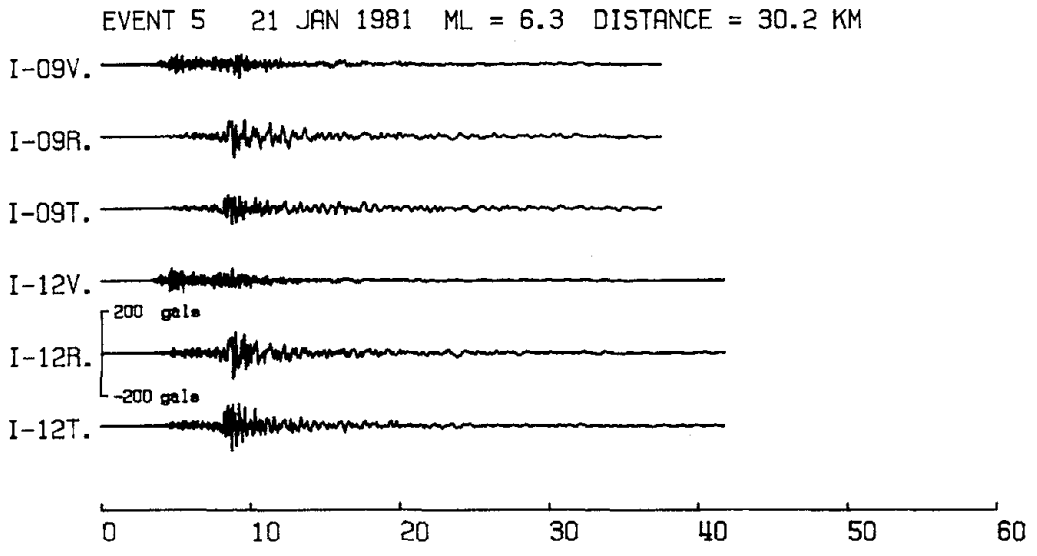

Figure A.4(continued): The three components of ground acceleration from event 5 for the 17(vertical) and 16(horizontal) station sub-array used in this dissertation. No record was obtained from the east-west component of station M-11.

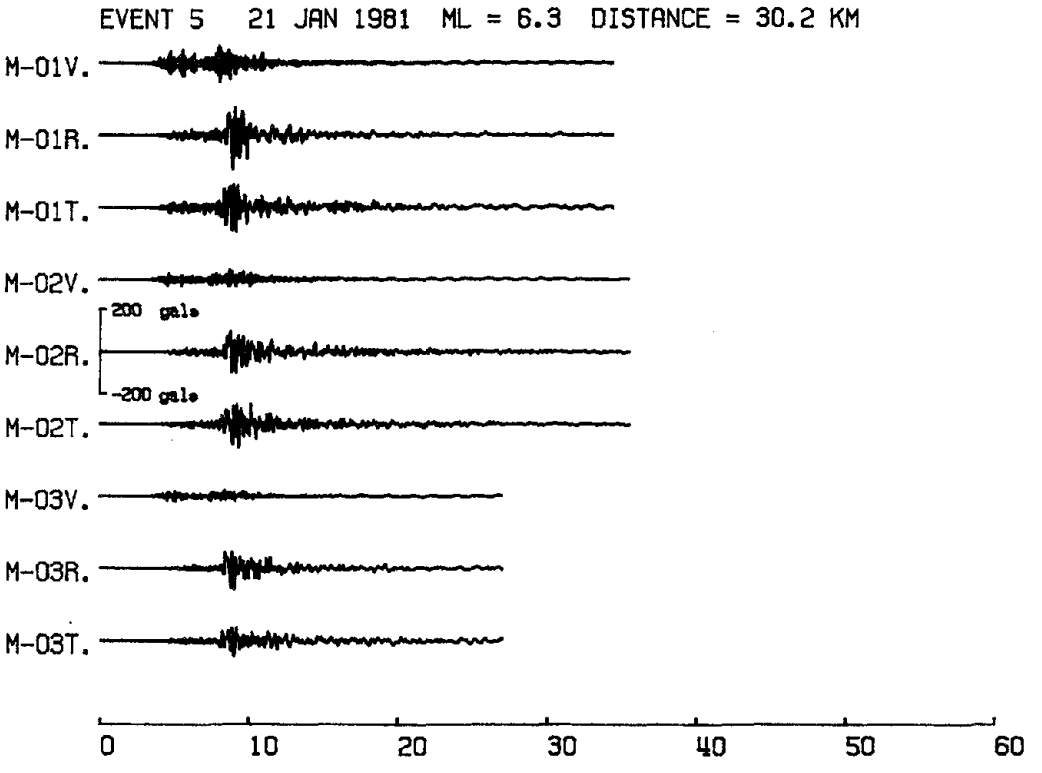

Figure A.4(continued): The three components of ground acceleration from event 5 for the 17(vertical) and 16(horizontal) station sub-array used in this dissertation. No record was obtained from the east-west component of station M-11.

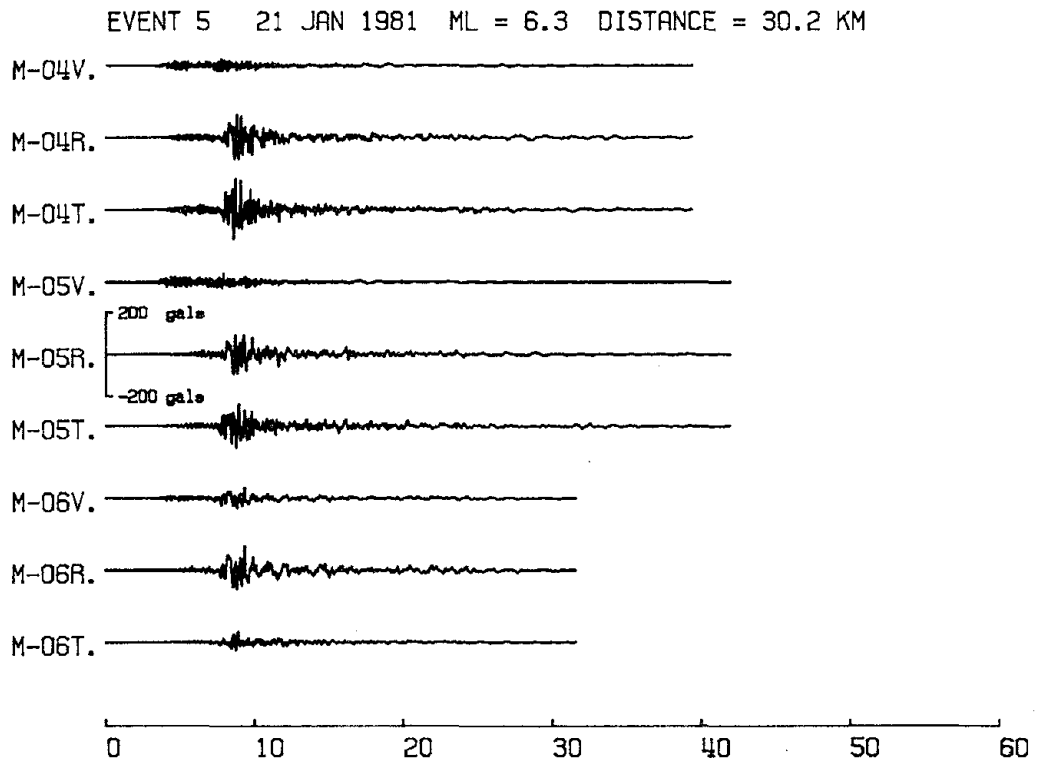

Figure A.4(continued): The three components of ground acceleration from event 5 for the 17(vertical) and 16(horizontal) station sub-array used in this dissertation. No record was obtained from the east-west component of station M-11.

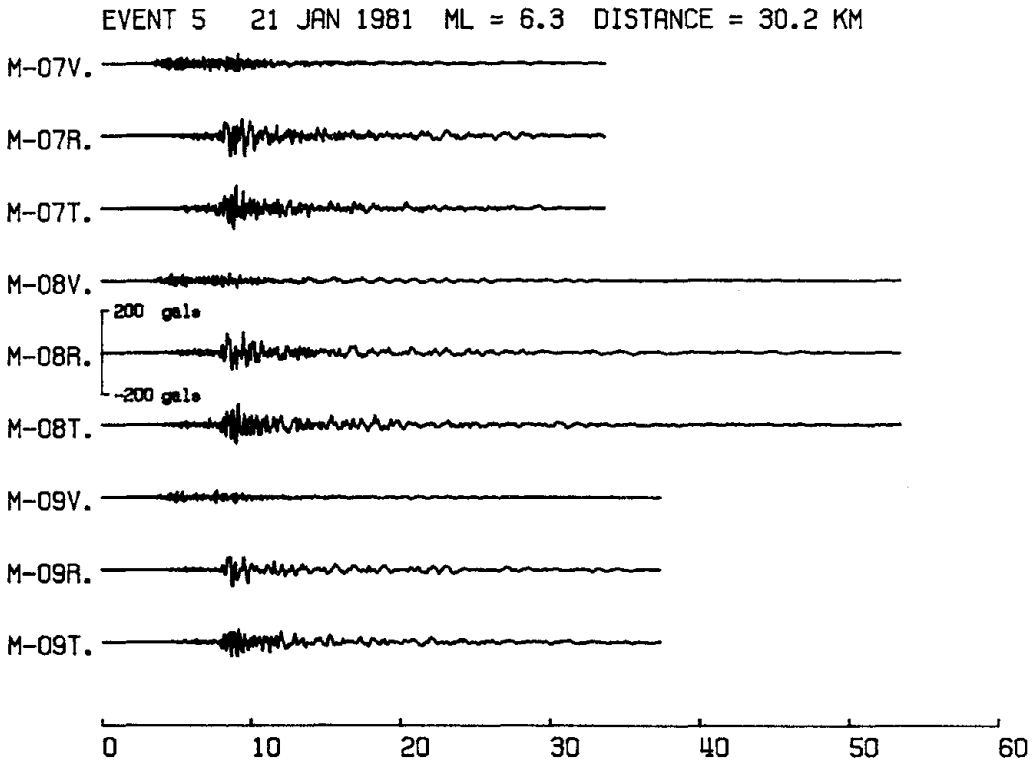

Figure A.4(continued): The three components of ground acceleration from event 5 for the 17(vertical) and 16(horizontal) station sub-array used in this dissertation. No record was obtained from the east-west component of station M-11.

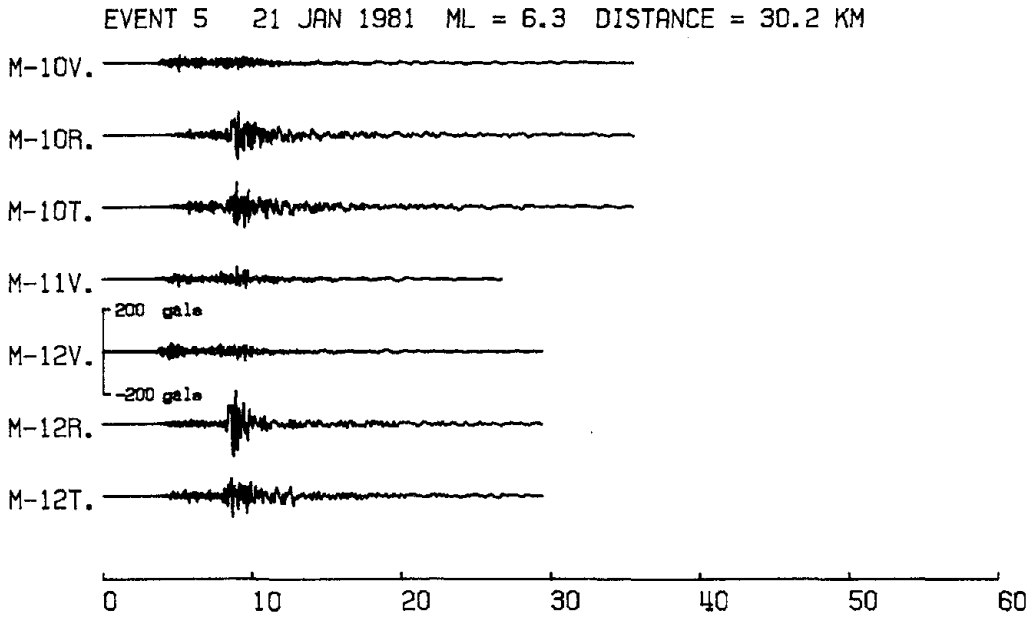

Figure A.4(continued): The three components of ground acceleration from event 5 for the 17(vertical) and 16(horizontal) station sub-array used in this dissertation. No record was obtained from the east-west component of station M-11.

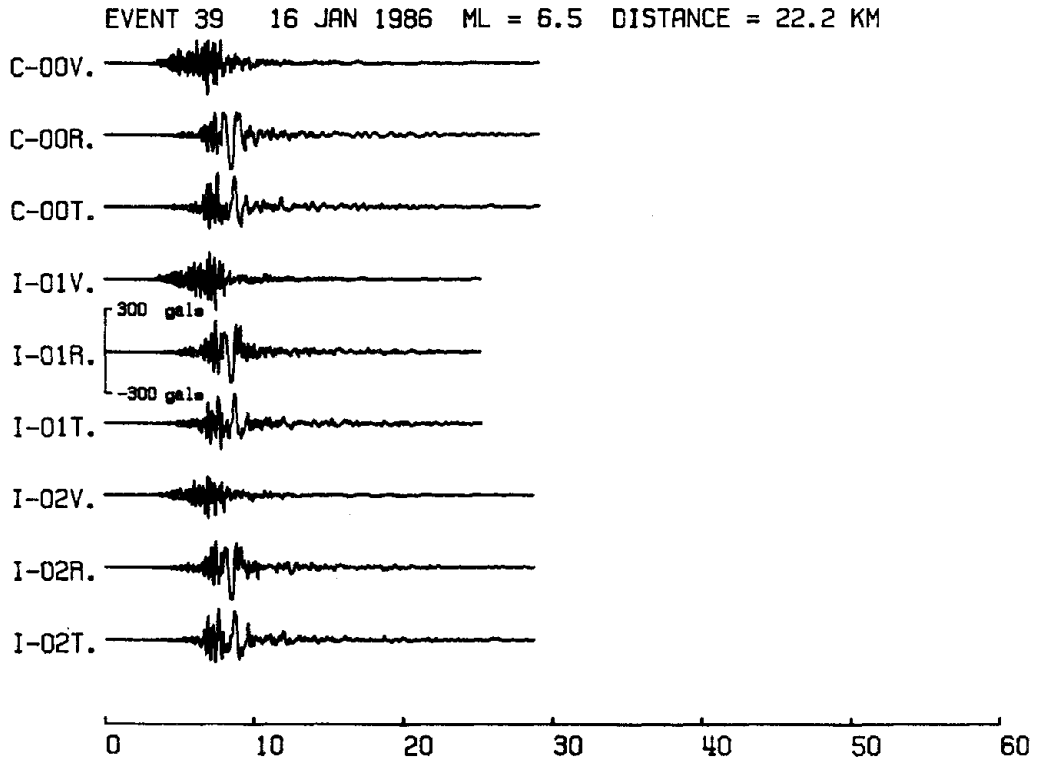

Figure A.5: The three components of ground acceleration from event 39 for the 23 station sub-array used in this dissertation.

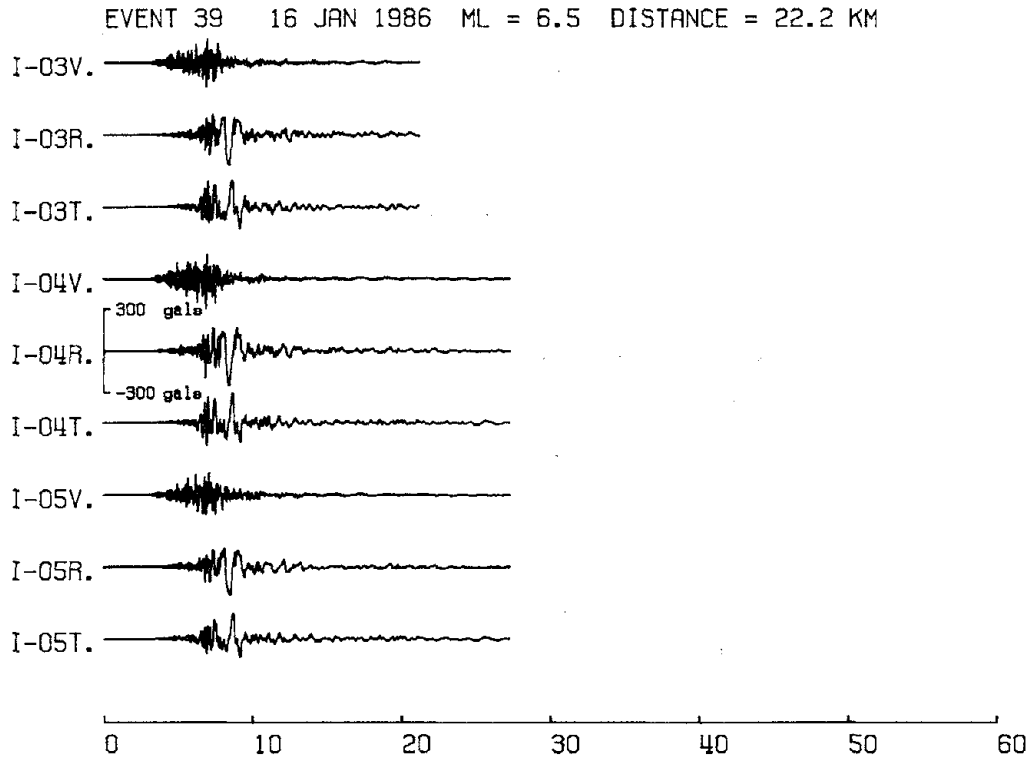

Figure A.5(continued): The three components of ground acceleration from event 39 for the 23 station sub-array used in this dissertation.

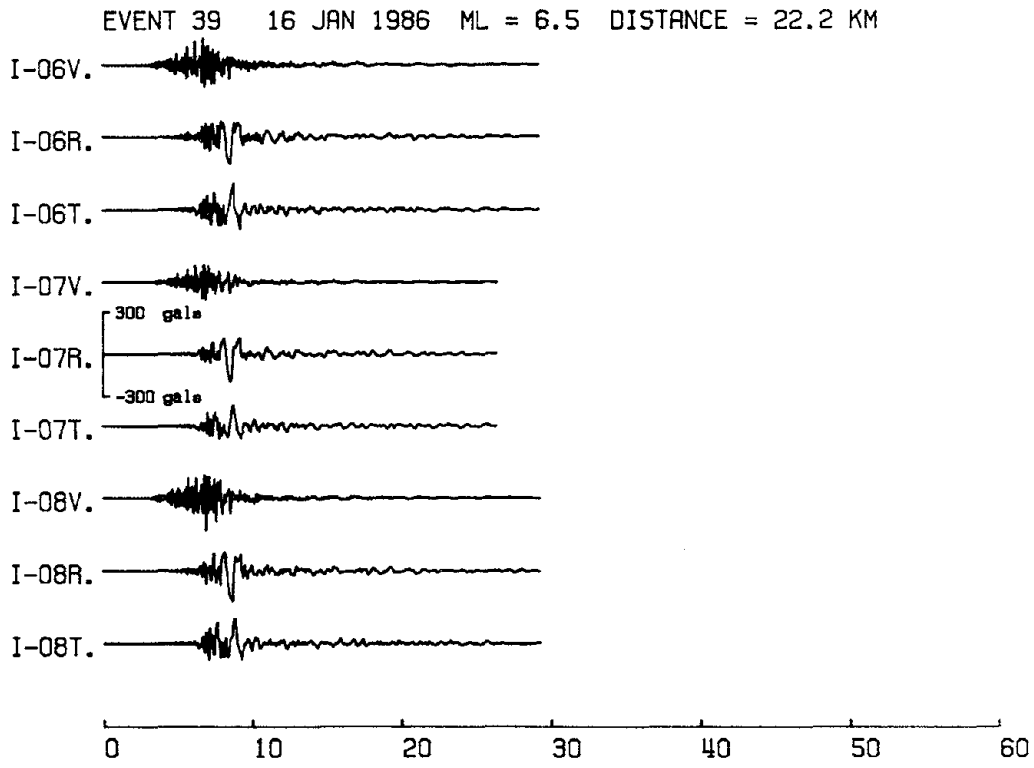

Figure A.5(continued): The three components of ground acceleration from event 39 for the 23 station sub-array used in this dissertation.

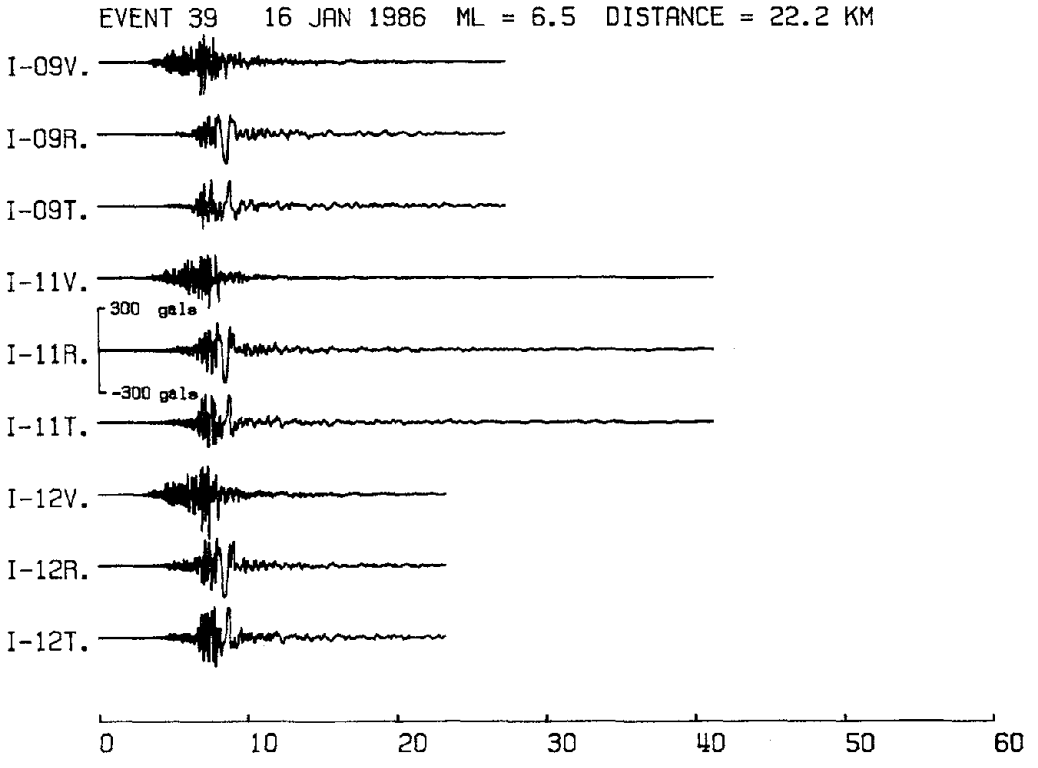

Figure A.5(continued): The three components of ground acceleration from event 39 for the 23 station sub-array used in this dissertation.

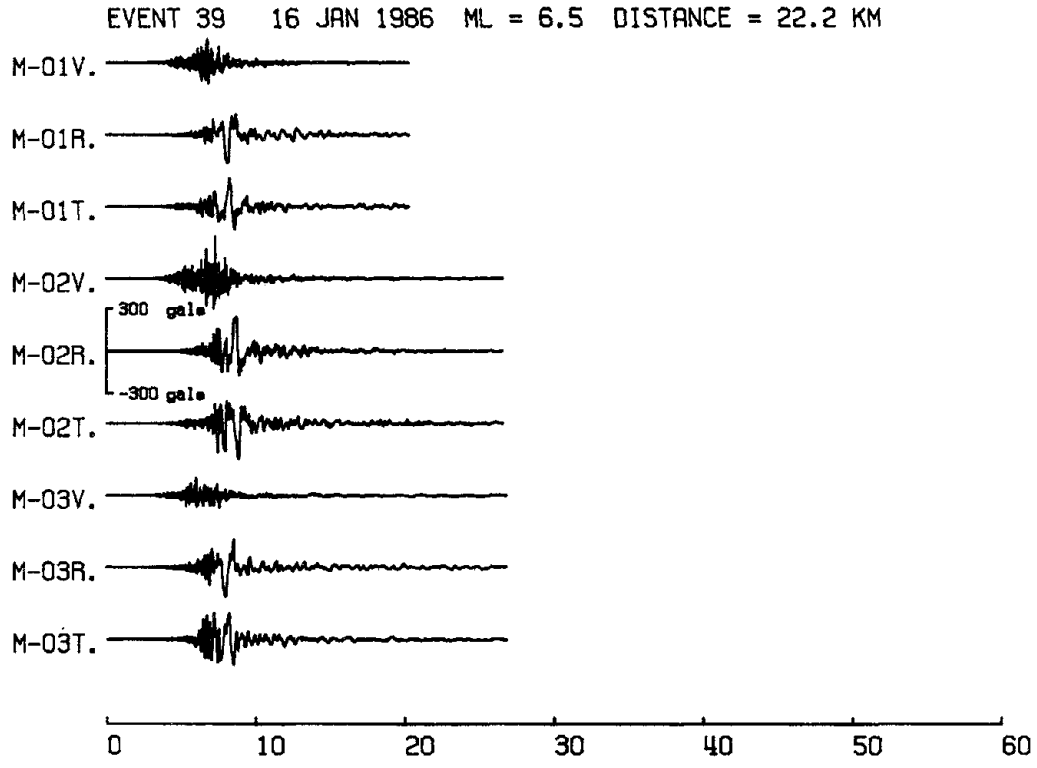

Figure A.5(continued): The three components of ground acceleration from event 39 for the 23 station sub-array used in this dissertation.

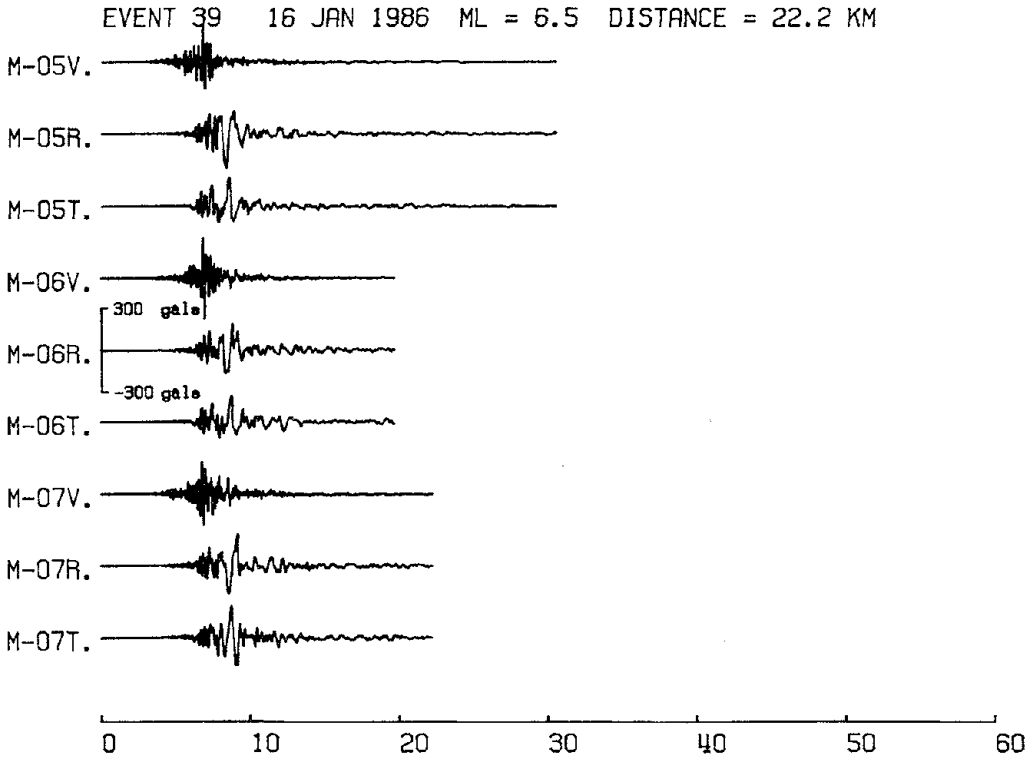

Figure A.5(continued): The three components of ground acceleration from event 39 for the 23 station sub-array used in this dissertation.

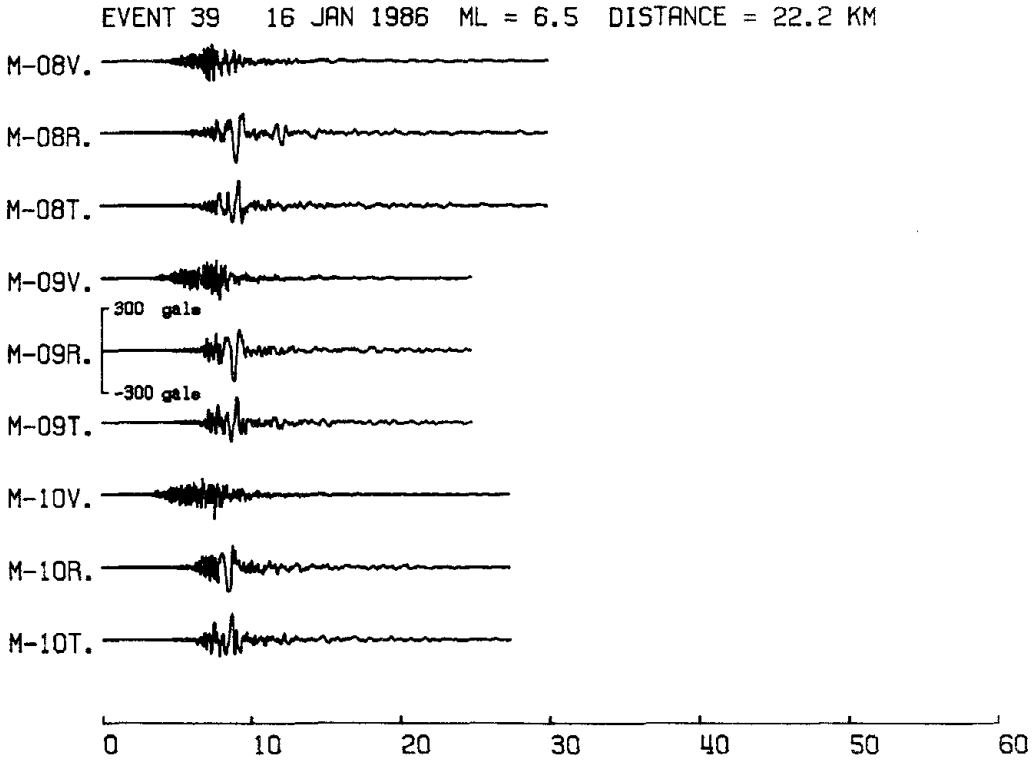

Figure A.5(continued): The three components of ground acceleration from event 39 for the 23 station sub-array used in this dissertation.

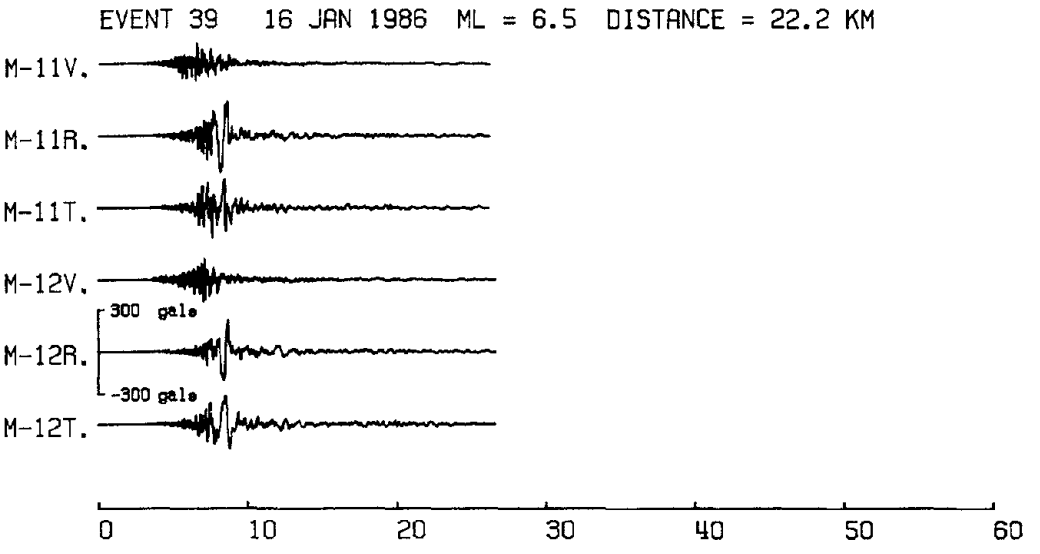

Figure A.5(continued): The three components of ground acceleration from event 39 for the 23 station sub-array used in this dissertation.

EARTHQUAKE ENGINEERING RESEARCH CENTER REPORT SERIES

EERC reports are available from the National Information Service for Earthquake Engineering(NISEE) and from the National Technical Information Service(NTIS). Numbers in parentheses are Accession Numbers assigned by the National Technical Information Service; these are followed by a price code. Contact NTIS, 5285 Port Royal Road, Springfield Virginia, 22161 for more information. Reports without Accession Numbers were not available from NTIS at the time of printing. For a current complete list of EERC reports (from EERC 67-1) and availablity information, please contact University of California, EERC, NISEE, 1301 South 46th Street, Richmond, California 94804.

UCB/EERC-80/01 "Earthquake Response of Concrete Gravity Dams Including Hydrodynamic and Foundation Interaction Effects," by Chopra, A.K., Chakrabarti, P. and Gupta, S., January 1980, (AD-A087297)A10.

UCB/EERC-80/02 "Rocking Response of Rigid Blocks to Earthquakes," by Yim, C.S., Chopra, A.K. and Penzien, J., January 1980, (PB80 166 002)A04.

UCB/EERC-80/03 "Optimum Inelastic Design of Seismic-Resistant Reinforced Concrete Frame Structures," by Zagajeski, S.W. and Bertero, V.V., January 1980, (PB80 164 635)A06.

UCB/EERC-80/04 "Effects of Amount and Arrangement of Wall-Panel Reinforcement on Hysteretic Behavior of Reinforced Concrete Walls," by Iliya, R. and Bertero, V.V., February 1980, (PB81 122 525)A09.

UCB/EERC-80/05 "Shaking Table Research on Concrete Dam Models," by Niwa, A. and Clough, R.W., September 1980, (PB81 122 368)A06.

UCB/EERC-80/06 "The Design of Steel Energy-Absorbing Restrainers and their Incorporation into Nuclear Power Plants for Enhanced Safety (Vol 1a): Piping with Energy Absorbing Restrainers: Parameter Study on Small Systems," by Powell, G.H., Oughourlian, C. and Simons, J., June 1980.

UCB/EERC-80/07 "Inelastic Torsional Response of Structures Subjected to Earthquake Ground Motions," by Yamazaki, Y., April 1980, (PB81 122 327)A08.

UCB/EERC-80/08 "Study of X-Braced Steel Frame Structures under Earthquake Simulation," by Ghanaat, Y., April 1980, (PB81 122 335)A11.

UCB/EERC-80/09 "Hybrid Modelling of Soil-Structure Interaction," by Gupta, S., Lin, T.W. and Penzien, J., May 1980, (PB81 122 319)A07.

UCB/EERC-80/10 "General Applicability of a Nonlinear Model of a One Story Steel Frame," by Sveinsson, B.I. and McNiven, H.D., May 1980, (PB81 124 877)A06.

UCB/EERC-80/11 "A Green-Function Method for Wave Interaction with a Submerged Body," by Kioka, W., April 1980, (PB81 122 269)A07.

UCB/EERC-80/12 "Hydrodynamic Pressure and Added Mass for Axisymmetric Bodies.," by Nilrat, F., May 1980, (PB81 122 343)A08.

UCB/EERC-80/13 "Treatment of Non-Linear Drag Forces Acting on Offshore Platforms," by Dao, B.V. and Penzien, J., May 1980, (PB81 153 413)A07.

UCB/EERC-80/14 "2D Plane/Axisymmetric Solid Element (Type 3-Elastic or Elastic-Perfectly Plastic)for the ANSR-II Program," by Mondkar, D.P. and Powell, G.H., July 1980, (PB81 122 350)A03.

UCB/EERC-80/15 "A Response Spectrum Method for Random Vibrations," by Der Kiureghian, A., June 1981, (PB81 122 301)A03.

UCB/EERC-80/16 "Cyclic Inelastic Buckling of Tubular Steel Braces," by Zayas, V.A., Popov, E.P. and Martin, S.A., June 1981, (PB81 124 885)A10.

UCB/EERC-80/17 "Dynamic Response of Simple Arch Dams Including Hydrodynamic Interaction," by Porter, C.S. and Chopra, A.K., July 1981, (PB81 124 000)A13.

UCB/EERC-80/18 "Experimental Testing of a Friction Damped Aseismic Base Isolation System with Fail-Safe Characteristics," by Kelly, J.M., Beucke, K.E. and Skinner, M.S., July 1980, (PB81 148 595)A04.

UCB/EERC-80/19 "The Design of Steel Energy-Absorbing Restrainers and their Incorporation into Nuclear Power Plants for Enhanced Safety (Vol.1B): Stochastic Seismic Analyses of Nuclear Power Plant Structures and Piping Systems Subjected to Multiple Supported Excitations," by Lee, M.C. and Penzien, J., June 1980, (PB82 201 872)A08.

UCB/EERC-80/20 "The Design of Steel Energy-Absorbing Restrainers and their Incorporation into Nuclear Power Plants for Enhanced Safety (Vol 1C): Numerical Method for Dynamic Substructure Analysis," by Dickens, J.M. and Wilson, E.L., June 1980.

UCB/EERC-80/21 "The Design of Steel Energy-Absorbing Restrainers and their Incorporation into Nuclear Power Plants for Enhanced Safety (Vol 2): Development and Testing of Restraints for Nuclear Piping Systems," by Kelly, J.M. and Skinner, M.S., June 1980.

UCB/EERC-80/22 "3D Solid Element (Type 4-Elastic or Elastic-Perfectly-Plastic) for the ANSR-II Program," by Mondkar, D.P. and Powell, G.H., July 1980, (PB81 123 242)A03.

UCB/EERC-80/23 "Gap-Friction Element (Type 5) for the Ansr-II Program," by Mondkar, D.P. and Powell, G.H., July 1980, (PB81 122 285)A03.

UCB/EERC-80/24 "U-Bar Restraint Element (Type 11) for the ANSR-II Program," by Oughourlian, C. and Powell, G.H., July 1980, (PB81 122 293)A03.

UCB/EERC-80/25 "Testing of a Natural Rubber Base Isolation System by an Explosively Simulated Earthquake," by Kelly, J.M., August 1980, (PB81 201 360)A04.

UCB/EERC-80/26 "Input Identification from Structural Vibrational Response," by Hu, Y., August 1980, (PB81 152 308)A05.

UCB/EERC-80/27 "Cyclic Inelastic Behavior of Steel Offshore Structures," by Zayas, V.A., Mahin, S.A. and Popov, E.P., August 1980, (PB81 196 180)A15.

UCB/EERC-80/28 "Shaking Table Testing of a Reinforced Concrete Frame with Biaxial Response," by Oliva, M.G., October 1980, (PB81 154 304)A10.

UCB/EERC-80/29 "Dynamic Properties of a Twelve-Story Prefabricated Panel Building," by Bouwkamp, J.G., Kollegger, J.P. and Stephen, R.M., October 1980, (PB82 138 777)A07.

UCB/EERC-80/30 "Dynamic Properties of an Eight-Story Prefabricated Panel Building," by Bouwkamp, J.G., Kollegger, J.P. and Stephen, R.M., October 1980, (PB81 200 313)A05.

UCB/EERC-80/31 "Predictive Dynamic Response of Panel Type Structures under Earthquakes," by Kollegger, J.P. and Bouwkamp, J.G., October 1980, (PB81 152 316)A04.

UCB/EERC-80/32 "The Design of Steel Energy-Absorbing Restrainers and their Incorporation into Nuclear Power Plants for Enhanced Safety (Vol 3): Testing of Commercial Steels in Low-Cycle Torsional Fatique," by Spanner, P., Parker, E.R., Jongewaard, E. and Dory, M., 1980.

UCB/EERC-80/33 "The Design of Steel Energy-Absorbing Restrainers and their Incorporation into Nuclear Power Plants for Enhanced Safety (Vol 4): Shaking Table Tests of Piping Systems with Energy-Absorbing Restrainers," by Stiemer, S.F. and Godden, W.G., September 1980, (PB82 201 880)A05.

UCB/EERC-80/34 "The Design of Steel Energy-Absorbing Restrainers and their Incorporation into Nuclear Power Plants for Enhanced Safety (Vol 5): Summary Report," by Spencer, P., 1980.

UCB/EERC-80/35 "Experimental Testing of an Energy-Absorbing Base Isolation System," by Kelly, J.M., Skinner, M.S. and Beucke, K.E., October 1980, (PB81 154 072)A04.

UCB/EERC-80/36 "Simulating and Analyzing Artificial Non-Stationary Earth Ground Motions," by Nau, R.F., Oliver, R.M. and Pister, K.S., October 1980, (PB81 153 397)A04.

UCB/EERC-80/37 "Earthquake Engineering at Berkeley - 1980," by , September 1980, (PB81 205 674)A09.

UCB/EERC-80/38 "Inelastic Seismic Analysis of Large Panel Buildings," by Schricker, V. and Powell, G.H., September 1980, (PB81 154 338)A13.

UCB/EERC-80/39 "Dynamic Response of Embankment, Concrete-Gavity and Arch Dams Including Hydrodynamic Interation," by Hall, J.F. and Chopra, A.K., October 1980, (PB81 152 324)A11.

UCB/EERC-80/40 "Inelastic Buckling of Steel Struts under Cyclic Load Reversal.," by Black, R.G., Wenger, W.A. and Popov, E.P., October 1980, (PB81 154 312)A08.

UCB/EERC-80/41 "Influence of Site Characteristics on Buildings Damage during the October 3,1974 Lima Earthquake," by Repetto, P., Arango, I. and Seed, H.B., September 1980, (PB81 161 739)A05.

UCB/EERC-80/42 "Evaluation of a Shaking Table Test Program on Response Behavior of a Two Story Reinforced Concrete Frame," by Blondet, J.M., Clough, R.W. and Mahin, S.A., December 1980, (PB82 196 544)A11.

UCB/EERC-80/43 "Modelling of Soil-Structure Interaction by Finite and Infinite Elements," by Medina, F., December 1980, (PB81 229 270)A04.

UCB/EERC-81/01 "Control of Seismic Response of Piping Systems and Other Structures by Base Isolation," by Kelly, J.M., January 1981, (PB81 200 735)A05.

UCB/EERC-81/02 "OPTNSR- An Interactive Software System for Optimal Design of Statically and Dynamically Loaded Structures with Nonlinear Response," by Bhatti, M.A., Ciampi, V. and Pister, K.S., January 1981, (PB81 218 851)A09.

UCB/EERC-81/03 "Analysis of Local Variations in Free Field Seismic Ground Motions," by Chen, J.-C., Lysmer, J. and Seed, H.B., January 1981, (AD-A099508)A13.

UCB/EERC-81/04 "Inelastic Structural Modeling of Braced Offshore Platforms for Seismic Loading," by Zayas, V.A., Shing, P.-S.B., Mahin, S.A. and Popov, E.P., January 1981, (PB82 138 777)A07.

UCB/EERC-81/05 "Dynamic Response of Light Equipment in Structures," by Der Kiureghian, A., Sackman, J.L. and Nour-Omid, B., April 1981, (PB81 218 497)A04.

UCB/EERC-81/06 "Preliminary Experimental Investigation of a Broad Base Liquid Storage Tank," by Bouwkamp, J.G., Kollegger, J.P. and Stephen, R.M., May 1981, (PB82 140 385)A03.

UCB/EERC-81/07 "The Seismic Resistant Design of Reinforced Concrete Coupled Structural Walls," by Aktan, A.E. and Bertero, V.V., June 1981, (PB82 113 358)A11.

UCB/EERC-81/08 "Unassigned," by Unassigned, 1981.

UCB/EERC-81/09 "Experimental Behavior of a Spatial Piping System with Steel Energy Absorbers Subjected to a Simulated Differential Seismic Input," by Stiemer, S.F., Godden, W.G. and Kelly, J.M., July 1981, (PB82 201 898)A04.

UCB/EERC-81/10 "Evaluation of Seismic Design Provisions for Masonry in the United States," by Sveinsson, B.I., Mayes, R.L. and McNiven, H.D., August 1981, (PB82 166 075)A08.

UCB/EERC-81/11 "Two-Dimensional Hybrid Modelling of Soil-Structure Interaction," by Tzong, T.-J., Gupta, S. and Penzien, J., August 1981, (PB82 142 118)A04.

UCB/EERC-81/12 "Studies on Effects of Infills in Seismic Resistant R/C Construction," by Brokken, S. and Bertero, V.V., October 1981, (PB82 166 190)A09.

UCB/EERC-81/13 "Linear Models to Predict the Nonlinear Seismic Behavior of a One-Story Steel Frame," by Valdimarsson, H., Shah, A.H. and McNiven, H.D., September 1981, (PB82 138 793)A07.

UCB/EERC-81/14 "TLUSH: A Computer Program for the Three-Dimensional Dynamic Analysis of Earth Dams," by Kagawa, T., Mejia, L.H., Seed, H.B. and Lysmer, J., September 1981, (PB82 139 940)A06.

UCB/EERC-81/15 "Three Dimensional Dynamic Response Analysis of Earth Dams," by Mejia, L.H. and Seed, H.B., September 1981, (PB82 137 274)A12.

UCB/EERC-81/16 "Experimental Study of Lead and Elastomeric Dampers for Base Isolation Systems," by Kelly, J.M. and Hodder, S.B., October 1981, (PB82 166 182)A05.

UCB/EERC-81/17 "The Influence of Base Isolation on the Seismic Response of Light Secondary Equipment," by Kelly, J.M., April 1981, (PB82 255 266)A04.

UCB/EERC-81/18 "Studies on Evaluation of Shaking Table Response Analysis Procedures," by Blondet, J. M., November 1981, (PB82 197 278)A10.

UCB/EERC-81/19 "DELIGHT.STRUCT: A Computer-Aided Design Environment for Structural Engineering," by Balling, R.J., Pister, K.S. and Polak, E., December 1981, (PB82 218 496)A07.

UCB/EERC-81/20 "Optimal Design of Seismic-Resistant Planar Steel Frames," by Balling, R.J., Ciampi, V. and Pister, K.S., December 1981, (PB82 220 179)A07.

UCB/EERC-82/01 "Dynamic Behavior of Ground for Seismic Analysis of Lifeline Systems," by Sato, T. and Der Kiureghian, A., January 1982, (PB82 218 926)A05.

UCB/EERC-82/02 "Shaking Table Tests of a Tubular Steel Frame Model," by Ghanaat, Y. and Clough, R.W., January 1982, (PB82 220 161)A07.

UCB/EERC-82/03 "Behavior of a Piping System under Seismic Excitation: Experimental Investigations of a Spatial Piping System supported by Mechanical Shock Arrestors," by Schneider, S., Lee, H.-M. and Godden, W. G., May 1982, (PB83 172 544)A09.

UCB/EERC-82/04 "New Approaches for the Dynamic Analysis of Large Structural Systems," by Wilson, E.L., June 1982, (PB83 148 080)A05.

UCB/EERC-82/05 "Model Study of Effects of Damage on the Vibration Properties of Steel Offshore Platforms," by Shahrivar, F. and Bouwkamp, J.G., June 1982, (PB83 148 742)A10.

UCB/EERC-82/06 "States of the Art and Pratice in the Optimum Seismic Design and Analytical Response Prediction of R/C Frame Wall Structures," by Aktan, A.E. and Bertero, V.V., July 1982, (PB83 147 736)A05.

UCB/EERC-82/07 "Further Study of the Earthquake Response of a Broad Cylindrical Liquid-Storage Tank Model," by Manos, G.C. and Clough, R.W., July 1982, (PB83 147 744)A11.

UCB/EERC-82/08 "An Evaluation of the Design and Analytical Seismic Response of a Seven Story Reinforced Concrete Frame," by Charney, F.A. and Bertero, V.V., July 1982, (PB83 157 628)A09.

UCB/EERC-82/09 "Fluid-Structure Interactions: Added Mass Computations for Incompressible Fluid," by Kuo, J.S.-H., August 1982, (PB83 156 281)A07.

UCB/EERC-82/10 "Joint-Opening Nonlinear Mechanism: Interface Smeared Crack Model," by Kuo, J.S.-H., August 1982, (PB83 149 195)A05.

UCB/EERC-82/11 "Dynamic Response Analysis of Techi Dam," by Clough, R.W., Stephen, R.M. and Kuo, J.S.-H., August 1982, (PB83 147 496)A06.

UCB/EERC-82/12 "Prediction of the Seismic Response of R/C Frame-Coupled Wall Structures," by Aktan, A.E., Bertero, V.V. and Piazzo, M., August 1982, (PB83 149 203)A09.

UCB/EERC-82/13 "Preliminary Report on the Smart 1 Strong Motion Array in Taiwan," by Bolt, B.A., Loh, C.H., Penzien, J. and Tsai, Y.B., August 1982, (PB83 159 400)A10.

UCB/EERC-82/14 "Shaking-Table Studies of an Eccentrically X-Braced Steel Structure," by Yang, M.S., September 1982, (PB83 260 778)A12.

UCB/EERC-82/15 "The Performance of Stairways in Earthquakes," by Roha, C., Axley, J.W. and Bertero, V.V., September 1982, (PB83 157 693)A07.

UCB/EERC-82/16 "The Behavior of Submerged Multiple Bodies in Earthquakes," by Liao, W.-G., September 1982, (PB83 158 709)A07.

UCB/EERC-82/17 "Effects of Concrete Types and Loading Conditions on Local Bond-Slip Relationships," by Cowell, A.D., Popov, E.P. and Bertero, V.V., September 1982, (PB83 153 577)A04.

UCB/EERC-82/18 "Mechanical Behavior of Shear Wall Vertical Boundary Members: An Experimental Investigation," by Wagner, M.T. and Bertero, V.V., October 1982, (PB83 159 764)A05.

UCB/EERC-82/19 "Experimental Studies of Multi-support Seismic Loading on Piping Systems," by Kelly, J.M. and Cowell, A.D., November 1982.

UCB/EERC-82/20 "Generalized Plastic Hinge Concepts for 3D Beam-Column Elements," by Chen, P. F.-S. and Powell, G.H., November 1982, (PB83 247 981)A13.

UCB/EERC-82/21 "ANSR-II: General Computer Program for Nonlinear Structural Analysis," by Oughourlian, C.V. and Powell, G.H., November 1982, (PB83 251 330)A12.

UCB/EERC-82/22 "Solution Strategies for Statically Loaded Nonlinear Structures," by Simons, J.W. and Powell, G.H., November 1982, (PB83 197 970)A06.

UCB/EERC-82/23 "Analytical Model of Deformed Bar Anchorages under Generalized Excitations," by Ciampi, V., Eligehausen, R., Bertero, V.V. and Popov, E.P., November 1982, (PB83 169 532)A06.

UCB/EERC-82/24 "A Mathematical Model for the Response of Masonry Walls to Dynamic Excitations," by Sucuoglu, H., Mengi, Y. and McNiven, H.D., November 1982, (PB83 169 011)A07.

UCB/EERC-82/25 "Earthquake Response Considerations of Broad Liquid Storage Tanks," by Cambra, F.J., November 1982, (PB83 251 215)A09.

UCB/EERC-82/26 "Computational Models for Cyclic Plasticity, Rate Dependence and Creep," by Mosaddad, B. and Powell, G.H., November 1982, (PB83 245 829)A08.

UCB/EERC-82/27 "Inelastic Analysis of Piping and Tubular Structures," by Mahasuverachai, M. and Powell, G.H., November 1982, (PB83 249 987)A07.

UCB/EERC-83/01 "The Economic Feasibility of Seismic Rehabilitation of Buildings by Base Isolation," by Kelly, J.M., January 1983, (PB83 197 988)A05.

UCB/EERC-83/02 "Seismic Moment Connections for Moment-Resisting Steel Frames.," by Popov, E.P., January 1983, (PB83 195 412)A04.

UCB/EERC-83/03 "Design of Links and Beam-to-Column Connections for Eccentrically Braced Steel Frames," by Popov, E.P. and Malley, J.O., January 1983, (PB83 194 811)A04.

UCB/EERC-83/04 "Numerical Techniques for the Evaluation of Soil-Structure Interaction Effects in the Time Domain," by Bayo, E. and Wilson, E.L., February 1983, (PB83 245 605)A09.

UCB/EERC-83/05 "A Transducer for Measuring the Internal Forces in the Columns of a Frame-Wall Reinforced Concrete Structure," by Sause, R. and Bertero, V.V., May 1983, (PB84 119 494)A06.

UCB/EERC-83/06 "Dynamic Interactions Between Floating Ice and Offshore Structures," by Croteau, P., May 1983, (PB84 119 486)A16.

UCB/EERC-83/07 "Dynamic Analysis of Multiply Tuned and Arbitrarily Supported Secondary Systems," by Igusa, T. and Der Kiureghian, A., July 1983, (PB84 118 272)A11.

UCB/EERC-83/08 "A Laboratory Study of Submerged Multi-body Systems in Earthquakes," by Ansari, G.R., June 1983, (PB83 261 842)A17.

UCB/EERC-83/09 "Effects of Transient Foundation Uplift on Earthquake Response of Structures," by Yim, C.-S. and Chopra, A.K., June 1983, (PB83 261 396)A07.

UCB/EERC-83/10 "Optimal Design of Friction-Braced Frames under Seismic Loading," by Austin, M.A. and Pister, K.S., June 1983, (PB84 119 288)A06.

UCB/EERC-83/11 "Shaking Table Study of Single-Story Masonry Houses: Dynamic Performance under Three Component Seismic Input and Recommendations," by Manos, G.C., Clough, R.W. and Mayes, R.L., July 1983, (UCB/EERC-83/11)A08.

UCB/EERC-83/12 "Experimental Error Propagation in Pseudodynamic Testing," by Shiing, P.B. and Mahin, S.A., June 1983, (PB84 119 270)A09.

UCB/EERC-83/13 "Experimental and Analytical Predictions of the Mechanical Characteristics of a 1/5-scale Model of a 7-story R/C Frame-Wall Building Structure," by Aktan, A.E., Bertero, V.V., Chowdhury, A.A. and Nagashima, T., June 1983, (PB84 119 213)A07.

UCB/EERC-83/14 "Shaking Table Tests of Large-Panel Precast Concrete Building System Assemblages," by Oliva, M.G. and Clough, R.W., June 1983, (PB86 110 210/AS)A11.

UCB/EERC-83/15 "Seismic Behavior of Active Beam Links in Eccentrically Braced Frames," by Hjelmstad, K.D. and Popov, E.P., July 1983, (PB84 119 676)A09.

UCB/EERC-83/16 "System Identification of Structures with Joint Rotation," by Dimsdale, J.S., July 1983, (PB84 192 210)A06.

UCB/EERC-83/17 "Construction of Inelastic Response Spectra for Single-Degree-of-Freedom Systems," by Mahin, S. and Lin, J., June 1983, (PB84 208 834)A05.

UCB/EERC-83/18 "Interactive Computer Analysis Methods for Predicting the Inelastic Cyclic Behaviour of Structural Sections," by Kaba, S. and Mahin, S., July 1983, (PB84 192 012)A06.

UCB/EERC-83/19 "Effects of Bond Deterioration on Hysteretic Behavior of Reinforced Concrete Joints," by Filippou, F.C., Popov, E.P. and Bertero, V.V., August 1983, (PB84 192 020)A10.

UCB/EERC-83/20 "Analytical and Experimental Correlation of Large-Panel Precast Building System Performance," by Oliva, M.G., Clough, R.W., Velkov, M. and Gavrilovic, P., November 1983.

UCB/EERC-83/21 "Mechanical Characteristics of Materials Used in a 1/5 Scale Model of a 7-Story Reinforced Concrete Test Structure," by Bertero, V.V., Aktan, A.E., Harris, H.G. and Chowdhury, A.A., October 1983, (PB84 193 697)A05.

UCB/EERC-83/22 "Hybrid Modelling of Soil-Structure Interaction in Layered Media," by Tzong, T.-J. and Penzien, J., October 1983, (PB84 192 178)A08.

UCB/EERC-83/23 "Local Bond Stress-Slip Relationships of Deformed Bars under Generalized Excitations," by Eligehausen, R., Popov, E.P. and Bertero, V.V., October 1983, (PB84 192 848)A09.

UCB/EERC-83/24 "Design Considerations for Shear Links in Eccentrically Braced Frames," by Malley, J.O. and Popov, E.P., November 1983, (PB84 192 186)A07.

UCB/EERC-84/01 "Pseudodynamic Test Method for Seismic Performance Evaluation: Theory and Implementation," by Shing, P.-S.B. and Mahin, S.A., January 1984, (PB84 190 644)A08.

UCB/EERC-84/02 "Dynamic Response Behavior of Kiang Hong Dian Dam," by Clough, R.W., Chang, K.-T., Chen, H.-Q. and Stephen, R.M., April 1984, (PB84 209 402)A08.

UCB/EERC-84/03 "Refined Modelling of Reinforced Concrete Columns for Seismic Analysis," by Kaba, S.A. and Mahin, S.A., April 1984, (PB84 234 384)A06.

UCB/EERC-84/04 "A New Floor Response Spectrum Method for Seismic Analysis of Multiply Supported Secondary Systems," by Asfura, A. and Der Kiureghian, A., June 1984, (PB84 239 417)A06.

UCB/EERC-84/05 "Earthquake Simulation Tests and Associated Studies of a 1/5th-scale Model of a 7-Story R/C Frame-Wall Test Structure," by Bertero, V.V., Aktan, A.E., Charney, F.A. and Sause, R., June 1984, (PB84 239 409)A09.

UCB/EERC-84/06 "R/C Structural Walls: Seismic Design for Shear," by Aktan, A.E. and Bertero, V.V., 1984.

UCB/EERC-84/07 "Behavior of Interior and Exterior Flat-Plate Connections subjected to Inelastic Load Reversals," by Zee, H.L. and Moehle, J.P., August 1984, (PB86 117 629/AS)A07.

UCB/EERC-84/08 "Experimental Study of the Seismic Behavior of a Two-Story Flat-Plate Structure," by Moehle, J.P. and Diebold, J.W., August 1984, (PB86 122 553/AS)A12.

UCB/EERC-84/09 "Phenomenological Modeling of Steel Braces under Cyclic Loading," by Ikeda, K., Mahin, S.A. and Dermitzakis, S.N., May 1984, (PB86 132 198/AS)A08.

UCB/EERC-84/10 "Earthquake Analysis and Response of Concrete Gravity Dams," by Fenves, G. and Chopra, A.K., August 1984, (PB85 193 902/AS)A11.

UCB/EERC-84/11 "EAGD-84: A Computer Program for Earthquake Analysis of Concrete Gravity Dams," by Fenves, G. and Chopra, A.K., August 1984, (PB85 193 613/AS)A05.

UCB/EERC-84/12 "A Refined Physical Theory Model for Predicting the Seismic Behavior of Braced Steel Frames," by Ikeda, K. and Mahin, S.A., July 1984, (PB85 191 450/AS)A09.

UCB/EERC-84/13 "Earthquake Engineering Research at Berkeley - 1984," by , August 1984, (PB85 197 341/AS)A10.

UCB/EERC-84/14 "Moduli and Damping Factors for Dynamic Analyses of Cohesionless Soils," by Seed, H.B., Wong, R.T., Idriss, I.M. and Tokimatsu, K., September 1984, (PB85 191 468/AS)A04.

UCB/EERC-84/15 "The Influence of SPT Procedures in Soil Liquefaction Resistance Evaluations," by Seed, H.B., Tokimatsu, K., Harder, L.F. and Chung, R.M., October 1984, (PB85 191 732/AS)A04.

UCB/EERC-84/16 "Simplified Procedures for the Evaluation of Settlements in Sands Due to Earthquake Shaking," by Tokimatsu, K. and Seed, H.B., October 1984, (PB85 197 887/AS)A03.

UCB/EERC-84/17 "Evaluation of Energy Absorption Characteristics of Bridges under Seismic Conditions," by Imbsen, R.A. and Penzien, J., November 1984.

UCB/EERC-84/18 "Structure-Foundation Interactions under Dynamic Loads," by Liu, W.D. and Penzien, J., November 1984, (PB87 124 889/AS)A11.

UCB/EERC-84/19 "Seismic Modelling of Deep Foundations," by Chen, C.-H. and Penzien, J., November 1984, (PB87 124 798/AS)A07.

UCB/EERC-84/20 "Dynamic Response Behavior of Quan Shui Dam," by Clough, R.W., Chang, K.-T., Chen, H.-Q., Stephen, R.M., Ghanaat, Y. and Qi, J.-H., November 1984, (PB86 115177/AS)A07.

UCB/EERC-85/01 "Simplified Methods of Analysis for Earthquake Resistant Design of Buildings," by Cruz, E.F. and Chopra, A.K., February 1985, (PB86 112299/AS)A12.

UCB/EERC-85/02 "Estimation of Seismic Wave Coherency and Rupture Velocity using the SMART 1 Strong-Motion Array Recordings," by Abrahamson, N.A., March 1985, (PB86 214 343)A07.

UCB/EERC-85/03 "Dynamic Properties of a Thirty Story Condominium Tower Building," by Stephen, R.M., Wilson, E.L. and Stander, N., April 1985, (PB86 118965/AS)A06.

UCB/EERC-85/04 "Development of Substructuring Techniques for On-Line Computer Controlled Seismic Performance Testing," by Dermitzakis, S. and Mahin, S., February 1985, (PB86 132941/AS)A08.

UCB/EERC-85/05 "A Simple Model for Reinforcing Bar Anchorages under Cyclic Excitations," by Filippou, F.C., March 1985, (PB86 112 919/AS)A05.

UCB/EERC-85/06 "Racking Behavior of Wood-framed Gypsum Panels under Dynamic Load," by Oliva, M.G., June 1985.

UCB/EERC-85/07 "Earthquake Analysis and Response of Concrete Arch Dams," by Fok, K.-L. and Chopra, A.K., June 1985, (PB86 139672/AS)A10.

UCB/EERC-85/08 "Effect of Inelastic Behavior on the Analysis and Design of Earthquake Resistant Structures," by Lin, J.P. and Mahin, S.A., June 1985, (PB86 135340/AS)A08.

UCB/EERC-85/09 "Earthquake Simulator Testing of a Base-Isolated Bridge Deck," by Kelly, J.M., Buckle, I.G. and Tsai, H.-C., January 1986, (PB87 124 152/AS)A06.

UCB/EERC-85/10 "Simplified Analysis for Earthquake Resistant Design of Concrete Gravity Dams," by Fenves, G. and Chopra, A.K., June 1986, (PB87 124 160/AS)A08.

UCB/EERC-85/11 "Dynamic Interaction Effects in Arch Dams," by Clough, R.W., Chang, K.-T., Chen, H.-Q. and Ghanaat, Y., October 1985, (PB86 135027/AS)A05.

UCB/EERC-85/12 "Dynamic Response of Long Valley Dam in the Mammoth Lake Earthquake Series of May 25-27, 1980," by Lai, S. and Seed, H.B., November 1985, (PB86 142304/AS)A05.

UCB/EERC-85/13 "A Methodology for Computer-Aided Design of Earthquake-Resistant Steel Structures," by Austin, M.A., Pister, K.S. and Mahin, S.A., December 1985, (PB86 159480/AS)A10 .

UCB/EERC-85/14 "Response of Tension-Leg Platforms to Vertical Seismic Excitations," by Liou, G.-S., Penzien, J. and Yeung, R.W., December 1985, (PB87 124 871/AS)A08.

UCB/EERC-85/15 "Cyclic Loading Tests of Masonry Single Piers: Volume 4 - Additional Tests with Height to Width Ratio of 1," by Sveinsson, B., McNiven, H.D. and Sucuoglu, H., December 1985.

UCB/EERC-85/16 "An Experimental Program for Studying the Dynamic Response of a Steel Frame with a Variety of Infill Partitions," by Yanev, B. and McNiven, H.D., December 1985.

UCB/EERC-86/01 "A Study of Seismically Resistant Eccentrically Braced Steel Frame Systems," by Kasai, K. and Popov, E.P., January 1986, (PB87 124 178/AS)A14.

UCB/EERC-86/02 "Design Problems in Soil Liquefaction," by Seed, H.B., February 1986, (PB87 124 186/AS)A03.

UCB/EERC-86/03 "Implications of Recent Earthquakes and Research on Earthquake-Resistant Design and Construction of Buildings," by Bertero, V.V., March 1986, (PB87 124 194/AS)A05.

UCB/EERC-86/04 "The Use of Load Dependent Vectors for Dynamic and Earthquake Analyses," by Leger, P., Wilson, E.L. and Clough, R.W., March 1986, (PB87 124 202/AS)A12.

UCB/EERC-86/05 "Two Beam-To-Column Web Connections," by Tsai, K.-C. and Popov, E.P., April 1986, (PB87 124 301/AS)A04.

UCB/EERC-86/06 "Determination of Penetration Resistance for Coarse-Grained Soils using the Becker Hammer Drill," by Harder, L.F. and Seed, H.B., May 1986, (PB87 124 210/AS)A07.

UCB/EERC-86/07 "A Mathematical Model for Predicting the Nonlinear Response of Unreinforced Masonry Walls to In-Plane Earthquake Excitations," by Mengi, Y. and McNiven, H.D., May 1986, (PB87 124 780/AS)A06.

UCB/EERC-86/08 "The 19 September 1985 Mexico Earthquake: Building Behavior," by Bertero, V.V., July 1986.

UCB/EERC-86/09 "EACD-3D: A Computer Program for Three-Dimensional Earthquake Analysis of Concrete Dams," by Fok, K.-L., Hall, J.F. and Chopra, A.K., July 1986, (PB87 124 228/AS)A08.

UCB/EERC-86/10 "Earthquake Simulation Tests and Associated Studies of a 0.3-Scale Model of a Six-Story Concentrically Braced Steel Structure," by Uang, C.-M. and Bertero, V.V., December 1986, (PB87 163 564/AS)A17.

UCB/EERC-86/11 "Mechanical Characteristics of Base Isolation Bearings for a Bridge Deck Model Test," by Kelly, J.M., Buckle, I.G. and Koh, C.-G., 1987.

UCB/EERC-86/12 "Effects of Axial Load on Elastomeric Isolation Bearings," by Koh, C.-G. and Kelly, J.M., 1987.

UCB/EERC-87/01 "The FPS Earthquake Resisting System: Experimental Report," by Zayas, V.A., Low, S.S. and Mahin, S.A., June 1987.

UCB/EERC-87/02 "Earthquake Simulator Tests and Associated Studies of a 0.3-Scale Model of a Six-Story Eccentrically Braced Steel Structure," by Whittaker, A., Uang, C.-M. and Bertero, V.V., July 1987.

UCB/EERC-87/03 "A Displacement Control and Uplift Restraint Device for Base-Isolated Structures," by Kelly, J.M., Griffith, M.C. and Aiken, I.G., April 1987.

UCB/EERC-87/04 "Earthquake Simulator Testing of a Combined Sliding Bearing and Rubber Bearing Isolation System," by Kelly, J.M. and Chalhoub, M.S., 1987.

UCB/EERC-87/05 "Three-Dimensional Inelastic Analysis of Reinforced Concrete Frame-Wall Structures," by Moazzami, S. and Bertero, V.V., May 1987.

UCB/EERC-87/06 "Experiments on Eccentrically Braced Frames with Composite Floors," by Ricles, J. and Popov, E., June 1987.

UCB/EERC-87/07 "Dynamic Analysis of Seismically Resistant Eccentrically Braced Frames," by Ricles, J. and Popov, E., June 1987.

UCB/EERC-87/08 "Undrained Cyclic Triaxial Testing of Gravels-The Effect of Membrane Compliance," by Evans, M.D. and Seed, H.B., July 1987.

UCB/EERC-87/09 "Hybrid Solution Techniques for Generalized Pseudo-Dynamic Testing," by Thewalt, C. and Mahin, S.A., July 1987.

UCB/EERC-87/10 "Investigation of Ultimate Behavior of AISC Group 4 and 5 Heavy Steel Rolled-Section Splices with Full and Partial Penetration Butt Welds," by Bruneau, M. and Mahin, S.A., July 1987.

UCB/EERC-87/11 "Residual Strength of Sand from Dam Failures in the Chilean Earthquake of March 3, 1985," by De Alba, P., Seed, H.B., Retamal, E. and Seed, R.B., September 1987.

UCB/EERC-87/12 "Inelastic Seismic Response of Structures with Mass or Stiffness Eccentricities in Plan," by Bruneau, M. and Mahin, S.A., September 1987.

UCB/EERC-87/13 "CSTRUCT: An Interactive Computer Environment for the Design and Analysis of Earthquake Resistant Steel Structures," by Austin, M.A., Mahin, S.A. and Pister, K.S., September 1987.

UCB/EERC-87/14 "Experimental Study of Reinforced Concrete Columns Subjected to Multi-Axial Loading," by Low, S.S. and Moehle, J.P., September 1987.

UCB/EERC-87/15 "Relationships between Soil Conditions and Earthquake Ground Motions in Mexico City in the Earthquake of Sept. 19, 1985," by Seed, H.B., Romo, M.P., Sun, J., Jaime, A. and Lysmer, J., October 1987.

UCB/EERC-87/16 "Experimental Study of Seismic Response of R. C. Setback Buildings," by Shahrooz, B.M. and Moehle, J.P., October 1987.

UCB/EERC-87/17 "Three Dimensional Aspects of the Behavior of R. C. Structures Subjected to Earthquakes," by Pantazopoulou, S.J. and Moehle, J.P., October 1987.

UCB/EERC-87/18 "Design Procedure for R-FBI Bearings," by Mostaghel, N. and Kelly, J.M., November 1987.

UCB/EERC-87/19 "Analytical Models for Predicting the Lateral Response of R C Shear Walls: Evaluation of their Reliability," by Vulcano, A. and Bertero, V.V., November 1987.

UCB/EERC-87/20 "Earthquake Response of Torsionally-Coupled Buildings," by Hejal, R. and Chopra, A.K., December 1987.

UCB/EERC-87/21 "Dynamic Reservoir Interaction with Monticello Dam," by Clough, R.W., Ghanaat, Y. and Qiu, X-F., December 1987.

UCB/EERC-87/22 "Strength Evaluation of Coarse-Grained Soils," by Siddiqi, F.H., Seed, R.B., Chan, C.K., Seed, H.B. and Pyke, R.M., December 1987.

UCB/EERC-88/01 "Seismic Behavior of Concentrically Braced Steel Frames," by Khatib, I., Mahin, S.A. and Pister, K.S., January 1988.

UCB/EERC-88/02 "Experimental Evaluation of Seismic Isolation of Medium-Rise Structures Subject to Uplift," by Griffith, M.C., Kelly, J.M., Coveney, V.A. and Koh, C.G., January 1988.

UCB/EERC-88/03 "Cyclic Behavior of Steel Double Angle Connections," by Astaneh-Asl, A. and Nader, M.N., January 1988.

UCB/EERC-88/04 "Re-evaluation of the Slide in the Lower San Fernando Dam in the Earthquake of Feb. 9, 1971," by Seed, H.B., Seed, R.B., Harder, L.F. and Jong, H.-L., April 1988.

UCB/EERC-88/05 "Experimental Evaluation of Seismic Isolation of a Nine-Story Braced Steel Frame Subject to Uplift," by Griffith, M.C., Kelly, J.M. and Aiken, I.D., May 1988.

UCB/EERC-88/06 "DRAIN-2DX User Guide.," by Allahabadi, R. and Powell, G.H., March 1988.

UCB/EERC-88/07 "Cylindrical Fluid Containers in Base-Isolated Structures," by Chalhoub, M.S. and Kelly, J.M. , April 1988.

UCB/EERC-88/08 "Analysis of Near-Source Waves: Separation of Wave Types using Strong Motion Array Recordings," by Darragh, R.B., June 1988.